NASA Technical Memorandum 103732

Property and Microstructural Nonuniformity in the Yttrium-Barium-Copper-Oxide Superconductor Determined from Electrical, Magnetic, and Ultrasonic Measurements

Don J. Roth
Lewis Research Center
Cleveland, Ohio

January 1991

NASA

PROPERTY AND MICROSTRUCTURAL NONUNIFORMITY IN THE YTTRIUM-BARIUM-COPPER-OXIDE SUPERCONDUCTOR DETERMINED FROM ELECTRICAL, MAGNETIC, AND ULTRASONIC MEASUREMENTS

Don J. Roth
National Aeronautics and Space Administration
Lewis Research Center
Cleveland, Ohio 44135

ABSTRACT

The purpose of this dissertation was to 1) characterize the effect of pore fraction on a comprehensive set of electrical and magnetic properties for the yttrium-barium-copper-oxide (YBCO) high temperature ceramic superconductor and 2) determine the viability of using a room-temperature, nondestructive characterization method to aid in the prediction of superconducting (cryogenic) properties. The latter involved correlating ultrasonic velocity measurements at room temperature with property-affecting pore fraction and oxygen content variations.

The dissertation is presented in two major chapters. In the first chapter, the use of ultrasonic velocity for estimating pore fraction in YBCO and other polycrystalline materials was reviewed, modeled and statistically analyzed. This chapter provided the basis for using ultrasonic velocity to interrogate microstructure. In the second chapter, 1) the effect of pore fraction (0.10 - 0.25) on superconductor properties of YBCO samples was characterized, 2) spatial (within-sample) variations in microstructure and superconductor properties were investigated and 3) the effect of

oxygen content on elastic behavior was examined. Experimental methods used included a.c susceptibility, electrical, and ultrasonic velocity measurements. Superconductor properties measured included transition temperature, magnetic transition width, transport and magnetic critical current density, magnetic shielding, a.c. loss, and sharpness of the voltage - current characteristic.

Superconductor properties including within-sample uniformity were generally poorest for samples containing the lowest (0.10) pore fraction. Ultrasonic velocity was linearly related to pore fraction thereby allowing sample classification. An ultrasonic velocity image constructed from measurements at 1 mm increments across a YBCO sample revealed microstructural variations that correlated with variations in magnetic shielding and a.c. loss behavior. Destructive examination using quantitative image analysis revealed pore fraction to be the varying microstructural feature.

Changes in superconducting behavior were observed consistent with changes in oxygen content. Velocity increases generally accompanied oxygen content increases, and this behavior was reversible. Similarly, elastic modulus increased with increasing oxygen content. Global patterns in velocity images were the same after oxidation and reduction treatments which correlated with destructive measurements showing insignificant changes in the pore distribution.

ACKNOWLEDGMENTS

The author wishes to especially thank Professor Mark R. DeGuire for his advice and encouragement during this investigation. Thanks are also extended to the other faculty members of the examination committee including Professors W. Williams and P. Pirouz, and Professor D. Hazony (Dept. of Electrical Engineering and Applied Physics). Thanks are additionally given to Dr. Leonard E. Dolhert at W.R. Grace, Inc. for providing many of the experimental specimens and thoughtful insight. I am also indebted to the many individuals at NASA - Lewis Research Center who provided timely assistance and helpful discussions.

TABLE OF CONTENTS

TABLE OF CONTENTS (cont.)

TABLE OF CONTENTS (cont.)

TABLE OF CONTENTS (cont.)

Chapter 1

Review, Statistical Analysis, and Modeling of The Utrasonic Velocity Method For Estimating The Pore Fraction in Yttrium-Barium-Copper-Oxide and Other Polycrystalline Materials

I. INTRODUCTION

The physical behavior of components manufactured from polycrystalline materials is in many cases directly dependent on the pore fraction (volume fraction of pores). As examples concerning key properties of technologically-important materials, pore fraction has been shown to affect: (1) the strength, toughness and modulus of structural and refractory materials such as steel (Goetzel, 1963), tungsten (Smith et al., 1966), SiC (Rice, 1977), Si_3N_4 (Rice, 1977), and Al_2O_3 (Rice, 1977), (2) the strength of nuclear fuel materials such as UO_2 (Burdick et al., 1956 and Knudsen et al., 1960), (3) the thermal shock behavior and strength of porcelain-based ceramics (Boisson et al., 1976 and Williams et al., 1963), (4) the dielectric and elastic properties of piezoelectric materials such as PZT (Patel et al., 1986), and (5) the critical current density, diamagnetic response, and modulus of superconducting ceramics such as $YBa_2Cu_3O_{7-x}$ (Alford et al., 1988a and 1988b; Blendell et al., 1987 and Hwu et al., 1987). In the latter case, Alford (1988a) has shown that pore fraction variations on the order of 1 percent in $YBa_2Cu_3O_{7-x}$ samples can result in an order of magnitude variation in critical current density. In such cases where physical properties are directly

dependent on pore fraction, the measurement of pore fraction becomes important in the quality assurance process for the material.

Currently, various methods are available for measuring the pore fraction of polycrystalline materials. The most common include dry-weight dimensional and liquid immersion (Jones et al., 1972). Other methods for obtaining pore fraction include estimates from optical areal analysis measurements (Vander Voort, 1984) and estimates from x-ray attenuation measurements (Clark et al., 1957). The choice of method is dependent on experimental conditions including sample geometry and whether additional investigation is required with the sample. For example, the dry-weight dimensional method can only be used for regularly-shaped samples with uniform dimensions such as cubes and rods, while liquid immersion is potentially destructive due to liquid infusion into the sample. Because of the lack of a truly universal pore fraction measurement method, it seems worthwhile to consider additional measurement / estimation methods that may be useful and convenient in certain laboratory and industrial situations. In this study, we consider the ultrasonic velocity measurement method for estimating pore fraction.

Ultrasonic velocity is a relatively simple measurement that requires the material specimen to have one pair of sides flat and parallel (Papadakis, 1972). The advantages of this method are that it is nondestructive and measurements can be made on different regions of a single specimen. Smith et al. (1966) and Nagarajan (1971) were some of the first researchers to establish empirical

correlations between pore fraction and ultrasonic velocity for polycrystalline materials. The correlations appeared relatively linear over the pore fraction ranges investigated. Smith's work concerned metallic samples while Nagarajan's work concerned ceramic samples. Other researchers began to investigate similar correlations with different materials. Here, a review, model and statistical analysis for these empirical correlations between ultrasonic velocity and pore fraction for polycrystalline materials is presented. First, a semi-empirical model is developed showing the origin of the linear relationship between ultrasonic velocity and pore fraction. Then, scatter plots of velocity versus percent porosity data are shown for Al_2O_3, CuO, MgO, porcelain-based ceramics, PZT, SiC, Si_3N_4, steel, tungsten, UO_2, $(U_{0.30}Pu_{0.70})C$, and $YBa_2Cu_3O_{7-x}$. Linear regression analysis produced predicted slope, intercept, correlation coefficient, level of significance, and confidence interval statistics for the data. Additionally, velocity values predicted from regression for fully-dense materials are compared with those calculated from elastic properties.

II. SEMI-EMPIRICAL MODEL

When there are no boundary effects present, the velocity of a longitudinal ultrasonic wave traveling in a solid is related to the elastic properties and density of the solid by (Szilard, 1982):

$$V = \{[E(1 - \nu)]/[\rho(1 + \nu)(1 - 2\nu)]\}^{1/2} \qquad (1)$$

where V, E, ρ, and ν are the velocity, elastic modulus, bulk

density, and Poisson's ratio, respectively, of the material. (The velocity of a shear ultrasonic wave traveling in a solid is related to the elastic properties and density of the solid by:

$$V = \{E/[2\rho(1 + \nu)]\}^{1/2} \qquad (1(a))$$

An "apparent" modulus (Rice, 1977) for porous materials can be considered which depends on the pore fraction. Several early empirical investigations provided evidence that the modulus increases exponentially with decreasing pore fraction according to (Ryshkewitch, 1953 and Spriggs, 1961):

$$E = E_o \exp(-bP') \qquad (2)$$

where E_o is the elastic modulus of a fully-dense (nonporous) material, b is an empirically-determined constant related to pore shape, pore distribution, and the ratio of open-to-closed pores, and P' is the pore fraction. The use of equation (2) to evaluate E_o by extrapolation from fitted experimental data has sometimes resulted in large discrepancies between the extrapolated and observed values (Soroka et al., 1968). An alternative to equation (2) has been suggested to describe the relationship between elastic modulus and pore fraction (Phani et al., 1986):

$$E = E_o(1 - P')^{2n+1} \qquad (3)$$

where n, like b, is an empirically-determined constant that

depends on pore distribution and pore geometry factors.[1]

Pore fraction, P′, can be expressed as:

$$P' = (1 - (\rho/\rho_o)) \tag{4}$$

where ρ_o is the theoretical (nonporous material) density. Rearranging equation (4) allows us to express bulk density as a function of pore fraction:

$$\rho = \rho_o(1 - P') \tag{5}$$

Substituting equations (3) and (5) into equation (1) allows velocity to be expressed as:

$$V = V_o(1 - P')^n \tag{6}$$

where V_o is a constant for a given material equal to:

$$V_o = \{[E_o(1 - \nu)]/[\rho_o(1 + \nu)(1 - 2\nu)]\}^{1/2} \tag{7}$$

V_o is the velocity in a fully-dense (nonporous) material, i.e., the "theoretical" velocity. (For shear waves:

$$V_o = (E_o/[2\rho_o(1 + \nu)])^{1/2} \tag{7(a)}$$

The general case for all n can be shown by expanding the right- hand side of equation (6) using the binomial theorem (Swokowski, 1975) so that:

---

[1]Concerning the relationship between Poisson's ratio and pore fraction, most of the limited studies of Poisson's ratio show it decreasing with increasing pore fraction less rapidly than for elastic modulus (Rice, 1977). In this development, it is assumed that Poisson's ratio is independent of pore fraction.

$$V = V_o(1 + [n(-P')] + [n(n - 1) \times (-P')^2/2!] + \ldots + [n(n - 1) \times \ldots (n - k + 1)(-P')^k/k!] + \ldots) \quad (8)$$

where k is the term in the binomial series minus 1. From the ratio test, equation (8) is absolutely convergent for $|P'| < 1$.

Setting $n = 1$ in equations (3) and (8) results in good agreement for a number of materials over a wide pore fraction range ($0.1 < P' < 0.7$) (Phani et al., 1986). In this case, the right-hand side of equation (8) is reduced such that:

$$V = V_o(1 - P') \quad (9)$$

Equation (9) shows a linear relationship between velocity and pore fraction and is the basis for selecting linear regression to analyze the empirical correlations reported in this study.

It is sometimes convenient to discuss the relationship between velocity and percent porosity, %P, where:

$$\%P = (P')100 \quad (10)$$

Solving equation (10) for P′ and substituting into equation (9) gives:

$$V = m(\%P) + V_o \quad (11)$$

where

$$m = -V_o/100 \quad (12)$$

Equation (11) shows a linear relationship between V and %P where m and V_o are the slope and intercept, respectively.

We can also define a "percent theoretical velocity," %TV, where:

$$\%TV = (V/V_o)100 \tag{13}$$

Solving equation (13) for V and substituting into equation (11) gives:

$$\%TV = m'(\%P) + 100 \tag{14}$$

where

$$m' = (m)100/V_o \tag{15}$$

Equation (14) shows a linear relationship between %TV and %P where m′ and 100 are the slope and intercept, respectively. Presenting the velocity versus pore fraction relationship in terms of equation (14) is essentially a normalization procedure in that the theoretical velocity of a material and the type of wave (longitudinal or shear) used in the velocity measurement are "removed" as variables. From the derivative of equation (14), the following quantity can be defined:

$$(1/m') = (\Delta\%P/\Delta\%TV) \tag{16}$$

where Δ is "change in."

III. DATA EXTRACTION PROCEDURE

Almost all of the data presented in this study were obtained from previously-published studies. The policy employed was that all of the available data should be tabulated and analyzed. In most cases, the reference provided V versus ρ data, either in the form of a table or plot. In some cases, the reference provided percent theoretical density ($\%\rho_o$) or P′ values instead of ρ values. Where necessary, ρ and $\%\rho_o$ values were converted to %P

values with the aid of equations (4) and (10).[2]

IV. STATISTICAL ANALYSIS METHOD

Linear regression analysis and its associated statistics utilized in this study are briefly described in the next several paragraphs. The authors felt that a comprehensive set of statistics was necessary for this analysis because of the variation among data sets in the number of velocity measurements and the pore fraction range over which those measurements were made.

Linear regression analysis is concerned with the problem of predicting or estimating the value of a (dependent) variable (V and %TV in eqs. (11) and (14), respectively) on the basis of another (independent) variable (%P in eqs. (11) and (14)). For the sake of simplicity, we have applied the classical regression model (Acton, 1959) which involves the following assumptions. V (and %TV) has been assumed to contain all the error while %P has

---

[2]In most cases, the references provided V and ρ data to 3 or 4 significant figures. For the sake of uniformity, all data and subsequent calculations including statistical values are presented in this report to at most 3 significant figures.

been assumed to contain no error.[3] The variance in V (and %TV) has been assumed to be constant for all values of %P, and the distribution about V has been assumed to be normal with mean values lying exactly on the regression line. It also has been assumed that only one V value was measured at a particular %P.

Linear regression analysis results in predicted slope (m and m′ in eqs. (11) and (14), respectively) and intercept (V_o in eq. (11)) values that describe the relationship between V (and %TV) and %P. The Pearson product-moment correlation coefficient and level of significance statistics describe the quality of the regression. The correlation coefficient measures the strength of the linear relationship for the sample data. The level of significance, determined by the number of data points and the value of the correlation coefficient, determines an acceptance or confidence region for the regression. A level of significance of 0.025 corresponds to a 95 percent confidence region. The smaller (better) the level of significance, the

---

[3]An analysis assuming errors in both variables is significantly more complicated. For some data sets, the uncertainty in %P may in fact be comparable to that of V. The total uncertainties in each of %P and V including experimental uncertainties, uncertainties in extracting data from plots, and different assumed values of ρ_o are estimated to be less than 5 percent in all cases.

lower the probability that the value of the correlation coefficient can be attributed to chance.

Confidence intervals for the predicted slope, intercept, and mean velocity values (the mean of further velocity measurements obtained at some %P value) are also presented. The 95 percent symmetric confidence interval was chosen for the analysis.[4] In practical terms, the 95 percent confidence interval means that in 95 percent of the cases, the true value of the parameter will fall within the calculated interval.

V. REVIEW AND ANALYSIS

The review and statistical analysis are presented in table 1 and figures 1 to 61. Most of the figures show scatter plots of V versus %P data for Al_2O_3 (Arons et al., 1982; Claytor et al., 1989; Jones et al., 1986; Nagarajan, 1971 and Stang, 1989), CuO (Roth et al., 1990a), MgO (Kupperman et al., 1984), porcelain-based ceramics (Boisson et al., 1976; Filipczynski et al., 1966; Shyuller et al., 1988), PZT (Patel et al., 1986), SiC (Baaklini et al., 1989; Friedman et al., 1987; Gruber et al., 1988; Klima et al., 1981

---

[4]The choice of a particular size confidence interval is "economic" rather than mathematical. It depends directly on the cost of an error, and hence on the frequency with which one can afford to be wrong. High confidence intervals lead to wide limits, and if these limits are too wide to be useful, the gap between them must be reduced either by accepting less confidence or by increasing the amount of data (Acton, 1959).

and Stang, 1989), Si_3N_4 (Derkacs et al., 1976; Mclean et al., 1975 and Thorp et al., 1985), steel (Papadakis et al., 1979), tungsten (Smith et al., 1966), UO_2 (Panakkal et al., 1984), $(U_{0.30}Pu_{0.70})C$ (Ghosh et al., 1985), and $YBa_2Cu_3O_{7-x}$ (Blendell et al., 1987; Gaiduk et al., 1988; Ledbetter et al., 1987; Roth et al., 1990b and Round et al., 1987). Table 1 presents the linear regression statistics corresponding to the scatter plots. The 95 percent confidence interval for the predicted slope and intercept values are presented in table 1 while the 95 percent confidence interval for mean predicted velocity values is shown by dashed lines on the scatter plots.[5] The quantity (Δ%P/Δ%TV) is provided for all plot lines in the corresponding table entries. (Note that this quantity also has a confidence interval associated with it, the width of which is similar to that for m').

Pertinent information concerning the reference's study

---

[5]Several issues concerning the 95 percent confidence intervals for predicted intercept, slope, and mean velocity values need to be noted. First, the assumption of only one V value for a particular %P value is a conservative assumption that we know is false for some of the data sets in this review (see "comments" in table 1). This assumption tends to make the limits of the confidence interval wider (worse) than if the confidence interval was calculated based on the mean of several velocity measurement values at a particular %P value. Second, the confidence intervals for predicted slope and intercept may not appear exactly symmetric in table 1 due to the round off procedure. Third, the 95 percent confidence interval for mean predicted velocity values is in most cases drawn (dashed line) over the entire %P range shown. In several cases, the interval extends beyond the %P range where velocity data exists. In these cases, the interval widens (worsens) as expected where no data exists.

including ultrasonic technique, measurement uncertainties,[6] microstructural anisotropy, material processing techniques, and velocity variation within specimens is also included in table 1. A blank table entry indicates that the information was unavailable. The "comments" in table 1 give the number of data points for that particular reference and in some cases point out a major conclusion determined by the reference concerning the V versus %P data.

The figures are organized as follows. Figures 1 to 4, 6 to 9, 12 to 15, 17 to 23, 25, 26, 28, 29, 33 to 36, 38, 40 to 42, 44, 45, 48 to 50, 52 to 54, 57 to 59, show scatter plots of V (and %TV) versus %P for a single reference's data.[7] Results of multiple investigations for a specific material were also combined and analyzed as one data set in figures 5, 10, 37, 43, 46, 55, and 60. Additionally, plots comparing predicted (in most cases) regression lines obtained for a specific material from different investigations are given in figures 11, 16, 24, 27, 30

---

[6]In most cases, the experimental uncertainties in the velocity and density measurements were provided by the reference. In the event that they were not, the uncertainties were estimated from the reference's description of samples and measurement techniques, and from experience.

[7]Because the range of %P values for which velocity measurements were obtained varied from reference to reference, the ranges shown on the horizontal and vertical axes of the plots differ from one to the next, i.e., the plots are not standardized. In some cases, the plot axes had to be adjusted to allow the presentation of the 95 percent confidence interval for mean predicted velocity values.

to 32, 39, 47, 51, 56, and 61. Where applicable for a material, scatter plots of longitudinal wave velocity data are presented before plots of shear wave velocity data. For most scatter plots, the solid line drawn is the linear regression line determined from the least-squares technique. For the plots with only two data points, a line is drawn through the points. In this case, the correlation coefficient, level of significance, and confidence interval statistics are not applicable.

VI. DISCUSSION

A. General Observations

Correlation coefficients with magnitudes greater than 0.95 were obtained in 31 out of 42 cases. Levels of significance with magnitudes less than 0.025 were obtained in 36 out of 42 cases. For longitudinal wave velocity, predicted intercepts (V_o) ranged from 0.443 cm/μsec for unpoled PZT4 and unpoled PZT5 of Patel et al. (1986) to 1.23 cm/μsec for SiC of Baaklini et al. (1989). For shear wave velocity, predicted intercepts (V_o) ranged from 0.313 cm/μsec for $YBa_2Cu_3O_{7-x}$ to 0.786 cm/μsec for SiC of Stang (1989). The quantity (Δ%P/Δ%TV) ranged from -0.52 for porcelain of Boisson et al. (1976) and poled PZT4 of Patel et al. (1986) to -8.26 for porcelain T2 of Shyuller et al. (1988). It is understandable that these quantities vary from one material to the next since each material has different elastic properties and density (eq. (1)). Predicted intercepts (V_o) for a specific material from different investigations

agree fairly well (see the plots and tabular entries for Al_2O_3, SiC, and Si_3N_4). Predicted slopes for a specific material from different investigations agree fairly well in most cases. However, significant slope disparity is evident for Al_2O_3; this may be due to the limited percent porosity range for the data of Stang (1989) and Arons et al. (1982) and the inclusion of green (not sintered) and prefired (partially sintered) sample data in the cases of Claytor et al. (1989) and Jones et al. (1986). For Stang (1989), the limited pore fraction range over which data was obtained is manifested in extremely wide 95 percent confidence limits for predicted slope, intercept and mean velocity values. In fact, one of the bounds for the confidence limits for predicted slope is a positive value.

Table 2 compares V_o predicted from regression analysis with that calculated from equations (7) (longitudinal wave velocity) and (7a) (shear wave velocity) for several materials. Values of elastic modulus, Poisson's ratio, and density for fully-dense (single crystal and/or polycrystalline) materials used in the calculation are presented. The values of V_o predicted from regression and those obtained from calculation agree within approximately 17 percent in 16 out of 16 cases, and within approximately 6 percent in 11 out of 16 cases.

B. Other Microstructural Variables Affecting Velocity

Although pore fraction seems to be a significant and perhaps the major microstructural feature affecting ultrasonic velocity,

several references point to other microstructural variables having an impact on velocity. These include slight compositional variations (Shyuller et al., 1988), preferred domain orientation (Patel et al., 1986), particle contact anisotropy (Papadakis et al., 1979), pore size distribution and geometry (Smith et al., 1966), and type of agglomeration (Jones et al., 1986). These variables may result in differences in predicted intercept (V_o) and slope for what is believed to be the same material from different investigations. Thus, the authors feel that the most accurate and precise application of the ultrasonic velocity method for estimating pore fraction first requires the development of accurate velocity versus pore fraction relationships / calibrations for the specific material of interest.

C. Ramifications

The estimation of batch-to-batch, sample-to-sample and within-sample pore fraction variations for a material can be accomplished if the quantity (Δ%P/Δ%TV) is known with reasonable confidence for that material. The nondestructive mapping of spatial pore fraction variations within a sample by means of an ultrasonic scanning technique has been reported recently (Generazio et al., 1988 and 1989a, and Kunnerth et al., 1989). This approach may also be useful in the analysis of the uniformity of composite materials (Gruber et al., 1988).

D. Concluding Remarks

A review, model and statistical analysis of the ultrasonic

velocity method for estimating the pore fraction in polycrystalline materials was presented. First, a semi-empirical model was developed showing the origin of the linear relationship between ultrasonic velocity and pore fraction. Then, from a compilation of data produced by many researchers, scatter plots of velocity versus percent porosity data were shown for Al_2O_3, CuO, MgO, porcelain-based ceramics, PZT, SiC, Si_3N_4, steel, tungsten, UO_2, $(U_{0.30}Pu_{0.70})C$, and $YBa_2Cu_3O_{7-x}$. Linear regression analysis produced slope, intercept, correlation coefficient, level of significance, and confidence interval statistics for the data. Velocity values predicted from regression analysis for fully-dense materials were in good agreement with those calculated from elastic properties. The estimation of batch-to-batch, sample-to-sample, and within-sample variations in pore fraction for a material can be accomplished with ultrasonic velocity measurements if reasonable confidence exists in the velocity versus percent porosity linear relationship.

Chapter 2

The Effect of Pore Fraction and Oxygen Content on Superconductor and Elastic Behavior in Untextured Polycrystalline Yttrium-Barium-Copper-Oxide

I. INTRODUCTION

The last several years have seen the remarkable development of a new class of ceramics that exhibit superconductivity to unprecedently high temperatures (Bednorz et al., 1986; Chu et al., 1987; Maeda et al, 1988, and Sheng et al., 1988). The 90K superconductor $YBa_2Cu_3O_{7-x}$ (YBCO) in its untextured polycrystalline form is the subject of this investigation. This material has shown potential for low-field magnetic shielding applications (Taylor et al., 1990). In untextured form, YBCO displays an undesirable variation in superconductor (electrical and magnetic) properties (table 3). As is the case for conventional superconductors (Ekin, 1983), this variation is likely to be due to batch-to-batch, sample-to-sample, and even within-sample variations/gradients in composition and microstructure. Additional property variations may result from different sample geometries (Alford et al., 1990; Cave et al., 1989; Chen et al., 1989; Dersch et. al., 1988; Osmura et al., 1990; and Stephens, 1989) and test specifications (Evetts et al., 1989) making study-to-study comparisons difficult.

In this study, 1) the effect of pore fraction (0.10 - 0.25) on

superconductor properties of YBCO samples was characterized, 2) spatial (within-sample) variations in microstructure and superconductor properties were investigated and 3) the effect of oxygen content on elastic behavior was examined. Experimental methods used included a.c. susceptibility, electrical and ultrasonic measurements.

Measured superconductor properties from susceptibility and electrical measurements were transition temperature (T_c), magnetic transition width (ΔT_{cm}), transport and magnetic critical current density (J_c and j_c, respectively), magnetic shielding, a.c. loss, and the sharpness of the voltage - current characteristic (n-value). Models of current flow and magnetic behavior in granular superconductors were reviewed. Measured values of properties were compared with those predicted from the models.

Ultrasonic velocity measurements at room temperature were correlated with changes in YBCO microstructure and oxygen content to aid in the prediction of superconducting (cryogenic) properties. Ultrasonic scan techniques were employed to examine within-sample microstructural and property uniformity. Optical image analysis was performed on several sample sections to quantify microstructural variations observed from ultrasonic scanning. Nondestructive, room-temperature ultrasonic methods are likely to prove useful in the examination of all bulk, high temperature superconductor materials including the textured (higher-J_c) materials.

II. BACKGROUND

A. Historical Development of Superconductors

The discovery of superconductivity at temperatures above the liquid nitrogen boiling point has been hailed as one of the most important scientific developments of the century. Here, we briefly review the chronology of the rise in the superconducting transition temperature (Ekin, 1983 and Ginsberg, 1989). Kammerlingh Onnes (1911) discovered superconductivity in mercury at 4.2 K in 1911. The highest observed values of T_c moved slowly upwards: Pb (T_c = 7.19 K) in 1913, Nb (T_c = 9.25K) in 1930, NbN (T_c = 15K) in 1940, Nb_3Sn (T_c = 18.3K) in 1950, and $Nb_3(Al,Ge)$ (T_c = 20.0K) in 1968. In the mid-1970's, Gavaler (1973) and Testardi et al. (1974) working independently found that sputtered films of Nb_3Ge showed T_c's of 22.3 K and 23.2 K, respectively. The first oxide superconductors with T_c > 10 K, $LiTi_2O_4$ (T_c = 13.7 K) and $BaPb_{1-x}Bi_xO_3$ (T_c = 13 K), were discovered by Johnston et al. (1973) and Sleight et al. (1975), respectively.

In 1986, a significant increase in T_c was achieved by Bednorz and Muller (1986) who observed that La-Ba-Cu-O ($La_{2-x}Ba_xCuO_4$) material began its superconducting transition as it was cooled below 35 K. Early in 1987, it was found that substitution of Sr for Ba in the La-Ba-Cu-O material raised the superconductivity onset

temperature to approximately 40 K (Tarascon et al., 1987a and Van Dover et al., 1987). Soon thereafter, Y-Ba-Cu-O ($YBa_2Cu_3O_{7-x}$) material (T_c = 90 K) became the first material capable of becoming superconducting in liquid nitrogen (Chu et al, 1987 and Tarascon et al., 1987b). In 1988, two other compound groups exhibiting even higher transition temperatures were discovered. A Bi-Sr-Ca-Cu-O ($Bi_2Sr_2Ca_2Cu_3O_{10}$) material had a T_c of approximately 110 K (Maeda et al., 1988) while Tl-Ba-Ca-Cu-O ($Tl_2Ba_2Ca_2Cu_3O_{10}$) material had a T_c of approximately 125 K (Sheng et al., 1988 and Hermann et al., 1988).

B. Structure of YBCO

$YBa_2Cu_3O_{7-x}$ ($7.0 \leq 7-x \leq 6.8$) is orthorhombic (figure 62) (Beyers et al., 1989 and Clarke, 1987). The unit cell parameters are a = 3.82 $\pm$ 0.005 A°, b = 3.89 $\pm$ 0.005 A°, and c = 11.68 $\pm$ 0.01 A° (a < b = c/3) (Wong-Ng et al., 1987). The unit cell can be described as a stacked sequence of seven planes along the c-axis. The planes are Cu-O, Ba-O, Cu-O, Y, Cu-O, Ba-O, and Cu-O. Y is surrounded by 8 nearest neighbor O's, Ba is surrounded by 10 nearest neighbor O's, and Cu is surrounded by either 4 or 5 nearest neighbor O's. Ordered O vacancies exist along the a-axis in the Cu-O basal plane. Cu-O chains exist along the b-axis in the basal planes. Changes in oxygen content are accommodated primarily by changes in the O occupancy on the basal planes (Clarke, 1987). Gallagher et al. (1987), found that as oxygen content decreases, c and a expand while b contracts.

If YBCO has approximately 6.0 to 6.5 O atoms per formula unit, it is tetragonal with unit cell parameters a = 3.86 $\pm$ 0.005 A° and c = 11.84 $\pm$ 0.01 A° (Wong-Ng et al., 1988). YBCO in this oxygen-deficient structure is semiconducting (Iye, 1989). Additional $YBa_2Cu_3O_{7-x}$ structures include the orthorhombic II (OII) and tetragonal T′ phase. The OII phase is characterized by approximately 6.5 - 6.8 O atoms per formula unit, a < b < c/3, (Chen et al., 1987 & Gallagher et al., 1987) and poorer superconducting properties (Beyers et al., 1989). An example of the OII structure is $YBa_2Cu_3O_{6.56}$ having unit cell parameters a = 3.834 A°, b = 3.881 A°, and c = 11.736 A°, with resistive transition onset at about 60 K (Wong-Ng et al., 1988). The tetragonal T′ phase is characterized by an oxygen content greater than 7.0 atoms per formula unit, a short c axis approximately equal to 11.60 A°, and semiconducting behavior (Lay, 1988; Nakazawa et al., 1987, and Torardi et al., 1987).

The cell volume for tetragonal YBCO with 6.0 O atoms per formula unit is 176.20 A^{o3} and its cell density is 6.125 g/cm^3. The cell volume for orthorhombic YBCO with 7.0 atoms per formula unit is 173.30 A^{o3} and its cell density is 6.381 g/cm^3. Thus, the tetragonal to orthorhombic structure transformation (oxygen gain) will result in volume decrease and bulk density increase. During the oxygen annealing procedure normally required to transform YBCO from nonsuperconducting (tetragonal) to superconducting (orthorhombic), O atoms fill the vacancies in the basal planes. Twinning within grains normally accompanies the structural transformation in

polycrystalline YBCO to relieve the induced shear stresses (Hoff et al., 1989). Observation and quantification of twinning thus provides a means for characterizing the degree of oxygenation (Clarke et al., 1989).

The YBCO tetragonal and orthorhombic structures can be differentiated in x-ray diffraction by the relative intensities of the peaks occurring at $2\theta = 32° - 33°$ as well as by least-squares refinement of the x-ray data to obtain the lattice parameters (Wong-Ng et al., 1987 and 1988). For the orthorhombic structure, the higher angle peak (103) has about twice the intensity of the lower angle peak (013) whereas for the tetragonal structure, the (013) has about twice the intensity of the (103) peak.

C. Microstructural and Compositional Effects For YBCO

1. General

Compositional and microstructural variations in YBCO result from differences in processing (Beyers et al., 1987; Cima et al., 1987; Clarke et al., 1989; Panson et al., 1987 and Yan et al., 1988a), handling conditions (contamination effects) (Yan, et al., 1988a and 1988b), storage conditions (temperature and humidity) (Frase et al., 1987; Gherardi et al., 1990; Loegel, et al., 1989 and Yan et al., 1987) and aging (Gherardi et al., 1990 and Loegel et al., 1989). The effects of oxygen content, phase purity, and texture on superconducting properties of the high-T_c materials has been characterized in previous studies. Oxygen content has been

shown to affect J_c, (Alford et al., 1988a), resistivity and susceptibility (Beyers et al., 1987 and 1989; Clarke et al., 1989; Dubots et al., 1988 and Tarascon et al., 1987c). $YBa_2Cu_3O_{7-x}$ exhibits its best superconducting properties for $6.8 < 7-x < 7.0$ (Beyers et al., 1989 and Clarke et al., 1989). Broad or depressed (resistive and magnetic) normal-to-superconducting transitions may result from reduced oxygen content or other compositional variations (Beyers et al., 1987; Clarke et al., 1989 and Park et al., 1988). Low J_c's may result from incomplete oxygenation of the YBCO bulk (Alford et al., 1988a).

An increased presence of second phases (such as silicon impurity, pores, etc.) in polycrystalline samples of YBCO generally limits critical current densities (Alford et al., 1988a; Camps, et al., 1987; Clarke, 1988; Ekin, 1987 and Newcomb et al., 1988) and susceptibilities (Hwu et al., 1987), and increases (worsens) the transition width (Cima et al., 1987 and Gaiduk et al., 1988). The existence of second-phase particles at grain boundaries is thought to cause weak coupling between high-J_c grains, thus limiting the bulk transport J_c (Clarke, 1988; Clarke et al., 1989; Ekin, 1987; Zandbergen, et al., 1990). Disruptions in the crystal lattice as small as the coherence length can result in weak coupling. Thus, weak coupling may also be caused by the mismatch between neighboring grains with different orientation, or by planar defects inside grains (Barbara et al., 1988; Ekin, 1987 and Deutscher et al., 1987). Bulk untextured YBCO samples have maximum J_c's on the order of 10^3 A/cm^2

at 77 K in zero applied magnetic field. Optimal granular orientation in bulk YBCO samples increases maximum J_c to 10^4 - 10^5 A/cm^2 (Jin et al., 1988 and Morita, et al., 1989). High quality YBCO thin films have maximum J_c's on the order of 10^5 - 10^6 A/cm^2 (Chaudhari et al., 1987 and Deshpandey et al., 1989).

2. Previously-Reported Pore Fraction Effects for YBCO

The effect of pore fraction on some superconducting properties has been previously investigated. Indications are that pore fraction can both directly and indirectly affect behavior. Concerning direct effects, pores and cracks located at grain boundaries may 1) increase the thickness of the tunnel barrier resulting in weaker coupling (Clarke, 1988) and 2) reduce the area of interconnection at grain boundaries for supercurrents to flow (Ekin, 1987). In either case, as pore fraction increases, reduced J_c's are expected. A study by Alford et al. (1988a) generally shows increasing J_c with decreasing pore fraction over the pore fraction range of 0.10 to 0.30.

Microcracks result from the axial thermal contraction anisotropy of YBCO grains upon 1) cooling from sintering and 2) transformation from the tetragonal to orthorhombic crystal structure during oxygenation. Higher density samples have also been seen to contain large, J_c-limiting macrocracks resulting from the oxygenation-induced stresses present between the incompletely-oxygenated bulk and fully-oxygenated surface (Clarke et al., 1989).

It has been speculated that pore fraction and distribution may

affect flux pinning characteristics (Saint-James et al., 1969) since several studies indicate that YBCO behaves as a conventional type II superconductor (appendix A). This is important since increased flux pinning site density leads to increased J_c (Tenbrink et al., 1990). Increased number of (very small) pores within superconducting grains may increase the pinning site density (Newcomb et al., 1988 and Kupfer et al., 1988a).

Concerning an indirect effect of pore fraction on superconductor behavior, pore fraction and type determine the oxygen transport mechanism during the critical oxygen annealing step required to transform YBCO from non-superconducting to superconducting. Alford et al. (1988a) has shown that pore fraction variations on the order of 0.01 - 0.03 in polycrystalline YBCO samples can result in an order of magnitude variation in J_c. This effect is thought to be due to the transition from interconnected porosity at larger pore fractions (approximately $\geq$ 0.10 pore fraction) to isolated closed pores at smaller pore fractions (approximately $\leq$ 0.10 pore fraction). Interconnected pore channels are desirable for rapid oxygen transport through the sample during oxygen annealing. Pore closure forces oxygen diffusion to occur by relatively slow bulk diffusion, and a much greater annealing time is required to achieve complete oxygenation. Samples containing smaller pore fractions receiving an insufficient annealing period may contain oxygen-deficient regions throughout the bulk thereby leading to dramatically decreased J_c. It is speculated that for YBCO materials

close to theoretical density, several hundred hours of oxygen annealing would be necessary to ensure complete oxygenation throughout the microstructure (Alford et al., 1988a and Clarke et al., 1989). Clarke et al. (1989) believes that the optimum microstructure for best YBCO superconductor properties is one having fine-scale interconnected porosity to ensure rapid oxidation (and fine grain size (approximately 1 um) to avoid microcracking from stresses induced during processing).

The following studies show examples where pore fraction may have been a variable affecting superconductor behavior for YBCO. In a study by Shelton et al. (1988), specimens containing approximately 0.33 pore fraction and 0.06 pore fraction had J_c's on the order of 20 and 250 A/cm^2, respectively, at 77K as determined by the 4-contact method. In a study by Evetts et al. (1989) the sharpness of the voltage - current characteristic (n-value) was observed to be linearly related to YBCO grain size and $(\text{pore fraction})^{-1}$. Evetts et al. (1989) believes that as grain size increases (and pore fraction decreases), the junction area between grains increases allowing increased efficiency of current transfer. In a study by Rosenblatt et al. (1990), differences in the resistance versus temperature behavior were observed for samples of small and large pore fraction.

Hein et al. (1989) illustrated differences in the real (χ') and imaginary (χ'') components of the a.c susceptibility versus temperature response for samples of 0.10 (sintered) and approximately 0.01 pore fraction (recrystallized from the melt).

Concerning χ', although T_c was approximately 90K for both samples, a sharper transition was observed for the sintered sample. Additionally, an inflection point in the χ' response for the sintered sample exists in the transition region. This possibly reveals the presence of two superconducting phases and transitions (Goldfarb et al., 1987a). Concerning χ'', the sintered sample exhibited a single, relatively large peak while the recrystallized sample displayed smaller and more rounded peaks which exhibited substructure.

Kupfer et al. (1988a) showed differences in the χ' and χ'' components of the a.c susceptibility response for samples of 0.10 and 0.05 pore fraction containing the same oxygen content. The less porous sample exhibited a broader transition in the χ' response and a broader intergrain peak in the χ'' response compared to the more porous sample. Additionally, the intragrain peak in the χ'' response was large for the less porous sample and almost totally suppressed for the more porous sample.

3. Within-Sample Uniformity in Superconductors

In conventional superconductors, local microstructure and its degree of uniformity are important factors in determining the amount of J_c that can be carried by any superconductor (Camps et al., 1987 and Evetts, 1983). Additionally, microstructural homogeneity is generally thought to be necessary for a component to exhibit consistent and predictable physical (electrical, magnetic, and/or mechanical) behavior (Kingery et al., 1976; Ledbetter et al., 1980

and McCauley, 1987). For example, it is required that the ceramic insulator in sparkplugs have a high degree of uniformity for consistent sparkplug performance (Kingery et al., 1976). One preliminary study indicates that YBCO superconductor behavior may vary from region-to-region in a sample due to compositional nonuniformity within samples (Clarke, et al., 1989). In that study, it was shown that broad or depressed transitions in the a.c susceptibility χ' versus temperature response may result from variations in chemistry from the interior to the exterior of a sample.

D. Superconductor Properties and Measurements

The reader is referred to appendix A for an introduction to magnetic and electrical phenomena in superconductors. In the following discussion, note the difference in the quantities J_c (the measured transport critical current density from the 4-contact method), j_{cJ} (the intergrain critical current density), and j_{cG} (the intragrain critical current density).

1. Bulk Transport J_c and the Sharpness of The Voltage-Current Characteristic

Transport critical current density (J_c) is generally defined as the maximum electrical current density below which a material exhibits superconductivity at some given temperature and magnetic field (ASTM B713-82). It is given by (ASTM B713-82)

$$J_c = I_c/A \qquad (17)$$

where I_c and A are the critical electrical current and the cross-sectional area of the conductor, respectively. J_c is normally measured using the 4-contact technique in which a direct current (I) is applied to the superconductor specimen and the voltage (V) generated along a section of the specimen is measured (ASTM B714-82). The current is increased from zero and the voltage-current characteristic is generated. The voltage will be zero as long as the sample is superconducting. The current that first generates a non-zero voltage corresponds to the threshold for depinning of the vortex array in a type II superconductor (Campbell et al., 1972). J_c is specifically defined as the current at which a specified electric field is exceeded in the specimen (ASTM B714-82). This electric field (E_c) is determined from (ASTM B714-82)

$$E_c = V/l \tag{18}$$

where l is the distance between the voltage contacts. The E_c specified generally corresponds to the smallest reliably measured voltage determined by the instrument precision and by the noise level. The ASTM specification B714-82 identifies $E_c = 10^{-6}$ V/cm as the electric field at which J_c is defined.

The sharpness of the voltage-current characteristic (resistive transition) generated in the measurement of J_c has been empirically described using a power law relation (Evetts et al., 1989)

$$V = kI^n \tag{19}$$

where k and n are constants. The n-value describes the slope of the transition and the efficiency of current transfer (Evetts et al.,

1989). The greater the efficiency of current transfer, the steeper the slope and the larger the n-value. The power law relation can be alternately expressed as

$$E = kJ^n \tag{20}$$

a. Considerations in the Interpretation of J_c

The following discussion presents a model for critical current flow in the high temperature superconductors. The model presents a framework from which to interpret empirical J_c results. It is shown that J_c in bulk, polycrystalline samples of these materials is in many cases limited by 1) the magnetic field generated from the measuring current and 2) the sample geometry as well as by 3) weak coupling between superconducting regions. J_c is shown to be limited by grain size and magnetic penetration depth as well. (This development follows mostly from Dersch et al. (1988), Stephens (1989), and Tinkham (1985).)

i. Modeling Oxide Superconductors as Weakly-Coupled Grains

In granular superconductors, superconducting grains may be modeled as coupled via insulating (Josephson weak link) (Clem et al., 1987 and Peterson et al., 1988) or normal-metal, semiconducting, or more poorly superconducting junctions (proximity effect) (Hariharan et al., 1989 and Shih et al., 1984). Both low field magnetization data (Dersch et al., 1988; Ekin, 1987 and Peterson et al., 1988) and a.c. susceptibility data (Chen et al., 1988; Goldfarb et al., 1987a; Mazaki et al., 1987 and Stephens,

1989) strongly support the weak link model which shows J_c decreasing with increasing applied magnetic field strength according to Fraunhofer diffraction behavior. Additionally, an observed approximately linear increase in J_c with decreasing temperature supports the Josephson weak link model (Aponte et al., 1989). In this study, we consider the Josephson weak link model for the YBCO superconductor.

The Josephson junction consists of two superconducting grains separated by an insulating intergranular layer. The intergranular layer constitutes a tunneling barrier such that the maximum supercurrent density passed by the junction (intergrain critical current density) is (Barone et al., 1982)

$$j_{cJ}(\text{zero field}) \cong (\pi/2)(h^*\Delta)/(eR_N) \qquad (21)$$

where h is Planck's constant, $h^*\Delta$ is the energy of the superconducting energy gap, e is the charge on an electron, and R_N is the resistance of the tunneling barrier (Barone et al., 1982)

$$R_N \quad \alpha \quad \exp[t(2mU/h^2)^{1/2}] \qquad (22)$$

which is exponentially dependent on the barrier thickness (t) and the square root of the junction's barrier height energy (U) and the mass of an electron (m). The current increases as the barrier thickness decreases and saturates at the intragranular current (j_{cG}) in the limit that the grain boundary cannot be distinguished from the grain (i.e., t -> 0) (Stephens, 1989).

Equations (21) and (22) show the very strong dependence of j_{cJ} on the thickness of any non-superconducting material at a grain

boundary junction. As Clarke (1988) wrote,

"Assuming that the 'thickness' of such material varies from one grain boundary to another, there will be a distribution in attainable critical current values throughout the microstructure. One can thus consider that there will be a variety of percolative transport paths through the microstructure depending on the applied current, and as the current is increased towards the macroscopic critical current, different percolative paths are successively cut off as the current across individual grain junctions exceeds the local critical current and current is shunted into the remaining paths."

ii. Field- and Sample Size-limited Critical Current

aa. Magnetic Penetration

For weakly-coupled granular superconductors, an analogous quantity to the lower critical field (H_{c1}) called the Josephson lower critical field (H_{c1J}) is defined. H_{c1J} is the field below which flux is completely excluded from the intergranular regions (Goldfarb et al., 1987a and Loegel et al., 1990). Alternatively, it can be described as the external field required to thread one quantum of flux through the area of the junction (Peterson et al., 1988 and Stephens, 1989). H_{c1J} is given by (Stephens, 1989 and Tinkham, 1985)

$$H_{c1J} = (hc/2e)\{1/[L(2*\lambda + t)]\} =$$
$$2.07 \times 10^{-7} \text{ gauss cm}^2 / [L(2*\lambda + t)] \qquad (23)$$

where L is grain size and λ is the London penetration depth. As an example at 77 K for YBCO, with L = 4 μm and $\lambda(77)$ = 0.25 μm (Gurvitch et al., 1987; Umezawa et al., 1988 and Worthington et al., 1987) and assuming $t << \lambda(77)$, $H_{c1J}(77)$ = 10 Gauss which is about 10 times less than estimates of $H_{c1}(77)$) of YBCO grains (Goldfarb et al.,

1987a) (appendix A). It can be inferred from the treatment by Loegel et al. (1990) that larger H_{c1J} at a given temperature indicates better superconductor sample quality and homogeneity.

Intergranular supercurrents tend to shield out external magnetic fields from the junction area with a weak meissner effect (Tinkham, 1985). However, the junction currents are less successful in preventing magnetic flux from penetrating into the junctions than into the grains (Stephens, 1989). The Josephson field penetration length characterizing the field penetration into the junction is given by (Peterson et al., 1988 and Stephens, 1989)

$$\lambda_j = \{hc^2/[8*\pi*e(2\lambda + t)j_{cJ}]\}^{1/2} \qquad (24)$$

$\lambda_j(77)$ (approximately 5 - 20 μm (Dersch et al., 1988)) is normally >> $\lambda(77)$ (approximately 0.25 μm). Peterson, et al. (1988) presents an example where $\lambda_j(77)$ is approximately 18 μm if $[2\lambda(77) + t]$ = 400 nm and $j_{cJ}(77)$ = 200 A/cm^2. Taking λ as the lower limit of λ_j as the barrier disappears (i.e., t -> 0 and intimate granular coupling results), it is expected that (Stephens, 1989)

$$\lambda_j/\lambda = (j_{cG}/j_{cJ})^{1/2} \qquad (25)$$

In the case where λ_j >> L, magnetic fields uniformly penetrate the junction area. They cause a phase shift between the quasiparticle wavefunctions on either side of the junction, which results in a decrease in the tunneling current. Specifically, J_c is dependent on H_{c1J} and j_{cJ} according to Fraunhofer diffraction behavior (Tinkham, 1985)

$$J_c(H) = j_{cJ}[\sin(\pi*H/H_{c1J})]/(\pi*H/H_{c1J}) \qquad (26)$$

Experimentally, the quantity $H_{1/2}$ is defined by (Stephens, 1989)

$$[J_c(H_{1/2})/J(H=0)] = 1/2 \qquad (27)$$

where $H_{1/2}$ is the field at which a large number of the junctions becomes resistive and J(H=0) is the critical current density measured in zero applied field. $H_{1/2}$ is taken to roughly equal the magnetic field above which bulk transport critical currents between grains will stop flowing. Values between 4 and 25 gauss were obtained for $H_{1/2}$ for specimens analyzed by Stephens (1989). Since these values were on the order of those obtained for H_{c1J}, Stephens (1989) used H_{c1J} in further discussion to approximate $H_{1/2}$ (which must be measured).

bb. Self-field Effects

The currents flowing in superconductors generate magnetic fields. When the fields approach $H_{1/2}$, the weak links start to become increasingly resistive, and the current redistributes so as to prevent the local self-generated fields, H(r) from exceeding $H_{1/2}$. According to Stephens (1989), the maximum current carried by a wire occurs when $H(r) = H_{1/2}$ at the surface of the sample. Stephens (1989) derives expressions from a surface current sheet model such that $H(r) = H_{1/2}$ occurs for a maximum average current density, J_{cmax} (for a rectangular bar of cross-section a x b) (Stephens, 1989)

$$J_{cmax} = (5/\pi)[(a + b)/ab]H_{1/2} \qquad (28)$$

It is seen that J_{cmax} is limited by $H_{1/2}$ and sample cross-section dimensions. Approximating $H_{1/2}$ by H_{c1J} and assuming $t \ll \lambda$, $H_{1/2}$ is

limited by grain size (L) and λ according to equation (23).

From measured values of transport critical current I_c, the self-critical field can be calculated from (for a rectangular bar) (Stephens, 1989)

$$H_s = (\pi/5)[I_c/(a + b)] \quad (29)$$

To interpret J_c in zero field, the effect of self-field needs to be taken into account. When $(H_s/H_{1/2})$ is around 1, the sample cross-section in many cases dominates published measurements of critical current density (Alford et al., 1990; Cave et al., 1989; Chen et al., 1989; Dersch et. al., 1988; Osmura et al., 1990; and Stephens, 1989). Stephens (1989) showed data for a sample in which 4-contact transport J_c was measured and H_s was calculated following repeated grindings without disturbing the current contacts. J_c was 213, 335, 396, and 426 A/cm^2 and H_s was 7.4, 7.9, 7.5, and 5.5 gauss for cross-sections of 0.11 x 0.10, 0.11 x 0.057, 0.11 x 0.042, and 0.11 x 0.025 cm^2, respectively. The cross-sectional dimensions at which the sample makes the transition between cross-section limited and field-limited can be determined by noting the dimensions at which H_s significantly changes. For the example just presented, H_s decreased significantly on the last measurement when the width was decreased from 0.042 to 0.025 cm.

iii. j_{cJ}-limited Critical Current

When j_{cJ} is too small to produce an H_s comparable to $H_{1/2}$ (H_{c1J}), then the measured value of critical current density becomes limited by j_{cJ} (very weak intergranular coupling) rather than sample

geometry. In this case, measured J_c is approximately equal to j_{cJ}. Small values of j_{cJ} can result from uniformly dirty junctions, or junctions which have only a small area in which tunneling can occur. Also, cracks (and porous regions) in the sample can reduce the effective cross-section of the sample thereby limiting the outside dimensions of the current distribution. In this case, the maximum average current distribution becomes

$$J_{cmax} = (5/\pi)[(a' + b')/ab]H_{1/2} \qquad (30)$$

where a′ and b′ are the reduced cross-sectional dimensions. H_s is correspondingly reduced by $[(a' + b')/(a + b)]$.

j_{cJ}-limited J_c depends in general on the weakest material and therefore may not be representative of the properties of the bulk in which a distribution of j_{cJ}'s may exist (Evetts et al., 1983 and Aponte et al., 1989).

iv. Sample Quality From Critical Current

From the previous discussion, Stephens (1989) concludes that

"only in the limit of very strong and very weak intergranular coupling is J_c a measure of the quality of the sample."

In between, J_c is field-limited and ultimately determined by λ, grain size, and sample geometry. The grain coupling possibilities are summarized in table 4.

Concerning intermediate coupling, Stephens (1989) states

"the details of the thickness or kind of barrier between the grain boundaries are relatively unimportant"

and

"very little improvement in J_c can be expected until the crystal

interfaces are so clean that magnetic fields cannot penetrate between superconducting grains."

1. A.C. Susceptibility

In this study, properties derived from a.c. susceptibility measurements are commonly referred to as magnetic properties.

a. General Principles

Generally, susceptibility per unit volume (volume susceptibility) is defined as (Cullity, 1972)

$$\chi = M/H \tag{31}$$

where M and H are the intensity of magnetization and applied field strength, respectively (appendix A). Susceptibility per unit mass (mass susceptibility) is given by (Cullity, 1972)

$$\chi_m = \chi/\rho \tag{32}$$

where ρ is the bulk density of the material. Static susceptibility can be determined using D.C. magnetization techniques involving the measurement of M versus H if the relation between these two quantities is uniquely defined (for example, if the relationship is linear). The use of a.c. methods is recommended when the relationship between M and H is unknown (Duyneveldt, 1989). In the limit of small applied field, a.c. volume susceptibility represents (Duyneveldt, 1989 and Goldfarb, 1986)

$$\chi_{H->0} = dM/dH \tag{33}$$

The a.c. susceptibility is a complex quantity which is used to measure a.c. flux exclusion and loss behavior in superconductors. It is an accepted technique for characterization of conventional and

high-temperature superconductors (Couach et al., 1985; Goldfarb et al., 1987a and 1987b; Hein, 1986; and Kupfer et al., 1988a). The measuring principle is as follows (Couach et al., 1985). An alternating magnetic field is applied to the sample by means of an alternating current through a primary coil. A system of two secondary coils oppositely wound and connected in series is used to detect the variation in magnetic flux created by the sample when it is located in one of the secondary coils. The resulting signal is measured by a phase-sensitive detector which produces a complex output voltage proportional to the complex susceptibility of the sample. The output voltage and thus the susceptibility are separated into real (in-phase) and imaginary (out-of-phase) parts. External (volume) susceptibility is calculated from (Couach et al., 1985)

$$\chi = (\alpha * V_s)/(S * f * H_{ac}) \tag{34}$$

Internal susceptibility, which accounts for the sample's internal demagnetization, is given by (Goldfarb, 1986)

$$\chi_{int} = \chi/(1-\chi * n') \tag{35}$$

where n′ is the demagnetization factor dependent on sample shape (Cullity, 1972 and Fickett et al., 1983), V_s is the measured RMS voltage due to the sample, f is the frequency of the a.c magnetic field, S is the sample volume, H_{ac} is the RMS a.c magnetic field and α is the system calibration coefficient, dependent on both sample and coil geometry.

From equation (34), it can be seen that susceptibility response

may vary with applied field strength and frequency. Measured RMS voltage (V) will generally scale with sample volume (S). For valid quantitative comparisons of the external susceptibility response for different specimens or materials, it is necessary to have the same applied H_{ac}, f, coil geometry, and sample shape.

A.C. susceptibility measured in the zero-field cooled mode involves first cooling to 4.2 K in zero applied field, applying H_{ac}, and then heating at a controlled rate through the superconducting-to-normal (S-N) transition. Applying an alternating magnetic field at 4.2 K causes currents to be established in the superconductor. The currents are composed of supercurrents flowing within grains plus intergranular supercurrents flowing in larger loops from grain to grain if the grains are coupled (Dersch et al., 1988).

b. Real Component of A.C. Susceptibility

For the zero-field cooled mode, as the temperature is increased from 4.2K, the real (χ') portion of the susceptibility in the S-N transition region essentially measures the degree of a.c. shielding (i.e., flux exclusion) as a function of temperature. Complete shielding is normally defined as χ' at 4.2 K. At 4.2 K, supercurrents flow such that the entire macroscopic volume of the sample is likely to be shielded from changes in an externally applied magnetic field (Hein et al., 1989). For ideal superconductors, $\chi' = -1$ (SI units). Percent of complete shielding at temperature T can be defined as

$$\% \text{ complete shielding}(T) = [\chi'(T)/\chi'(4.2\ K)]100 \qquad (36)$$

where $\chi'(T)$ is the shielding at temperature T. The degree to which flux exclusion is achieved when heating through T_c is likely to be a function of sample homogeneity (Hein et al., 1989). It is desirable that a given % complete shielding be achieved at the highest possible temperature. Alternately, it is desirable that the largest % complete shielding be achieved at any given temperature.

Some studies have indicated that χ' or % complete shielding scales with volume fraction superconductor (Chu et al., 1976 and 1981, and Kupfer et al., 1988b). However, this view is strongly disputed by Hein et al (1986 and 1989) and Kittel et al. (1988). Kittel et al. (1988) states that even a relatively thin surface layer or a network of superconductor surface strings can cause substantial shielding of a.c. magnetic fields. Hein (1986) shows this to be true for a hollow lead cylinder and concludes that a.c. susceptibility techniques cannot determine if superconductivity is a bulk phenomenon.

(Some high temperature superconductors in the normal state are paramagnetic but with χ' on the order of only 10^{-3}. Thus, it appears that in the normal state, the a.c. susceptibility from paramagnetism for YBCO is negligible (Chen et al., 1989))

c. Imaginary Component of the A.C. Susceptibility

The imaginary portion (χ'') of the a.c susceptibility is generally associated with heat-generating a.c. power losses including eddy current losses, surface losses, and/or bulk-pinning

losses from hysteresis of flux tube motion (Barbara et al., 1988; Chen et al., 1989; Dersch et al., 1988; Goldfarb et al, 1987b; Loegel et al., 1989 and Mehdaoui et al., 1988). A peak or peaks in the χ'' versus temperature response occurring near the S-N transition are characteristic of losses. The magnitude and shape of the peak(s) may vary with sample geometry (Chen et al., 1989), applied field, and applied frequency (Loegel et al., 1989 and Mehdaoui et al., 1988).

The significance of several peaks in the χ'' response is still a matter of controversy. Some investigators feel that the presence of more than one peak is thought to indicate the presence of more than one superconducting phase with different T_c's identified at the loss peak centers (Goldfarb et al., 1987a). The presence of two phases with very different T_c's supports the possibility of oxygen inhomogeneity in the sample since T_c is so critically dependent on oxygen content. Others show that the presence of impurities can lead to additional peaks (Hein et al., 1989). A model has been presented that attributes dual peaks to the onset of intragranular and intergranular supercurrent flow (Bean, 1962; Chen et al., 1989; Clem, 1988; Kim et al., 1962 and 1963, and Kupfer et al., 1988a). The application of this model will be discussed in more detail in the upcoming BACKGROUND section entitled "Critical Current Density From A.C. Susceptibility". Dual peaks are generally accompanied by abrupt slope changes in the χ' versus temperature curve. Kupfer et al. (1988a) states that the larger the peak in the χ'' response, the greater the shielding.

d. Significance of Applied Field Strength

In general, the a.c. susceptibility response of sintered untextured YBCO samples is strongly sensitive to the a.c. field strength (Loegel et al., 1989; Goldfarb et al. 1987a; Mehdaoui, et al., 1988 and Kupfer et al., 1988a). This results from the more rapid decrease of the intergrain current with field in comparison to the intragrain current (Kupfer et al., 1989). (In powder samples of YBCO, a.c. susceptibility response is less field-dependent since susceptibility is likely to be due only to the intragrain current since the grains have been decoupled (Kupfer et al., 1987 and Strobel et al., 1988) Since it is believed from BCS theory (Bardeen et al., 1957) that YBCO is a type II superconductor (appendix A) and is granular in nature, the a.c. magnetic field penetration within the sample likely depends on the strength of the applied H_{ac} in relation to the Josephson lower critical field (H_{c1J}) and to the larger lower critical field of the grains (H_{c1}) (appendix A). Here, a likely magnetic interaction scenario is formulated.

For $H_{ac} < H_{c1J}$, flux penetrates to a depth approximately equal to λ into superconducting grains and approximately equal to λ_j into the grain boundary regions (Clem et al., 1987 and 1988). Pinning effects should be negligible for this situation (Loegel et al., 1989) and $\chi'' = 0$. For H_{ac} less than approximately 100 mOe, H_{ac} is likely to be less than H_{c1J} and (hence H_{c1}) at all temperatures below T_c except possibly those very close to T_c (since the critical fields decrease with increasing temperature (appendix A)).

For $H_{c1J} < H_{ac} < H_{c1}$, flux vortices penetrate into the intergranular regions of the material. The vortices will be pinned with depth of penetration determined from the pinning force and the grain size (Dersch et al., 1988). Hysteresis loss arises when penetrating intergranular magnetic flux experiences pinning forces and a peak in χ'' is expected (Goldfarb et al., 1987b). Goldfarb et al. (1987a and 1987b) indicates that an estimate of H_{c1J} can be obtained from H_{ac} at the temperature where this occurs. For a given H_{ac}, the higher the temperature at which H_{c1J} is achieved (i.e., the temperature where the rise in χ'' first occurs), the better the sample quality and homogeneity (Loegel et al., 1990).

For $H_{c1} < H_{ac} < H_{c2}$, a mixed normal-superconducting state is present with flux vortices penetrating through the bulk in flux tubes as well as penetrating through the intergranular regions. If eddy current and surface loss are minimized, further hysteresis loss arises from pinning of the flux tubes in the bulk and another peak in χ'' may occur. As H_{ac} approaches H_{c2}, the flux tubes begin to overlap as the material approaches its normal state.

In general, very low applied H_{ac} (with respect to H_{c1J} and H_{c1}) will lead to sharp peaks while higher applied H may result in broadened peaks (Goldfarb et al., 1987a and 1987b and Loegel, et al., 1989). The experimental situation may be difficult to interpret when measuring inhomogeneous materials having a range of critical fields and/or transition temperatures. However, by starting with very low H_{ac} at 4.2 K and then heating, the temperature at which

initial flux penetration occurs can be obtained from the initial rise in χ''.

e. Significance of Applied A.C. Frequency

The a.c. susceptibility response of YBCO materials has been shown to be heavily frequency-dependent in some cases (Loegel et al., 1989 and Mehdaoui et al., 1988) and close to frequency-independent in other cases (Dersch et al., 1988 and Kupfer et al., 1987) over several decades of frequency. Frequency-dependent susceptibility response may indicate 1) eddy current (Cullity, 1972 and Goldfarb et al., 1987b) and/or surface resistance (Doss, 1989) effects and/or 2) that the intergranular supercurrents dominate the a.c. susceptibility (Chen et al., 1989). A.C. susceptibility utilizing low frequencies ($f \leq 100$ Hz) and low a.c fields ($H_{ac} < 100$ mOe) have been used in the search for and study of new superconductors (Davis et al., 1989 and Hein et al., 1989). Low frequencies minimize the effects of eddy currents (Hein et al., 1989 and Chen et al, 1989) and surface resistance (Doss, 1989). According to Chen et al. (1989), χ' and χ'' originating from eddy currents are less than 10^{-3} in the normal state for frequencies less than 10 KHz in a high temperature superconductor of 2 mm diameter and normal state resistivity approximately equal to 10^{-4} Ω-cm. If the χ'' response is independent of applied frequency or low frequencies are used, eddy current and surface resistance effects can be ruled out and the peak(s) in χ'' are likely to be due to hysteresis (bulk pinning) effects (Goldfarb et al, 1987b and Cullity, 1972).

According to Loegel et al., 1989, at low frequencies ($f \leq 100$ Hz), information can be obtained on the bulk properties of a YBCO sample since the skin depth is approximately 5 mm (normal-state resistivity = 10^{-4} Ω-cm just before the N-S transition.

f. Transition Temperature (T_c) and Magnetic Transition Width From A.C. Susceptibility

The transition temperature, sometimes referred to as the critical temperature and written T_c, is the temperature at which a "normal" material becomes superconducting. This definition is ambiguous when the transition does not occur sharply or abruptly. Additionally, the transition can be determined from resistive and magnetic (susceptibility, eddy current) methods, each of which will generally show the transition at somewhat different temperatures. (A single "strand" of superconducting material is all that is necessary to achieve zero resistance). Previously, T_c was given as $T_{1/2}$, where the resistance had fallen to half of its value at the onset of the transition (Ginsberg, 1989 and Couach et al., 1985). Since in many cases, the bulk of the magnetic transition from χ' takes place at lower temperatures than where zero resistance first occurs (Hein et al., 1989), T_c determined magnetically is reported here as the onset temperature of the N-S transition or the temperature where 1 % of complete magnetic shielding occurs, i.e.

$$T_c = T(\%\ \text{complete shielding} = 1\%) \tag{37}$$

The magnetic transition width from χ' is defined for this study as the difference in temperatures for which 10 and 90 percent of

complete shielding are achieved during the S-N transition, i.e.

$$\Delta T_{cm} = T(\%\ \text{complete shielding}=10\%) - T(\%\ \text{complete shielding}=90\%) \quad (38)$$

g. Critical Current Density from A.C. Susceptibility

According to weakly-coupled granular models of the high-temperature superconductors proposed by Bean (1962), Kim et al. (1962 and 1963) and Clem (1988) and applied by Kupfer et al. (1987 and 1988a), Dersch et al. (1988), Dubots et al. (1988), Cave et al. (1989), and Chen et al. (1989), critical current density can be determined at the temperature where the peak(s) in χ'' occurs. In the χ'' response, up to two main peaks can be observed with the lower temperature peak corresponding to intergranular current flow and the higher temperature peak corresponding to the intragranular current flow. The two distinct peaks occur due to the different field and temperature dependences of the inter- and intragrain current. The temperatures at which these peaks occur bound a phase-locking temperature for which the Josephson coupling energy (E_J) equals the thermal fluctuation energy (kT).

Consider the lower temperature or intergrain peak. Below the phase-locking temperature, $E_J > kT$, the weak links are able to carry a supercurrent, and a coherent network of junctions is established allowing a transport current to travel through the sample via the first percolating path. Supercurrents induced by the applied a.c. field probe intergrain properties (such as T_c of the grain boundaries). The temperature at which the a.c. field has just

penetrated to the center of the sample occurs at the maximum in the lower temperature peak. At this temperature,

$$j_{cJ} = H_{ac} / R_s \qquad (39)$$

where j_{cJ} is the intergrain critical current density and R_s is the sample radius. For the same H_{ac} and R_s for different samples, the calculated j_{cJ}'s will be the same. However, the temperatures at which the loss peak center occurs may be different. In this case, since j_{cJ} is temperature-dependent, better sample quality can be concluded for the samples exhibiting the loss peak center at the highest temperature. It is expected that as pore fraction is decreased, the increased contact area between the grains would result in higher j_{cJ} thus raising the critical temperature of the intergranular peak (Nikolo, 1990).

Now consider the higher temperature or intragrain peak. Above the phase-locking temperature, weak links are resistive because $E_J < kT$. However, supercurrents induced by the applied a.c field still flow within grains probing intragrain properties (such as T_c for the grains). The temperature at which the a.c. field has just penetrated into the center of the grain occurs at the maximum in the higher temperature peak. At this temperature,

$$j_{cG} = H_{ac} / R_g \qquad (40)$$

where j_{cG} is the intragrain critical current density and R_g is the mean grain radius. Kupfer et al. (1988a) states that observed intragrain peaks can be considerably smaller than predicted theoretically because 1) the grains cover only a part of the sample

volume (porosity, other nonsuperconducting phases and grain boundaries make up the other part); 2) the demagnetiztion of the decoupled grains is not considered; and mainly 3) λ is $\geq R_g$ resulting in magnetic invisibility of the grains (Clem, et al., 1987). Kupfer et al. (1988a) believes that the intragrain peak may be completely suppressed for $\lambda \geq R_g$. In this case, j_{cG} cannot be determined from a.c. susceptibility. The intergrain peak should still be apparent if the grains are coupled such as in a sintered sample. The presence of a single peak due to intergranular losses in sintered samples can be proven if the sample is crushed into a fine powder (decoupled grains) and the loss peak disappears upon rerunning the a.c. susceptibility measurement under the same conditions as for the sintered sample.

According to Chen et al. (1989), the current density determination from a.c. susceptibility has some advantages over the four-contact measurement method including the following: 1) electrical contacts are not required, 2) rectangular or circular cross-section for the sample is not required, 3) there is no problem with contact heating, and 4) information on both intragrain and intergrain J_c can be obtained. For an isotropic sample and if J_c is field independent, J_c's obtained from the four-contact and a.c. susceptibility methods should agree. However, J_c is almost always field dependent and the J_c's obtained by both techniques are likely to be different (Chen et al., 1989).

E. Summary of Expected Pore Fraction Effects

Considering the models of Stephens (1989), Ekin (1987), Evetts et al. (1989), at higher pore fractions, interconnection area between grains is smaller, connections are less frequent, the efficiency of current flow is limited, and sample cross-section dimensions are effectively reduced (equation (30)). In this case, lower J_c, lower n-value, lower temperature for initial flux penetration, and poorer shielding at any given temperature are expected. At lower pore fractions, interconnection area between grains is larger, connections are more frequent, and the efficiency of current flow is increased. In this case, higher J_c, higher n-value, higher temperature for initial flux penetration, and greater shielding at any given temperature are expected.

Depending on the processing conditions, grain size may increase along with decreasing pore fraction. In this case, if Stephen's (1989) model is considered further, J_c may be adversely affected by the increasing grain size (equations (28) and (23) and approximating $H_{1/2}$ by H_{c1J}). Complicating matters further, the effects of oxygen deficit, impurities, and cracking have been seen to outweigh the effects of pore fraction (Alford et al. 1988a and Newcomb et al., 1988).

F. Ultrasound As A Microstructural Probe

1. General

Ultrasound is a sensitive probe of microstructure since it interacts (via absorption and scattering) with grains, pores, and

inclusions in polycrystalline materials (Birring et al., 1987; Bridenbaugh et al., 1987 and Papadakis, 1987). Furthermore, ultrasonic techniques offer nondestructive means for examining microstructures. Ultrasonic velocity and attenuation measurements have been used previously to examine and image microstructural features such as grain and porosity distributions in metals and ceramics (Baaklini et al., 1989; Evans et al., 1978; Generazio et al., 1988; Gilmore et al., 1986; Gruber et al., 1988; Kunnerth et al., 1989; Roth et al., 1987 and 1990c; Szilard, 1982 and Vary, 1988). In the last several years, at least 100 studies have been reported concerning ultrasonic analysis of the high-temperature superconductors (Dominec, 1989). These studies were performed mainly for the determination of elastic constants (from velocity measurements) (Ledbetter et al., 1990 and Round et al., 1987) and examination of structural changes as a function of temperature (from velocity and attenuation measurements) (Ramachandran et al., 1988 and Sun et al., 1988).

The potential exists for using ultrasonic characterization at room temperature for improving the properties of high temperature superconductors and aiding in the prediction of their behavior at cryogenic temperatures. Ultrasonic methods might be useful for process (sintering, oxidation, etc.) control, final inspection before application, and in-service monitoring. By providing feedback in the earliest stages of processing and allowing inspection without the need to section / dismantle a component,

ultrasonic characterization can provide a unique capability resulting in significant cost and time savings.

2. Ultrasonic Velocity and Material Change

As discussed in chapter 1, when there are no boundary effects present, the velocity (V) of a longitudinal elastic wave in a bulk solid is determined by the elastic modulus (E), density (ρ), and Poisson's ratio (ν) of the solid according to (Szilard, 1982):

$$V = \{[E(1-\nu)]/[\rho(1+\nu)(1-2\nu)]\}^{1/2} \qquad (1)$$

Modulus and Poisson's ratio are normally thought of as "intrinsic" material properties, that is, they don't change with microstructural condition. They can be directly related to the strength and nature of interatomic forces in a material (Ledbetter, 1983). The introduction of pores into a solid theoretically does not change modulus for the solid regions of the material. However, the apparent modulus (or stiffness) of the bulk solid is reduced by the introduction of pores as was discussed in Chapter 1. Similarly, dislocations decrease the apparent modulus of crystalline materials because motion of dislocations under an applied stress decreases the rigidity of the solid (at least before work hardening occurs.) In theory, any material change that affects the apparent ρ, E, or ν should affect the ultrasonic velocity, i.e., velocity should be sensitive to any changes in the elastic strain state (dynamic or static) of the solid (Alers, 1966 and Truell et al., 1969). Such changes may occur from deformation, heating, phase transformations, etc. Additionally, velocity should be sensitive to gradients and

discontinuities in the elastic state of the lattice.

In practice, ultrasonic velocity is an extremely sensitive measure of material change; under the best experimental conditions, it is estimated that velocity differences on the order of 0.00001 % can be detected (Truell et al., 1969). (Absolute accuracy of velocity measurements under the best test conditions is on the order of 0.001 % (Truell et al., 1969).) Changes in "monocrystal" features such as crtstal structure, crystalline orientation, twin density, dislocation density, irradiation damage, charge carrier density, magnetic and electric domain wall orientation and motion, vacancy quantity, and interstitial and substitutional atom motion all have their effect in changing the velocity of high-frequency stress waves in solids (Alers, 1966; Granato et al., 1958; Hikata et al., 1962 and Truell, 1959). Changes in features normally associated with bulk, polycrystalline materials such as pore fraction, granular orientation, impurity concentration, residual stress, and possibly pore/impurity particle size distribution and geometry also affect velocity (as previously presented and discussed in Chapter 1). One microstructural variable that does not appear to significantly affect elastic properties and ultrasonic velocity is grain size (Baaklini et al., 1989; Birring et al., 1987; Papadakis, 1987 and Rice, 1977).

3. Ultrasonic Velocity and Pore Fraction: Empirical Results

Chapter 1 gives detailed empirical results concerning the effect of pore fraction on ultrasonic velocity for different materials. Figure 59 and the corresponding entry in table 1 of that chapter show the effect of pore fraction on the ultrasonic velocity of YBCO for a set of specimens obtained from one manufacturer. The relationship

$$\text{Velocity (cm/}\mu\text{sec)} = -0.007 \times \text{Percent Porosity} + 0.565 \qquad (41)$$

was obtained.

4. Ultrasonic Velocity and Oxygen Content: Empirical Results

The following studies were performed to investigate methods for nondestructively determining oxygen content and also to determine the effect of oxygen on the elastic properties of the material. Hsu et al. (1971) found that longitudinal wave velocity and bulk density increased as the oxygen content of titanium-oxygen alloy specimens was increased. Buxbaum et al (1984) found that longitudinal wave velocity decreased and density increased with increasing oxygen content in titanium-6211 alloy specimens. Note that in the latter study, velocity decreased with increasing density which is contrary to all of the empirical data presented in Chapter 1. However, this shows that other effects of an oxidation besides a density increase (such as phase and structural transformations) may significantly influence velocity.

5. Ultrasound and Within-Sample Uniformity

In recent years, the development of nondestructive evaluation (NDE) methods for the determination of global microstructural state

have been developed to address the needs of the structural materials design community (Baaklini et al., 1988; Ellingson et al., 1989; Generazio et al., 1988; Gruber et al., 1988 and Kunnerth et al., 1989) To fully understand and predict the mechanical behavior of new structural materials (so that reliable and safe structures are ultimately built), it is believed that (in-process and final product) characterization of global uniformity as well as characterization of discrete, potentially failure-causing flaws is necessary (Vikram et al., 1986). Examples of both types of characterization are shown in figure 63 using ultrasonic NDE techniques to examine sintered SiC. As shown in figure 63(b), ultrasonic velocity scan techniques have been shown to be useful for determining differences in the microstructural condition (strain state) from region to region within a solid (Generazio et al., 1988; Gruber et al., 1988; Hsu et al., 1982; Kino et al., 1980 and Shyne et al., 1981). The development of the high-temperature ceramic superconductors may demand similar characterization, since within-sample uniformity is likely to be important for optimum electrical and magnetic behavior (see BACKGROUND section entitled "Within-Sample Uniformity in Superconductors"). (This characterization may also be necessary with respect to the mechanical behavior of these materials since superconductors within high-field magnets can be subjected to large mechanical loads (Ekin, 1981).)

III. ORGANIZATION OF EXPERIMENTAL STUDY

Three experiments were performed in this study. A composite EXPERIMENTAL PROCEDURES section was presented since several procedures / specimens were common to the three experiments. Separate RESULTS AND DISCUSSION sections were presented for each experiment. The following paragraphs briefly review the main points of each experiment.

In experiment 1, the superconductor properties and microstructural characteristics were determined for similarly-processed, polycrystalline, untextured YBCO specimens of pore fraction 0.10 to 0.25. Properties and microstructure were compared for the different specimens and different regions within specimens.

In experiment 2, an ultrasonic scan technique was used to point to microstructural inhomogeneity within a YBCO disk. The disk was destructively examined to determine the origin of the inhomogeneity. Bars cut from areas of different microstructure as indicated from the ultrasonic and destructive results were tested for superconducting behavior.

In experiment 3, the effects of changes in oxygen content on superconducting behavior, velocity, elastic modulus, and microstructure for YBCO specimens of different densities were examined. Additionally, the ultrasonic scan technique was used to determine if spatial changes in macrostructure occur upon oxygenation / reduction treatments.

IV. EXPERIMENTAL PROCEDURE

A. Specimens

YBCO disk-shaped samples approximately 1 inch diameter by 0.25 inches thick were manufactured at the Research Division of W.R. Grace & Co. (Columbia, MD 21044). Table 5 gives a summary of the samples and their condition with respect to atmospheric treatment for the various experiments in this study. The following paragraphs describe the processing / preparation of the specimens in detail.

1. Powder-Processing

Previously-synthesized YBCO powder in quantities of 500 grams was ball-milled for 1.5 hours. A polyurethane-lined 1.6 gallon jar mill charged with 10 kg of highly wear-resistant yttria-stabilized zirconia 20 mm balls was used for ball-milling. The powder and balls were separated by shaking them in a stainless-steel 100-mesh sieve. Ball-mill loading and unloading as well as sieving were done in a low-CO_2/low-H_2O glovebox. The powder produced in this way had an average particle size of about 1.5 μm. Samples named 52A, 53A, 59A, 60A, and 51A were made from the same batch of starting (and ball-milled) powder and all were die-pressed at 5000 psi, followed by cold isostatic-pressing at 20,000 psi for 5 minutes.

2. Thermal and Atmospheric Treatments

The peak sintering temperature was altered to obtain a range of pore fractions (determined from sample mass and dimensions) for this batch of samples. Samples 52A, 53A, 59A, 60A, and 51A had peak sintering temperatures ($\pm$ 2 °C) of 937, 947, 954, 966, and 976 °C,

respectively. Samples 53A, 59A, and 60A were heated, sintered, and cooled according to schedule 1 (table 6(a)). The oxygen atmosphere in the furnace was ultra-high purity O_2 with a flow rate of 238 cm^3 per minute (through a 2.75" diameter tube feeding into the furnace). The specimens were sintered on 20-mesh MgO single crystals (predominantly {100} crystallographic faces), as YBCO does not react with MgO.

To study the effects of oxygenation, samples 52A and 51A first experienced the sintering and argon cooling schedule of schedule 2 (table 6(b)). The disks were then sectioned into two thinner circular disks, one of which was to be used for ultrasonic experiments and the other for microstructural analysis. Upon completion of the ultrasonic experiments, the disks cut from samples 52A and 51A were oxidized according to schedule 3 (table 7). Argon flow rate was 215 cm^3/min in schedules 2 and 3. The disks cut from 51A were further oxidized (extended oxidation) at a later date according to schedule 4 (table 8). However, a power failure occurred at 45 hours into a 48 hour hold at 600 °C and rapid cooling took place. The schedule was started over and an 8 hour hold at 600 °C took place. Then, to study the effects of reduction, the 51A disks were reduced in Ar according to schedule 5 (table 9). Additional bars were cut randomly from 53A, 59A, and 60A and reduced in Argon (Ar) gas according to schedule 5 (table 9).

3. Cutting and Machining

The samples were dry cut into two thinner disks (as previosuly

mentioned) 3 mm thick. A bar of approximate dimensions 10 mm by 3 mm by 2 mm was then dry cut from the edge and center regions of one of the disks from samples 52A (after oxidation), 53A, 59A, and 60A. The cutting was accomplished using a slitting saw with a 180 grit diamond-impregnated steel blade. Spindle speed was 500 revolutions per minute with the feed rate 0.5 to 0.75 inches per minute. In preparation for electrical, susceptibility, and ultrasonic measurements, the bars were machined flat and parallel to a 0.025 mm tolerance on a surface grinder using a 150 grit diamond wheel. The center- and edge-cut bars are designated -E and -C, respectively. In preparation for ultrasonic experiments after oxidation/reduction steps, disks from samples 52A and 51A were machined flat and parallel with a 320 grit diamond wheel to $\pm$ 0.002 mm while removing a minimum of material (approximately 0.05 - 0.1 mm) from the surfaces. Additional pieces from all samples were cut and/or fractured for microstructural and compositional analysis.

4. Sample Handling and Storage

Samples were handled with plastic gloves to minimize contamination. Samples were stored in a dessicator filled with dessicant (replaced monthly) to avoid atmospheric attack.

5. Additional Specimens

Several other samples 85 - 95 percent of theoretical density and 1 inch in diameter were obtained from W.R. Grace. These samples were processed in the same general manner as those previously discussed. Die size, die-pressing pressure, pressing procedure

(die-pressing only as opposed to die-pressing plus cold-isostatic pressing), O_2 flow rate into the furnace, and sintering temperature were varied. For example, sample 46B was processed using the same steps as for specimens previously discussed; however, a different starting powder was used, die-pressing took place at 3000 psi (instead of 5000 psi), peak sintering temperature was 942 °C in schedule 1 (table 6(a)), O_2 flow rate was approximately 200 cm^3 (instead of 230) per minute, segment 7 was omitted, and the as-received dimensions were approximately 1 inch diameter by 0.125 inches thick. All specimens were machined flat and parallel in preparation for ultrasonic scanning. Sample 46B, 89.5% of theoretical density, was machined flat and parallel to 2.678 $\pm$ 0.002 mm. Sample 99, 93% of theoretical density, was machined flat and parallel to 2.788 $\pm$ 0.002 mm also in preparation for ultrasonic scanning. Before experimental work began, each sample was tested for the Meissner effect (Hellman, et al., 1988) at 77 K by attempting to suspend a small magnet over the sample cooled in liquid nitrogen.

B. Current Density and n-value Measurement

Critical current density (J_c) was determined using ASTM B714 - 82. This method is intended for use with superconductors having a critical current of less than 600 A. J_c measurements were made at 77 K in zero applied field. J_c was defined in this study where the critical electric field (E_c) = 10^{-5} V/cm. J_c was calculated according to equation (17) (with the cross-sectional area (A) of the

conductor taken to be the cross-sectional area of the bar). The value for E_c is a factor of 10 larger than that specified in ASTM B714-82 because of the small distance between voltage contacts which caused $E_c = 10^{-6}$ V/cm to be reached at very small voltages hard to measure accurately. N-value at 77 K was obtained from the generated voltage-current characteristic by a regression fit of equation (20). Measured J_c at 77 K was compared with maximum critical current density (J_{cmax}) predicted for moderate intergranular coupling (self-field and cross-section limited case calculated from equation (28) by approximating $H_{1/2}$ with H_{c1J} (equation (23) with $\lambda = 0.25$ μm) (Stephens, 1989).) The generated self-field (H_s) was calculated from the measured values of J_c according to equation (29) and compared with the Josephson critical field (H_{c1J}) calculated from equation (23).

The following is a description of the procedures and apparatus used to make the measurements. Gold contacts for current leads were sputtered on the two end faces of each of the edge- and center-cut rectangular bars (eight total) from samples 52A, 53A, 59A, and 60A. In addition, two gold contacts for voltage leads were sputtered on one side of each bar. Contacts were also sputtered onto smaller edge- and center-cut bars of sample 46B in the same fashion. The sputtering was accomplished with a table-top vacuum sputtering system. The spacing between the voltage contacts was approximately 0.4 cm for each sample. (The following procedures were performed at Ceramphysics, Inc., Westerville, Ohio 43081.) Short current leads

of 0.005" silver wire were attached to the current contacts using air-dry silver paste. Short voltage leads of 40 gauge bare copper wire cleaned with acid were attached to the voltage contacts in the same manner. After the leads were placed on the bars, and the silver paste had dried for approximately one hour, the bars were placed in a desiccator until measurements were made.

The J_c probe is shown in figure 64. The bars were attached to the J_c probe by bending the silver current leads in a loop and suspending the sample horizontally in a strain-free manner. All leads were soldered to the probe using Lead/Tin solder. The leads were run up a center post which also carries the evaporating nitrogen gas. This allows cooling of the leads and minimization of heat leak down the leads. All leads exited through the current connector at the top of the probe. The probe and connectors are designed to carry up to 30 A. A magnetic-field independent glass-ceramic capacitance thermometer was mounted at the bottom of the probe for temperature measurement.

The probe and YBCO sample were lowered into a dewar containing liquid nitrogen such that the fluid completely surrounded the sample. This allows efficient cooling of the sample and current leads, which in turn simplifies the sample mounting posts and allows for much smaller leads to be used to carry the current. A copper can was placed over the lower assembly for protection of the samples and for electrical shielding.

Five H-P model 6216B power supplies connected in parallel (with

a total current capability of approximately 2 A) were used as the current source. The current was measured as the voltage drop across a 0.001 ohm resistor. The accuracy of the current measurement includes four significant figures with a noise of $\pm$ 2 digits in the fourth place. The voltage across the bars was measured with a Keithley Model 181 digital voltmeter. The accuracy of the voltage measurement includes three significant figures with a noise of $\pm$ 4 digits in the last digit. The values given for J_c contain three significant figures with an estimated uncertainty of approximately 10 %. The reproducibility of the voltage-current characteristic was obtained from several successive measurements followed by remeasurement at a later date for bar 59A-E. Each measurement took about 20 minutes. If samples were not superconducting at 77 K, resistivities over the current range 5 - 17 mA were measured.

Contact resistance measurements were performed on an additional bar cut from sample 59A that had Au-sputtered contacts. These measurements were performed to determine whether contact heating would limit the J_c measurement (Ekin et al., 1988). Leads were applied as previously discussed. Two external connections were made to each of the four leads and all possible 2-contact combinations were measured for resistance. For the two external connections to each lead, the applied current was attached to one lead and the measuring voltage probe was attached to the other lead. The current was approximately 0.1 mA and was applied in both the forward and reverse directions so that any thermal EMF present could

be determined and eliminated from the contact resistance determination. The thermal EMF was eliminated by obtaining an average of the forward and reverse measured voltages. The average contact resistance was then obtained by dividing the 2-contact combination resistance by 2. A current of 0.2 mA was also used to check whether the contacts were ohmic (whether the voltage would vary in a linear fashion according to Ohm's law of V = IR). An additional four-lead measurement was made to ensure that the sample was superconducting during contact resistance measurements.

C. A.C. Susceptibility

A.C. susceptibility measurements were made using the Lakeshore Cryotronics Model 7000 susceptometer. A schematic of the entire system and the cross-section of the coil assembly are shown in figure 65. The major principles of the susceptibility measurements were described in the BACKGROUND section entitled "A.C. Susceptibility". The following is a description of the procedures and apparatus used to make the measurements. Each specimen was placed (long axis first) into a small nonmagnetic plastic sample container. The container with specimen was attached to a nonmagnetic plastic rod which was connected to a stepping motor. The container was positioned at the center of one of the secondary (sensing) coils as shown in figure 65(b). The coil assembly resides inside of a cryostat that can be cooled to 4.2 K and then heated in a controlled manner ($\pm$0.5 K). The coil assembly is surrounded by shielding

material to minimize the influence of the earth's magnetic field.

The specimens were cooled to 4.2 K in zero field, the field was applied (parallel to the specimen long axis), and the assembly was heated to 100 K through the S-N transition at a rate of 0.7 K per minute. Unless otherwise specified, the (low) applied a.c. field (H_{ac}) and frequency (f) were 20 mOe and 100 Hz, respectively. As previously discussed, low H_{ac} allows the determination of the temperature of initial flux penetration while low f allows eddy current and surface effects to be minimized if any frequency-dependence is apparent. A slight offset voltage is measured by the Model 7000 susceptometer's extremely sensitive electronics even with no sample present because the two oppositely wound sensing coils are close to, but not completely, identical. This offset voltage is a function of temperature, frequency, and applied field. To null the offset voltage, the sample was precisely and automatically moved between the centers of the two secondary coil during data acquisition. This was accomplished as follows:

$$\text{Voltage read in top coil} = V_{top} = V_s + V_{cup} + V_o \qquad (42)$$

and

$$\text{Voltage read in bottom coil} = V_{bot} = -V_s - V_{cup} + V_o \qquad (43)$$

where V_s, V_{cup}, and V_o are the voltage due only to the sample, the voltage due to the sample holder and sample rod, and the offset voltage. The offset voltage is eliminated by averaging the top and bottom coil voltage readings according to

$$(V_{top} - V_{bot})/2 = V_s + V_{cup} \qquad (44)$$

The contribution to the measured voltage arising from the sample cup and rod was accounted for in these measurements by recording data for an empty sample cup plus rod over the full temperature range and subtracting this contribution out during data processing. Therefore, the voltage due to the sample is all that is left.

The system calibration coefficient (α) was calculated to be 1.761 from the coil geometry assuming a small sample approximating a magnetic dipole and assuming no interaction with the second sensing coil. Even for large spherical samples which fill the sample holder, this value was still valid to within a few percent. In addition, the calculated value of α was experimentally verified for accuracy by measuring NIST standard materials.

Volume and mass (external) susceptibilities were obtained from equations (33) and (32), respectively. (The demagnetization factor is estimated at 0.05 for rectangular bars of the dimensions used in this study (Cullity, 1972).) Susceptibility was calculated taking sample volume to be the bulk volume (material + pores) of the sample. The absolute accuracy of the external susceptibility accuracy is limited mainly by the accuracy with which the sample volume can be measured and the accuracy with which the voltage is read by the phase-sensitive detector (approximately $\pm$ 3%).

Edge- and center-cut bars from samples 52A, 53A, 59A, and 60A were measured for susceptibility response. Additional bars from these samples were measured for susceptibility after the samples had undergone the reduction treatment in schedule 5 (table 9).

Additionally, bars cut from sample 51A were measured for susceptibility before oxidation, after a first oxidation, after a second extended oxidation, and after a subsequent reduction treatment according to the schedules 2 - 5 (tables 6b - 9). The H_{ac} field-dependence of the susceptibility was also examined over the range 10 - 80 mOe on a bar cut from sample 46B. Additionally, the frequency-dependence of the susceptibility was examined over the range 10 - 1000 Hz on bars cut from sample 52A. Further, a rectangular bar was cut from sample 51A, tested, crushed into a powder, and retested to compare the loss characteristics of sintered versus powdered samples. The bars cut from samples 52A, 53A, 59A, and 60A were run with sputtered contacts for the J_c measurements already in place. Edge- and center-cut bars from sample 46B were measured for susceptibility response. A bar cut from sample 46B was run with and without contacts to determine if eddy current effects in the contacts might affect the susceptibility results.

D. Ultrasonics

1. Velocity Measurement

Longitudinal wave velocity was measured in this study. The widely-used pulse-echo contact technique (Breazeale et al., 1981; Firestone, 1946; Hull et al., 1985 and Papadakis, 1975) (figure 66) was used to obtain ultrasonic waveform data. A single broadband ultrasonic pulse (main pulse) is propagated (via the crystal) into the buffer rod. The pulses labeled FS'_1 and FS_2 (figure 66(a)) are

the first front surface reflections without and with the specimen present on the buffer rod, respectively. With the sample in place on the buffer rod, the ultrasonic pulse is partially reflected at the buffer rod-couplant-sample (BCS) interface. The main pulse travels forward through the sample, reflects off the back surface, and again interacts with the BCS interface. In this journey (twice the specimen thickness), the ultrasonic pulse may be considered as having integrated the microstructural information in the volume element sampled. Echo B'_1 is partially reflected at the BCS interface and is subsequently reflected again at the back surface. The second back-surface reflection is labeled B'_2. Echoes B'_1 and B'_2 are not directly measureable in this experimental configuration. Their reduced waveform amplitudes, labeled B_1 and B_2 in figure 66(b), are measureable.

The back-surface-reflected pulses B_1 and B_2, which have their shape and path length altered by the microstructural information in the volume element probed, were used to calculate cross-correlation velocity (Hull et al., 1985) The volume element probed is determined by the ultrasonic beam diameter (Lempriere, 1989 and Krautkramer et al., 1977). Cross-correlation velocity is essentially a mathematical formulation of echo overlap (Hull et al., 1985 and May, 1958) where similar features of two waveforms that were produced from the same initial excitation, but shifted in time, are matched. In this manner, the time shift (delay) between the two waveforms can be precisely and accurately determined.

Cross-correlation velocity is given by

$$V = 2X / \tau_o \qquad (46)$$

where τ_o is the time shift for which

$$\left|\lim_{T\to\infty}\int_{-T}^{T} B_1(t) \odot B_2(t+\tau)\right|_{-\infty\le\tau\le\infty}$$

reaches a maximum value. Here X is the sample thickness, V is the velocity, t is time, T is the time duration (width) of the pulse, and τ is the time shift. Cross-correlation velocity was determined by transforming B1 and B2 into the frequency domain using discrete fourier transforms, multiplying the complex conjugate of B2(f) by B1(f), retransforming the result back to the time domain, and obtaining the time shift where the maximum in the cross-correlation function occurs (τ_o) (Bendat et al., 1980). A software routine (in FORTRAN, with callable VAXLAB-VMS routines) was written to perform these procedures. Velocity determined from cross-correlation is essentially a group velocity as the entire wave train (containing a broad band of frequencies) is considered in the calculation. Cross-correlation is a preferred method of determining velocity since it produces accurate velocities even with noisy signals (Hull et al., 1985).

2. Velocity Measurement Error

Potential errors in the velocity measurement arise from 1) thickness variability of the sample, 2) inaccuracy of the micrometer in measuring thickness, 3) couplant thickness variations, 4) time

base precision, 5) diffraction (beam spreading) phase shift, and 6) smearing of received pulses from intrinsic dispersion (velocity in the material varying with frequency), geometrical dispersion (specimens of finite width leading to side wall effects) and frequency-dependent attenuation (Breazeale et al., 1981; Lynnworth, 1989 and Papadakis, 1975). For our experimental configuration and analysis methods, 1), 2) and 3) will generally outweigh the other potential errors. It is estimated that the uncertainty is $\leq$ 0.36 % if 1), 2) and 3) are on the order of $\pm$ 10 μm or less. The time base error and the diffraction phase shift correction are on the order of 0.001 μsec and 0.0004 μsec (10 MHz broadband transducer), respectively, and were negligible in the calculation of the velocity measurement uncertainty. The velocity determination was done in the frequency-domain (as previously described) to minimize errors from smearing (Lynnworth, 1989).

3. Instrumentation

Basic instrumentation for velocity measurements included a transducer, pulser-receiver, time synthesizer, time base, voltage amplifier, waveform digitizer, and video monitors (one of which is digital). The time synthesizer, time base, voltage amplifier, and waveform digitizer were all GPIB (general purpose interface [IEEE-488] bus) programmable and daisy-chained together via GPIB cables. A minicomputer was used to control the GPIB instrumentation and transmit the acquired waveforms via GPIB. Software (in FORTRAN, with callable subroutines in IEX-VMS interface software to

communicate with the GPIB instruments) was written for instrument control and waveform acquisition (Generazio et al., 1989b).

The instruments were interfaced according to figures 67(a) and (b). The pulser-receiver applied the voltage pulse to the transducer to generate the ultrasonic waves into the sample and also received the raw ultrasonic waveforms FS'_1, FS_2, B_1, and B_2. The approximate times where the waveforms were expected to occur were determined *a priori* using the time synthesizer to find and position the waveforms on video. These times were then input into a data file. During data acquisition, the time synthesizer sequenced through the three time positions where waveforms were located.

The time base and voltage amplifier were used to modify the time and voltage scales to view the waveforms on video. The time base and time synthesizer were externally triggered by the pulser-receiver (a +2 volt synchronizing pulse). Triggering occurred on the positive slope of the pulse. The time base could be adjusted over a range 1 psec - 500 msec/div with the optimum setting for the waveforms determined *a priori* and inputted to a data file. The output of the pulser-receiver was attached to the voltage amplifier. The voltage amplifier, selectable over the range 50 mV - 1 V/div, was automatically adjusted by the digitizer so that the entire received analog waveform with maximum amplitude fit onto the waveform digitizer monitor. The waveforms were subsequently digitized into 512 point arrays (at a sampling rate ranging from 0.512 - 1.024 GHz depending on the time base time/division setting

in these experiments). Each waveform was acquired 64 times and averaged to obtain a "smoother" waveform with averaged noise levels. Outputs from the waveform digitizer were attached to the video monitors.

The pulser-receiver had several controls that are user-selectable to obtain the optimally-shaped FS'_1 from the transducer. The controls include repetition rate for the internal voltage pulse used to excite the transducer, internal pulse energy, damping to vary the resistance load presented to the transducer by the pulser-receiver, received signal attenuation, and high-pass filter for bandwidth adjustment.

Two different types of longitudinal wave transducers were used in this investigation. The first type of transducer (Ultran Laboratories, Inc., State College, Pa. 16801) consisted of a critically-damped lead metaniobate element. One transducer of this type had a center frequency of 5 MHz with an active diameter approximately 1.27 cm. Another transducer of this type had a center frequency of 10 MHz and an active diameter of 0.6 cm respectively. The 5-MHz element was bonded to a polystyrene buffer rod 1.6 cm in diameter and 1.9 cm in length. The 10-MHz element was bonded to a polystyrene buffer rod 0.8 cm in diameter and 0.79 cm in length. A thin (0.04 cm) pliable polymer material on the other end of the buffer rod allowed ultrasound to be transmitted into the specimen without the need for liquid coupling. Dry-coupling avoids contamination and possibly inaccurate results when porous materials

absorb a liquid couplant.

The second type of transducer (Panametrics, Waltham, MA 02254) consisted of either a 10-MHz or 20-MHz broadband lead metaniobate element with an active diameter of 0.6 cm. The element was bonded to a silica glass buffer rod approximately 1.75 cm in diameter and 1.27 cm in length. With this transducer, liquid couplant was necessary between the transducer and specimen to transmit ultrasound into the specimen.

4. Point Measurement

Point measurements (i.e., measurements at a single location) were made at room temperature on the edge- and center-cut bars of samples 52A, 53A, 59A, and 60A using the 10-MHz dry-coupling transducer connected to a pulser-receiver of 0.01 - 10 MHz bandwidth. Measurements were made on semicircular specimens from samples 53A, 59A, and 60A before (schedule 1, table 6(a)) and after reduction (schedule 5, table 9) using the 5-MHz dry-coupling transducer and the same pulser-receiver. Additional measurements were made on pieces cut from sample 52A before (schedule 2, table 6(b)) and after oxidation (schedule 3, table 7) using the 5-MHz dry-coupling transducer and the same pulser-receiver. The specimen to be measured for ultrasonic velocity was lightly clamped to the transducer using a small mechanical clamp. The clamp was tightened until stable B_1 and B_2 waveforms of highest signal-to-noise ratio were visible on the video screen. Waveforms were acquired in 25 repeated velocity measurements at the same point.

5. Elastic Modulus

In experiment 3, apparent elastic modulus was calculated from velocities (equation (1)). Elastic moduli are generally calculated from phase velocities, i.e., velocity at one specific frequency, since the elasticity of a material may depend on the loading rate (Lynnworth et al., 1989). Group and phase velocity will be essentially equal over the frequency range investigated if dispersion (velocity varying with frequency) due to the material itself and sample geometry are negligible (Breazeale et al., 1981 and Lynnworth, 1989). For the (1" diameter, semicircular) samples of experiment 3, velocity was seen to be essentially constant over the frequency range investigated. Additionally, change in elastic modulus values upon oxidation / reduction rather than absolute accuracy was of interest.

6. Scanning

Velocity measurements over an ordered array of points across the surface were obtained for several YBCO disk-shaped samples by means of a scanning technique at room temperature (Generazio et al., 1988). In general, scans were performed to locate regions of varying pore fraction or other microstructural inhomogeneity at room temperature and subsequently compare the superconductor behavior of the different regions. Scanning was accomplished through the use of computer-controlled x-, y-, and z- microscanning positioner tables (having a step resolution of 1.0 um) in addition to the instrumentation previously described (figure 68). Software (in

FORTRAN with callable subroutines in IEX-VMS interface software to communicate with the various GPIB instruments) was written to control movement of the positioner tables (Generazio et al., 1989b). The ultrasonic and data acquisition instrumentation was the same as that for the point measurements except that the 20 MHz transducer requiring liquid coupling and a pulser-receiver having a 1 - 150 MHz bandwidth were used.

Samples were mounted in a Lucite holder. A non-aqueous liquid couplant (Dow Corning 704 diffusion pump fluid) was used between the buffer rod and sample. A displacement pressure gauge was mounted over the transducer to control the contact pressure of the transducer on the sample. Unless otherwise specified, force was maintained at 12 $\pm$ 0.1 lbs. via computer control. After a set of waveforms was acquired at one point, the x- and or y- positioner table was moved the specified increment to the next point. A vibrator (made from a modified electric scribing tool) was used during this movement to aid in repositioning of transducer and couplant and to prevent the transducer from jamming on the sample. The volume element probed is determined by the ultrasonic beam diameter. For our experimental scan configuration, significant beam spreading is not likely to occur as the beam does not extend into the far field (figure 69). Thus, the (0 to -20 dB) beam width can be estimated by the active transducer diameter which is approximately 0.6 cm (0.93 x quoted transducer diameter (Krautkramer et al., 1977 and Panametrics, Waltham, MA 02254)).

Scanning over the sample/holder interface risks damage to the buffer rod. Thus several scans were usually necessary to image a significant portion of the sample. For most samples scanned, one or two square or rectangular areas were scanned. For sample 99 (0.07 pore fraction), several scans were run over 8 mm by 8 mm square areas near the center of the disk with measurements made every 0.1 mm (81 by 81 data grid). Force on the transducer was maintained at 5 $\pm$ 1 lbs. for the scan of sample 99. For sample 46B (0.105 pore fraction), three areas were scanned as shown in figure 70. Scan 1 was over a 20 mm by 5 mm rectangular area (area 1) with measurements made every 1 mm. Scan 2 was over a 10 mm x 10 mm square area (area 2) overlapping area 1 with measurements made every 1 mm. Scan 3 was over a 6 mm x 6 mm square area (area 3) that fit into the upper right hand corner of area 2 with measurements made every 0.5 mm. If one considers the volume element probed by the beam, ultrasonic data was actually obtained over a larger region by about 6 mm for each of the x and y dimensions as shown in figure 71. Another YBCO disk sample of 0.10 pore fraction was also scanned in a similar manner to determine if liquid couplant is absorbed through the pores during scanning of YBCO samples of this density.

Sample 51A, also near 0.10 pore fraction, was scanned using the 10 MHz transducer requiring liquid couplant and the pulser-receiver having a 0.01 - 10 MHz bandwidth. Before the first oxidation (schedule 2, table 6(b)), after the second oxidation (schedule 4, table 8), and after the subsequent reduction treatment (schedule 5,

table 9), a scan was run over a 3 mm by 5 mm area near the center of the disk with measurements made every 0.5 mm to determine the effect of oxygenation / reduction on the velocity profile. Additionally, point measurements with this same experimental configuration were made at the scan origin in coincidence with the scans to focus on the change at a single point on the disk. Sample 51A was ultrasonically cleaned in ethanol for 5 - 10 minutes after each scan to minimize contamination effects during oxidation/reduction treatments.

Typical scan and analysis times for scans consisting of 100 - 150 measurements were about 1 - 2 hours. Scans were run at least twice for each specimen region examined to determine reproducibility.

7. Ultrasonic Image

An ultrasonic image was constructed from the velocity values obtained at each scan point. A continuous scale consisting of 256 shades of gray (or color) and linear interpolation between points allowed the display of subtle velocity changes across the sample (Generazio et al., 1988). The image can be thought of as a two-dimensional projection representing averaged microstructural information for the volume of sample scanned.

E. Radiography

Conventional x-ray radiography was used to examine YBCO samples 99 and 46B for gross microstructural and/or compositional nonuniformity. Briefly, x-rays are attenuated exponentially by

matter, and their transmitted intensity can be expressed as (Macovski, 1983)

$$I = I_o \exp[(-\mu/\rho)(\rho * t)] \quad (47)$$

where I_o is the original beam intensity, μ/ρ is the mass attenuation coefficient (cm^2/g), μ is the linear attenuation coefficient (cm^{-1}), ρ is the bulk density (g/cm^3), and t is the section thickness (cm). When x-raying a specimen, second-phase regions (including pores) having mass attenuation coefficients different from the matrix generally show up as different gray levels on video or film if present in large enough concentrations along the path of the x-ray beam (Baaklini et al., 1986). Film radiographic techniques are capable of resolving porosity variations on the order of 3 % in ceramics (Klima et al., 1984).

Radiographs were made through the thickness of the YBCO disk with conventional contact methods, under conditions optimized to yield high accuracy and contrast. The radiographs were made with a tungsten source (target) and beryllium window. The source-to-disk distance was approximately 3 ft, and the exposure conditions were 120 kV, 5 mA, and 11 to 12 min. The disk was masked with lead and covered with thin lead screens to offset the effects of x-ray scattering from the sample edges and lead mask, respectively.

F. Compositional Analysis

1. X-ray Diffraction

X-ray diffraction (Cullity, 1984) was performed on top and

bottom surfaces of bulk YBCO samples with a computer-controlled diffractometer using CuK(α) radiation. Scans were performed over the range $2\theta = 15^\circ - 80^\circ$ at a rate of 2°/minute. Approximately 1 mm^2 of the surface was sampled by the x-ray beam. In several instances, material was ground from the surfaces and the sample rescanned to obtain compositional profiles through the sample thickness.

The relative intensities of the two peaks occurring at $2\theta = 32.5^\circ - 33^\circ$ were used to determine whether the structure was orthorhombic or tetragonal (see BACKGROUND section entitled "STRUCTURE OF YBCO"). A least-squares refinement procedure which first required choosing structure type and approximate unit cell lengths was used to determine the actual unit cell axis lengths. From the c-axis length, oxygen content was determined from relationships established by Wolf et al. (1988) (atoms O = 76.40 - 5.95*c-axis) and Ono (1987) (atoms O = 70.512 - 5.45*c-axis) for which the estimated uncertainty was $\pm$ 0.05 atoms O.

2. Inert Gas Fusion

An inert gas fusion technique was used to determine oxygen weight percent in the YBCO samples (Fricioni et al., 1988). Briefly, 50 mg - 100 mg of sample was placed into a graphite crucible. The crucible acted as a carbon resistor completing a high current circuit in an impulse fusion furnace. The circuit applied an impulse current of 600 to 1300 A through the crucible, heating it to about 3000 °C and causing the sample to decompose. The carbon bonded with oxygen to form CO. Helium carrier gas was used to sweep the CO

from the fusion chamber. CO was then further reacted with heated CuO_2 to form CO_2. The gases in the carrier stream were introduced into the chamber of an infrared detection system. An infrared source (nichrome wire resistance heated to approximately 850 °C) transmitted a broad spectrum of energy through the chamber. The CO_2 absorbed energy at a precise wavelength within the IR spectrum which resulted in less energy being received at the detector. All other IR energy was eliminated from reaching the detector by a precise wavelength filter. Thus, the absorption of IR energy was attributed to only CO_2. The concentration of CO_2 was detected as changes in energy at the detector, producing a voltage offset relative to a starting reference level. Estimated uncertainty in the oxygen determination is 1 % of the reading.

3. Colorimetry

Colorimetric analysis was used to determine the weight percent of Si in YBCO samples (Brabson, 1988). YBCO powder samples were fused in soda ash in a platinum crucible. Solutions were made by dissolving fused material in HCl. The amount of Si in YBCO was determined using a spectrophotometer in which the intensity of a narrow band of light wavelengths passing through the analytical solution was compared to the intensity of the light passing through a "blank" solution. Estimated uncertainty was about 10 % of the reading.

4. Inductively-Coupled Plasma Atomic Emission Spectroscopy (ICP - AES)

Simultaneous weight percent determinations of Y, Ba, and Cu in the YBCO samples were accomplished with ICP - AES (Faires, 1988). Chunks cut from the YBCO sample were ground to a fine powder in a boron carbide mortar. 50 mg of powder was dissolved in 1:1 HCl in preparation for analysis. The inductively-coupled plasma excitation source consisted of an induction coil encircling a quartz torch in which argon gas was flowing upward. Radio frequency energy was applied to the coil which resulted in an intense oscillating magnetic field. The argon was exposed to an electric discharge and seed electrons and ions were formed. The ions were accelerated in the magnetic field and encountered resistance through collision with argon atoms producing a high temperature argon plasma. The YBCO in solution was aspirated through the torch into the plasma where vaporization, atomization, and excitation of the atoms and ions occurred. Upon relaxation to the ground state, radiation was emitted at wavelengths characteristic of the elements. Multielement analyses are accomplished using the direct reading spectrometer detection system. Estimated uncertainty was about at 3 to 5 % of the reading.

5. Scanning Electron Microscopy

Scanning electron microscopy (SEM) (Verhoeven, 1988) in both the backscatter (BSE) and secondary (SE) electron modes was used to examine polished and fracture surfaces of YBCO samples for topography and possible contamination. Magnification ranged from about 40X to 3000X. Electron beam spot size was about 1 μm in diameter. Energy dispersive (EDS) and wavelength dispersive (WDS)

x-ray spectroscopy were used for elemental analysis of foreign structures.

6. Transmission Electron Microscopy

Transmission electron microscopy (TEM) (Romig Jr., 1988) in conjunction with electron diffraction and EDS was used to identify the presence of CuO in thin sections of YBCO. Preparation consisted of mechanically dimpling by grinding followed by ion milling until the section was electron transparent. Magnification range was 10,000X to 20,000X.

G. Microstructural Analysis

1. Image Analysis

In experiment 2, the Quantimet 900 computer-controlled image analysis system was employed to quantify the average sizes (length and breadth) and volume fractions of pores and CuO grains. The essential features of the analysis system and procedure are described here. Images were obtained by placing samples under an upright reflected-light microscope using bright-field illumination. The microscope light source, aligned for even illumination, was interfaced with a scanner to display the image on a television screen. Each scan line consisted of 719 pixels and there were 566 scan lines for a total of about 400,000 pixels. A central electronic processor was used for image detection and measurement of stereological parameters.

Gray level thresholding was used to distinguish the pores

(black), CuO particles (white), and the YBCO matrix (orange). The gray scale consisted of 64 levels. The microscope magnification, 400X, made the smallest features appear around 1 mm in length on the live video frame. The sample area analyzed in the frame was on the order of 0.01 mm^2. Estimate of volume fraction was obtained from areal fraction (the ratio of the number of detected pixels to the total number of pixels in the measurement field) (ASTM E1245-88). Areal fraction generally produces lower errors than lineal analysis and point counting procedures (Vander Voort, 1984). Mean pore and CuO particle dimensions were estimated from eight ferets separated by 22.5° encompassing a 180° rotation. Mean length and breadth are determined from the average of the maximum and minimum, respectively, of all the ferets for each particle. A computer program accumulated and analyzed the data. The analyzer was operated in the semi-automatic mode with manual readjustment of gray level and focus at each measurement field. Precision of the measurement was determined by repeated measurements on a single field. (Absolute accuracy of the measurements is primarily determined by the resolution and gray level discrimination capabilities of the image analyzer (Vander Voort, 1988a) and the choice of gray level threshold made by the operator.)

Upon completion of ultrasonic scanning, sample 46B was cut into two semicircular halves in preparation for microstructural analysis. These were mounted and polished on automatic polishers to expose the top and the cross-section of the disk (figure 72). The top of the

disk had 300 μm removed during polishing whereas the cross-section initially had 100 μm removed during polishing. On the top section, 1 measurement field at 5 locations across the section was analyzed using the image analysis system. For the cross-section, at each of 5 locations from left to right across the diameter, 21 fields in a straight line downward through the entire thickness were analyzed and the resulting sizes and areal fractions averaged. Averaging these values through the sample thickness mimics the ultrasonic measurement, which essentially averages the microstructural information as the beam travels between the faces of the sample. The cross-section was examined two more times after removing 1.1 mm and then 6 mm of material as shown in figure 72(b). For the first two cuts of the cross-section, the 5 left to right locations examined were separated by 5 mm as shown in figure 72. For the last examination, only 3 locations separated by 5 mm were examined since the disk was substantially reduced in size. Estimated uncertainties in the size and volume fraction measurements from repeated trials was on the order of $\pm$ 10%.

2. Optical Microscopy

Bright field optical microscopy (Vander Voort, 1988b) was used to obtain pore and grain distribution micrographs of YBCO samples. Magnification ranged from 25X to 1500X. Grain distribution micrographs were obtained with polarized light. Mean grain size was obtained from optical micrographs using the Heyn-intercept method (ASTM E112-85). Grain size was determined for four orientations of

the micrograph. Estimated uncertainty in mean grain size was approximately ± 20 %.

V. RESULTS AND DISCUSSION 1: Pore Fraction Effects

A. Specimen Characterization

Tables 10(a) - (e) summarize the dimensional, microstructural and compositional characteristics, respectively, of the edge- (E) and center- (C) cut bars from samples 52A, 53A, 59A, and 60A. Figures 73 - 76 show photomicrographs of the porosity and grain distributions for polished sections of the edge- and center-cut bars from samples 52A and 60A. Figure 77 shows x-ray diffraction patterns for the center-cut bars of samples 52A, 53A, 59A and 60A.

Sample 60A was the only disk of the four that was visibly macrocracked on the surface before the cutting and machining procedures. After these procedures, surface macrocracks were not apparent on any of the bars. Bars 52A-C and 52A-E had a smaller height and cross-sectional area than the other bars which had close to identical dimensions. The pore fraction range was approximately 0.10 (for sample 60A) to 0.25 (for sample 52A) with smaller pore fraction corresponding to higher peak sintering temperature. Interconnected porosity was easily seen for the bars cut from sample 52A but was less obvious for the other bars. Mean grain diameter increased with decreasing pore fraction and increasing sintering temperature for the samples (figure 78). Elongated grains were present but appeared randomly oriented in all bars (i.e. random

texture). Twinning was evident in most, but not all grains, during examination of the grain distribution with polarized light microscopy up to 1500X. This potentially indicated incompletely oxygenated grains (Clarke et al., 1989).

Single point longitudinal wave ultrasonic velocity (center frequency of transducer = 10 MHz) increased with decreasing pore fraction in a similar linear fashion (figure 79) to that previously reported in chapter 1 (figure 59). Pore fraction was converted to % porosity in figure 79 in keeping with the convention of chapter 1. (Eight out of thirteen data points in figure 59 of chapter 1 were obtained from ultrasonic measurements on these bars.) Linear regression analysis yielded

$$\text{Velocity } (\text{cm}/\mu\text{sec}) = -0.007 \times \text{Percent Porosity} + 0.560 \qquad (48)$$

and

$$\text{Percent Theoretical Velocity} = -1.23 \times \text{Percent Porosity} + 100 \qquad (49)$$

with correlation coefficient and level of significance of 0.994 and 0.001, respectively. 95 percent confidence interval widths are less than approximately 10% of slope and intercept values (the smaller the confidence interval, the better). The velocities for edge and center pieces varied by no more than approximately 1 %. Within-sample microstructural uniformity appeared good as indicated from the pore fraction, grain size, and ultrasonic velocity results.

Comparison of the x-ray diffraction patterns and lattice parameters for the bar surfaces examined showed no major differences.

The structures were all orthorhombic according to the lattice parameters. The relative intensities of the double split peak at $2\theta = 32^\circ - 33^\circ$ also indicated the orthorhombic phase although the peak split was not as sharp as expected. The orthorhombic II (OII) phase characterized by $a < b < c/3$ was not observed. From ICP-AES, the elements Y, Ba, and Cu were present in close to identical amounts in the bars. From colorimetry, the common impurity Si was approximately 0.15 weight percent or less in the samples. Sample 59A contained the least amount of Si by at least a factor of 2. From the porosity distribution photomicrographs, trace amounts (< 1 volume percent) of CuO second phase (white regions as determined from EDS and TEM analysis) were apparent between YBCO grains for the bars cut from samples 53A, 59A, and 60A. A larger amount (2 - 5 volume percent) is apparent for the bars cut from sample 52A. From these results, relatively good sample-to-sample and within-sample compositional uniformity was apparent although some differences were pointed out in this discussion.

Oxygen content was approximately the same for all of the bars according to inert gas fusion and the O atom values derived from the Wolf et al. (1988) and Ono (1987) empirical relationships. The inert gas fusion system gave larger values of oxygen contents (approximately 18 weight %) than would be expected (16.5 - 16.8 weight %) for orthorhombic YBCO suggesting that these values may have some systematic error. On the other hand, the inert gas fusion data might indicate the presence of the semiconducting tetragonal

phase T′ which contains greater than 7.0 O atoms per YBCO formula unit (Lay, 1988; Nakazawa et al., 1987 and Torardi et al., 1987). The empirical relations of Wolf and Ono yielded 6.8 - 7.0 O atoms per YBCO formula unit which is the desired oxygen content for optimum superconducting properties. Two iodometric titrations (Nazzal et al., 1988) performed at the IBM Almaden research center on 50 mg pieces of sample 59A yielded 6.94 +/- 0.03 O atoms per YBCO formula unit which agreed fairly well with values obtained from the Wolf and Ono relations. To summarize the oxygen content results for the bars cut from YBCO samples 52A, 53A, 59A and 60A, the oxygen contents determined from the Wolf and Ono relations and from iodometric titrations support the existence of the optimum orthorhombic phase. Oxygen content as determined from inert gas fusion and possibly low twin density suggest the existence of a T′ phase. In any case, good sample-to-sample and within-sample uniformity with respect to oxygen content was apparent.

B. Bulk Transport J_c and n-value

Table B1 (appendix B) and figures 80 and 81 give the raw data for the transport J_c and n-value at 77 K for the center-(C) and edge-(E) cut bars from samples 52A, 53A, 59A, and 60A. The correlation coefficient for the n-value fit was greater than 0.985 in all cases indicating a good logarithmic fit. Figures 82 and 83 show measured J_c and n-value at 77 K versus pore fraction for the bars, respectively. The largest J_c's and n-values were obtained for bars

59A-C and 59A-E and were on the order of 21 A/cm^2 and 25 - 35, respectively. The lowest J_c and n-value were obtained for bar 60A-E and were approximately 2 A/cm^2 and 4, respectively. Note that sample 60A contained the lowest pore fraction of the four samples and showed the poorest electrical behavior. The latter result was unexpected based on the models of Ekin (1987) and Evetts et al. (1989). Figure 84 shows generated H_s (equation (29)) at 77 K versus pore fraction for the bars. Small H_s was obtained in each case due to the low J_c's.

Figure 85 shows the relationships at 77 K between calculated H_{c1J} and grain size, and between H_{c1J} and pore fraction (based on the observed relationship between pore fraction and grain size shown in figure 78). Similarly, figure 86 shows the relationships at 77 K between expected J_{cmax} (for moderate intergranular coupling) and grain size, and between J_{cmax} and pore fraction for the bars. It is seen that H_{c1J} and J_{cmax} are expected to increase with decreasing grain size (and thus increasing pore fraction for these samples) (ignoring effective cross-section reductions in the bars caused by the presence of pores (equation (30)). Of most significance here, the measured J_c's for all bars were approximately an order of magnitude lower than the corresponding J_{cmax}. This result indicates very weak intergranular coupling, i.e. moderate intergranular coupling is not exhibited by these bars (Stephens, 1989) (BACKGROUND section entitled "Considerations in the Interpretation of J_c").

Possible causes of weak coupling include cracks, pores or

impurities at grain boundaries. Impurity phases may include YBCO tetragonal semiconducting phase resulting from a poorly or overly oxygenated bulk. Since the oxygen content appeared to be approximately 6.8 O atoms per formula unit or better for all bars, it appears unlikely that oxygen deficit is the cause of the low J_c's. However, the possibility of oxygen content in excess of 7 O atoms per formula unit (as determined from inert gas fusion) characteristic of the tetragonal T′ semiconducting phase has been discussed.

Surface macrocracks were obviously visible only for sample 60A. However, it is possible that microcracks (not visible to the eye) were introduced into all bars or extended during cutting and machining, leading to severe weak-link behavior. Si contamination was previously shown to possibly reduce J_c and n-value (Newcomb et al., 1988) but not to the extent seen in this study. However, the specimens (59A-C and 59A-E) having the largest J_c's and n-values contained the least amount of Si impurity by at least a factor of 2. Since the sample 60A from which 60A-E was cut showed visible surface cracking, the macrocracking might have contributed to an even more severely weak-coupled material than for the other samples resulting in the poorest electrical behavior. Cracking can also reduce the effective cross-section of the conducting path resulting in a reduced J_c (Stephens, 1989). As previously noted, J_c limited by weak links may depend on the weakest material and therefore may not be representative of the properties of the bulk containing a distribution of j_{cJ}'s (Evetts et al., 1983 and Aponte et al., 1989).

The average contact resistance was approximately 0.75 Ω or less for sputtered contacts on a bar from sample 59A. This contact resistance, although significantly larger than obtained by Ekin et al. (1988), is likely to cause minimal joule heating effects. For sample 59A-C and given $P = I^2R$, approximately 1.8 W were generated with I_c = 1.56 A and R = 0.75 Ω. Considering that the bars were immersed in liquid nitrogen during the J_c measurement, it is unlikely that the contact heating raised the bar temperature enough to affect the measurement (Scheel et al., 1987). The contacts were determined to be ohmic from the measurements at two current levels.

J_c data could not be obtained for bars 53A-E and 60A-C. The following detailed explanation concerning the measurement results for these bars is provided as it may also give clues concerning the cause of low J_c's (origin of weak links) for the other bars. These bars were tested several times each with similar results. As the current was increased, the current and voltage readings each suddenly became very noisy making the data unreliable. When the samples were warmed after each test, it was found that a current lead had popped off at the silver paste - gold sputtered contact junction. In no case did the gold contact come off also. After several failed attempts, it was determined that at 77 K for each sample there was low lead-to-lead resistance among three of the leads and very high resistance (approximately 500 Ω) between the current lead that had popped off and any of the other leads. Considering joule heating effects again, for sample 59A-C, about 1200 W were generated with I_c

= 1.56 A and R = 500 Ω. At room temperature, the lead-to-lead resistance for the "good" leads was approximately 5 Ω while the resistance between the "bad" lead and any other (good) lead was approximately 15 Ω. The decrease in resistance at from 77 K to room temperature for the bad - good lead path may be characteristic of a semiconductive resistance mechanism within the sample (Kittel, 1986), possibly indicating the presence of tetragonal YBCO. It appeared that one end of each of these samples was non-superconducting and there was significant local heating at this end while the current was increasing, thus causing the silver paste joint to pop off. These ends were examined optically up to 1500X but nothing out of the ordinary (such as cracking) was detected.

C. A. C. Susceptibility

The susceptibilities shown are external, i.e., those calculated from equations (34) and (32) with demagnetization corrections not included. Susceptibility response was not affected by the presence of the gold contacts as determined from measurements before and after applying contacts to sample 46B-C.

1. Effect of Pore Fraction

The plots of a.c. mass susceptibility versus temperature (χ'_m and χ''_m) at H_{ac} = 20 mOe and f = 100 Hz for the center- (C) and edge- (E) cut bars of samples 52A, 53A, 59A, and 60A are given in figures B1(a) - (h) (appendix B). Plots B1(a) - (h), all of which showed a single loss peak in the χ''_m response, were used to derive the

information shown in figures 87 - 92 and in tables B2 - B4 (appendix B). Tables B2 - B4 give the detailed shielding and loss peak characteristics for the bars.

Figures 87 and 88 show transition temperature (T_c) and magnetic transition width (ΔT_{cm}) versus pore fraction for the bars. Figure 89 shows % complete shielding at 77 K versus pore fraction. Figures 90 and 91 show the temperature where the loss peak center occurs, and the width of the loss peak, versus pore fraction. Both 60A-E and 60A-C generally showed poorer magnetic properties than the other bars. Thus, as was the case for the electrical properties, the sample containing the lowest pore fraction (60A) showed the poorest magnetic properties. Poorer shielding capability at most temperatures including 77 K, lower T_c (for 60A-E), larger ΔT_{cm} (for 60A-C), lower temperature for initial flux penetration, lower loss peak center temperature and a wider loss peak (for 60A-C) were observed for bars cut from sample 60A as compared to the other bars. As previously discussed, a high degree of shielding at the highest possible temperature is desirable. High temperatures for the loss peak, indicating the onset of power losses as flux penetration and pinning occur, are also desirable.

Magnetic properties were also nonuniform from edge to center for sample 60A (figure 92) which indicates possible microstructural and/or compositional inhomogeneity (Clarke et al., 1989). The large ΔT_{cm}'s and loss peak widths for bar 60A-C may indicate inhomogeneity within the bar itself (Clarke et al., 1989 and Ekin, 1983). Better

within-sample uniformity with respect to magnetic properties was observed for samples 52A, 53A, and 59A.

The calculated intergranular current density j_{cJ} was a miniscule 0.032 A/cm^2 for all the bars. However, opposite to what was expected, the loss peak center temperatures (as well as the initial rise temperatures in the loss peaks) where j_{cJ} is determined were 5 - 10 K lower in bars 60A-C and 60A-E than those of the other bars. It was expected that as pore fraction decreased, the increased contact area between the grains would result in higher j_{cJ} and thus raise the temperature of the intergranular peak (Nikolo, 1990). The observed value of j_{cJ} is several orders of magnitude less than that obtained from transport measurements. However, except for bars 60A-E and 60A-C, the temperature at which j_{cJ} was determined was higher than the temperature (77 K) at which transport J_c was measured. It is expected that J_c will decrease with increasing temperature for YBCO (Aponte et al., 1989). Additionally, the transport measurements were made in zero field while the susceptibility measurements were made with an applied field of 20 mOe. Critical current density has previously been observed to decrease with increasing applied field (Dersch et al., 1988; Ekin, 1987; Peterson et al., 1988 and Stephens, 1989).

2. Shielding Per Unit Mass

Figure 93 indicates the relative shielding capability per unit mass for the bars. Large negative values for mass susceptibility indicate greater shielding capability. The largest negative values

were obtained for bars 52A-C and 52A-E which had the largest pore fraction (lowest bulk density). This may support contentions by Hein (1986) and Kittel et al. (1988) that a surface layer of superconducting material can provide shielding similar to that of bulk superconductors. (I.e., a fully-dense material may not be necessary for optimum a.c. shielding.)

3. Magnetic Field Dependence

Figure 94 shows the magnetic field (H_{ac}) dependence of the susceptibility measurement for a center-(C) cut from sample 46B. (Sample 46B-C appeared to be a very poor superconductor (note the low T_c) as will be discussed in more detail later.) The χ'_m transition shifted slightly to lower temperatures (by about 0.25 K) and broadened with each doubling of H_{ac}. The peak in the χ''_m response broadened with increasing H_{ac} and at the largest field (H = 80 mOe), it shifted to lower temperature as well. These results agree with previous investigations (Goldfarb et al., 1987a and 1987b and Loegel et al., 1989). This indicates the necessity of measuring the samples at the same H_{ac} in order to make valid comparisons.

4. Frequency-Dependence

Figure 95 shows the frequency dependence of the susceptibility measurement over the range 10 - 1000 Hz for bars cut from sample 52A. The χ'_m and χ''_m responses appear to be relatively frequency-independent compared to results shown by Loegel et al. (1989) over a similar frequency range for YBCO. This indicated that eddy current and surface resistance effects were negligible in this frequency

range and that losses seen in the χ'' were likely to be due to hysteresis in the bulk pinning mechanism (Goldfarb et al, 1987b and Cullity, 1972).

5. Single-Loss Peak Origin

Figure 96 show the susceptibility responses of a sintered bar and the same sample in powdered form for material from sample 51A. The disappearance of the loss peak in the χ''_m response upon pulverizing (grain decoupling) may indicate that 1) the single peak seen in the χ''_m response for the sintered samples is the intergranular peak, i.e., the intragranular peak was suppressed for the sintered samples agreeing with the models from Kupfer et al. (1988a) and Clem et al. (1987) and that 2) hysteretic bulk pinning losses observed from the χ''_m response of the sintered sample are likely to be intergranular in nature (Kupfer et al., 1987). The low temperature tail of χ'_m in the powdered sample may be due to inhomogeneity (Kupfer et al., 1987).

D. Within-Sample Uniformity of Superconductor Behavior

Consider first the electrical (J_c and n-value at 77 K) properties. If $J_c = 0$ for bars 53A-E and 60A-C, it is seen that J_c is fairly uniform from edge-to-center for all samples. Recall that the experimental uncertainty in J_c was approximately ± 10 %. The n-value within-sample variation is greater, varying by as much as 33 % for sample 52A.

Consider the properties derived from a.c. susceptibility

measurements including T_c, ΔT_{cm}, and the loss peak width. The within-sample variation of these properties was essentially zero for all samples except sample 60A which exhibited significant variations. Not surprisingly, sample 60A exhibited the worst overall superconductor behavior as previously discussed.

The nonuniformity of sample 60A is likely to originate from compositional and/or microstructural gradients as observed by Clarke et al. (1989). However, microstructural (grain size and pore fraction), compositional (x-ray diffraction and oxygen content), and single point ultrasonic velocity measurements were not able to discriminate significant differences in these variables for 60A-C and 60A-E. It is possible that 1) property-affecting microstructural and compositional (such as oxygen) gradients with respect to the variables we considered were present but occurred on a small enough scale such that they were not detectable with our analyses methods; 2) other property-affecting compositional gradients such as Si impurity gradients were present; Si content was analysed from bar-to-bar by the ICP - AES technique but the results were believed to be false and not enough bar material was left for further colorimetric analysis; and/or 3) other property-affecting compositional (such as YBCO tetragonal semiconducting phase and/or S, Ca, and Al common impurities) and microstructural gradients not considered in this investigation were present.

D. Concluding Remarks

The superconductor properties of similarly-processed, untextured YBCO specimens of pore fraction 0.10 - 0.25 were compared. From electrical and a.c. susceptibility measurements, superconductor properties including within-sample uniformity were poorest for sample 60A which contained the lowest pore fraction. Ultrasonic velocity measurements proved to be a simple, reliable and nondestructive means of estimating pore fraction due to the strong linear dependence of velocity on pore fraction. This is important if improved properties occur at an intermediate pore fraction for bulk, untextured YBCO as is indicated by this and other studies. However, neither the velocity nor the destructive measurements were able to discern the microstructural and/or compositional inhomogeneity causing the different superconducting behavior of bars 60A-C and 60A-E. The edge- and center-cut bars from samples 52A, 53A, 59A, and 60A exhibited low critical current densities (as compared to those expected for moderate intergranular coupling). The very low J_c's are attributed to the presence of weak links between superconducting regions.

VI. RESULTS AND DISCUSSION 2: Spatial Variations

A. Radiographic Characterization

The x-ray radiograph negatives and films of samples 99 and 46B did not reveal any definite gray scale variation thruought the disks. Therefore, if any gross nonuniformity existed, it apparently

was below the detectability limit of conventional radiography for this material.

B. Ultrasonic Characterization

Ultrasonic scanning at a center frequency of 20 MHz was performed on several YBCO disks 1" in diameter and 85 - 95 % dense (0.15 to 0.05 pore fraction) (as described previously in the EXPERIMENTAL PROCEDURES section entitled "Ultrasonics"). All resulting velocity images were identically reproducible within 0.1 %. For all samples except one, 1) a random pattern of velocity variation was apparent in the resulting ultrasonic image and 2) the total velocity variation was on the order of 1% (normalizing the minimum and maximum velocity values to the velocity expected for a fully-dense sample, i.e., the theoretical velocity of 0.560 cm/μsec (see chapter 1)). For example, figure 97(a) shows an ultrasonic velocity image for an 8 mm by 8 mm area (measurements were made every 0.1 mm) of sample 99 (0.07 pore fraction). The lack of a regular pattern of velocity variation indicated that no regular pattern of microstructural variation existed within the sample. Thus, it was not practical to section sample 99 and the others showing random variation to determine the microstructural feature(s) responsible for the variation.

Sample 46B (0.105 pore fraction) was the one sample scanned that exhibited a regular pattern of velocity variation. Figure 98 shows the resulting images constructed from scans at the areas

identified. Scan 1 covered a 20 mm by 5 mm rectangular area (area 1) with measurements every 1 mm. Scan 2 covered a 10 mm x 10 mm square area (area 2) with measurements every 1 mm. Scan 3 covered a 6 mm x 6 mm area (area 3) that fit into the upper right hand corner of area 2 with measurements every 0.5 mm. A regular pattern of velocity variation of $\leq$ 2 % from edge (largest velocities) to center (lowest velocities) was observed.

C. Microstructural Analysis

Sample 46B was sectioned for microstructural analysis in an attempt to determine the cause of the velocity variations (figure 72). Three thickness cross-sectional areas (figure 72(b)) were examined as previously described in the PROCEDURES section entitled "Image Analysis". Cuts 1, 2, and 3 had 0.1 mm, 1.2 mm, and 7.2 mm, respectively, of material removed from the thickness cross-section with respect to the initial center cut.

1. Grain Diameter and Grain Orientation

Within the uncertainty of the Heyn-intercept grain size measurement (approximately $\pm$ 20%), the mean grain diameter was constant and around 2.2 - 2.4 μm from left to right edge. (Note that grain size is not expected to have a major effect on elastic properties anyway (Baaklini et al., 1989; Birring et al., 1987; Papadakis, 1987 and Rice, 1977).)

Figure 99 shows grain diameter versus orientation for sample 46B for four grain/micrograph orientations. This plot shows an

almost constant grain size of approximately 2.3 μm for each orientation despite the fact that YBCO grains are severely nonequiaxed. Thus, grain orientation, which can have a significant effect on elastic properties, was not present.

2. CuO Volume Fraction and Particle Size

SEM and TEM analysis confirmed that the white spots seen during image analysis were CuO particles. For each of the three cuts, a trace amount (0.003 to 0.004 volume fraction) of CuO was present on average from left to right edge across the thickness cross-section. Average particle length and breadth were observed to be about 1 μm and 0.7 μm, respectively, irrespective of position. Particle orientation appeared random from image analysis and optical micrographs.

3. Pore Fraction and Size

SEM analysis confirmed that the black spots seen during image analysis were pores (figure 100). Figure 101 shows pore fraction versus position for the three cuts. Figure 101(a) shows a significant systematic mean pore fraction variation from 0.10 at the edge to 0.15 in the center for cut 1 (0.1 mm from the midplane). Figures (b) and (c) both show an essentially uniform pore fraction of 0.09 to 0.10 for cuts 2 (1.2 mm from the midplane) and 3 (7.2 mm from the midplane). On average for each of three cuts, pore length and breadth were observed to be about 1.8 μm and 1 μm, respectively, irregardless of position. Pore orientation appeared random from image analysis and optical micrographs.

D. Correlation of Microstructural and Ultrasonic Results

To summarize the microstructural results for sample 46B, CuO volume fraction, CuO particle size, pore size and grain size were, on average, independent of position from left to right edge. Grain size was also independent of orientation. Pore fraction was the only microstructural variable that exhibited significant, systematic average variation. This pore fraction variation occurred in cut 1 and ranged on average from 0.10 (edge) to 0.15 (center). Pore fraction was uniform from edge to center in cuts 2 and 3. Based on the fact that velocity decreases with increasing pore fraction for YBCO as established in chapter 1, the pore fraction results from cut 1 are consistent with the velocity image shown in figure 98(a). Concerning cut 1, figures 98(a) and 101(a) show that higher velocities correspond to lower pore fractions at the sample edges and lower velocity corresponds to higher pore fraction at the sample center. For cut 3, the uniform pore fraction seen from edge to center agrees with the nearly uniform velocity seen across the top of the velocity image shown in figure 98(b). From the microstructural results of cuts 1 and 3, and the velocity versus pore fraction relationship established in chapter 1 for YBCO (see figure 59 in chapter 1), it appears that the velocity variations seen in the images of figure 98 result from pore fraction variations. This conclusion is summarized in figure 102 and agrees with conclusions of Generazio et al. (1988) and Kunnerth et al. (1989) for velocity variations seen in SiC.

Based on the velocity image shown in figure 98(a), systematic pore fraction variations similar (although maybe not quite as large) to those seen for cut 1 might have been expected for cut 2 since cut 2 was only about 1 mm away from cut 1. The expected pore fraction variation may have been seen at a plane on either side of, and 100 μm from, cut 2, for example. This illustrates the difficulty involved in absolute correlations between ultrasonic image results and microstructural results. The ultrasonic image represents averaged microstructural information in the volume of sample probed and provides a three-dimensional capability that optical microscopy does not. Theoretically, for absolute correlation, all two-dimensional thickness cross-sections would have to be optically examined and the stereological parameters quantified and averaged at each plane. Additional difficulties concerning correlations arise due to the uncertainty in the location and width of the ultrasonic beam used to approximate the volume of sample probed (Lempriere, 1989).

From figure 59 in chapter 1, it was determined that a 1% increase in percent porosity resulted in about a 1.3% decrease in percent theoretical velocity for YBCO. Considering just the pore fraction results from cut 1 in sample 46B, a 5 % increase in percent porosity was apparent corresponding to a 1.5 - 2 % decrease in velocity from edge to center (figure 102). About a 6 - 7% decrease in velocity would have been expected considering the former result from chapter 1. The discrepancy can be explained by noting that the average pore fraction in the volume of sample probed should be

considered, not just the pore fraction in one two-dimensional plane. For example, if the pore fraction results of cuts 1 and 2 are averaged, a 3 % increase in percent porosity corresponding to the 1.5 - 2% decrease in velocity results from edge to center (figure 103) which is more consistent with the relation established in chapter 1.

E. Further Microstructural Considerations

Analyzing 1 horizontal plane from left to right edge across the thickness cross-section would possibly have provided unrepresentative information compared to the average of 21 planes covering top-to-bottom for any of the stereological parameters examined. Figure 104 illustrates this by showing pore fraction versus position along the edge of the semicircular section of sample 46B as indicated in figure 72(a). This edge position corresponded to one horizontal plane in the thickness cross-section of cut 1. No regular variation from edge to center is indicated.

Several of what appeared to be second-phase inclusions about 100 μm in diameter (figure 105) were seen in the thickness cross-sections examined. From back-scatter electron microscopy, and energy and wavelength dispersive spectrometry (EDS and WDS, respectively), these inclusions appeared to be composed of a white CuO finger-like structure surrounding a gray Si-O oval structure. Some Si signal was observed on random fracture surfaces of sample 46B as well. However, no source of Si contamination could be pinpointed. The starting and ball-milled YBCO powders were found to

contain less than 0.04 weight percent Si from colorimetry while the sintered sample after ultrasonics was found to contain about 0.45 weight percent Si. Some leakage of ultrasonic couplant (Dow Corning 704 diffusion pump fluid containing Si) into pores may have occurred. However, another YBCO disk of 90% theoretical density was found to gain only 0.00015 grams (0.002 weight percent) after a similar ultrasonic scanning procedure. Another possible source of Si contamination was the diamond extender fluid used during polishing (after ultrasonic scanning) in preparation for microstructural analysis. The value of bulk density obtained from the dry-weight dimensional measurement of sample 46B (5.71 g/cm^3, 89.5% of theoretical density) was essentially identical to that calculated from pore fraction measurements (5.72 g/cm^3) (assuming a unit cell density of 6.38 g/cm^3 for YBCO). This indicated a negligible formation of additional solid phase. In any case, if the Si contamination occurred during processing, and the Si / Si-O inclusions were thus solid, it is unlikely that velocity was significantly affected because the volume fraction of Si was so small (especially when compared to the pore fraction).

Residual stresses are likely to exist in YBCO (Fisher, 1975) but their variation and resulting effect on velocity were not considered in this investigation. Velocity changes on the order of only 0.15% (steel) (Shyne et al., 1981) and 0.025% (aluminum) (Zeiger et al., 1982) have been measured for specimens stressed up to 200 MPa.

F. Microstructural and Compositional Analysis of Edge and Center Pieces

Because of the variation seen in both the ultrasonic image and the pore fraction from edge (E) to center (C) for sample 46B, bars at edge and center locations were cut from the other, still-intact half of the sample (figure 72(a)). The bars were lightly ground on the polished surface to remove possible contaminants from polishing and then ultrasonically cleaned in ethanol. They then underwent superconductor measurements and microstructural and compositional analysis. The results of microstructural and compositional analysis of bars 46B-C and 46B-E are presented in table 11 and figures 106 and 107. No significant differences were noted in either the unit cell parameters, grain size or oxygen content determined from the different methods for bars 46B-C and 46B-E. The weight percents of Y, Ba, and Cu were measured on random pieces from sample 46B using the ICP-AES method with the resulting ratio 1:2:3. Surface macrocracks were evident on the received sample but were not apparent after machining. The weight percent oxygen as determined from inert gas fusion gave smaller values with larger scatter than those seen for the bars cut from samples 52A, 53A, 59A, and 60A. This may have indicated some oxygen deficiency and/or oxygen content inhomogeneity. However, most other experimental measurements indicated the orthorhombic phase for bars 46B-C and 46B-E. These measurements included 1) the oxygen content obtained from the Wolf et al. (1988) and Ono (1987) relations, 2) significant twinning of the

YBCO grains (figure 106), and 3) the relative intensities of the two peaks at $2\theta = 32.5° - 33°$ in the x-ray diffraction pattern. The orthorhombic II (OII) phase characterized by $a < b < c/3$ was not observed.

G. Superconductor Behavior of Edge and Center Pieces

The results of a.c. mass (external) susceptibility (χ'_m and χ''_m) and electrical tests are given in figure 108 and table 12. The susceptibility was run under the same conditions as those previously described in chapter 1 for samples 52A, 53A, 59A, and 60A. The uncertainty in the susceptibility values was approximately 6 % mainly due to the uncertainty in the measurement of the bar dimensions. Both pieces exhibited poorer properties than those seen for the bars cut from samples 52A, 53A, 59A, and 60A in chapter 1. Markedly different behavior was observed for bars 46B-C and 46B-E. Considering the χ_m' response, bar 46B-C exhibited a $T_c = 75$ K and a relatively sharp transition width (ΔT_{cm}) of 4 K. Bar 46B-E exhibited a higher T_c of about 86 K and a broader, double-sloped transition of about 16.5 K. A single peak was observed in the χ''_m response of bar 46B-C while dual peaks were observed in the χ''_m response of bar 46B-E.

Bar 46B-E was the only sample in the entire investigation to exhibit two distinct peaks in χ''_m and a coinciding severe slope change in χ'_m. Using the model previously presented (BACKGROUND section entitled "Critical Current Density from A.C.

Susceptibility"), $j_{cJ}(67.5)$ = 0.14 A/cm^2 for bar 46B-C while $j_{cJ}(70)$= 0.14 A/cm^2 and $j_{cG}(84)$=124 A/cm^2 for bar 46B-E.

Two distinct peaks in χ''_m and an accompanying slope change in χ'_m may also indicate 1) two distinct superconducting components (Goldfarb et al., 1987a) with T_c's indicated by the temperature at the center of the loss (χ''_m) peak or 2) the presence of impurities (Hein et al., 1989). For bar 46B-E, T_c's of the 2 possible phases would be 84 K and 70 K, respectively. The presence of two phases with very different T_c's supports the possibility of oxygen inhomogeneity in the sample since T_c is so critically dependent on oxygen content (Beyers et al., 1989).

Concerning electrical behavior at 77 K, for a range of applied current (5 - 17 mA), both bars were resistive and ohmic. The resistivities of bars 46B-C and 46B-E were 2.15 x 10^{-3} Ω-cm and 7.06 x 10^{-4} Ω-cm, respectively (using the bulk dimensions for the resistivity (ρ = R*A/l) calculation). A similar resistivity was obtained for bar 46B-E when retested with μA currents. Bar 46B-C being resistive at 77 K was expected since the magnetic transition onset did not occur until 75 K. (In many cases, the bulk of the magnetic transition takes place at lower temperatures than where zero resistance first occurs (Hein et al., 1989).) However, it was unexpected that bar 46B-E would be resistive at 77 K since its magnetic transition onset was near 85K. The fact that the resistivity of bar 46B-C was three times larger (worse) than that of bar 46B-E is consistent with the poorer magnetic behavior exhibited

by bar 46B-C.

As for sample 60A, the within-sample property nonuniformity seen for sample 46B is likely to originate from compositional and/or microstructural nonuniformity / gradients (Clarke et al. (1989)). The exact cause of the nonuniform behavior as well as the generally poor superconducting behavior for the bars cut from sample 46B cannot be pinpointed from the microstructural and compositional analysis. The scatter in the oxygen content data obtained from inert gas fusion may have indicated some oxygen content deficiency and/or inhomogeneity resulting in poorer and/or inhomogeneous superconductor behavior. Some degradation of properties may have occurred during ultrasonic scanning and/or subsequent polishing (in preparation for microstructural analysis) of the sample. However, the ultrasonic couplant and polishing compounds / fluid were non-aqueous so as to avoid any significant YBCO reaction with water, and the bars were ground and ultrasonically cleaned in fresh ethanol to remove any contamination before superconductor testing. Furthermore, similarly-dense sample 99 underwent machining and ultrasonic scanning with T_c remaining around 90 K after these procedures (Roth et al., 1990c). Any moisture degradation results in oxygen loss and the formation of Y_2BaCuO_5, $Ba(OH)_2$ and CuO. The former two compounds were not detectable with x-ray diffraction and only a very small amount (about 0.03 volume fraction) of the latter compound was detected from image analysis. In any case, the entire sample and cut bars experienced the same respective procedures prior to

superconductor testing so that any property degradation due to preparation should have been uniform. Thus, it is believed that the within-sample nonuniformity of superconductor behavior was not caused by these procedures (although the poorer properties in general may have been). Further possibilities regarding within-sample property nonuniformity were given in the RESULTS AND DISCUSSION 1 section regarding sample 60A.

Microcracks possibly introduced during cutting of the bars may have caused resistive behavior at 77K. The effect of microcracks on susceptibility response is unknown. However, similar cutting procedures were used for the bars cut from samples 52A, 53A, 59A, and 60A, and the former three generally exhibited better susceptibility response than did bars 46B-C and 46B-E.

Samples 46B and 60A, containing almost identical pore fraction (approximately 0.10), exhibited significant susceptibility behavior nonuniformity from edge to center and poorer electrical characteristics overall than samples 52A, 53A, 59A which contained larger pore fractions. Additionally, previous results on YBCO samples near 0.10 pore fraction (Alford et al., 1988a and Clarke et al., 1989) showed poorer superconducting behavior than samples of higher pore fractions. Thus, evidence to date indicates that improved properties are obtained for YBCO samples of intermediate pore fraction. This behavior is opposite to what is expected considering the models of Ekin (1987) and Evetts et al. (1989) and indicates the presence of some compositional and/or microstructural

anomaly (as previously discussed) preventing improved behavior at lower pore fractions.

H. Concluding Remarks

Spatial variations in microstructure and superconductor properties for YBCO samples were investigated. Ultrasonic scanning at increments of 1 mm revealed microstructural nonuniformity within a YBCO sample of 0.105 pore fraction. From destructive examination using quantitative optical image analysis, it was determined that edge (center) areas in the sample containing low pore fraction (high pore fraction) corresponded to high (low) velocity regions in the ultrasonic image. Bars cut from the sample at the low and high velocity regions exhibited significantly different magnetic shielding and A.C. loss behavior. Thus, the velocity image revealed microstructural variations that correlated with variations in superconductor behavior. Similar within-sample nonuniform superconducting behavior has been seen for YBCO samples of comparable pore fraction.

VII. **RESULTS AND DISCUSSION** 3: Oxygen Content Effects

Density is not normalized to pore fraction in this experiment because oxidized / reduced samples may be wholly or partly tetragonal and cannot be assumed to have the same theoretical density of 6.38 g/cm^3 (as orthorhombic YBCO).

A. Specimen Characterization

Tables 13 - 15 show the microstructural, compositional, elastic, and superconducting characteristics of the YBCO samples examined. Table 16 summarizes the changes in oxygen content, structure, superconducting behavior, density, velocity and elastic modulus of the samples after undergoing reduction and oxidation treatments. Figures 109 and 110 show optical micrographs of the grain (1500X) and porosity (400X) distributions for polished sections of sample 51A after oxidation and reduction treatments. Figure 111 show x-ray diffraction patterns for sample 51A after the treatments.

The following comments generally apply to all of the samples except where noted. From x-ray diffraction results, the structure transformed from orthorhombic to tetragonal upon reduction and tetragonal to orthorhombic upon oxidation. The two peaks at 2θ = 32.5° - 33° was seen to reverse in relative intensity and the unit cell parameters changed as expected upon structure transformation. Oxygen content decreased upon reduction and increased upon oxidation. Data obtained from inert gas fusion appeared to give larger absolute oxygen weight percents than expected as was seen previously in EXPERIMENT 2. However, the direction and magnitude of change appeared reasonable. Oxygen atom values obtained from the Wolf et al. (1988) and Ono (1987) relations (using the c-axis length determined from x-ray diffraction) yielded values close to those expected for samples undergoing oxidation / reduction. Oxygen

content changed most drastically (a 10% decrease) for sample 51A upon reduction.

Bulk density generally decreased (decrease in mass and increase in volume) upon reduction and increased (increase in mass and decrease in volume) after oxidation, as expected. A 4 % decrease in theoretical density is expected after reduction for the case where the oxygen stoichiometry decreases from 7 to 6. An exception occurred for sample 51A where density remained approximately constant upon reoxidation. From Heyn-intercept (ASTM E112-85) measurements at local areas, mean grain size was not found to change after the various treatments. A 2 % increase in grain volume (less than a 1% increase in linear dimension) is expected upon reduction for the case where the oxygen stoichiometry decreases from 7 to 6. Twinning, not observed before oxidation and after reduction, was apparent after oxidation.

From the optical micrographs, it appeared that pore distribution (size and fraction) generally appeared to remain constant before and after reduction and oxidation treatments. In general for these specimens, the peak treatment temperature (around 800 °C) was lower than the sintering temperature where significant continuous grain growth resulting in pore fraction reductions (densification) occurred. (This is not to say that some grain growth could not have occurred. For example, during secondary recrystallization, a small fraction of grains grow to a large size and the pore distribution remains relatively unchanged (Kingery et

al., 1976)). However, densification of sample 52A (the lowest density sample) beyond that expected for the tetragonal to orthorhombic transformation occurred.

B. Velocity and Elastic Modulus

Longitudinal wave ultrasonic velocity (center frequency = 5 MHz) obtained at one location generally decreased upon reduction and increased upon oxidation. In this manner, velocity increased with increasing oxygen content and density as expected. Velocity changes accompanied structure change and the superconductor-normal transformation. An exception to this occurred for the first oxidation of sample 51A where velocity remained constant even though oxygen content and density increased, and transformations in structure and superconducting behavior were observed. This result was unexpected and may indicate some competing effects of density and oxygen content on velocity. An increase in velocity was noted upon reoxidation of sample 51A where oxygen content increased 1% but density did not increase.

The effective elastic modulus (equation (1)) decreased upon reduction and increased upon oxidation, indicating that the structure stiffens with the addition of oxygen. Sample 52A (the lowest density sample), showed the greatest changes in velocity and modulus upon oxidation. Since in most instances, bulk density changed with changes in oxygen content, and velocity is strongly dependent on density, the dependence of velocity on oxygen content

in YBCO was difficult to quantify in this study.

C. Superconductor Behavior from A.C. Susceptibility

Figure 112 shows the a.c. mass (external) susceptibility versus temperature for sample 51A after oxidation and reduction treatments. From a.c. susceptibility measurements (χ'_m), the normal-to-superconducting transition was not observed for the reduced and unoxidized samples except for 59A which had a T_c about 40 K upon reduction. In the latter case, it is likely that the orthorhombic structure was transformed to the orthorhombic II (OII) phase characterized by $6.5 < O < 6.8$ and poorer superconducting properties upon reduction. The reason why this occurred for sample 59A and not for samples 53A, 60A and 51A is unknown. After oxidation, all samples were superconducting with T_c about 90 K. However, reoxidation of sample 51A lowered the transition by about 10 K and broadened the transition. This may have resulted due to the transformation of some orthorhombic material to the overoxygenated, semiconducting tetragonal T' phase.

D. Ultrasonic Scanning

Figure 113 shows ultrasonic velocity images (center frequency = 10 MHz) obtained over a 3 mm by 5 mm region (measurements made every 0.5 mm) of a disk cut from sample 51A after oxidation and reduction treatments. (Scans were not performed after the initial oxidation on this region of sample 51A). Total velocity variation was less than 1

% for each case. The same global pattern of velocity variation was evident with the highest (lower portion of image) and lowest (upper portion of image) velocity regions remaining intact after the treatments. This supports optical microscopy results showing that pore (fraction and size) distribution was not significantly altered during the treatments. Had pore distribution been significantly altered, it is believed that the velocity image would have changed much more drastically as was shown previously by Generazio et al. (1989a) for step-sintered SiC samples. The most significant global velocity changes appeared to occur upon reduction where the total velocity variation doubled from 0.4 % to 0.8 % accompanying a 10 % decrease in oxygen content. The mean, minimum, and maximum velocity values changed in an almost identical fashion to that shown for the point measurements (table 16) after the treatments for sample 51A.

E. Concluding Remarks

The effect of changes in oxygen content on elastic behavior for YBCO was investigated. Changes in superconducting behavior were observed consistent with oxidation and reduction treatments performed. Velocity increases generally accompanied oxygen content increases, and this behavior was reversible. Therefore, ultrasonic velocity showed potential as a monitor of oxygen content and thus superconducting behavior. Elastic modulus increased with increasing oxygen content indicating a stiffening of the structure with the addition of oxygen; these changes were also reversible. Global

patterns in the velocity images stayed approximately the same after oxidation and reduction treatments. This correlated with destructive measurements showing insignificant changes in the pore distribution.

VIII. CONCLUSIONS

The purpose of this dissertation was to 1) characterize the effect of pore fraction on a comprehensive set of electrical and magnetic properties for the yttrium-barium-copper-oxide high temperature ceramic superconductor and 2) determine the viability of using a room-temperature, nondestructive characterization method to aid in the prediction of superconducting (cryogenic) properties. The latter involved correlating ultrasonic velocity measurements at room temperature with property-affecting pore fraction and oxygen content variations. To this end:

1. A review, model and statistical analysis of the ultrasonic velocity method for estimating the pore fraction in polycrystalline materials was presented. First, a semi-empirical model was developed showing the origin of the linear relationship between ultrasonic velocity and pore fraction. Then, from a compilation of data produced by many researchers, scatter plots of velocity versus percent porosity data were shown for Al_2O_3, CuO, MgO, porcelain-based ceramics, PZT, SiC, Si_3N_4, steel, tungsten, UO_2, $(U_{0.30}Pu_{0.70})C$, and $YBa_2Cu_3O_{7-x}$. Linear regression analysis produced slope, intercept, correlation coefficient, level of significance, and confidence

interval statistics for the data. Velocity values predicted from regression analysis for fully-dense materials were in good agreement with those calculated from elastic properties. The estimation of batch-to-batch, sample-to-sample, and within-sample variations in pore fraction for a material can be accomplished with ultrasonic velocity measurements if reasonable confidence exists in the velocity versus percent porosity linear relationship.

2. The superconductor properties of similarly-processed, untextured YBCO specimens of pore fraction 0.10 - 0.25 were compared. From electrical and a.c. susceptibility measurements, superconductor properties including within-sample uniformity were poorest for the sample containing the lowest (0.10) pore fraction. Ultrasonic velocity measurements proved to be a simple, reliable and nondestructive means of estimating pore fraction due to the strong linear dependence of velocity on pore fraction. This is important if improved properties occur at intermediate pore fraction for bulk, untextured YBCO as is presently indicated by this and other studies. Neither the velocity nor the destructive measurements were able to discern the microstructural and/or compositional inhomogeneity causing the different superconducting behavior of edge- and center-cut bars from the sample containing the lowest pore fraction. The bars cut from all samples exhibited low critical current densities (as compared to those expected for moderate intergranular coupling). The very low J_c's are attributed to the presence of weak

links between superconducting regions.

3. Spatial variations in microstructure and superconductor properties for YBCO samples were investigated. Ultrasonic scanning at increments of 1 mm revealed microstructural nonuniformity within a YBCO sample containing 0.105 pore fraction. From destructive examination using quantitative optical image analysis, it was determined that edge (center) areas in the sample containing low pore fraction (high pore fraction) corresponded to high (low) velocity regions in the ultrasonic image. Bars cut from the sample at the low and high velocity regions exhibited significantly different magnetic shielding and A.C. loss behavior. Thus, the velocity image revealed microstructural variations that correlated with variations in superconductor behavior. Similar within-sample nonuniform superconducting behavior has been seen for YBCO samples of comparable pore fraction.

4. The effect of changes in oxygen content on elastic behavior for YBCO was investigated. Changes in superconducting behavior were observed consistent with oxidation and reduction treatments performed. Velocity increases generally accompanied oxygen content increases, and this behavior was reversible. Therefore, ultrasonic velocity showed potential as a monitor of oxygen content and thus superconducting behavior. Elastic modulus increased with increasing oxygen content indicating a stiffening of the structure with the

addition of oxygen; these changes were also reversible. Global patterns in the velocity images stayed approximately the same after oxidation and reduction treatments. This correlated with destructive measurements showing insignificant changes in the pore distribution.

5. Ultrasonic velocity measurements proved to be a simple and reproducible means of distinguishing specimens on the basis of pore fraction and oxygen content changes and were thus useful for aiding in superconducting behavior prediction. Global determinations of sample uniformity from velocity imaging proved useful in predicting nonuniform superconducting behavior and examining microstructural change during processing. These nondestructive, room-temperature methods are likely to prove useful in the examination of all bulk, high temperature superconductor materials including textured (higher-J_c) materials having more commercial potential than the untextured materials of this study.

IX. FUTURE RESEARCH POSSIBILITIES

Several future directions of research can be defined based on this work. These include 1) comparisons of velocity versus pore fraction relations obtained from the semi-empirical model presented in chapter 1 with those obtained from multiple scattering calculations (Truell et al., 1969); 2) further attempts at the correlation of spatial variations from ultrasonic velocity imaging with superconductor behavior variations and the underlying

microstructural / compositional causes of the variability; 3) ultrasonic attenuation imaging in YBCO and its correlation with velocity imaging, superconductor behavior and destructive results; 4) in-situ (cryogenic) ultrasonic examination of superconductors to determine and correlate with any degradation in superconductor performance as it occurs; 5) ultrasonic examination of YBCO specimens of the same pore fraction but different oxygen contents so that the effect of oxygen content on ultrasonic velocity can be more distinctly defined; 6) in-situ ultrasonic monitoring of the oxidation of YBCO, so that structural changes can be studied as they occur, and for process control so the optimum oxygen content can be obtained consistently if velocity versus oxygen content relations are well-defined.

X. BIBLIOGRAPHY

Acton, F.S., 1959, Analysis of Straight Line Data. Wiley.

Alers, G.A. 1966. The Measurement of Very Small Sound Velocity Changes and Their Use in The Study of Solids. Physical Acoustics, Volume IV, Part A. edited by W. P. Mason, Academic Press. 277 - 297.

Alford, N.McN., Clegg, W.J., Harmer, M.A., Birchall, J.D., Kendall, K. and Jones, D.H. 1988a. The Effect of Density on Critical Current and Oxygen Stoichiometry of $YBa_2Cu_3O_x$ Superconductors. Nature. 332:58-59.

Alford, N.McN., Birchall, J.D., Clegg, W.J., Harmer, M.A. and Kendall, K. 1988b. Physical and Mechanical Properties of $YBa_2Cu_3O_{(7-x)}$ Superconductors. J. Mater. Sci. 23:761-768.

Alford, N.McN., Button, T.W., Jones, D.H., Birchall, J.D., Gough, C.E. and Penn, S.J. 1989. Critical Current Densities of Bulk, Polycrystalline High T_c Superconductor Wires and Tubes. Cryogenics, 29:800 - 808.

Aponte, J., Abache, H. and Octavio, M. 1989. Critical Currents in Bulk Samples of $YBa_2Cu_3O_{7-x}$ and $DyBa_2Cu_3O_{7-x}$. Cryogenics 29:334 - 337.

Arons, R.M. and Kupperman, D.S. 1982. Use of Sound-Velocity Measurements to Evaluate the Effect of Hot Isostatic Pressing on the Porosity of Ceramic Solids. Mater. Eval. 40:1076-1078.

Baaklini, G.Y. and Roth, D.J. 1986. Probability of Detection of Internal Voids in Structural Ceramics Using Microfocus Radiography. J. Mater. Res. 1:457 - 467.

Baaklini, G.Y. and Sanders, W.A. 1988. Correlation of Processing and Sintering Variables With The Strength and Radiography of Silicon Nitride. Adv. Ceram. Mater. 3:88 - 94.

Baaklini, G.Y., Generazio, E.R. and Kiser, J.D. 1989. High Frequency Ultrasonic Characterization of Sintered Silicon Carbide. J. Am. Ceram. Soc. 72:383-387.

Barbara, B., Khoder, A.F., Couach, M. and Henry, J.Y. 1988. Supercurrent Lengthscale Crossover and Twin Boundaries in $YBa_2Cu_3O_{7-x}$ Single Crystals. Europhys. Lett. 6:621 - 627.

Bardeen, J., Cooper, L.N. and Schrieffer, J.R. 1957. Theory of Superconductivity. Phys. Rev. 108:1175 - 1204.

Barone, A. and Paterno, G. 1982. Physics and Applications of The Josephson Effect. John Wiley & Sons. 20 - 26 and 36 - 52.

Battelle Columbus Laboratories. 1979. Engineering Property Data On Selected Ceramics. Vol. II., Carbides. Metals and Ceramics Information Center, Columbus, OH. 5.2.3-10.

Battelle Columbus Laboratories. 1981. Engineering Property Data On Selected Ceramics. Vol. III, Single Oxides. Metals and Ceramics Information Center, Columbus, OH. 5.4.1-25.

Bean, C.P. 1962. Magnetization of Hard Superconductors. Phys. Rev. Lett. 8:250 - 253.

Bednorz, J.G., and Muller, K.A. 1986. Possible High T_c Superconductivity in The Ba-La-Cu-O System. Z. Phys. B 64:189 - 193.

Bendat, J.S. and Piersol, A.G. 1980. Engineering Applications of Correlation and Spectral Analysis. John Wiley & Sons. 43 - 77.

Beyers, R., Lim, G., Engler, E.M., Lee, V.Y., Ramirez, M.L., Savoy, R.J. and Jacowitz, R.D. 1987. Annealing Treatment Effects on Structure and Superconductivity in $Y_1Ba_2Cu_3O_{9-x}$. Appl. Phys. Lett. 51:614 - 616.

Beyers, R., Ahn, B.T., Gorman, G., Lee, V.Y., Parkin, S.S.P., Ramirez, M.L., Roche, K.P. Vazquez, J.E., Gur, T.M. and Huggins, R.A. 1989. Ordered Oxygen Arrangements in $Y_1Ba_2Cu_3O_{7-x}$. Mat. Res. Soc. Symp. Proc. 156:77 - 82.

Birring, A.S. and Hanley, J.J. 1987. Effect of Cavities on Ultrasonic Attenuation and Velocity. Nondestructive Characterization of Materials. edited by J.F. Bussiere, J-P. Monchalin, C.O. Ruud and R.E. Green, Jr., Plenum Press. 673 - 681.

Blendell, J.E., Chiang, C.K., Cranmer, D.C., Freiman, S.W., Fuller Jr., E.R., Drescher-Krasicka, E., Johnson, W.L., Ledbetter, H.M., Bennett, L.H., Swartzendriber, L.J., Marinenko, R.B., Myklebust, R.L., Bright, D.S. and Newbury, D.E. 1987. Processing-Property Relations for $YBa_2Cu_3O_{(7-x)}$ High-Tc Superconductors. Adv. Ceram. Mater. 2:512-529.

Boisson, J. Platon, F. and Boch, P. 1976. Constanti Electriche E. Attrito Interno in Alconi Materiali in Funzione Della Porosita. Ceramurgia, anno VI:74-80.

Brabson, G.D. 1988. Ultraviolet / Visible Absorption Spectroscopy. Metals Handbook, Materials Characterization, Volume 10. American Society For Metals. 60 - 71.

Breazeale, M.A., Contrell Jr., J.H. and Heymann, J.S. 1981. Ultrasonic Wave Velocity and Attenuation Measurements. Methods of Experimental Physics, Ultrasonics, Volume 19. edited by P. D. Edmonds, Academic Press. 67 - 135.

Bridenbaugh, P.R., Shabel, B.S. and Govada, A.K. 1987. Material Characterization For Process control For Aluminum Alloys and Advanced Materials. Nondestructive Characterization of Materials. edited by J.F. Bussiere, J-P. Monchalin, C.O. Ruud and R.E. Green, Jr., Plenum Press. 179 - 194.

Burdick, M.D. and Parker, H.S.. 1956. Effect of Particle Size on Bulk Density and Strength Properties of Uranium Dioxide Specimens. J. Am. Ceram. Soc. 39:181-187.

Buxbaum, S.R. and Green Jr., R.E. 1984. Ultrasonic Characterization of Titanium 6211 Weldments. Nondestructive Methods For Material Property Determination. edited by C.O. Ruud and R.E. Green, Jr., Plenum Press. 271 - 287.

Campbell, A.M. and Evetts, J.E. 1972. Flux Vortices And Transport Currents in Type II Superconductors. Adv. Phys. 21:199 - 428.

Camps, R.A., Evetts, J.E., Glowacki, B.A., Newcomb, S.B., Somekh, R.E. and Stobbs, W.M. 1987. Microstructure and Critical Current of Superconducting $YBa_2Cu_3O_{7-x}$. Nature. 329:229 - 232.

Cave, J.R., Mautref, M., Agnoux, C., Leriche, A. and Fevrier, A. 1989. Electromagnetic Properties of Sintered YBaCuO Superconductors: Critical Current Densities, Transport Currents and A. C. Losses. Cryogenics 29:341 - 346.

Chaudhari, P., Koch, R.H., Laibowitz, R.B., McGurie, T.R. and Gambino, R.J. 1987. Critical-Current Measurements in Epitaxial Films of $YBa_2Cu_3O_{7-x}$ Compound. Phys. Rev. Lett. 58:2684 - 2686.

Chen, I., Keating, S.J., Keating, C.Y., Wu, X., Xu, J., Reyes- Morel, P.E. and Tien, T.Y. 1987. Structural Behavior and Superconductivity of $YBa_2Cu_3O_x$. Sol. St. Comm. 63:997 - 1001.

Chen, D.X., Goldfarb, R.B., Nogues, J. and Rao, K.V. 1988. Magnetic Susceptibility of Sintered And Powdered Y-Ba-Cu-O. J. Appl. Phys. 63:980 - 983.

Chen, D.X., Nogues, J. and Rao, K.V. 1989. A.c. Susceptibility and Intergranular Critical Current Density of High T_c Superconductors. Cryogenics. 29:800 - 808.

Chu, C.W., Huang, S. and Sleight, A.W. 1976. Hydrostatic Pressure

Effect on T_c of $Ba_{0.9}K_{0.1}Pb_{0.75}Bi_{0.25}O_3$. Sol. St. Comm. 18:977 - 979.

Chu, C.W., Huang, S.Z., Lin, C.H., Meng, R.L., Wu, M.K. and Schmidt, P.H. 1981. High-Pressure Study of The Anomalous Rare-Earth Ternaries $Eu_{1.2}Mo_6S_8$ and $Eu_{1.2}Mo_6Se_8$. Phys. Rev. Lett. 46:276 - 279.

Chu, P.H., Hor, P.H., Meng, R.L., Gao, L., Huang, Z.J., Wang, Y.Q. and Huang, C.J. 1987. High Pressure Study of The New Y-Ba-Cu-O Superconducting Compound System. Phys. Rev. Lett. 58:911 - 912.

Cima, M.J. and Rhine, W.E. 1987. Powder Processing For Microstructural Control in Ceramic Superconductors," Adv. Ceram. Mater. 2:329 - 336.

Clark, G.L. and Liu, C.H. 1957. Quanititave Determination of Porosity by X-Ray Absorption. Anal. Chem. 29:1539-1541.

Clarke, D.R. 1987. The Development of High-T_c Ceramic Superconductors: An Introduction. Adv. Ceram. Mater., 2:273 - 292.

Clarke, D. R. 1988. Microstructure and Critical Current Densities of Superconducting Ceramics. Proc. Sintering '87. 1415 - 1420.

Clarke, D.R., Shaw, T.M. and Dimos, D. 1989. Issues in The Processing of Cuprate Ceramic Superconductors. J. Amer. Ceram. Soc. 72:1103 - 1113.

Claytor, T.N., Frost, H.M., Feirtag, T.H., Sheppard, G.A. and Shalek, P.D. 1989. Nondestructive Measurement of Microstructure Evolution in Ceramics. Mater. Eval. 47:532-535.

Clem, J.R. and Kogan, V.G. 1987. Theory of The Magnetization of Granular Superconductors: Application to High-T_c Superconductors. Proc. 18th Int. Conf. on Low Temperature Physics, Kyoto, 1987, Jpn. J. Appl. Phys. 26:Supplement 26 - 3, 1161 - 1162.

Clem, J.R. 1988. Granular and Superconducting-Glass Properties of the High-Temperature Superconductors. Physica C. 153 - 155:50 - 55.

Couach, M., Khoder, A.F. and Monnier, F. 1985. Study of Superconductors by A. C. Susceptibility. Cryogenics. 25:695 - 699.

Cullity, B.D. 1972. Introduction to Magnetic Materials. Addison - Wesley, 1972. 1 - 24, 49 - 61, 493 - 504.

Cullity, B.D. 1984. Elements Of X-Ray Diffraction, Addison-Wesley.

Davis, M., Wolf, S., Soulen, R. and Fuller, W., Report on DARPA Round Robin. 1989. DARPA High Temperature Superconductor Measurements

Workshop. April 17 - 18, 1989. Washington, D. C..

Deiter, G.E., 1986. Mechanical Metallurgy. Third ed., McGraw-Hill, 50.

Derkacs, T., Matay, I.M. and Brentnall, W.D. 1976. Nondestructive Evaluation of Ceramics. Contract Report No.: AD-A027357, TRW-ER-7798-F; TRW, Inc.

Dersch, H. and Blatter, G. 1988. New Critical-State Model For Critical Currents in Ceramic High-T_c Superconductors. Phys. Rev. B. 38:11391 - 11404.

Deshpandey, C. and Bunshah, R.F. 1989. Synthesis of High Temperature Superconducting Films - Processing Science and Issues. Studies of High Temperature Superconductors, Volume 3. edited by A. Narlikar, Nova Science. 75 - 105.

Deutscher, G. and Muller, K.A., 1987. Origin of Superconductive Glassy State And Extrinsic Critical Currents in High-T_c Oxides. Phys. Rev. Lett. 59:1745 - 1747.

Dominec, J. 1989. Sound Attenuation and Velocity in Superconductive Ceramics - A Review. Superconductor Sci. & Tech. 2:91 - 102.

Doss, J.D. 1989. Engineer's Guide To High-Temperature Superconductivity. John Wiley & Sons. 81 - 88, 111 and 122 - 124.

Dubots, P. and Cave, J. 1988. Critical Currents of Powder-Based Superconducting Wires. Cryogenics 28:661 - 667.

Duyneveldt, A.J.V. 1989. AC - Susceptibility Studies in Solid State Magnetism. Proc. Letnia Szkola Magnetyzmu, Bialowieza. 1 - 39.

Ekin, J. 1981. Mechanical Properties and Strain Effects in Superconductors. Superconductor Materials Science. Plenum Press. 455 - 510.

Ekin, J.W. 1983. Superconductors. Materials at Low Temperatures. edited by R.P. Reed and A.F. Clark, American Society For Metals. 465 - 513.

Ekin, J.W. 1987. Transport Critical Current in Bulk Sintered $Y_1Ba_2Cu_3O_x$ and Possibilities For Its Enhancement. Adv. Ceram. Mater. 2:586 - 592.

Ekin, J.W., Panson, A.J. and Blankenship, B.A. 1988. Method For Making Low-Resistivity Contacts to High T_c Superconductors. Appl. Phys. Lett. 52:331 - 333.

Ellingson, W.A., Wong, W.S., Dieckman, S.L., Ackerman, J.L. and Garrido, L. 1989. Magnetic Resonance Imaging: A New Characterization Technique For Advanced Ceramics. Amer. Cer. Soc. Bull. 68:1180 - 1186.

Evans, A.G., Tittmann, B.R. and Ahlberg, L. 1978. Ultrasonic Attenuation in Ceramics. J. Appl. Phys. 49:2669 - 2679.

Evetts, J. E. 1983. The Characterization of Superconducting Materials - Conflicts and Correlations. IEEE Trans. Magn., MAG - 19:1109 - 1119.

Evetts, J.E., Glowacki, B.A., Sampson, P.L. and Blamire, M.G. 1989. Relation of The N-value of The Resistive Transition to Microstructure and Inhomogeneity For $YBa_2Cu_3O_7$ Wires. IEEE Trans. Magn. 25:2041 - 2044.

Faires, L.M. 1988. Inductively Coupled Plasma Atomic Emission Spectroscopy. Metals Handbook, Materials Characterization, Volume 10. American Society For Metals. 31 - 42.

Fickett, F.R. and Goldfarb, R.B. 1983. Magnetic Properties. Materials at Low Temperatures. edited by R.P. Reed and A.F. Clark, American Society For Metals. 203 - 236.

Filipczynski, Prof. Dr. in z . Leszek, Pawlowski, Dr. in z Zozislaw, and Wehr, Dr. in z Jerry. 1966. Ultrasonic Methods of Testing Materials. 2nd Edition, Translation, Butterworths. 255.

Firestone, F.A. 1946. The Supersonic Reflectoscope, an Instrument For Inspecting The Interior of Solid Parts By Means of Sound Waves. J. Acoust. Soc. Am. 18:287 - 299.

Fisher, E.A. 1975. Residual Stresses in Ceramic Turbine Components. Proc. Workshop Nondestructive Evaluation of Residual Stress. 125 - 126.

Flukiger, R., Muller, T., Goldacker, W., Wolf, T., Seibt, E., Apfelstedt, I., Kupfer, H. and Schauer, W. 1988. Metallurgy and Critical Currents in $YBa_2Cu_3O_7$ Wires. Physica C. 153 - 155:1574 - 1579.

Frase, K.G., Liniger, E.G. and Clarke, D.R. 1987. Environmental and solvent Effects on Yttrium Barium Cuprate ($Y_1Ba_2Cu_3O_x$). Adv. Ceram. Mater. 2:698 - 700.

Fricioni, R.B. and Essig, L. 1988. Inert Gas Fusion. Metals Handbook, Materials Characterization, Volume 10. American Society For Metals. 226 - 232.

Friedman, W.D., Harris, R.D., Engler, P., Hunt, P.K. and Srinivasan, M. 1987. Characterization of Green Ceramics With X-Ray Tomography and Ultrasonics. Proc. Nondestructive Testing: High Performance Ceramics. American Ceramic Society. 128-131.

Gaiduk, A.L., Zherlitsyn, S.V., Prikhod'ko, O.R., Seminozhenko, V.P., Nesterenko, V.F. and Pershin, S.A. 1988. High-Frequency Acoustic Properties of Yttrium Ceramic. Sov. J. Low Temp. Phys. **14**:395-402.

Gallagher, P.K., O'Bryan, H.M., Sunshine, S.A. and Murphy, D.W. 1987. Oxygen Stoichiometry in $Ba_2Cu_3O_x$. Mater. Res. Bull., **22**:995 - 1006.

Gavaler, J.R. 1973. Superconductivity in Nb-Ge Films Above 22 K. Appl. Phys. Lett. **23**:480 - 482.

Generazio, E.R., Roth, D.J., and Baaklini, G.Y. 1988. Acoustic Imaging of Subtle Porosity Variations in Ceramics. Mater. Eval. **46**:1338-1343.

Generazio, E.R., Roth, D.J. and Stang, D.B. 1989a. Ultrasonic Imaging of Porosity Variations Produced During Sintering. J. Am. Ceram. Soc. **72**:1282-1289.

Generazio, E.R., Stang, D.B. and Roth, D.J. 1989b. Interfacing Laboratory Instruments to Multiuser, Virtural Memory Computers. NASA TM-4106.

Gherardi, L., Metra, P., Vellego, G. and Radaelli, P. 1990. Critical Current Decay With Ageing For Polycrystalline YBCO Wires and Rings. Cryogenics. **30**:576 - 580.

Ghosh, J.K., Panakkal, J.P., and Roy, P.R.. 1985. Ultrasonic Velocity Measurement in The Characterisation of Nuclear Fuel Pellets. World Conference on Nondestructive Testing. Butterworths. 1201-1205.

Gilmore, R.S., Tam, K.C., Young, J.D. and Howard, D.R. 1986. Acoustic Microscopy From 10 to 100 MHz For Industrial Applications. Phil. Trans. R. Soc. Lond. A. **320**:215 - 235.

Ginsberg, D.M. 1989. Introduction, History, and Overview of High Temperature Superconductivity. Physical Properties of High Temperature Superconductors I. edited by D.M. Ginsberg, World Scientific, 1989. 1 - 38.

Goetzel, C., 1963, Treatise on Powder Metallurgy. Wiley.

Goldfarb, R.B. 1986. Internal Fields in Magnetic Materials and Superconductors. Cryogenics. **26**:621 - 622.

Goldfarb, R.B., Clark, A.F. and Branginski, A.I. 1987a. Evidence For Two Superconducting Components in Oxygen-Annealed Single-Phase Y-Ba-Cu-O. Cryoenics. 27:475 - 480.

Goldfarb, R.B., Clark, A.F., Panson, A.J. and Braginski, A.I. 1987b. AC Susceptibility Measurements Near The Critical Temperature Of A Y-Ba-Cu-O Superconductor. High Temperature Superconductors. edited by D.U. Gubser and M. Schluter, Materials Research Society. 261 - 263.

Granato, A., DeKlerk, J. and Truell, R. 1957. Dispersion of Elastic Waves in Sodium Chloride. Phys. Rev. 108:895 - 896.

Gruber, J.J., Smith, J.M., and Brockelman, R.H. 1988. Ultrasonic Velocity C-Scans for Ceramic and Composite Material Characterization. Mater. Eval. 46:90-96.

Gurvitch, M. and Fiory, A.T., Resistivity of $La_{1.825}Sr_{1.75}CuO_4$ and $YBa_2Cu_3O_{7-x}$ To 1100 K: Absence of Saturation and Its Implications. 1987. Phys. Rev. Lett. 59:1337 - 1339.

Hariharan, Y., Sundar, C.S., Janaki, J., Sood, A.K., Janawadkar, M.P., Bharathi, A., Sastry, V.S., Baskaran, R. and Radhakrishnan, T.S. 1989. Effect of Oxygen Ordering on The Superconductivity of $Y_1Ba_2Cu_3O_{7-x}$. Studies of High Temperature Superconductors, Volume 3. edited by A. Narlikar, Nova Science. 107 - 143.

Hein, R.A. 1986. AC Magnetic Susceptibility, Meissner Effect, and Bulk Superconductivity. Phys. Rev. B. 33:7539 - 7549.

Hein, R.A., Hojani, H., Barkatt, A., Shafii, H., Michael, K.A., Thorpe, A.N., Ware, M.F., and Alterescu, S. 1989. The Low Magnetic Field Properties of Superconducting Bulk Yttrium Barium copper Oxide - Sintered Versus Partially Melted Material. J. Superconductivity. 2:427 - 461.

Hellman, F. Gyorgy, E.M., Johnson Jr., D.W., O'Bryan, H.M. and Sherwood, R.C. 1988. Levitation of a Magnet Over a Flat Type II Superconductor. J. Appl. Phys. 15:447 - 450.

Hermann, A.M., Sheng, Z.Z., Vier, D.C., Shultz, S. and Oseroff, S.B. 1988. Magnetization of The 120-K Tl-Ca-Ba-Cu-O Superconductor. Phys. Rev. B 37:9742 - 9744.

Hikata, A., Chick, B., Elbaum, C. and Truell, R. 1962. Ultrasonic Attenuation and Velocity Data on Aluminum Single Crystals as A Function of Deformation and Orientation. Acta Metallurg. 10:423 - 429.

Hoff, H.A. and Pande, C.S. 1989. Twins in High T_c Superconductors.

Studies of High Temperature Superconductors, Volume 3. edited by A. Narlikar, Nova Science. 333 - 368.

Hor, P.H., Meng, R.L., Huang, J.Z., Chu, C.W. and Huang, C.Y. 1987. Upper Critical Field of High Temperature $Y_{1.2}Ba_{0.8}CuO_{4-x}$ Superconductor. Appl. Phys. Comm. 7:129 - 133.

Hsu, N. and Conrad, H. 1971. Ultrasonic Wave Velocity Measurements on Titanium-Oxygen Alloys. Scripta Metall. 5:905 - 908.

Hsu, N.N., Proctor Jr., T.M. and Blessing, G.V. 1982. An Analytical Approach to Reference Samples For Ultrasonic Residual Stress Measurement. J. Testing and Evaluation. 10:230 - 234.

Hull, D.R., Kautz, H.E. and Vary, A., Measurement of Ultrasonic Velocity Using Phase-slope and Cross-Correlation Methods. Mater. Eval. 43:1455 - 1460.

Hwu, S.J., Song, S.N., Ketterson, J.B., Mason, T.O. and Poeppelmeier, K.R. 1987. Subsolidus Compatibilities in The Y_2O_3- BaO-CuO System Via Diamagnetic Susceptibility. J. Am. Ceram. Soc. Comm., 70:C165 - C167.

Iye, Y. 1989. Anisotropic Superconducting and Normal State Transport Properties of HTSC Single Crystals. Studies of High Temperature Superconductors, Volume 2. edited by A. Narlikar, Nova Science, 1989. 199 - 223.

Jin, S., Tiefel, T.H., Sherwood, R.C., Davis, M.E., Van Dover, R.B., Kammlott, G.W., Fastnacht, R.A. and Keith, H.D. 1988. High Critical Currents in Y-Ba-Cu-O Superconductors. Appl. Phys. Lett. 52:2074 - 2076.

Johnston, D.C., Prakash, H., Zachariasen, W.H. and Viswanthan, R. 1973. High Temperature Superconductivity in The Li-Ti-O Ternary System. Mater. Res. Bull. 8:777 - 784.

Jones, J.T. and Berard, M.F. 1972. Ceramics Industrial Processing and Testing. Iowa State University Press.

Jones, M.P., Blessing, G.V., and Robbins, C.R. 1986. Dry-Coupled Ultrasonic Elasticity Measurements of Sintered Ceramics. Mater. Eval. 44:859-862.

Kim, Y.B., Hempstead, C.F. and Strnad, A.R. 1962. Critical Persistent Currents in Hard Superconductors. Phys. Rev. Lett. 9:306 - 309.

Kim, Y.B., Hempstead, C.F. and Strnad, A.R. 1963. Magnetization and Critical Supercurrents. Phys. Rev. 129:528 - 535.

Kingery, W.D., Bowen, H.K., and Uhlmam, D.R. 1976. Introduction To Ceramics. John Wiley & Sons. 9 and 461 - 466.

Kino, G.S., Barnett, D.M., Grayelli, N., Herrman, G., Hunter, J.B., Ilic, D.B., Johnson, G.C., King, R.B., Scott, M.P. and Shyne, J.C. 1980. Acoustic Measurements of Stress Fields and Microstructure. J. Nondestructive Eval. 1:67 - 77.

Kittel, C. 1986. Introduction To Solid State Physics. John Wiley & Sons, 1986, 6th edition. 210 - 211 and 317 - 358.

Kittel, C. Fahy, S. and Louie, S.G. 1988. Magnetic Screening By A Thin Superconducting Surface Layer. Phys. Rev. B. 37:642 - 643.

Klima, S.J., Watson, G.K., Herbell, T.P. and Moore, T.J. 1981. Ultrasonic Velocity for Estimating Density of Structural Ceramics. NASA TM-82765.

Klima, S.J. and Baaklini, G.Y. 1984. Ultrasonic Characterization of Structural Ceramics. in NASA CP-2383. 117 - 126.

Knudsen, F.P., Parker, H.S., and Burdick, M.D. 1960. Flexural Strength of Specimens Prepared from Several Uranium Dioxide Powders--Its Dependence on Porosity and Grain Size And the Influence of Additions of Titania. J. Am. Ceram. Soc. 43:641-647.

Krautkramer, J. and Krautkramer, H. 1977. Ultrasonic Testing of Materials. 2nd edition, Springer-Verlag, 63 - 75.

Kunnerth, D.C., Telschow, K.L. and Walter, J.B. 1989. Characterization of Porosity Distributions in Advanced Ceramics: A Comparison of Ultrasonic Methods. Mater. Eval. 47:571 - 575.

Kupfer, H., Apfelstedt, I., Schauer, W., Flukiger, R., Meier- Hirmer, R. and Wuhl, H. 1987. Critical Current and Upper Critical Field Of Sintered and Powdered Superconducting $YBa_2Cu_3O_7$. Z. Phys. B. 69:159 - 166.

Kupfer, H., Apfelstedt, I., Flukiger, R., Keller, C., Meier - Hirmer, R., Runtsch, B., Turowski, A., Weich, U. and Wolf, T. 1988a. Investigation of Inter- and Intragrain Critical Currents in High T_c Ceramic Superconductors. Cryogenics. 28:650 - 660.

Kupfer, H., Green, S.M., Jiang, C., YuMei, LuO, H.L., Meier-Hirmer, R. and Politis, C. 1988b. Weak Link Problem and Intragrain Current Density in Polycrystalline $Bi_1Ca_1Sr_1Cu_2O_x$ and $Tl_2Ca_2Ba_2Cu_3O_{10}$. Z. Phys. B. 71:63 - 37.

Kupfer, H., Keller, C., Salama, K. and Selvamanickam, V. 1989.

Inductive Current Measurements in an Oriented Grained $YBa_2Cu_3O_x$ Superconductor. Appl. Phys. Lett. 55:1903 - 1905.

Kupperman, D.S. and Karplus H.B., 1984. Ultrasonic Wave Propagation Characteristics of Green Ceramics. Am. Ceram. Soc. Bull. 63:1505-1509.

Lay, K.W. 1988. The Formation of Yttrium Barium Cuprate at Low Temperatures. General Electric Corporate Research and Development Technical Information Series, Report #88CRD144.

Ledbetter, H.M., Frederic, N.V. and Austin, M.W. 1980. Elastic-constant Variability in Stainless Steel - 304. J. Appl. Phys., 51:305 - 309.

Ledbetter, H.M., 1983. Elastic Properties. Materials at Low Temperatures, edited by R.P. Reed and A.F. Clark, American Society For Metals. 1 - 74.

Ledbetter, H.M., Austin, M.W., Kim, S.A. and Lei, M. 1987. Elastic Constants and Debye Temperature of Polycrystalline $YBa_2Cu_3O_{7-x}$. J. Mater. Res. 2:786-789.

Ledbetter, H. and Lei, M. 1990. Is $Y_1Ba_2Cu_3O_7$ Soft or Stiff ? J. Mater. Res. 5:241 - 244.

Lempriere, B.M. 1989. Standardizing Ultrasonic Attenuation Measurements. Proc. JANNAF 1989, CPIA publication 514.

Loegel, B., Mehdaoui, A. and Bolmont, D. 1989. Characterization of Bulk Superconducting High-Temperature Ceramics by Very Low Field a.c. Initial Susceptibility. J. Less Common Metals. 150:193 - 199.

Loegel, B., Mehdaoui, A., Bolmont, D., Eckhardt, A. and Muller, F. 1990. Quality of High Temperature Superconducting Poly- and single Crystals in Relation to Their Critical Dynamic Field. Cryogenics. 30:623 - 627.

Lynnworth, L.C. 1989. Ultrasonic Measurements For Process Control: Theory, Techniques, Applications. Academic Press. 113 - 118.

Macovski, A. 1983. Medical Imaging Systems. Prentice-Hall. 23 -25.

Maeda, H., Tanaka, Y., Fukutomi, M., Asano, T. 1988. A New High-T_c Oxide Superconductor Without a Rare Earth Element. Jpn. J. Appl. Phys. Lett. 27:L209 - L210.

May, J.E. 1958. Precise Measurement of Time Delay. IRE Natl. Conv. Rec. 6:Part 2, 134 - 142.

Mazaki, H. and Ishida, T. 1987. Bulk Nature of High-T_c Superconductivity in $ErBa_2Cu_3O_{\sim 6+x}$. Jpn. J. Appl. Phys. Lett. 26:L1508 - L1510.

McCauley, J.W. 1987. Materials Testing in The 21st Century. Nondestructive Testing of High-Performance Ceramics, edited by A. Vary and J. Snyder, American Ceramic Society. 1 - 18.

McLean, A.F., Fisher, E.A., Bratton, R.J. and Miller, D.G. 1975. Brittle Materials Design, High Temperature Gas Turbine, Interim Report Number 7, July 1, 1974 to December 31, 1974. AMMRC CTR 75-8, 97. NOTE: RESTRICTED MATERIAL

Mehdaoui, A. Loegel, B., Bolmont, D., Baron, J., Nanse, G. and Soulard, M. 1988. Low Field Frequency Dependent Complex Susceptibility of $YBa_2Cu_3O_x$. Sol. St. Comm. 68:333 - 336.

Morita, M., Murakami, M., Miyamoto, K., Sawano, K. and Matsuda, S. 1989. Superconducting Properties of Bulk Yttrium Barium Copper Oxide ($YBa_2Cu_3O_{7-x}$) Prepared By a Quench and Melt Growth Process. Physica C. 162-164:1217-1218.

Nagarajan, A. 1971. Ultrasonic Study of Elasticity-Porosity Relationship in Polycrystalline Alumina. J. Appl. Phys. 42:3693-3696.

Nakazawa, Y., Ishikawa, M., Takabatake, T., Koga, K. and Terakura, K. 1987. Characterization of Metamorphic Phases of $Ba_2YCu_3O_{9-x}$. Jap. J. Appl. Phys. Lett. 26:L796 - L798.

Nazzal, A.I., Lee, V.Y., Engler, E.M., Jacowitz, R.D., Tokura, Y. and Torrance, J.B. 1988. New Procedure For Determination of $[Cu\text{-}O]^{+P}$ Charge and Oxygen Content in High T_c Copper Oxides. Physica C. 153 - 155:1367 - 1368.

Newcomb, S.B., Glowacki, B.A., Campbell, A.M., Evetts, J.E., and Stobbs, W.M. 1988. Microstructure, Critical Currents and Flux Pinning in Y-Ba-Cu-O Superconductors. Brit. Ceram. Proc. 40:161 - 173.

Nikolo, M. 1990. Density and Texture Dependence of Grain Coupling in Sintered Y-Ba-Cu-O Superconductors. Physics and Materials Science of High Temperature Superconductors. edited by R. Kossowsky et al., Kluwer Academic. 711 - 717.

Onnes, H.K. 1911. Disappearance of the Electrical Resistance of Mercury at Helium Temperatures. Leiden Commun. 122b.

Ono, A., 1987. A Crystallographic Study On $Ba_2YCu_3O_{7-y}$. Jap. J. Appl. Phys. 26:L1223 - 11225.

Osamura, K., Takayama, T. and Ochiai, S. 1990. Dependence of Critical Current Density on Microstructure in Ag-Sheathed $Ba_2YCu_3O_{6+x}$ Tapes. Cryogenics. **29**:430 - 433.

Panakkal, J.P. and Ghosh, J.K. 1984. Ultrasonic Velocity in Sintered Uranium-Dioxide Pellets. J. Mater. Sci. Lett. 3:835-836.

Panson, A.J., Braginski, A.I., Gavaler, J.R., Hulm, J.K., Janocko, M.A., Pohl, H.C., Stewart, A.M., Talvacchio, J., and Wagner, G.R. 1987. Effect of Compositional Variation and Annealing in Oxygen on Superconducting Properties of $Y_1Ba_2Cu_3O_{8-y}$. Phys. Rev. B Rapid Comm. **35**:8774 - 8777.

Papadakis, E.P. 1972. Absolute Accuracy of the Pulse-Echo Overlap Method and the Pulse Superposition Method for Ultrasonic Velocity. J. Acous. Soc. Am. **52**:843-846.

Papadakis, E.P. 1975. Ultrasonic Diffraction From Single-Apertures With Application to Pulse Measurements and Crystal Physics. Physical Acoustics, Volume XI. edited by W.P. Mason and R.N. Thurston, Academic Press. 152 - 211.

Papadakis, E.P. and Petersen, B.W. 1979. Ultrasonic Velocity as a Predictor of Density in Sintered Powder Metal Parts. Mater. Eval. **37**:76-80.

Papadakis, E. P. 1987. The Inverse Problem in Materials Characterization Through Ultrasonic Attenuation and Velocity Measurements. in Nondestructive Characterization of Materials, edited by J.F. Bussiere, J-P. Monchalin, C.O. Ruud and R.E. Green, Jr., Plenum Press. 151 - 160.

Park, S.I., Tseui, C.C. and Tu, K.N. 1988. Effect of Oxygen Deficiency on the Normal and Superconducting Properties of $YBa_2Cu_3O_{7-y}$. Phys. Rev. B. **37**:2305 - 2308.

Patel, N.D. and Nicholson, P.S. 1986. Comparison of Piezoelectric Properties of Hot-Pressed and Sintered PZT. Am. Ceram. Soc. Bull. **65**:783-787.

Perez-Ramirez, J.G., Baberschke, K., and Clark, W.G. 1988. Meissner Effect, Critical Fields, and Superconducting Parameters of $YBa_2Cu_3O_{7-x}$. Sol. St. Comm. **65**:845 - 848.

Peterson, R.L. and Ekin, J. W. 1988. Josephson-junction Model of Critical Current in Granular $Y_1Ba_2Cu_3O_{7-x}$ Superconductors. Phys. Rev. B. **37**:9848 - 9851.

Phani, K.K. and Niyogi, S.K. 1986. Porosity Dependence of Ultrasonic

Velocity and Elastic Modulus in Sintered Uranium Dioxide--A Discussion. J. Mater. Sci. Lett. 5:427-430.

Ramachandran, V., Ramadass, G.A. and Srinivasan, R. Acoustic Wave Velocity and Attenuation in The High-T_c Superconductor $YBa_2Cu_3O_{7-x}$. Physica C. 153 - 155:278 - 279.

Rice, R.W. 1977. Microstructure Dependence of Mechanical Behavior of Ceramics. Properties of Microstructure: Treatise on Materials Science and Technology, 11. edited by R.K. MacCrone, Academic Press. 199-381.

Romig Jr., A.D. 1988. Analytical Transmission Electron Microscopy. Metals Handbook, Materials Characterization, Volume 10. American Society For Metals. 429 - 489.

Rosenblatt, J., Raboutou, A., Peyral, P. and Lebeau, C. 1990. Intragranular and Intergranular Transitions in Y-Ba-Cu-O Ceramics. Revue Phys. Appl. 25:73 - 78.

Roth, D.J., Generazio, E.R. and Baaklini, G.Y. 1987. Quantitative Void Characterization in Structural Ceramics By Use of Scanning Laser Acoustic Microscopy. Mater. Eval. 45:958 - 966.

Roth, D.J. and Dolhert, L.E. 1990a. Unpublished research, NASA Lewis Research Center, Cleveland, Ohio.

Roth, D.J., Dolhert, L.E. and Kerwin, D.P. 1990b. Unpublished research, NASA Lewis Research Center, Cleveland, Ohio.

Roth, D.J., Generazio, E.R. Stang, D.B. and Hepp, A.F. 1990c. Subtle Porosity Variation in The $YBa_2Cu_3O_{7-x}$ High-Temperature Superconductor Revealed by Ultrasonic Imaging. NASA TM-102130.

Round, R. and Bridge, B. 1987. Elastic-Constants of the High-Temperature Ceramic Superconductor $YBa_2Cu_3O_{7-x}$. J. Mater. Sci. Lett. 6:1471-1472.

Ryshkewitch, E. 1953. Compressive Strength of Porous Sintered Alumina and Zirconia. J. Am. Ceram. Soc. 36:65-68.

Saint-James, D., Sarma, G., and Thomas, E.J. 1969. Type II Superconductivity. Pergamon Press. 214.

Scheel, K.M., Clark, C.F. and Lawless, W.N. 1987. Capacitive Energy Storage at Cryogenic Temperatures, Interim Report. AFOSR-SBIR Phase II, contract F49620-86-C-0029.

Shelton, R.N., Andreasen, D., Klavins, P., Chan, H.W., Oslin, B.L.

and Anderson, R.L. 1988. Microstructure and Superconducting Properties of High-density Consolidated $YBa_2Cu_3O_x$. J. Am. Ceram. Soc. Comm. **71**:C487 - C489.

Sheng, Z.Z. and Hermann, A.M. 1988. Superconductivity in The Rare-Earth Free Tl-Ba-Cu-O System Above Liquid Nitrogen Temperatures. Nature, **332**:55 - 58.

Shih, W.Y., Ebner, C. and Stroud, D. 1984. Frustration and Disorder in Granular Superconductors. Phys. Rev. B. **30**:134 - 144.

Shyne, J.C., Grayelli, N. and Kino, G.S. 1981. Acoustic properties As Microstructure Dependent Materials Properties. Nondestructive Evaluation. edited by O. Buck and S.M. Wolf, Metallurgical Society of AIME. 133 - 146.

Shyuller, K.G., Khennike, G.V., and Kovziridze, Z.D. 1988. Specific Features of Structure Evolution in a Low-Temperature Ceramic. Glass and Ceramics. **44**:473-477.

Sleight, A.W., Gillson, J.L. and Bierstedt, P.E. 1975. High Temperature Superconductivity in The $BaPb_{1-x}Bi_xO_3$ System. Sol. St. Comm. **17**:27 - 28.

Smith, J.T. and Lopilato, S.A. 1966. The Correlation of Density of Porous Tungsten Billets and Ultrasonic-Wave Velocity. Trans. Metall. Soc. AIME. **236**:597-598.

Solin, S.A., Garcia, N., Vieira, S. and Hortal, M. 1988. Field-Induced Orientation of Nonlevitated Microcrystals of Superconducting $YBa_2Cu_3O_{7-x}$. Phys. Rev. Lett. **60**:744 - 747.

Soroka, I. and Sereda, P.J. 1968 Interrelation of Hardness Modulus of Elasticity and Porosity in Various Gypsum Systems. J. Am. Ceram. Soc. **51**:337-338.

Spriggs, R.M. 1961. Expression for Effect of Porosity on Elastic Modulus of Polycrystalline Refractory Materials, Particularly Aluminum Oxide. J. Am. Ceram. Soc. **44**:628-629.

Stang, D.S. 1989. Unpublished research, NASA Lewis Research Center, Cleveland, Ohio.

Stephens, R.B. 1989. Critical Current Limitations in Ceramic Oxide Superconductors. Cryogenics. **29**:399 - 404.

Stroebel, P. Paulsen, C. and Tholence, J.L. 1988. Superconducting Properties of Substituted $YBa_2Cu_{3(1-x)}M_{3x}O_{7-y}$. Sol. St. Comm. **65**:585 - 589.

Sun, K.J., Levy, M., Sarma, B.K., Hor, P.H., Meng, R.L., Wang, Y.Q. and Chu, C.W. 1988. Ultrasonic Measurements on Polycrystalline $YBa_2Cu_3O_7$. Phys. Lett. A **131**:541 - 544.

Swokowski, E.W. 1975 Calculus With Analytical Geometry. Prindle, Weber & Schmidt. 461 - 462.

Szilard, J. 1982. Physical Principles of Ultrasonic Testing. Ultrasonic Testing. edited by J. Szilard. Wiley. 1-23, 217 - 261.

Tarascon, J.M., Greene, L.H., Mckinnon, W.R., Hull, G.W. and Geballe, H. 1987a. Superconductivity at 40K in The Oxygen-Deficient Perovskites $La_{2-x}Sr_xCuO_{4-y}$. Science. **235**:1373 - 1376.

Tarascon, J.M., Greene, L.H., McKinnon, W.R. and Hull, G.W. 1987b. Superconductivity at 90 K In A Multiphase Oxide of Y-Ba-Cu. Phys. Rev. B. **35**:7115 - 7118.

Tarascon, J.M., McKinnon, W.R., Greene, L.H., Hull, G.W., Bagley, B.G. and Vogel, E.M. 1987c. Processing and Superconducting Properties of Perovskite Oxides. Adv. Ceram. Mater. **2**:498 - 505.

Taylor, K.N.R., Russel, G.J., Bosi, S., Mattews, D.N., Cochrane, J., Town, S., Hunter, B., Puzzer, T., Bailey, A. and Vaile, R.A. 1990. The Growth of Large Single Crystals, Textured Materials and The Electromagnetic Shielding Effectiveness of High T_c Superconductors. Physics and Materials Science of High Temperature Superconductors. edited by R. Kossowsky et al., Kluwer Academic. 245 - 259.

Tenbrink, J., Heine, K. and Krauth, H. 1990. Critical Currents and Flux Pinning in Ag Stabilized High T_c Superconductor Wires. Cryogenics, **30**:422 - 426.

Testardi, L.R., Wernick, J.H. and Royer, W.A. 1974. Superconductivity With Onset Above 23 K in Nb-Ge Sputtered Films. Sol. St. Comm. **15**:1 - 4.

Thorp, J.S. and Bushell, T.G. 1985. Ultrasonic Examination of Reaction-Bonded Silicon-Nitride. J. Mater. Sci. **20**:2265-2274.

Tinkham, M. 1985. Introduction To Superconductivity. Robert E. Krieger Publ. 74 and 143 - 229.

Torardi, C.C., McCarron, E.M., Subramanian, M.A., Horowitz, H.S., Michel, J.B. and Sleight, A.W. 1987. Structure - Property Relationships For $RBa_2Cu_3O_x$ Phases. Chemistry Of High-Temperature Superconductors. edited by D.L. Nelson, M.S. Whittingham and T.F. George, ACS Symposium Series, **351**, American Chemical Society, 152 - 163.

Truell, R. 1959. Nature of Defects Arising From Fast Neutron Irradiationof Silicon Single Crystals. Phys. Rev. 116:890 - 892.

Truell, R. Elbaum, C. and Chick, B.B. 1969. Ultrasonic Methods in Solid State Physics. Academic Press. 77 - 78 and 159 - 179.

Umezawa, A. Crabtree, G.W., Liu, J.Z., Moran, T.J., Malik, S.K., Nunez, L.H., Kwok, W.L. and Sowers, C.H. 1988. Anisotropy of The Lower Critical Field, Magnetic Penetration Depth, and Equilibrium Shielding Current in Single Crystal $YBa_2Cu_3O_{7-x}$. Phys. Rev. B. 38:2843 - 2846.

Vander Voort, G.F. 1984. Metallography Principles and Practices. McGraw-Hill. 426.

Vander Voort, G.F. 1988a. Image Analysis. Metals Handbook, Materials Characterization, Volume 10, American Society For Metals. 309 - 322.

Vander Voort, G.F. 1988b. Optical Microscopy. Metals Handbook, Metallography And Microstructures, Volume 9. American Society For Metals. 71 - 88.

Van Dover, R.B., Cava, R., Batlogg, B. and Rietman, E. 1987. Composition-Dependent Superconductivity on $La_{2-x}Sr_xCu_{4-y}$. Phys. Rev. B. 35:5337 - 5339.

Vary, A., 1988. Concepts For Interrelating Ultrasonic Attenuation, Microstructure, and Fracture Toughness in Polycrystalline Solids. Mater. Eval. 46:642 - 649.

Verhoeven, J.D. 1988. Scanning Electron Microscopy. Metals Handbook, Materials Characterization, Volume 10. American Society For Metals. 490 - 515.

Vikram, C.S. and Ruud, C.O. 1986. Morphological Investigation of Ultrasonic Techniques For Materials Evaluation. Review of Progress in Quantitative Nondestructive Evaluation, Volume 5B. edited by D.O. Thompson and D.E. Chimenti, Plenum Press. 1327 - 1334.

Williams, E.C., Reid-Jones, R.C. and Dorrill, D.T. 1963. The Physical Properties and Behavior in Kiln of Hard Electrical Porcelain as Interpreted from Density Measurements. Trans. Brit. Ceram. Soc. 62:405-420.

Wolf, T., Apfelstedt, I., Goldacker, W., Kupfer, H. and Flukiger, R. 1988. Preparation and Characterization of Isotropic and Textured $YBa_2Cu_3O_{7-x}$ With High Density and Low Residual Resistivity. Physica C. 153 - 155:351 - 352.

Wong-Ng, W., McMurdie, H.F., Paretzkin, B., Zhang, Y., Davis, K. L., Hubbard, C.R., Dragoo, A.L. and Stewart, J.M. 1987. Standard X- Ray Diffraction Powder Patterns of Sixteen Ceramic Phases. Powder Diffraction. 2:191 - 201.

Wong-Ng, W., McMurdie, H.F., Paretzkin, B., Hubbard, C.R. and Dragoo, A.L. 1988. Standard X-Ray Diffraction Powder Pattersn of Fourteen Ceramic Phases. Powder Diffraction. 3:113 - 121.

Worthington, T.K., Gallagher, W.J. and Dinger, T.R. 1987. Anisotropic Nature of High-Temperature Superconductivity in Single- Crystal $YBa_2Cu_3O_{7-x}$. Phys. Rev. Lett. 59:1160 - 1163.

Yan, M.F., Barns, R.L., O'Bryan, H.M., Gallagher, P.K., Sherwood, R.C. and Jin, S. 1987. Water Interaction With The Superconducting $YBa_2Cu_3O_7$ Phase. Appl. Phys. Lett. 51:698 - 700.

Yan, M.F., Ling, H.C., O'Bryan, H.M., Gallagher, P.K. and Rhodes, W.W. 1988a. Processing of Ceramic Superconductors. Proc. IEEE Electronic Components Conference. IEEE. 130 - 135.

Yan, M.F., Rhodes, W.W. and Gallagher, P.K. 1988b. Dopant Effects on The Superconductivity of $YBa_2Cu_3O_7$ Ceramics. J. Appl. Phys. 63:821 - 828.

Zandbergen, H.W., Fu, W.T., de Jong, L.J. and Tendeloo, G.V. 1990. Electron Microscopy Study of Grain Boundaries in 1-2-3 Superconductors. Cryogenics 30:628 - 632.

Zeiger, A. and Jasby, K. 1982. Measurement of Acoustoelastic Coefficients of Rayleigh Waves in Steel Alloys. J. Nondestructive Eval. 3:115 - 124.

XI. REFERENCE KEY FOR FIGURES 1 - 61 AND TABLES 1 AND 2

REFERENCE	AUTHOR
2	Smith et al., 1966
3	Rice, 1977
7	Boisson et al., 1976
8	Patel et al., 1986
11	Blendell et al., 1987
16	Nagarajan, 1971
24	Claytor et al., 1989
25	Jones et al., 1986
26	Stang, 1989
27	Arons et al., 1982
28	Roth et al., 1990a
29	Kupperman et al., 1984
30	Filipczynski et al., 1966
31	Shyuller et al., 1988
32	Friedman et al., 1987
33	Baaklini et al., 1989
34	Gruber et al., 1988
35	Klima et al., 1981
36	Derkacs et al., 1976
37	McLean et al., 1974
38	Thorp et al., 1985
39	Papadakis et al., 1979
40	Panakkal et al., 1984
41	Ghosh et al., 1985
42	Gaiduk et al., 1988
43	Roth et al., 1990b
44	Ledbetter et al., 1987
45	Round et al., 1987
46	Alford et al., 1988b
47	Deiter, 1986
48	Engineering Property Data, 1981
49	Engineering Property Data, 1981

XII. FIGURES

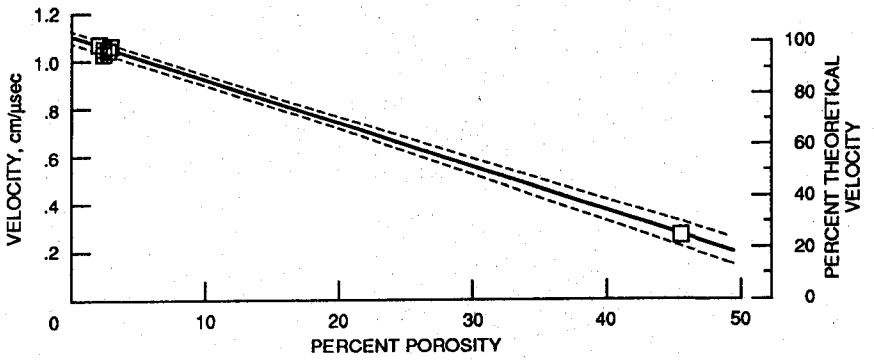

Figure 1. - Longitudinal velocity versus percent porosity for Al_2O_3 (ref. 24).
Velocity = –0.018 x percent porosity + 1.09.
Percent theoretical velocity = –1.65 x percent porosity + 100.
Correlation coefficient = –0.999.

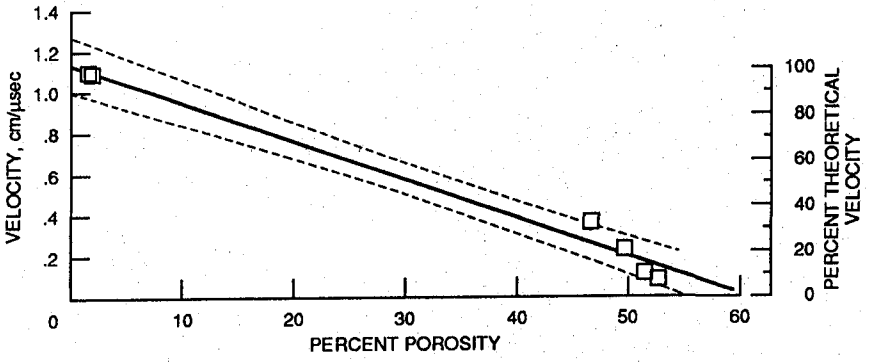

Figure 2. - Longitudinal velocity versus percent porosity for Al_2O_3 (ref. 25).
Velocity = –0.019 x percent porosity + 1.13.
Percent theoretical velocity = –1.64 x percent porosity + 100.
Correlation coefficient = –0.992.

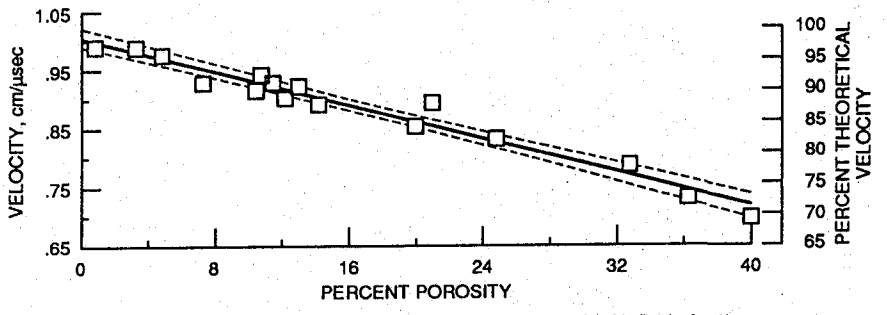

Figure 3. - Longitudinal velocity versus percent porosity for Al_2O_3 (ref. 16).
Velocity = –0.007 x percent porosity + 1.00.
Percent theoretical velocity = –0.736 x percent porosity + 100.
Correlation coefficient = –0.982.

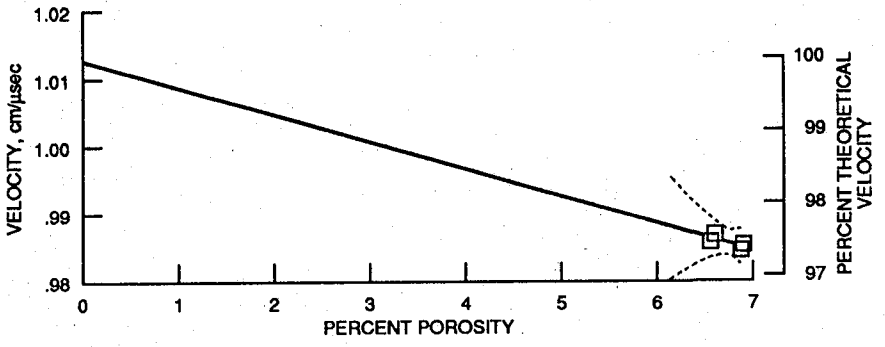

Figure 4. - Longitudinal velocity versus percent porosity for Al_2O_3 (ref. 26).
Velocity = –0.004 x percent porosity + 1.01.
Percent theoretical velocity = –0.377 x percent porosity + 100.
Correlation coefficient = –0.698.

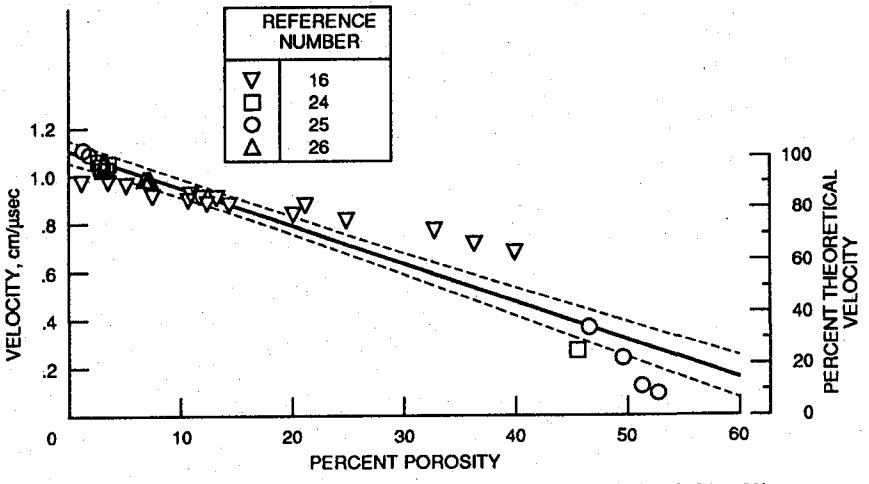

Figure 5. - Longitudinal velocity versus percent porosity for Al_2O_3 (refs. 16, 24 to 26).
Velocity = –0.016 x percent porosity + 1.10.
Percent theoretical velocity = –1.43 x percent porosity + 100.
Correlation coefficient = –0.949.

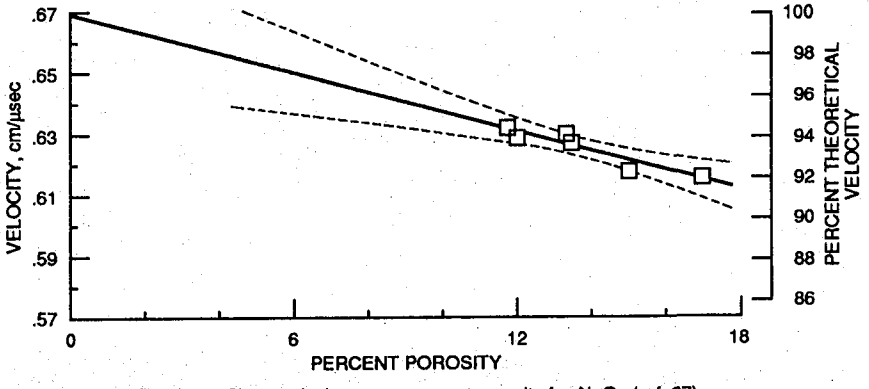

Figure 6. - Shear velocity versus percent porosity for Al_2O_3 (ref. 27).
Velocity = –0.003 x percent porosity + 0.669.
Percent theoretical velocity = –0.477 x percent porosity + 100.
Correlation coefficient = –0.936.

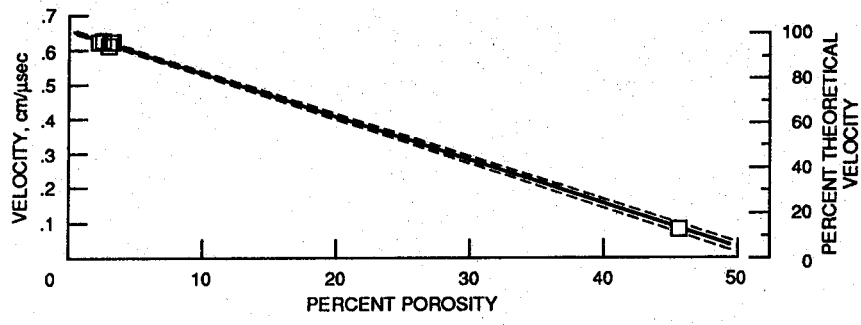

Figure 7. - Shear velocity versus percent porosity for Al_2O_3 (ref. 24).
Velocity = –0.012 x percent porosity + 0.655.
Percent theoretical velocity = –1.87 x percent porosity + 100.
Correlation coefficient = –1.00.

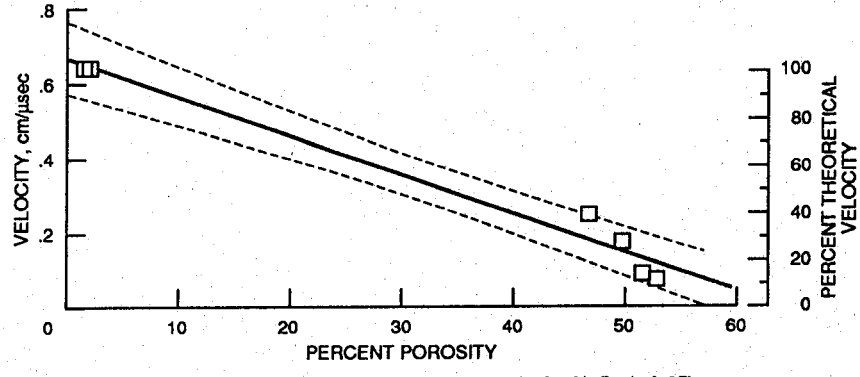

Figure 8. - Shear velocity versus percent porosity for Al_2O_3 (ref. 25).
Velocity = –0.010 x percent porosity + 0.666.
Percent theoretical velocity = –1.55 x percent porosity + 100.
Correlation coefficient = –0.987.

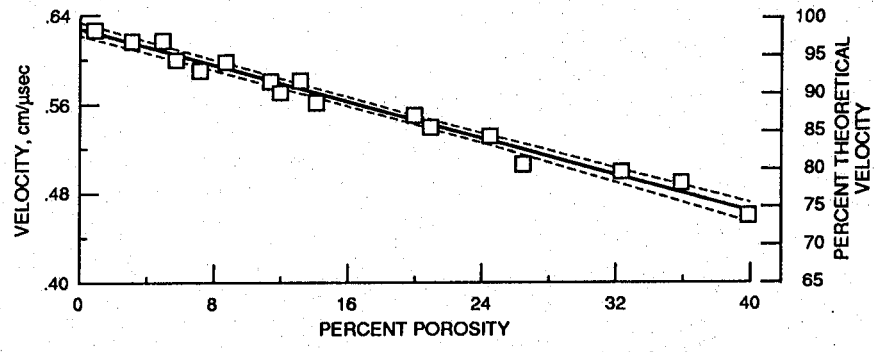

Figure 9. - Shear velocity versus percent porosity for Al_2O_3 (ref. 16).
Velocity = –0.004 x percent porosity + 0.628.
Percent theoretical velocity = –0.662 x percent porosity + 100.
Correlation coefficient = –0.990.

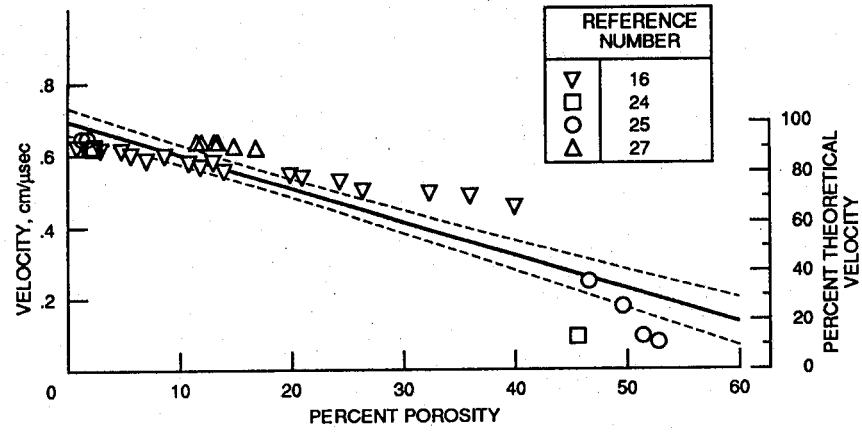

Figure 10. - Shear velocity versus percent porosity for Al_2O_3 (refs. 16, 24, 25, 27).
Velocity = –0.009 x percent porosity + 0.693.
Percent theoretical velocity = –1.35 x percent porosity + 100.
Correlation coefficient = –0.910.

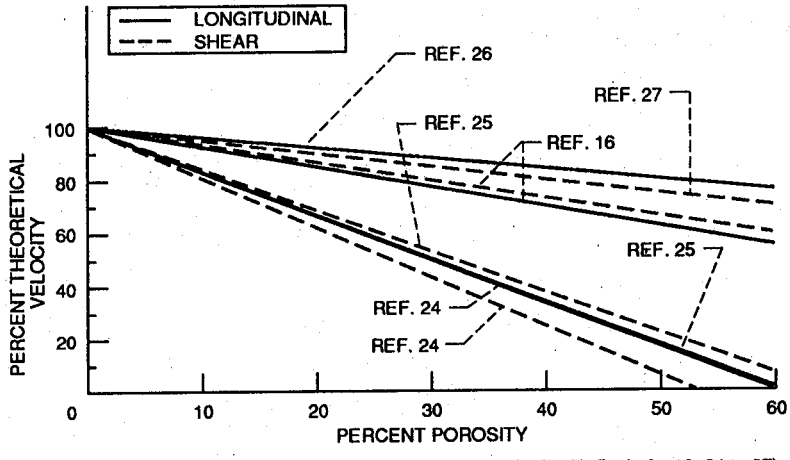

Figure 11. - Ultrasonic velocity versus percent porosity for Al_2O_3 (refs. 16, 24 to 27).

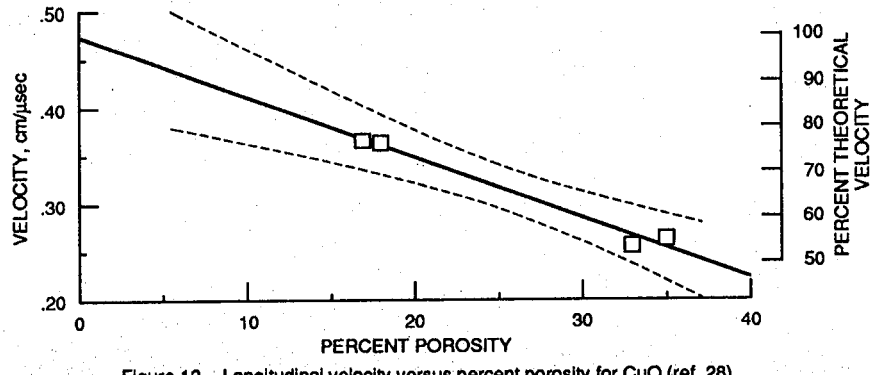

Figure 12. - Longitudinal velocity versus percent porosity for CuO (ref. 28).
Velocity = –0.006 x percent porosity + 0.474.
Percent theoretical velocity = –1.34 x percent porosity + 100.
Correlation coefficient = –0.990.

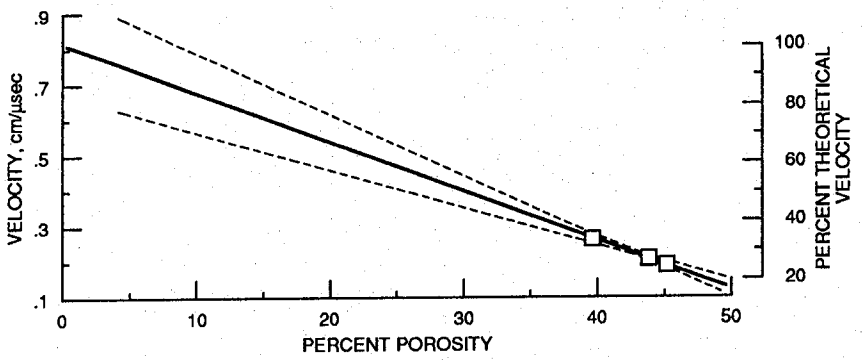

Figure 13. - Longitudinal velocity versus percent porosity for "green" M_gO (ref. 29).
Velocity = −0.018 x percent porosity + 0.817.
Correlation coefficient = −1.00.

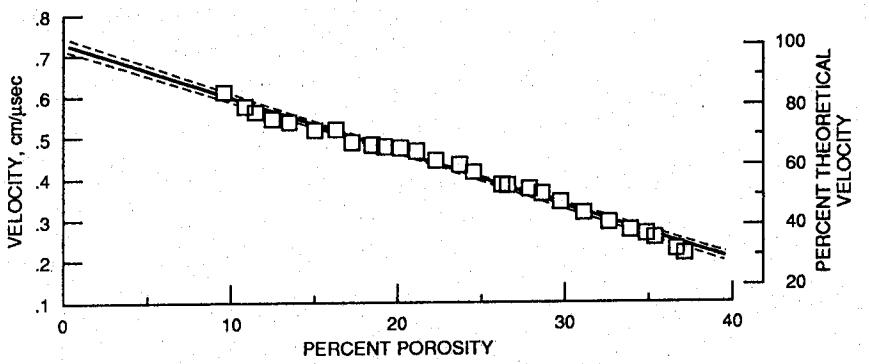

Figure 14. - Longitudinal velocity versus percent porosity for porcelain (ref. 7).
Velocity = −0.013 x percent porosity + 0.728.
Percent theoretical velocity = −1.78 x percent porosity + 100.
Correlation coefficient = −0.994.

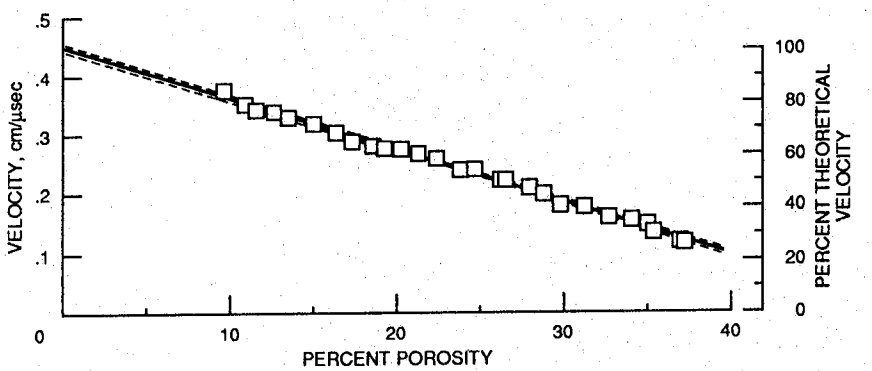

Figure 15. - Shear velocity versus percent porosity for porcelain (ref. 7).
Velocity = −0.009 x percent porosity + 0.448.
Percent theoretical velocity = −1.93 x percent porosity + 100.
Correlation coefficient = −0.998.

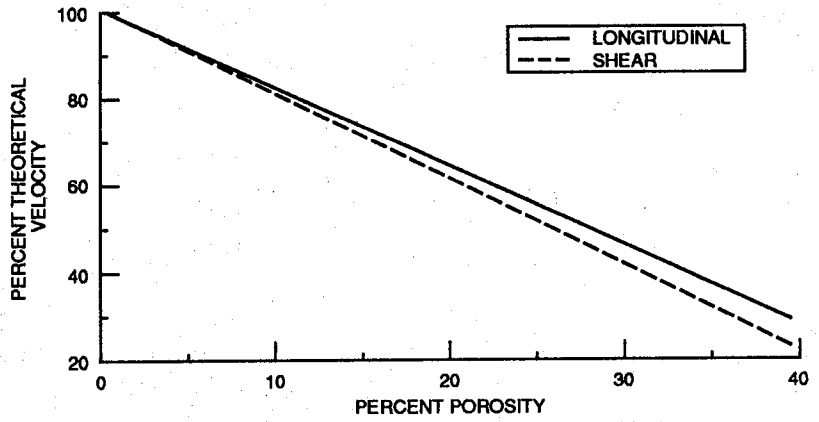

Figure 16. - Ultrasonic velocity versus percent porosity for porcelain (ref. 7).

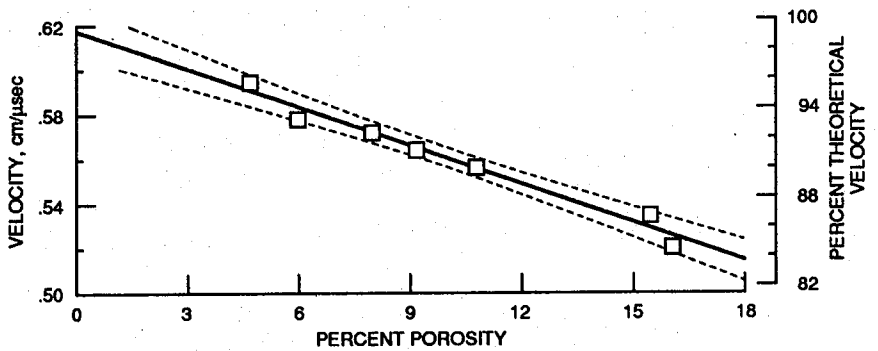

Figure 17. - Longitudinal velocity versus percent porosity for porcelain (ref. 30).
Velocity = –0.006 x percent porosity + 0.618.
Percent theoretical velocity = –0.935 x percent porosity + 100.
Correlation coefficient = –0.987.

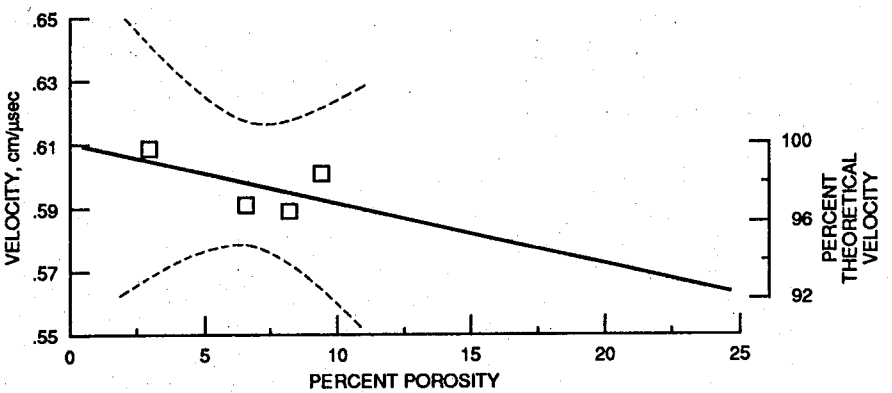

Figure 18. - Longitudinal velocity versus percent porosity for porcelain P1 (ref. 31).
Velocity = –0.002 x percent porosity + 0.611.
Percent theoretical velocity = –0.312 x percent porosity + 100.
Correlation coefficient = –0.586.

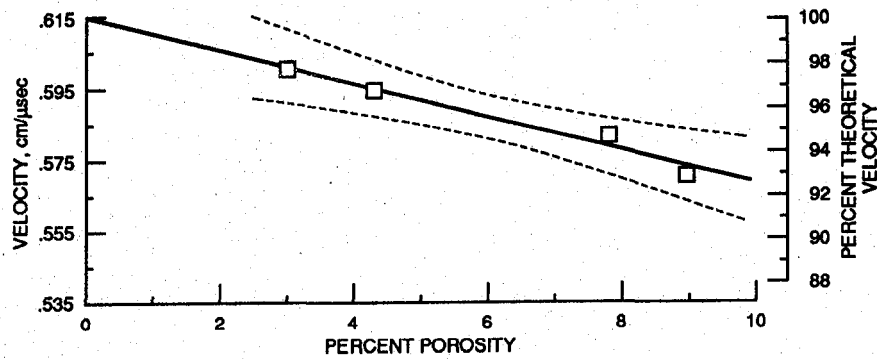

Figure 19. - Longitudinal velocity versus percent porosity for porcelain P2 (ref. 31).
Velocity = –0.005 x percent porosity + 0.615.
Percent theoretical velocity = –0.740 x percent porosity + 100.
Correlation coefficient = –0.983.

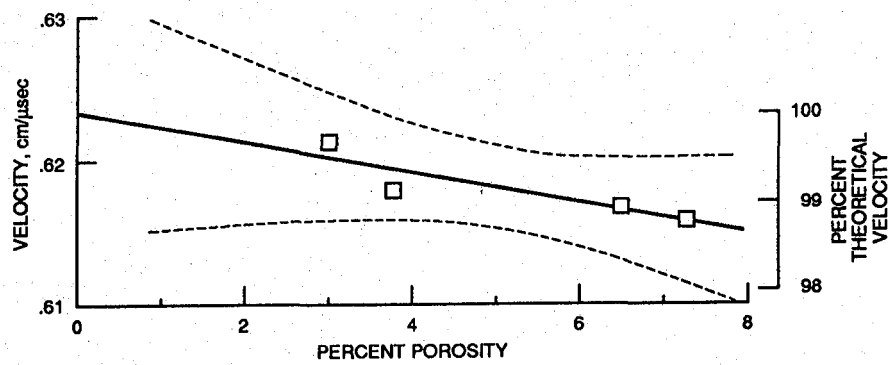

Figure 20. - Longitudinal velocity versus percent porosity for porcelain T1 (ref. 3).
Velocity = –0.001 x percent porosity + 0.623.
Percent theoretical velocity = –0.167 x percent porosity + 100.
Correlation coefficient = –0.894.

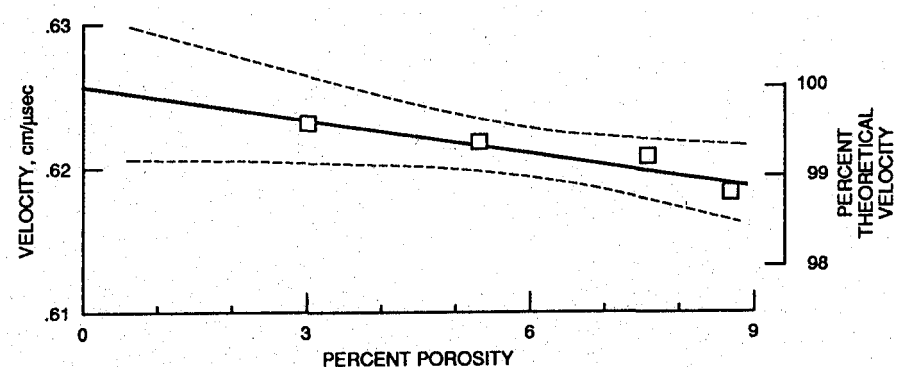

Figure 21. - Longitudinal velocity versus percent porosity for porcelain T2 (ref. 31).
Velocity = –0.001 x percent porosity + 0.626.
Percent theoretical velocity = –0.121 x percent porosity + 100.
Correlation coefficient = –0.947.

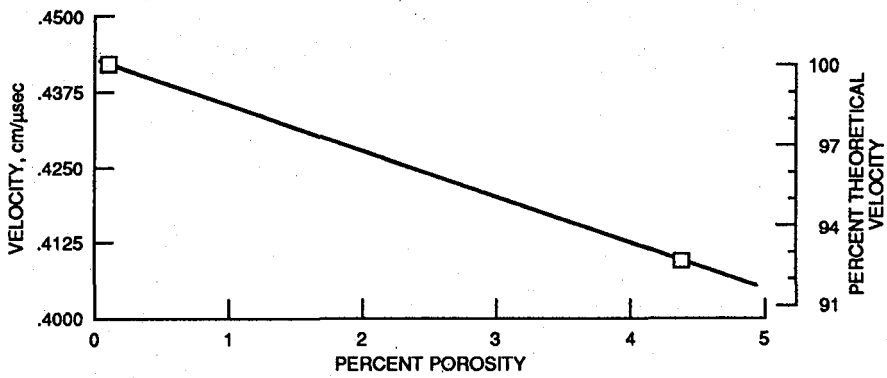

Figure 22. - Longitudinal velocity versus percent porosity for unpoled PZT4 (ref. 8).
Velocity = –0.007 x percent porosity + 0.443.
Percent theoretical velocity = –1.68 x percent porosity + 100.

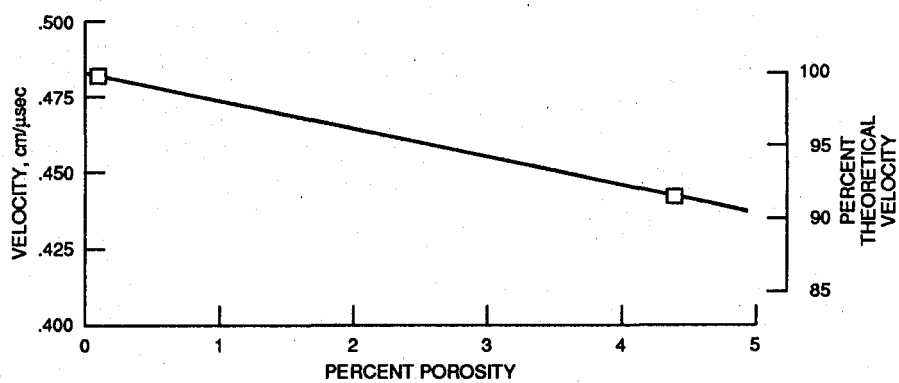

Figure 23. - Longitudinal velocity versus percent porosity for poled PZT4 (ref. 8).
Velocity = –0.009 x percent porosity + 0.483.
Percent theoretical velocity = –1.93 x percent porosity + 100.

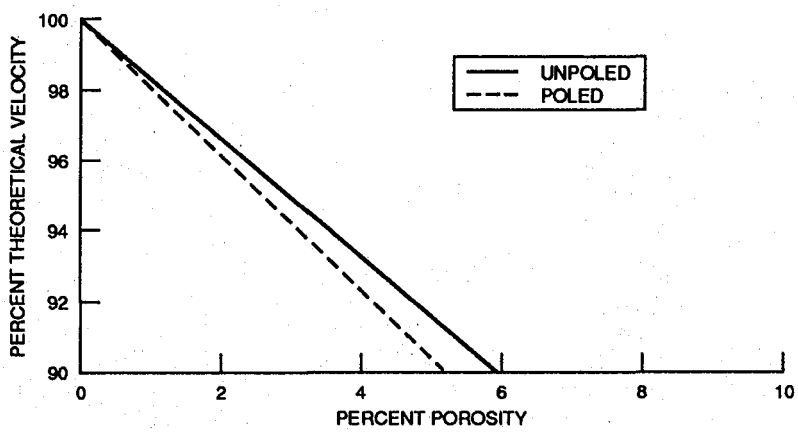

Figure 24. - Ultrasonic velocity versus percent porosity for PZT4 (ref. 8).

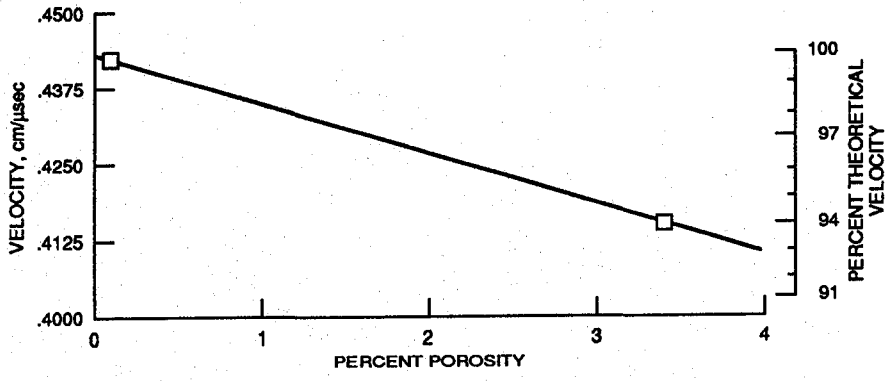

Figure 25. - Longitudinal velocity versus percent porosity for unpoled PZT5 (ref. 8).
Velocity = –0.008 x percent porosity + 0.443.
Percent theoretical velocity = –1.85 x percent porosity + 100.

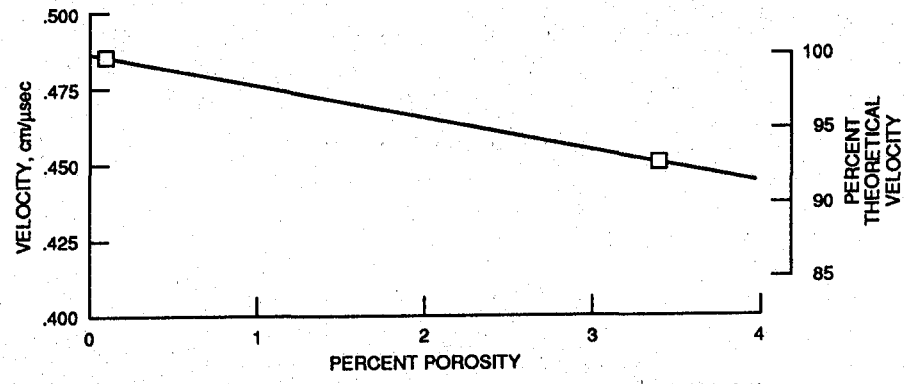

Figure 26. - Longitudinal velocity versus percent porosity for poled PZT5 (ref. 8).
Velocity = –0.010 x percent porosity + 0.486.
Percent theoretical velocity = –2.12 x percent porosity + 100.

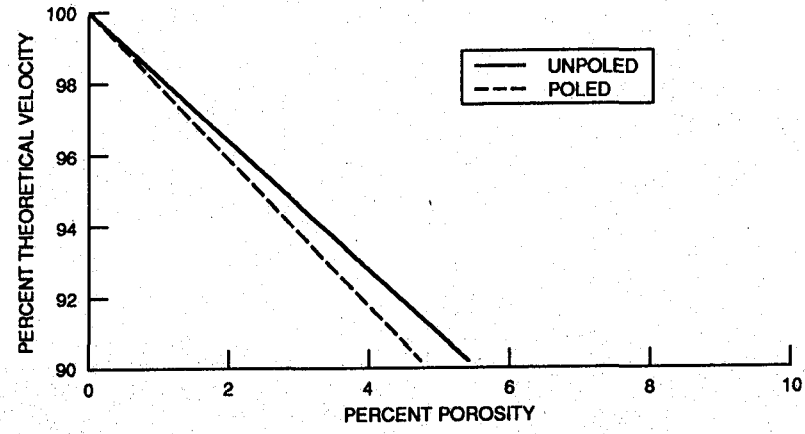

Figure 27. - Ultrasonic velocity versus percent porosity for PZT5 (ref. 8).

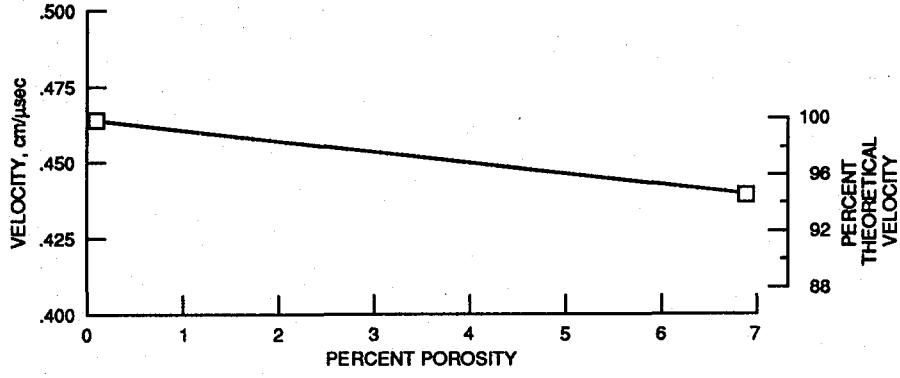

Figure 28. - Longitudinal velocity versus percent porosity for unpoled PZT7 (ref. 8).
Velocity = –0.004 x percent porosity + 0.464.
Percent theoretical velocity = –0.760 x percent porosity + 100.

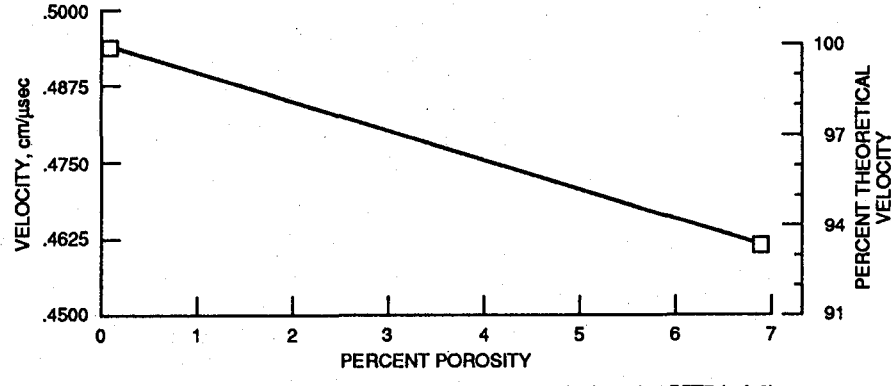

Figure 29. - Longitudinal velocity versus percent porosity for poled PZT7 (ref. 8).
Velocity = –0.005 x percent porosity + 0.494.
Percent theoretical velocity = –0.952 x percent porosity + 100.

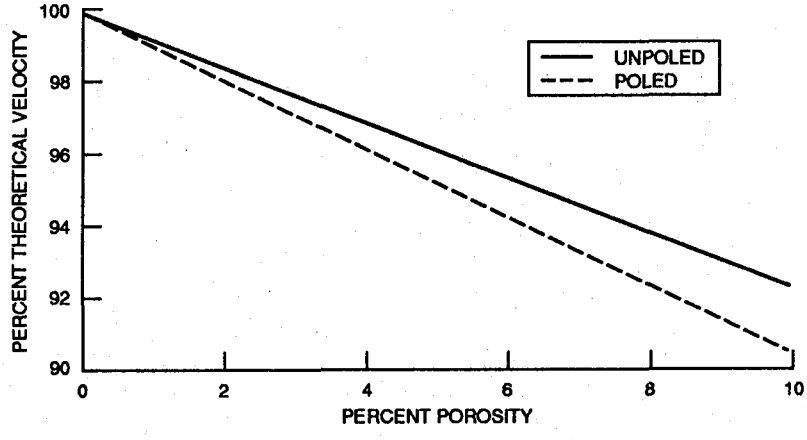

Figure 30. - Ultrasonic velocity versus percent porosity for PZT7 (ref. 8).

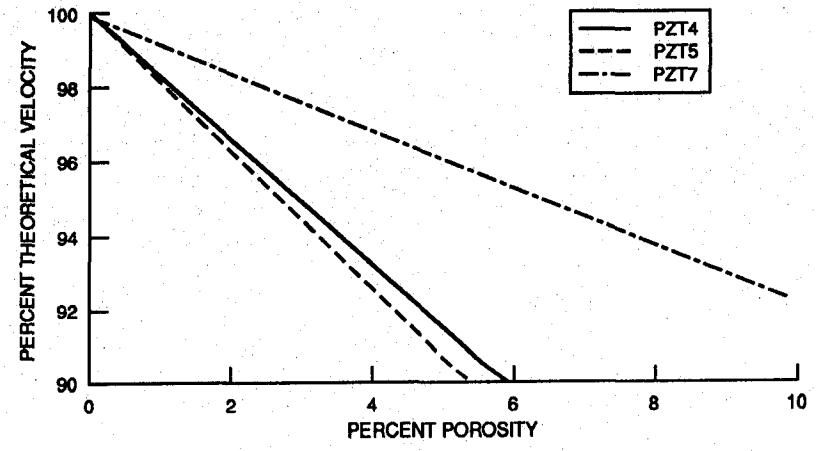

Figure 31. - Ultrasonic velocity versus percent porosity for unpoled PZT (ref. 8).

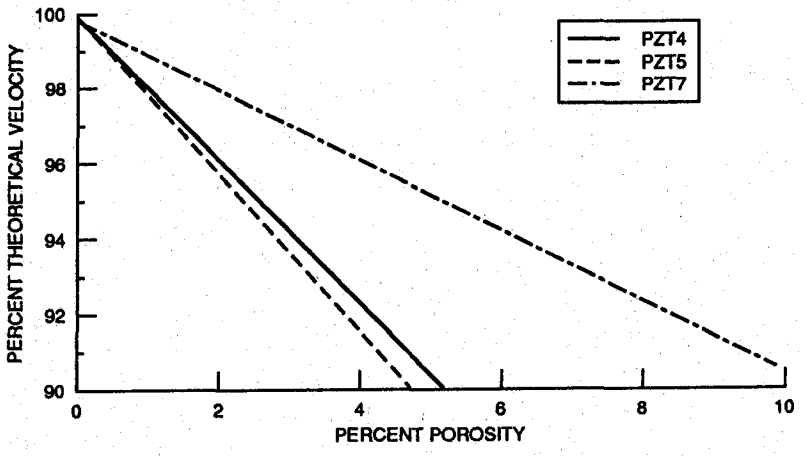

Figure 32. - Ultrasonic velocity versus percent porosity for poled PZT (ref. 8).

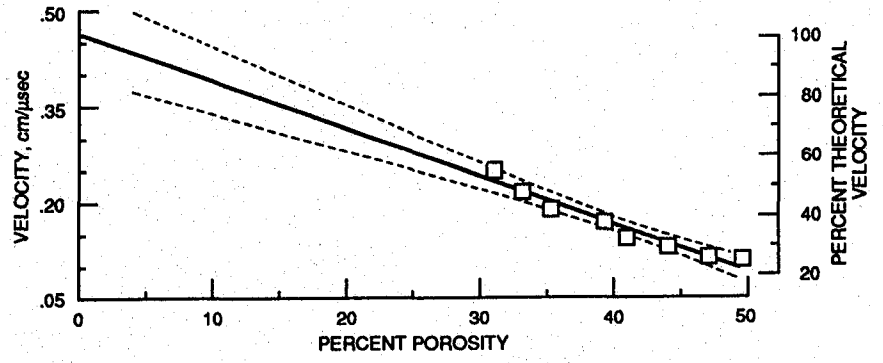

Figure 33. - Longitudinal velocity versus percent porosity for green SiC (ref. 32).
Velocity = –0.007 x percent porosity + 0.464.
Correlation coefficient = –0.974.

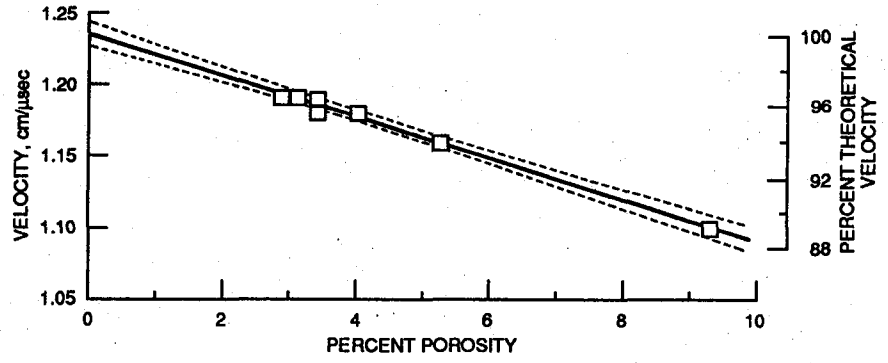

Figure 34. - Longitudinal velocity versus percent porosity for SiC (ref. 33).
Velocity = –0.014 x percent porosity + 1.23.
Percent theoretical velocity = –1.16 x percent porosity + 100.
Correlation coefficient = –0.993.

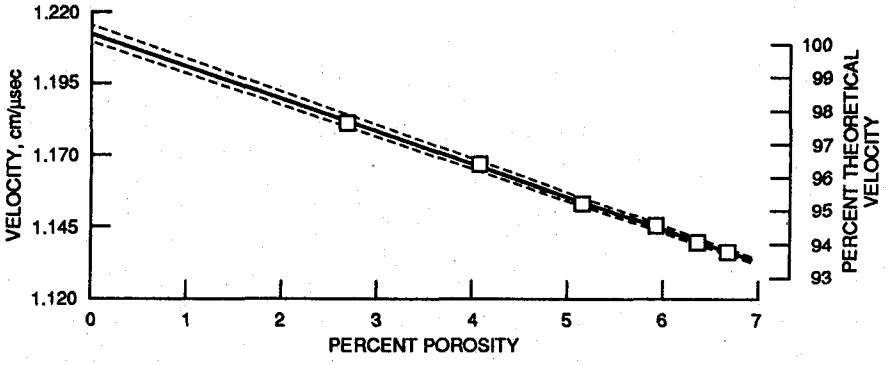

Figure 35. - Longitudinal velocity versus percent porosity for SiC (ref. 34).
Velocity = –0.011 x percent porosity + 1.21.
Percent theoretical velocity = –0.916 x percent porosity + 100.
Correlation coefficient = –0.999.

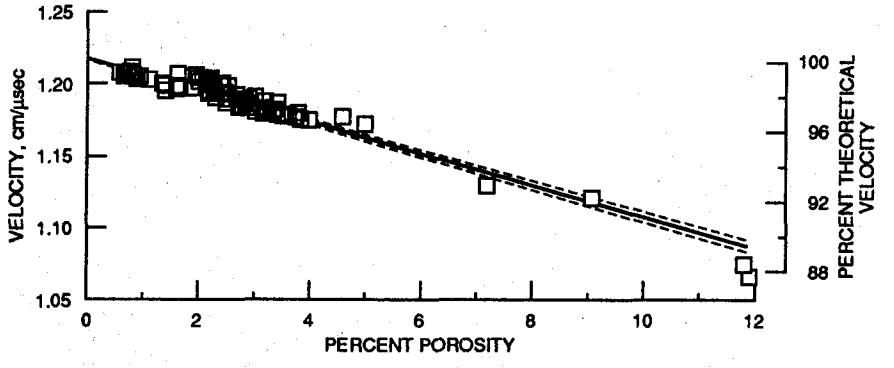

Figure 36. - Longitudinal velocity versus percent porosity for SiC (ref. 35).
Velocity = –0.011 x percent porosity + 1.22.
Percent theoretical velocity = –0.883 x percent porosity + 100.
Correlation coefficient = –0.957.

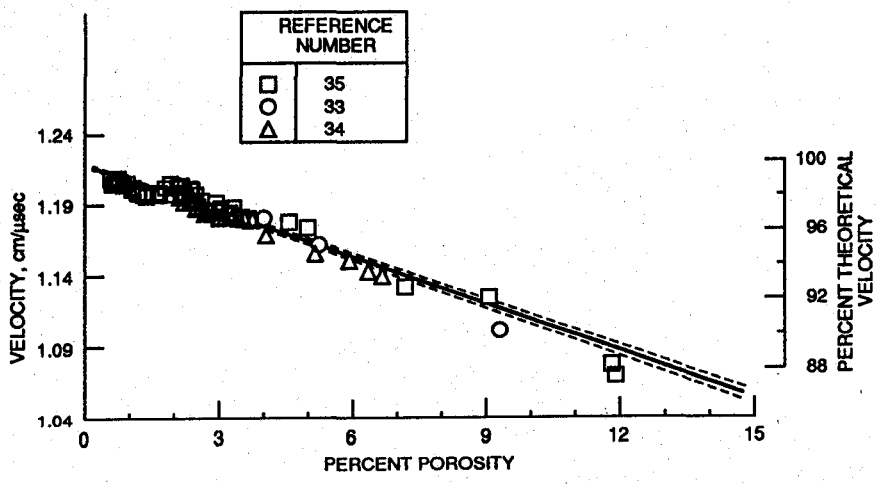

Figure 37. - Longitudinal velocity versus percent porosity for SiC (refs. 33 to 35).
Velocity = –0.011 x percent porosity + 1.22.
Percent theoretical velocity = –0.912 x percent porosity + 100.
Correlation coefficient = –0.964.

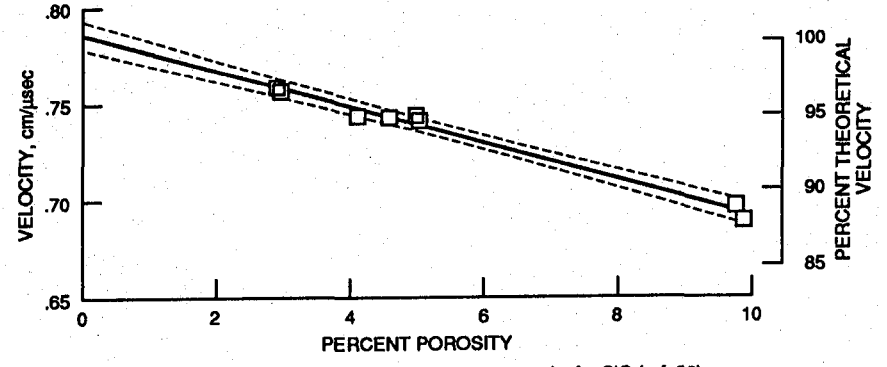

Figure 38. - Shear velocity versus percent porosity for SiC (ref. 26).
Velocity = –0.009 x percent porosity + 0.786.
Percent theoretical velocity = –1.16 x percent porosity + 100.
Correlation coefficient = –0.991.

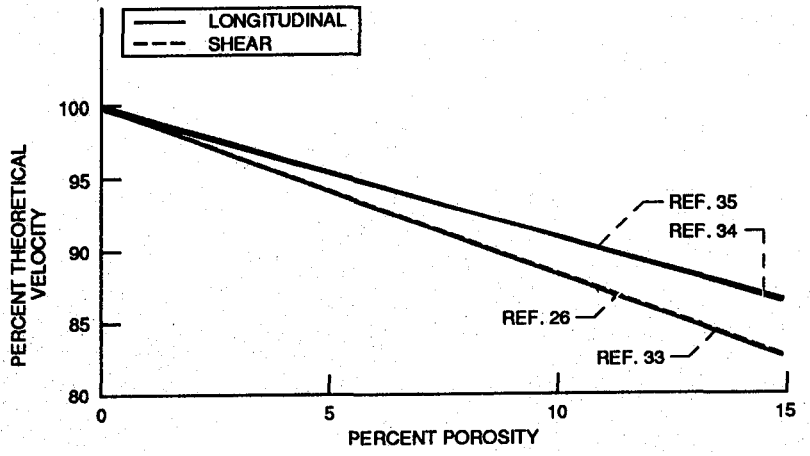

Figure 39. - Ultrasonic velocity versus percent porosity for SiC (refs. 26, 33 to 35).

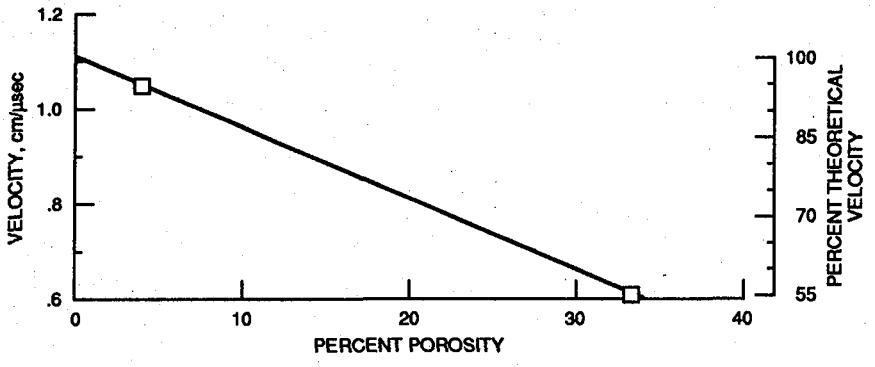

Figure 40. - Longitudinal velocity versus percent porosity for Si_3N_4 (ref. 36).
Velocity = –0.015 x percent porosity + 1.11.
Percent theoretical velocity = –1.34 x percent porosity + 100.

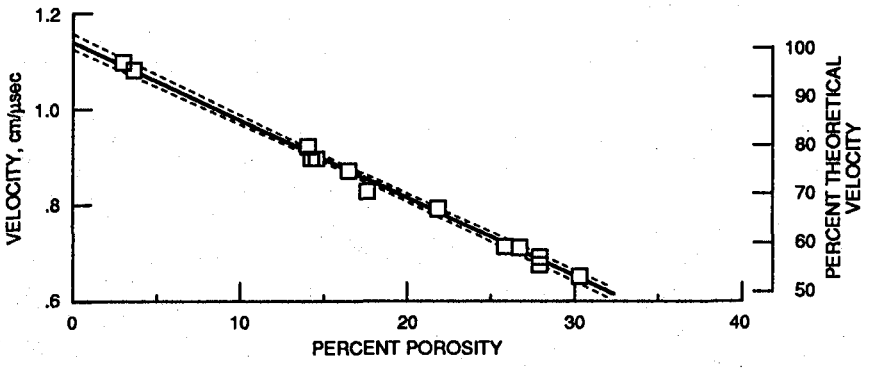

Figure 41. - Longitudinal velocity versus percent porosity for Si_3N_4 (ref. 37).
Velocity = –0.016 x percent porosity + 1.14.
Percent theoretical velocity = –1.41 x percent porosity + 100
Correlation coefficient = –0.997.

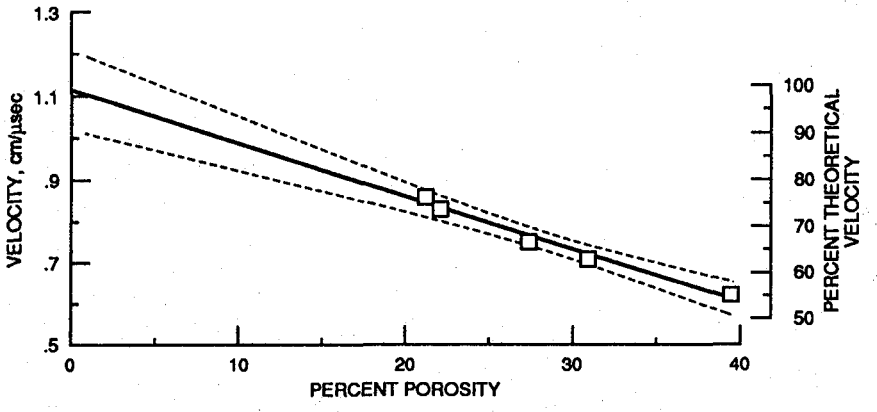

Figure 42. - Longitudinal velocity versus percent porosity for Si_3N_4 (ref. 38).
Velocity = –0.013 x percent porosity + 1.12.
Percent theoretical velocity = –1.15 x percent porosity + 100
Correlation coefficient = –0.991.

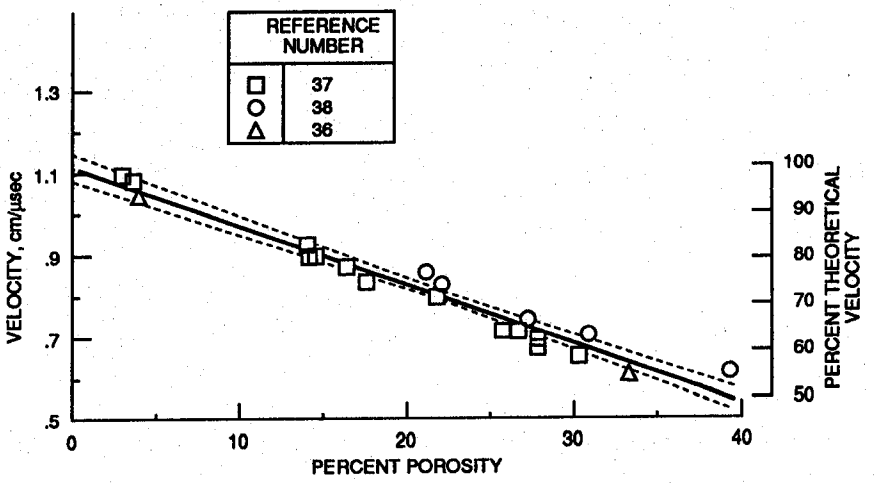

Figure 43. - Longitudinal velocity versus percent porosity for Si_3N_4 (refs. 36 to 38).
Velocity = –0.014 x percent porosity + 1.12.
Percent theoretical velocity = –1.27 x percent porosity + 100
Correlation coefficient = –0.981.

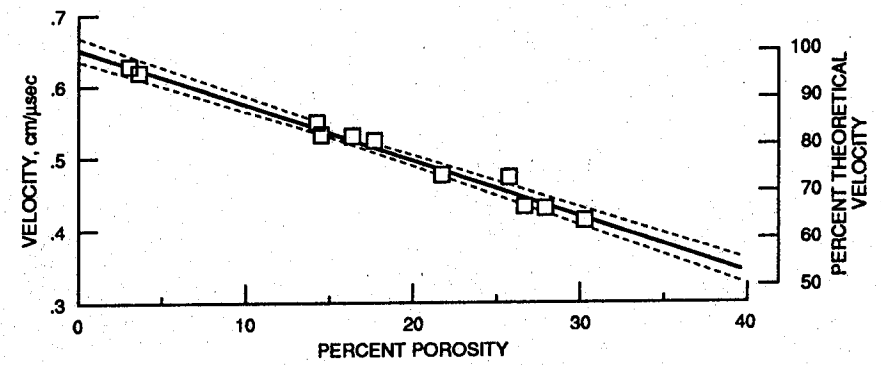

Figure 44. - Shear velocity versus percent porosity for Si_3N_4 (ref. 37).
Velocity = –0.008 x percent porosity + 0.652.
Percent theoretical velocity = –1.18 x percent porosity + 100
Correlation coefficient = –0.991.

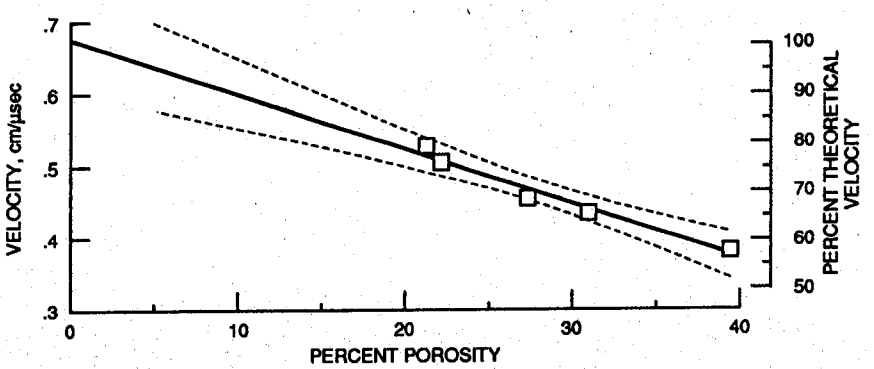

Figure 45. - Shear velocity versus percent porosity for Si_3N_4 (ref. 38).
Velocity = –0.007 x percent porosity + 0.675.
Percent theoretical velocity = –1.10 x percent porosity + 100
Correlation coefficient = –0.984.

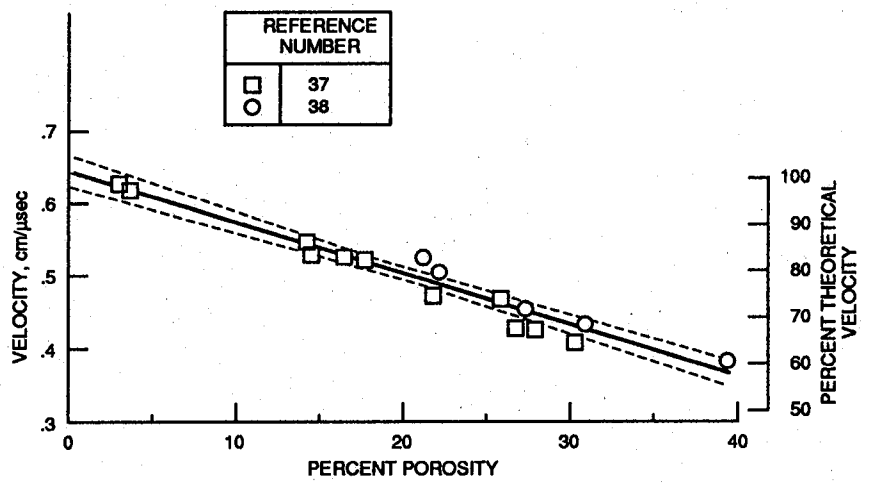

Figure 46. - Shear velocity versus percent porosity for Si_3N_4 (refs. 37, 38).
Velocity = –0.007 x percent porosity + 0.645.
Percent theoretical velocity = –1.07 x percent porosity + 100
Correlation coefficient = –0.973.

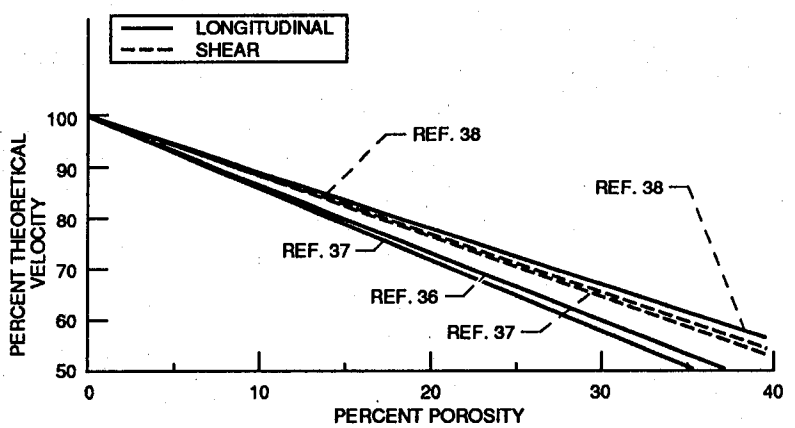

Figure 47. - Ultrasonic velocity versus percent porosity for Si_3N_4 (refs. 36 to 38).

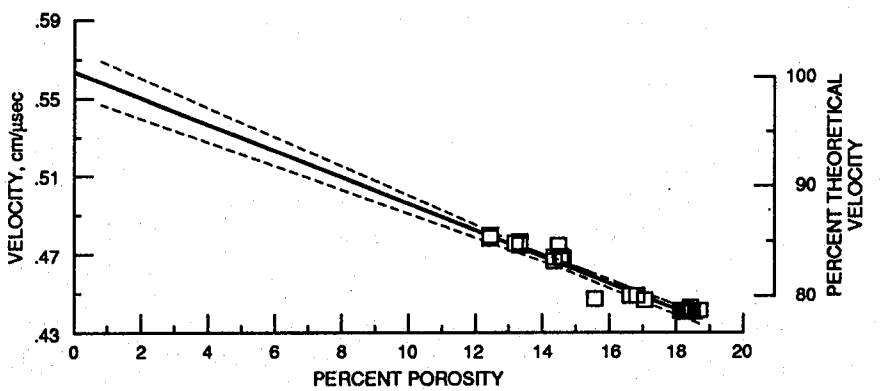

Figure 48. - Longitudinal velocity measured in the A direction versus percent porosity for steel (ref. 39).
Velocity = –0.007 x percent porosity + 0.563.
Percent theoretical velocity = –1.19 x percent porosity + 100.
Correlation coefficient = –0.972.

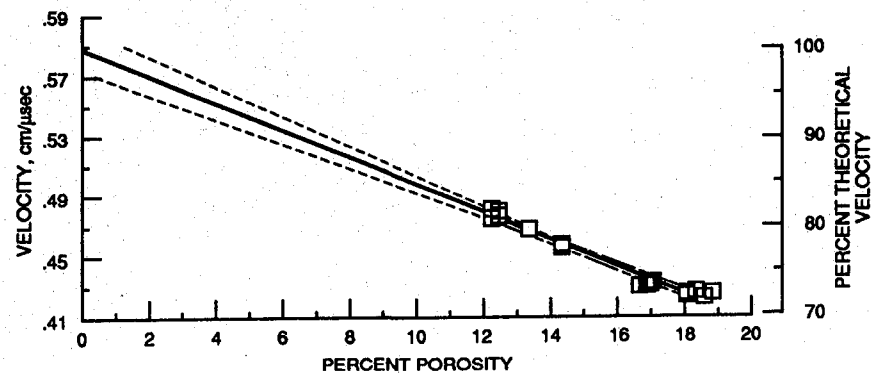

Figure 49. - Longitudinal velocity measured in the B direction versus percent porosity for steel (ref. 39).
Velocity = –0.009 x percent porosity + 0.588.
Percent theoretical velocity = –1.53 x percent porosity + 100.
Correlation coefficient = –0.985.

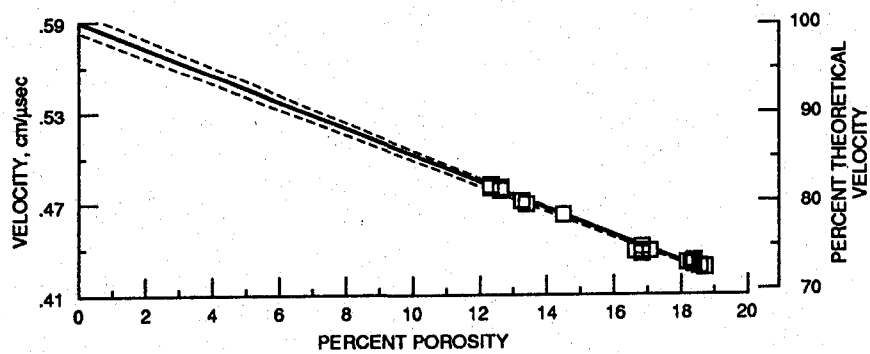

Figure 50. - Longitudinal velocity measured in the C direction versus percent porosity for steel (ref. 39).
Velocity = –0.009 x percent porosity + 0.590.
Percent theoretical velocity = –1.48 x percent porosity + 100.
Correlation coefficient = –0.996.

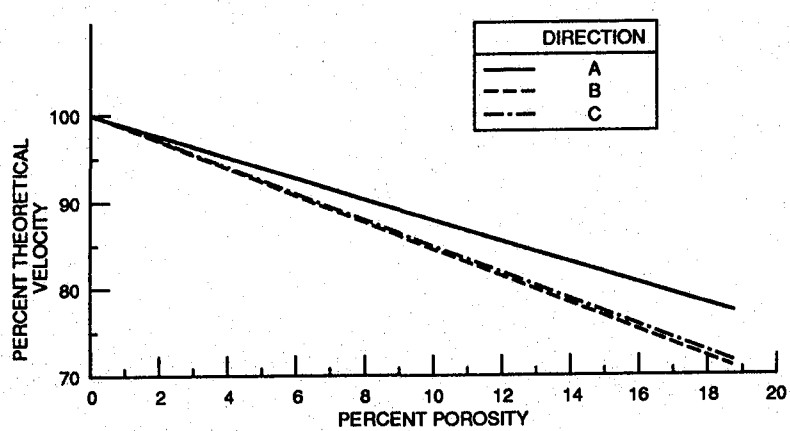

Figure 51. - Ultrasonic velocity versus percent porosity for steel (ref. 39).

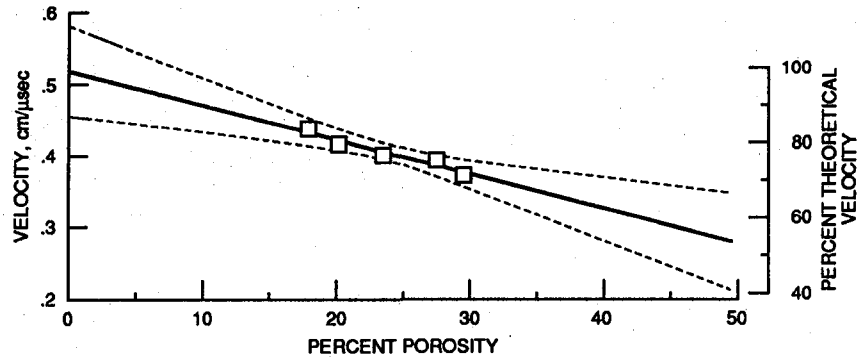

Figure 52. - Longitudinal velocity versus percent porosity for tungsten (ref. 2) with Kenna nominal 4 μm starting powder size.
Velocity = –0.005 x percent porosity + 0.520.
Percent theoretical velocity = –0.939 x percent porosity + 100.
Correlation coefficient = –0.960.

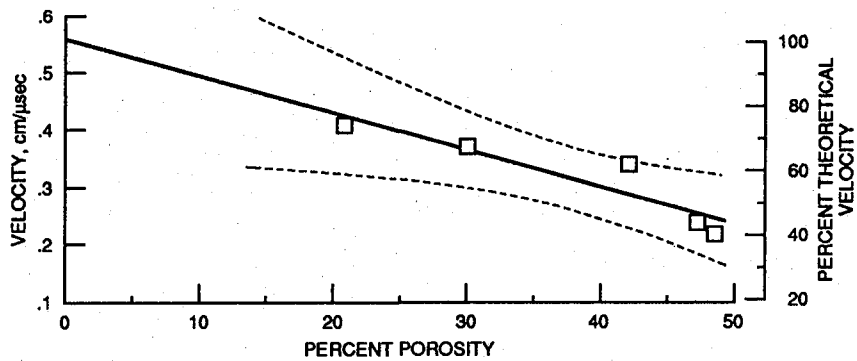

Figure 53. - Longitudinal velocity versus percent porosity for tungsten (ref. 2) with General Electric nominal 4 μm starting powder size.
Velocity = –0.006 x percent porosity + 0.558.
Percent theoretical velocity = –1.13 x percent porosity + 100.
Correlation coefficient = –0.918.

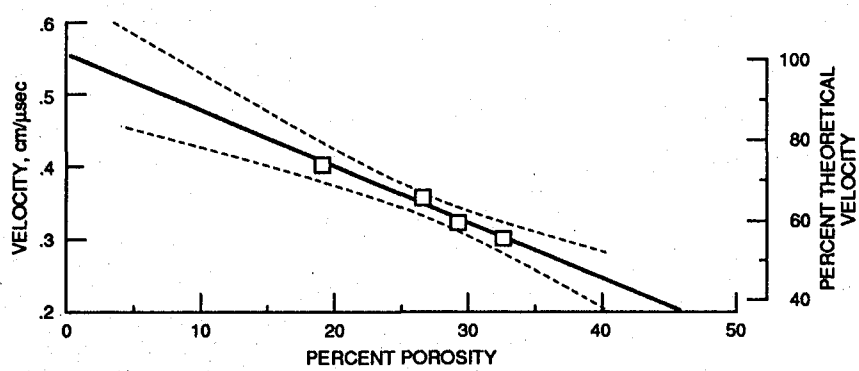

Figure 54. - Longitudinal velocity versus percent porosity for tungsten (ref. 2) with General Electric nominal 18 μm starting powder size.
Velocity = –0.008 x percent porosity + 0.554.
Percent theoretical velocity = –1.38 x percent porosity + 100.
Correlation coefficient = –0.992.

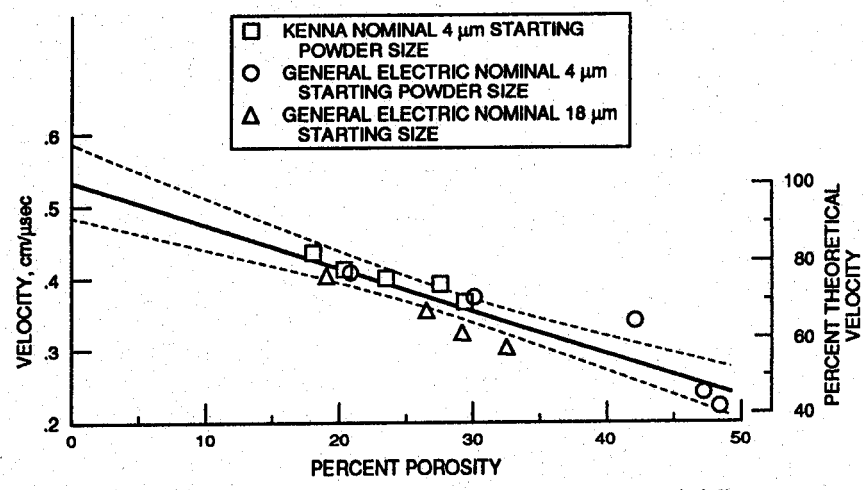

Figure 55. - Longitudinal velocity versus percent porosity for tungsten (ref. 2).
Velocity = –0.006 x percent porosity + 0.533.
Percent theoretical velocity = –1.11 x percent porosity + 100.
Correlation coefficient = –0.916.

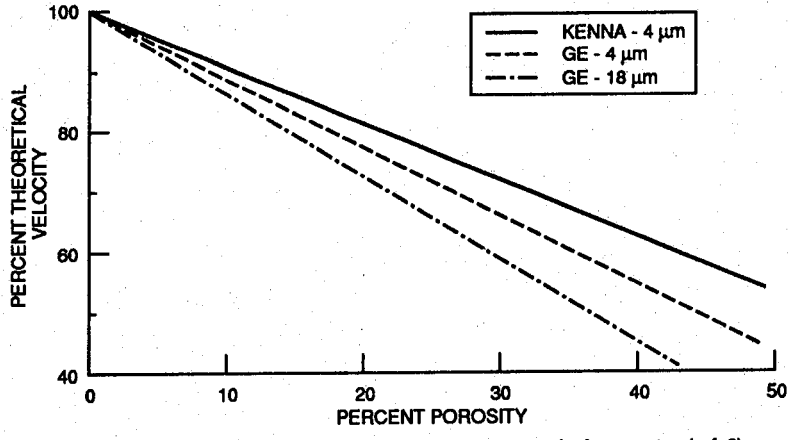

Figure 56. - Longitudinal velocity versus percent porosity for tungsten (ref. 2).

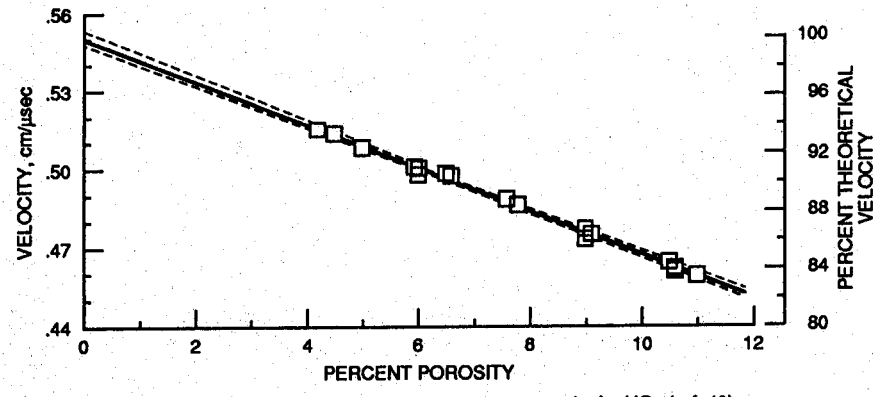

Figure 57. - Longitudinal velocity versus percent porosity for UO_2 (ref. 40).
Velocity = –0.008 x percent porosity + 0.550.
Percent theoretical velocity = –1.49 x percent porosity + 100.
Correlation coefficient = –0.997.

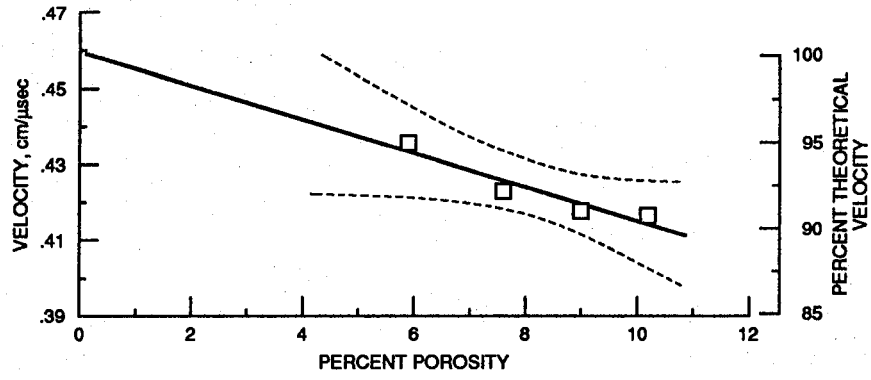

Figure 58. - Longitudinal velocity versus percent porosity for $(U_{0.30}Pu_{0.70})C$ (ref. 41).
Velocity = –0.004 x percent porosity + 0.460.
Percent theoretical velocity = –0.958 x percent porosity + 100.
Correlation coefficient = –0.949.

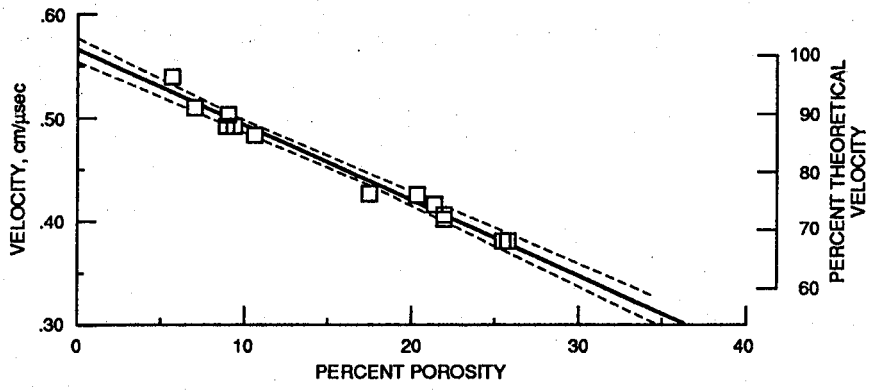

Figure 59. - Longitudinal velocity versus percent porosity for $YBa_2Cu_3O_{7-x}$ (ref. 43).
Velocity = –0.007 x percent porosity + 0.565.
Percent theoretical velocity = –1.28 x percent porosity + 100.
Correlation coefficient = –0.991.

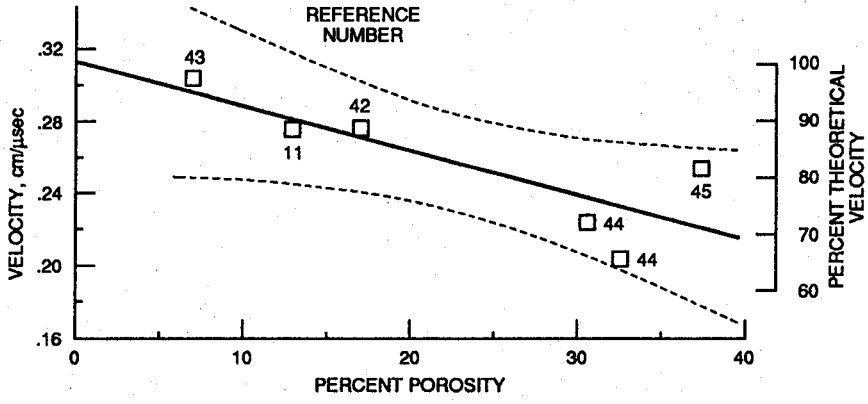

Figure 60. - Shear velocity versus percent porosity for $YBa_2Cu_3O_{7-x}$ (refs. 11, 42 to 45).
Velocity = –0.002 x percent porosity + 0.313.
Percent theoretical velocity = –0.768 x percent porosity + 100.
Correlation coefficient = –0.814.

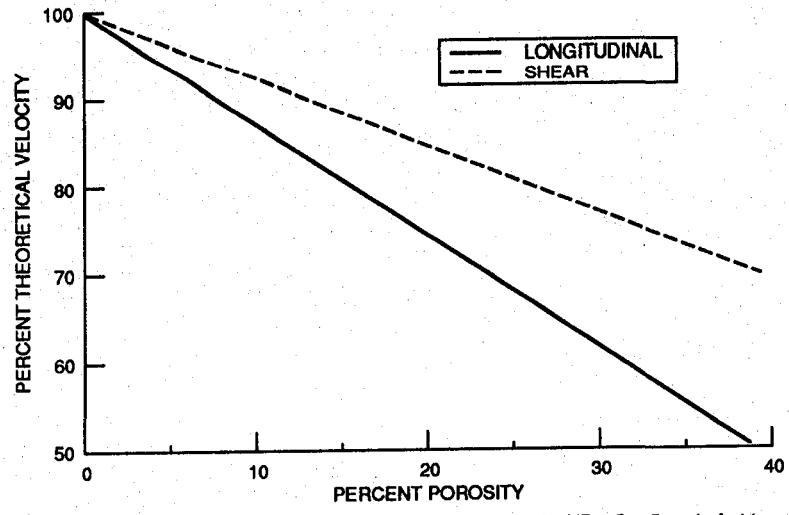

Figure 61. - Ultrasonic velocity versus percent porosity for $YBa_2Cu_3O_{7-x}$ (refs 11, 42 to 45).

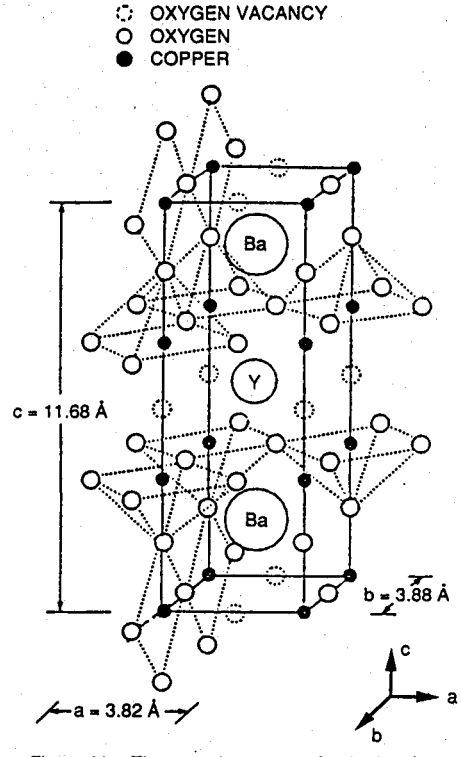

Figure 62. - The crystal structure of orthorhombic $YBa_2Cu_3O_{7-x}$.

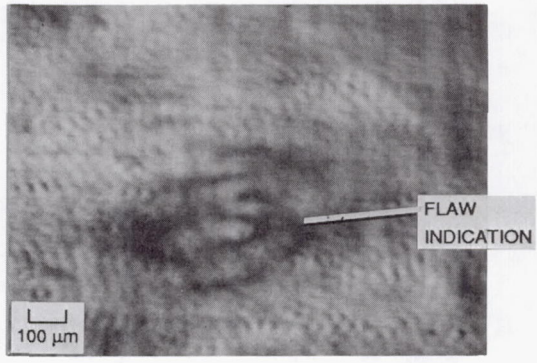

(a) Scanning laser acoustic micrograph of sub-surface flaw in sintered silicon carbide (Roth, et al., 1987).

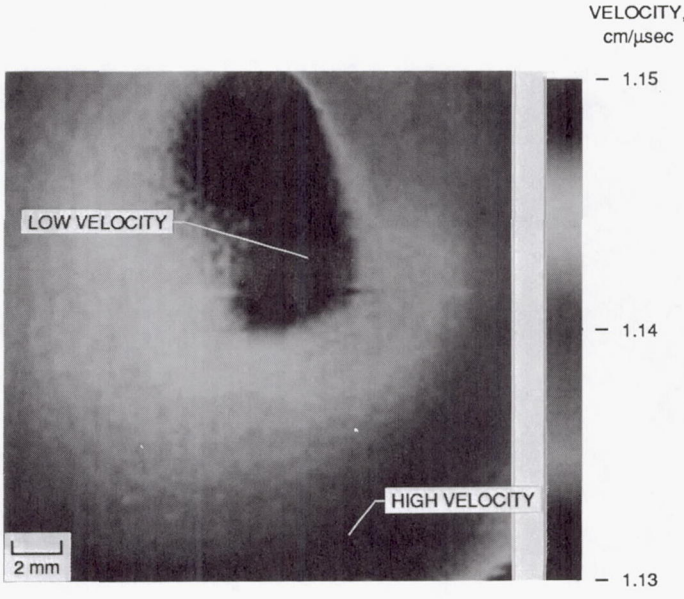

(b) Ultrasonic velocity image of region of sintered silicon carbide specimen (Generazio, et al., 1989).

Figure 63. - Discrete flaw characterization and global microstructure characterization with ultrasonic NDE techniques

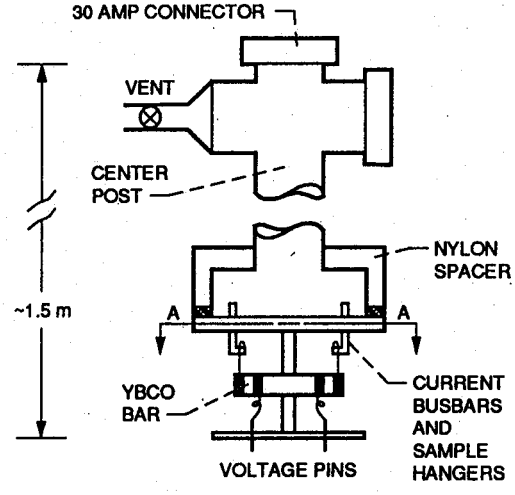

(a) Overall assembly.

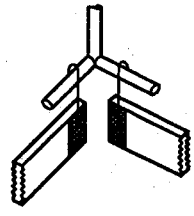

(b) Hanger detail.

Figure 64. - Probe used to make J_c measurements.

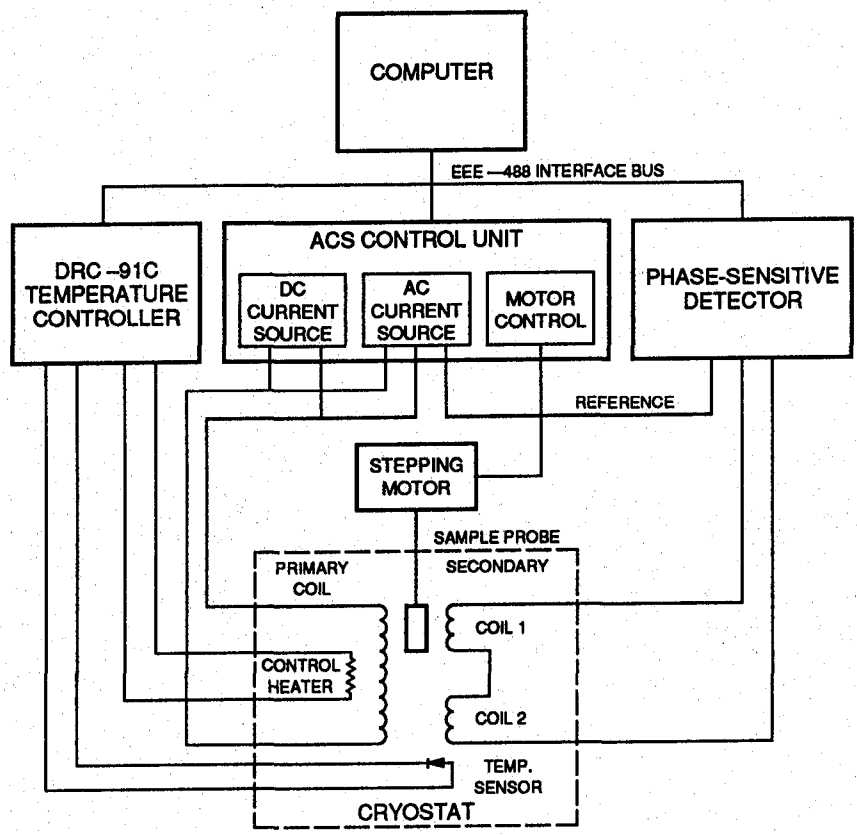

(a) Schematic of Lake Shore Cryotronics Model 7000 susceptometer.

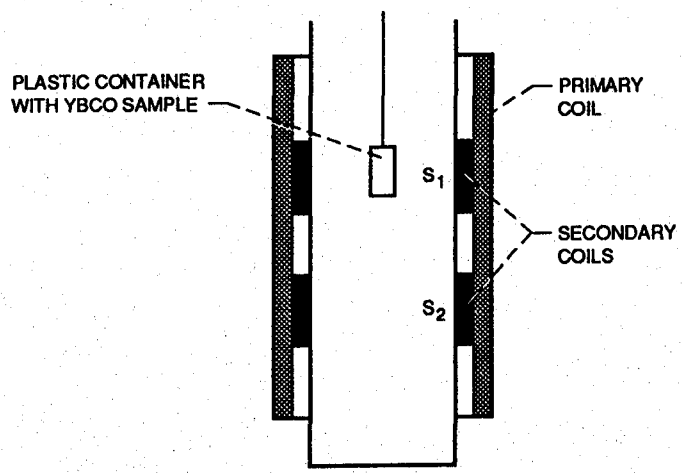

(b) Cross-sectional view of the sample/coil assembly.

Figure 65. - Instrumentation and set-up for a.c. susceptibility measurements.

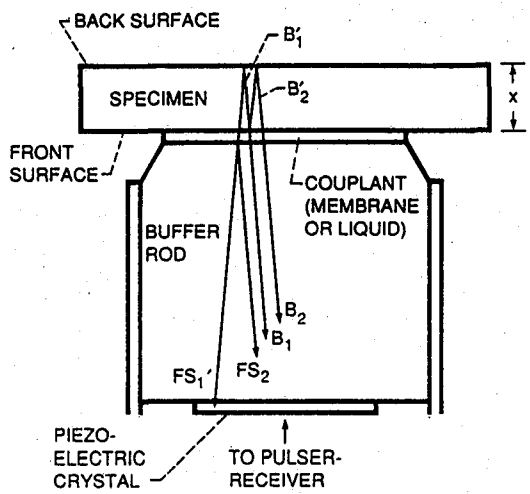

(a) Diagram of transducer/specimen configuration for pulse-echo ultrasonics.

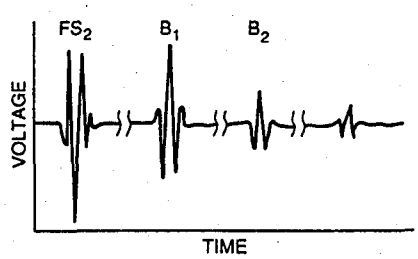

(b) Resulting waveforms.

Figure 66. - Pulse-echo contact technique.

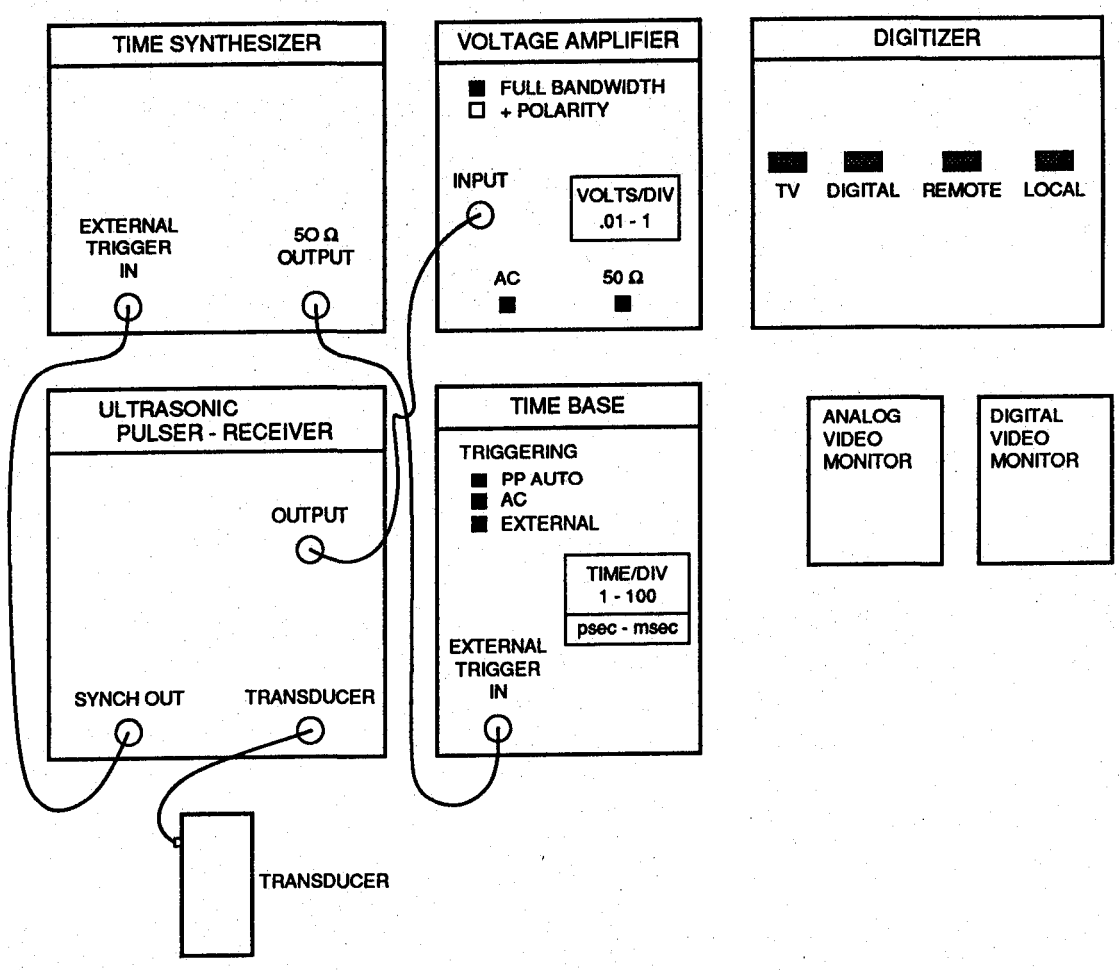

(a) Front.

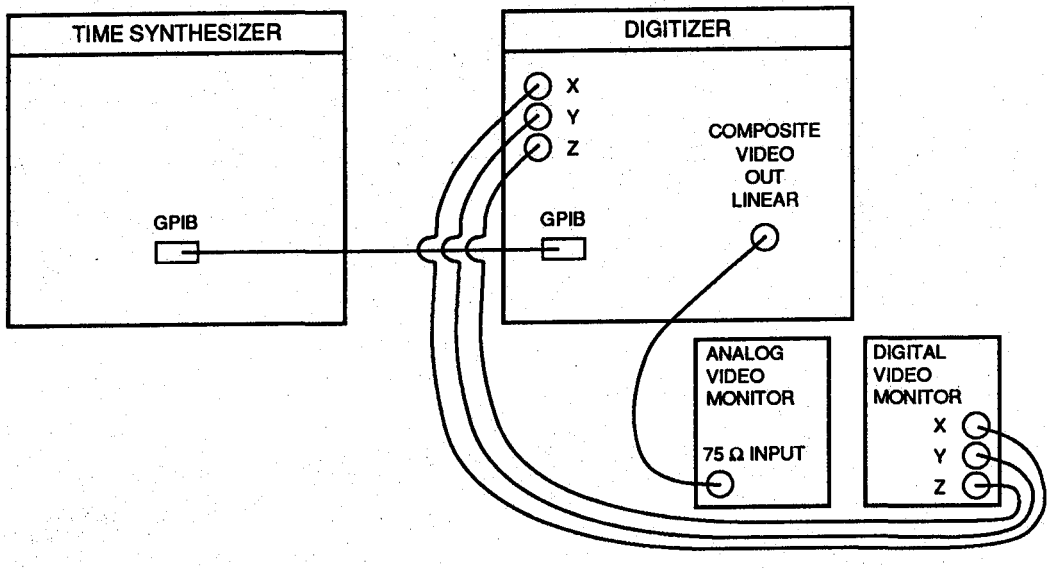

(b) Back.

Figure 67. - Instrumentation for ultrasonic measurements.

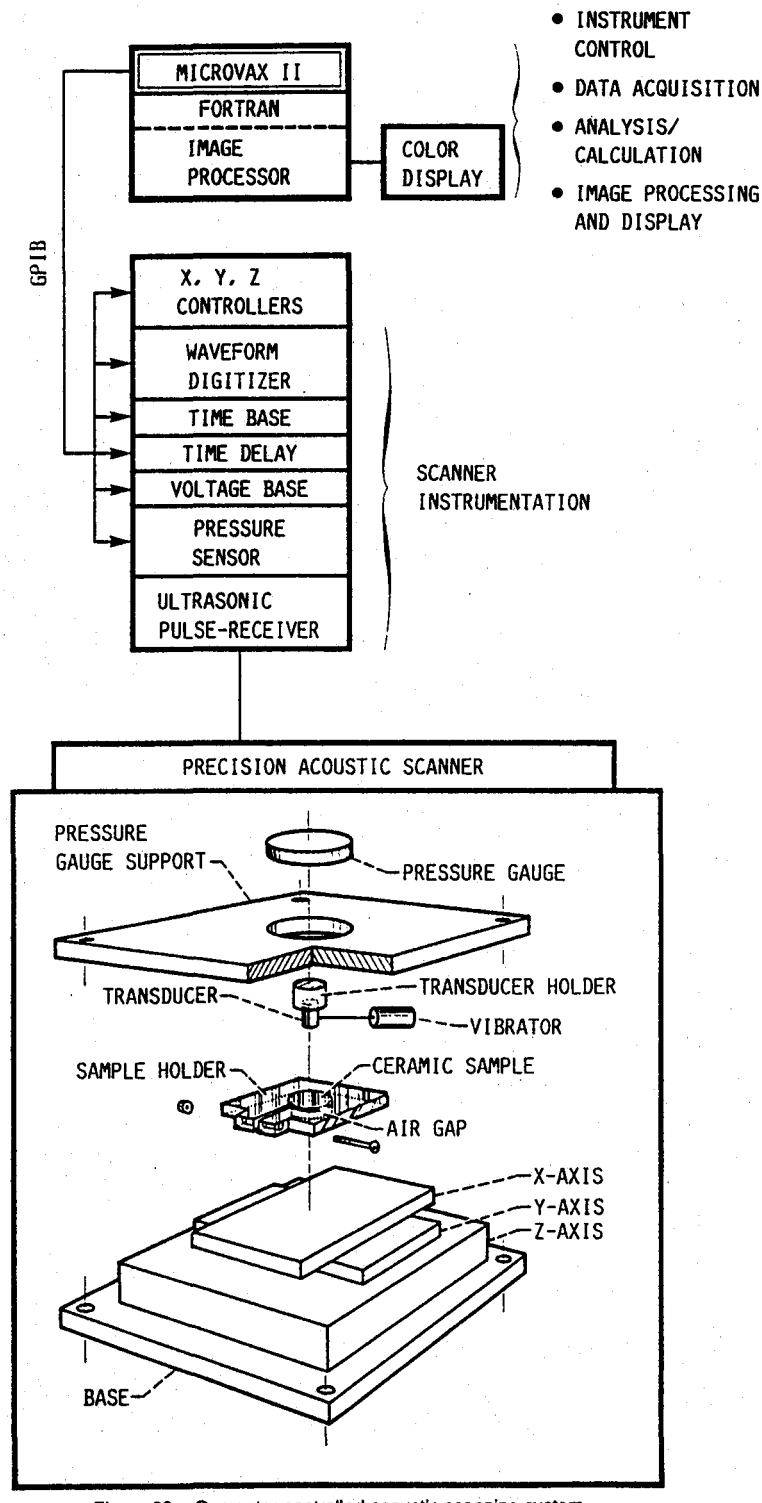

Figure 68. - Computer-controlled acoustic scanning system.

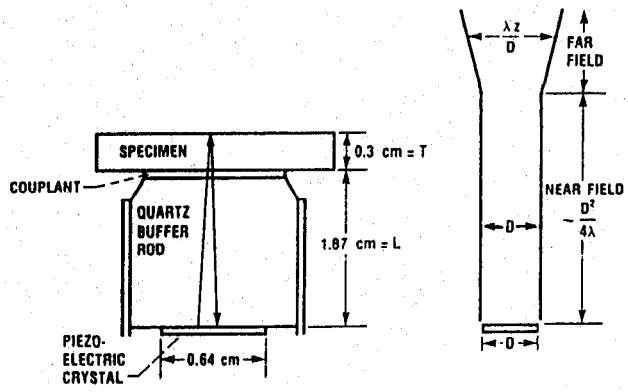

CD-90-45493

- BEAM DIAMETER IS DEPENDENT ON WHETHER WE ARE IN NEAR FIELD OR FAR FIELD
- FOR f = 20 MHz, WITH YBCO, NEAR FIELD ~ $\frac{D^2}{4\lambda} \sim \frac{D^2 \cdot f}{4c}$ ~ 4 cm
- ULTRASOUND PATH LENGTH ~ [2(T + L)] ~ 4 cm

$\therefore$ BEAM DIAMETER ~ D

Figure 69. - Pulse-echo configuration showing estimation of beam diameter (0 - –20 dB).
D = Active transducer diameter.
f = Frequency of ultrasonic transducer.
λ = Wavelength of ultrasound.
c = Velocity of ultrasound.
T = Specimen thickness.
L = Buffer rod length.

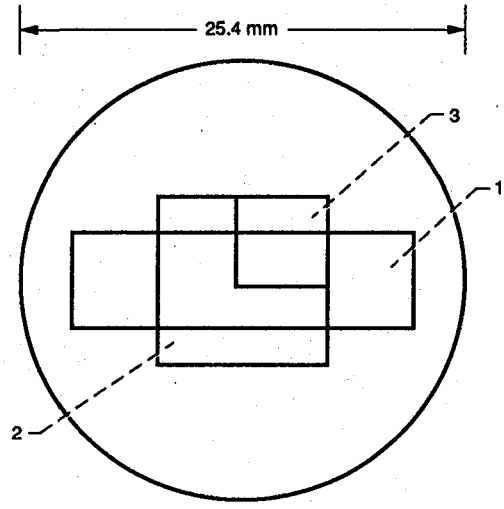

Figure 70. - Top view of sample 46B showing regions that were ultrasonically scanned.

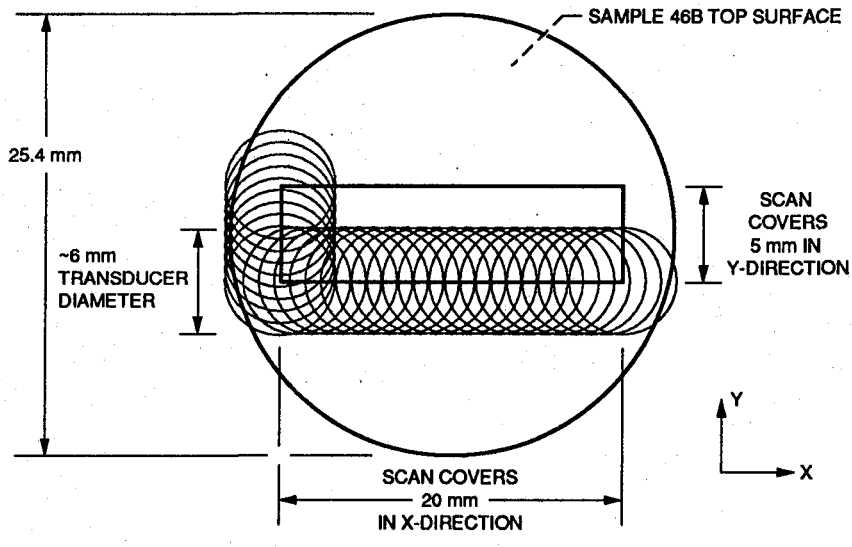

Figure 71. - Schematic of ultrasonic scan for region of sample 46B. 20 mm (x-direction) by 5 mm (y-direction) scan with 1-mm transducer increments. Transducer positions shown for x = 1 – 21, y = 0, and x = 0, y = 1 – 6. In total, there are 21 transducer positions along x-axis and 6 transducer positions along y-axis to give 126 measurements in scan.

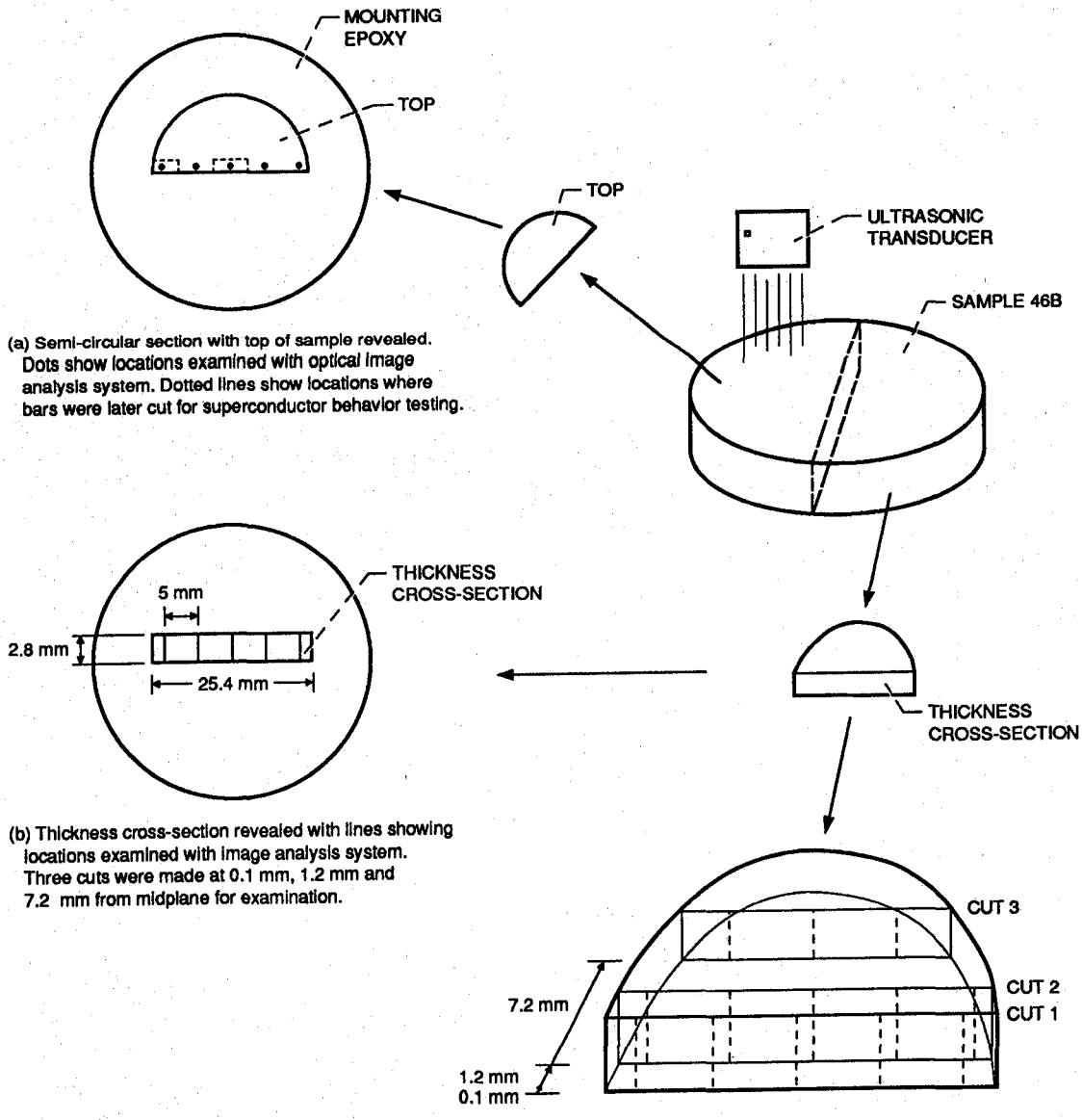

(a) Semi-circular section with top of sample revealed. Dots show locations examined with optical image analysis system. Dotted lines show locations where bars were later cut for superconductor behavior testing.

(b) Thickness cross-section revealed with lines showing locations examined with image analysis system. Three cuts were made at 0.1 mm, 1.2 mm and 7.2 mm from midplane for examination.

Figure 72. - Sections cut from sample 46B for optical examination.

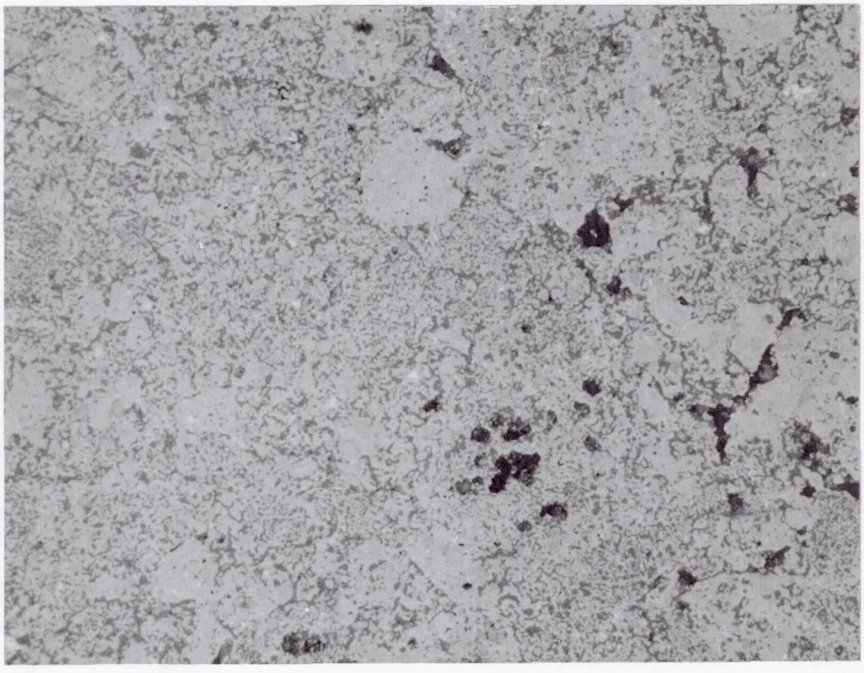

(a) Center-cut bar.

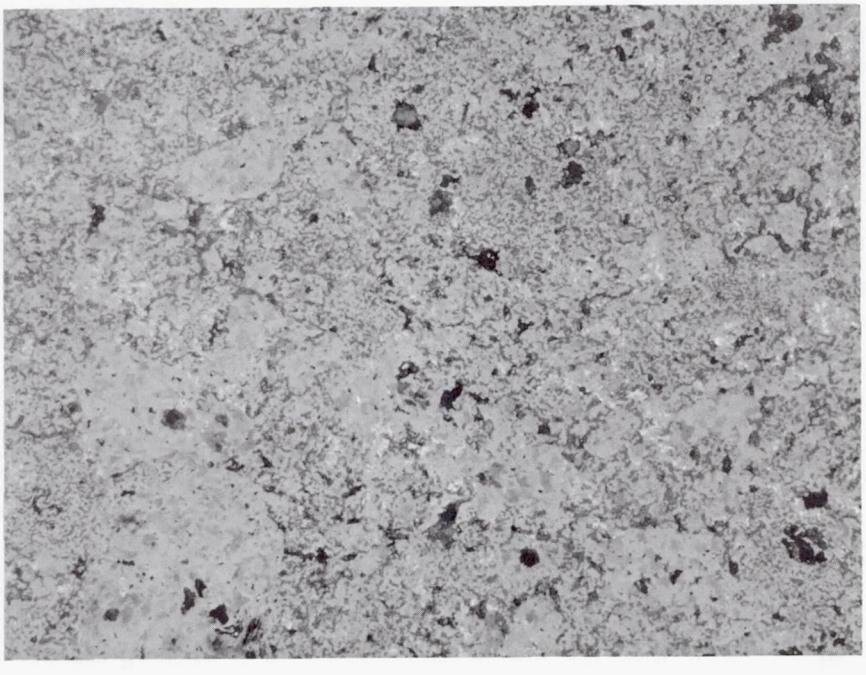

(b) Edge-cut bar.

Figure 73. - Optical micrographs of porosity distribution for bars cut from sample 52A.

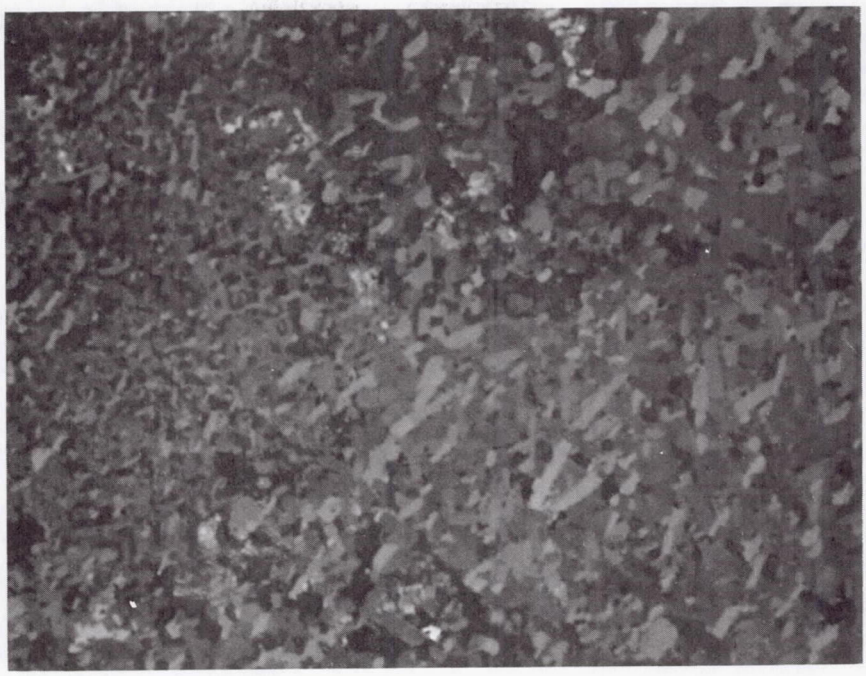

10 μm

(a) Center-cut bar.

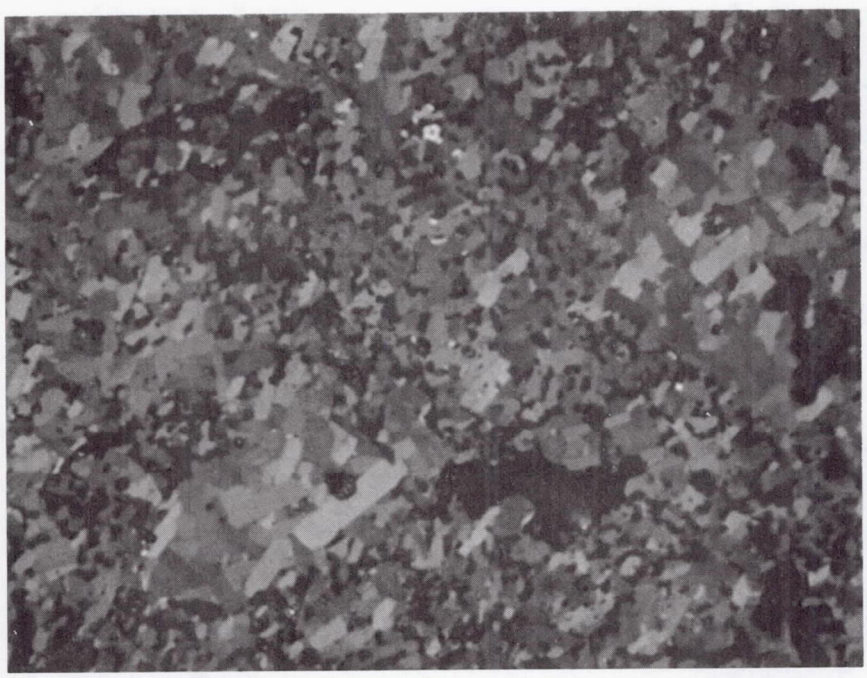

10 μm

(b) Edge-cut bar.

Figure 74. - Optical micrographs of grain distribution for bars cut from sample 52A. Polarized light.

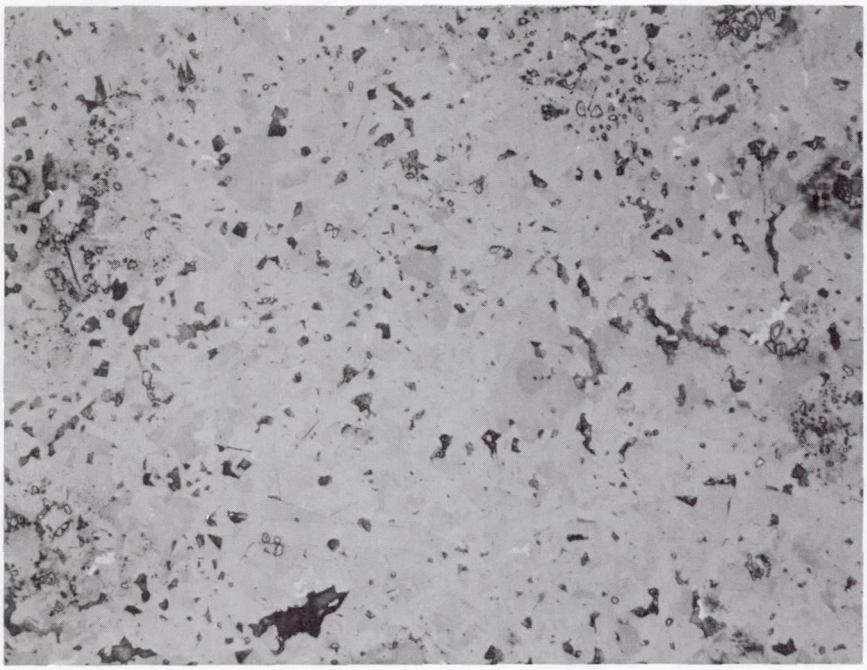

50 μm

(a) Center-cut bar.

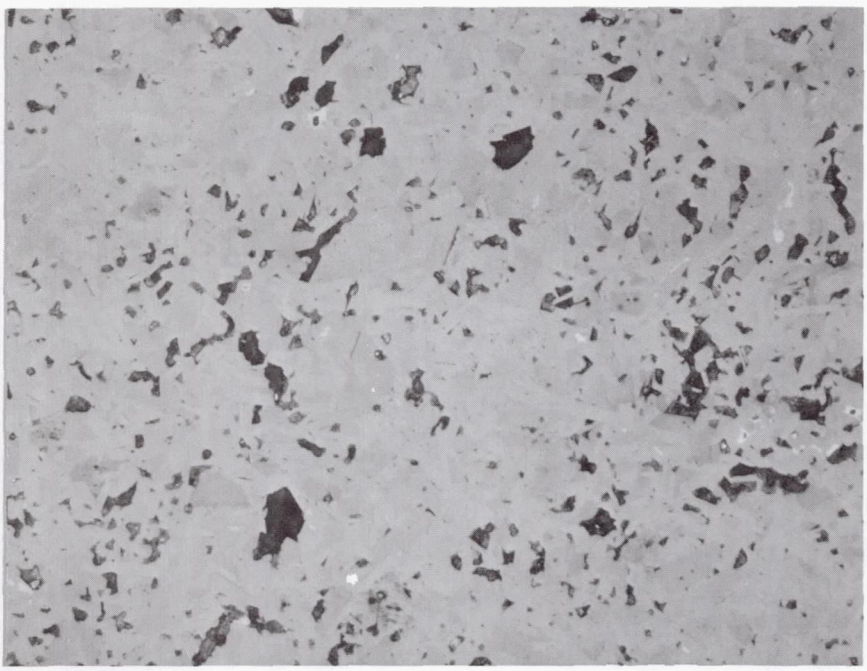

50 μm

(b) Edge-cut bar.

Figure 75. - Optical micrographs of porosity distribution for bars cut from sample 60A.

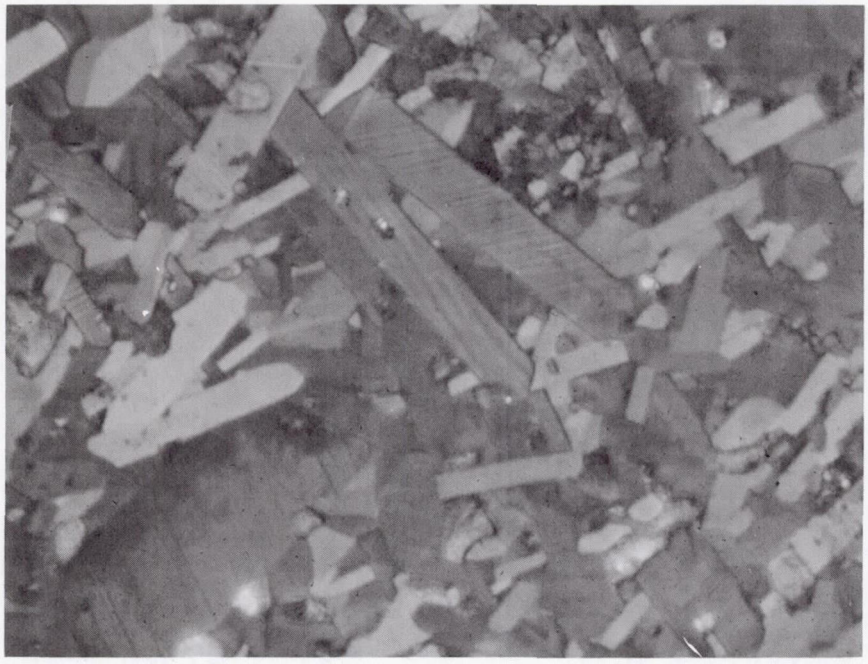

10 μm

(a) Center-cut bar.

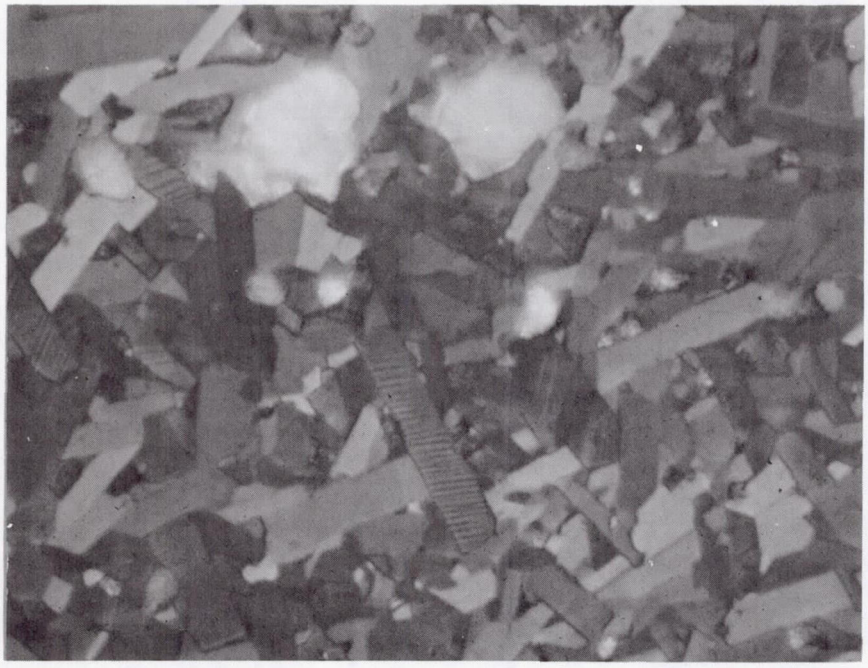

10 μm

(b) Edge-cut bar.

Figure 76. - Optical micrographs of grain distribution for bars cut from sample 60A. Polarized light.

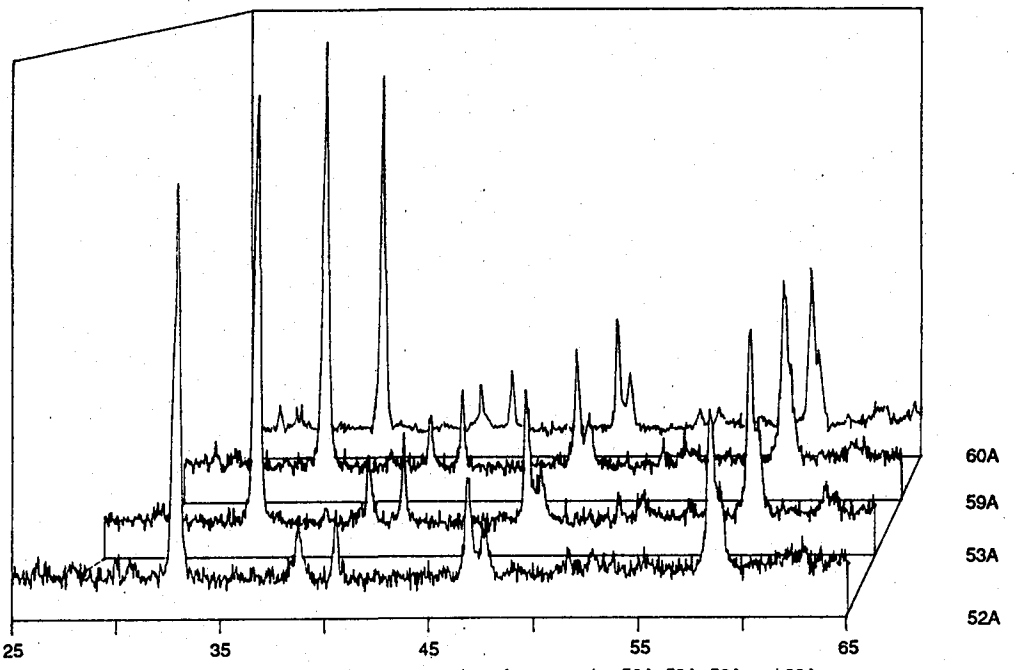

Figure 77. - X-ray diffraction patterns for center-cut bars from samples 52A, 53A, 59A and 60A.

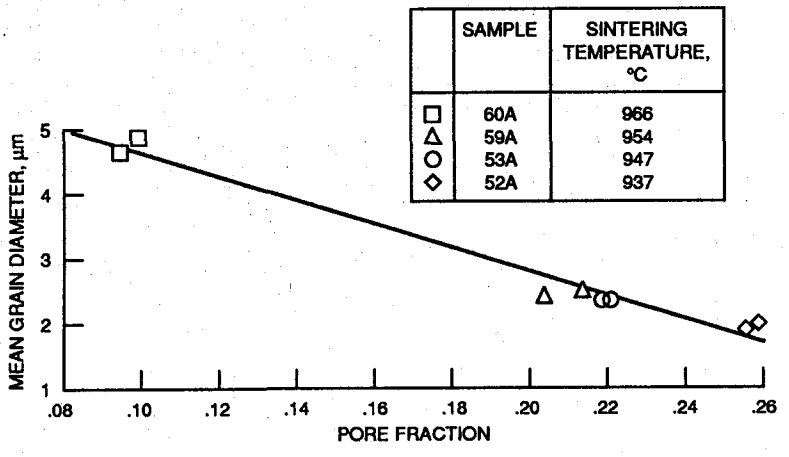

Figure 78. - Mean grain diameter versus pore fraction for bars cut from samples 52A, 53A, 59A, and 60A.
Estimated uncertainty in grain diameter is approximately ±20 percent.
At least 100 grains sampled for each bar using Heyn-intercept method.
Estimated uncertainty in pore fraction is ≤ 0.5 percent.

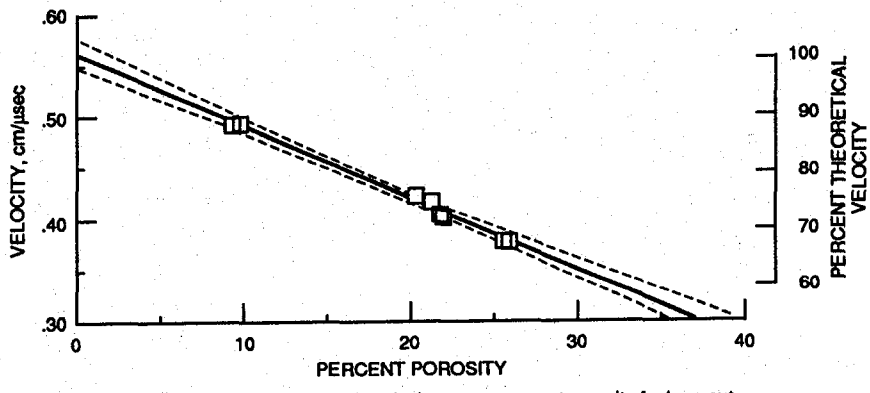

Figure 79. - Longitudinal ultrasonic velocity versus percent porosity for bars cut from samples 52A, 53A, 59A and 60A.
Center frequency = 10 MHz.
Velocity (cm/μsec) = −0.007 x percent porosity + 0.560.
Percent theoretical velocity = −1.23 x percent porosity + 100.
Correlation coefficient = −0.994.
Dashed lines enclose 95 percent confidence interval for mean predicted velocity values.

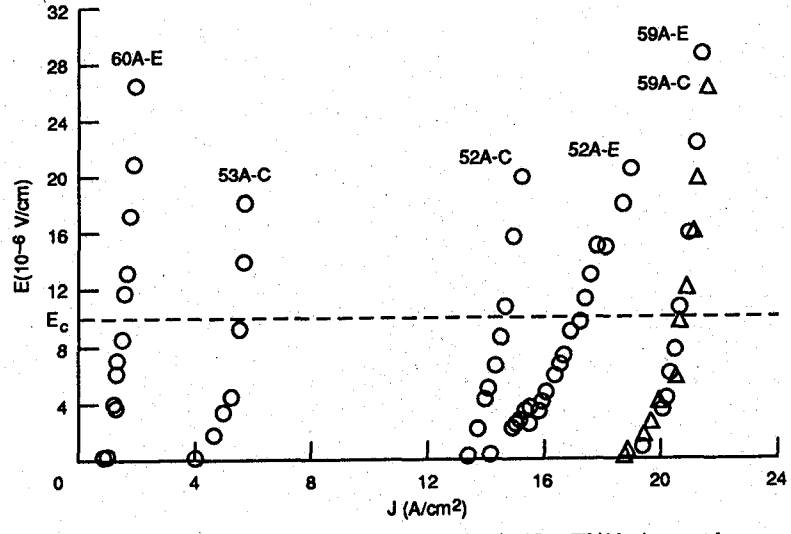

Figure 80. - Electric field (E) versus current density (J) at 77 K for bars cut from samples 52A, 53A, 59A and 60A. Experimental uncertainty in J_c estimated at approximately ±10 percent. The reproducibility of the voltage-current characteristic was obtained from several successive measurements.

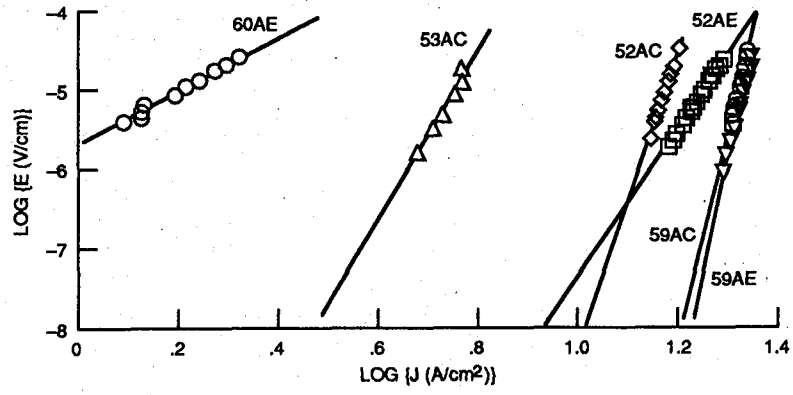

Figure 81. - Log E versus log J at 77 K for bars cut from samples 52A, 53A, 59A and 60A. From $E = kJ^n$; log E = log k + (n)log J and slope of plot is n–value. Values excluded where $E < 10^{-7}$ V/cm since this was in noise range of measuring system.

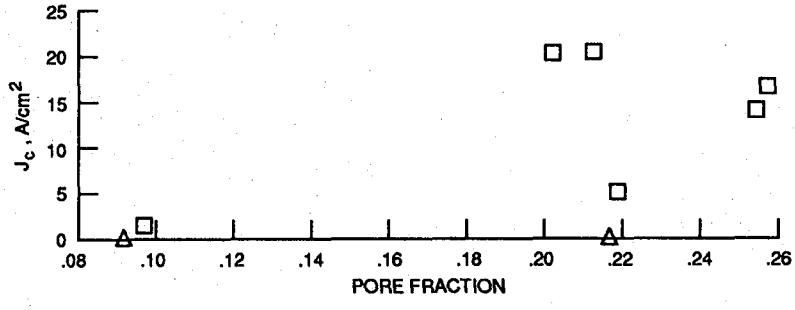

Figure 82. - J_c at 77 K versus pore fraction for bars cut from samples 52A, 53A, 59A and 60A. For $J_c = 0$ (shown as Δ), one current lead popped off, thought to be due to local heating at that end of sample.

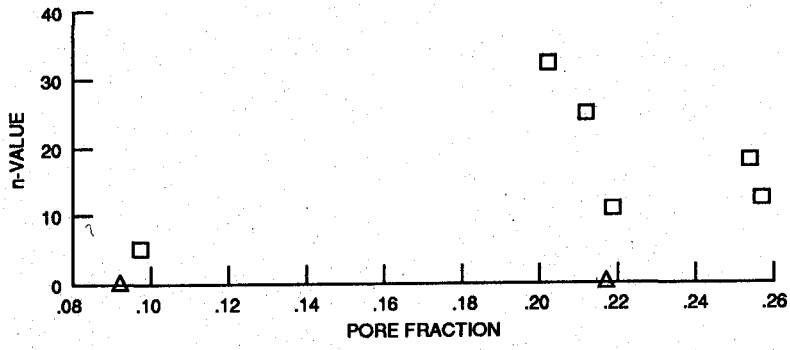

Figure 83. - n-value at 77 K versus pore fraction for bars cut from samples 52A, 53A, 59A and 60A. n-value from regression fit of $E = kJ^n$. n-value = 0 (shown as △) indicates no critical current obtained for bar.

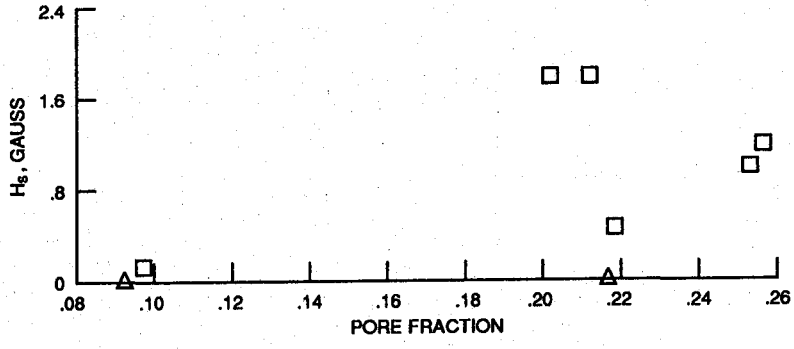

Figure 84. - Generated self-field (H_s) at 77 K for bars cut from samples 52A, 53A, 59A and 60A. $H_s = 0$ (shown as △) indicates no critical current obtained for bar.

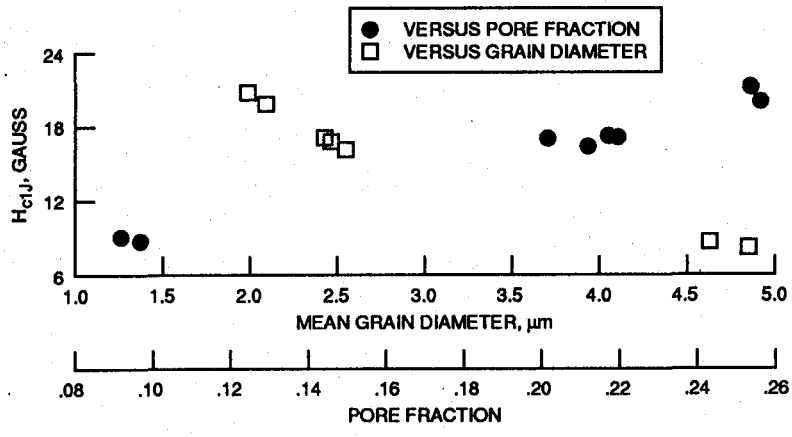

Figure 85. - Expected Josephson lower critical field (H_{c1J}) at 77 K versus grain diameter and pore fraction for bars cut from samples 52A, 53A, 59A and 60A. H_{c1J} is inversely proportional to grain size (and thus directly proportional to pore fraction for our samples). (Equation (23)).

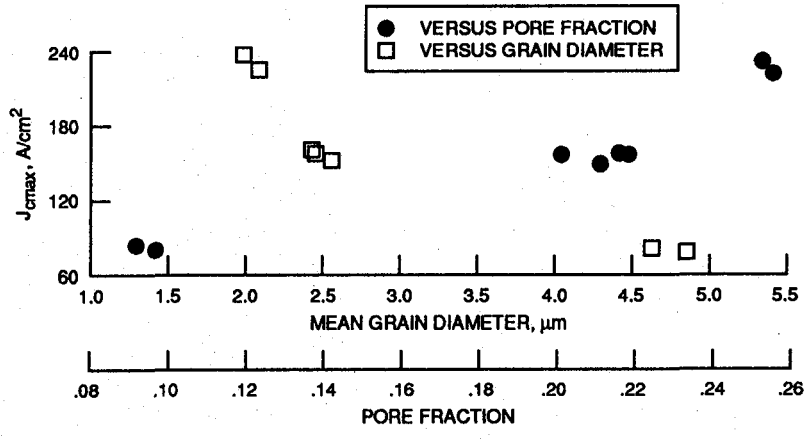

Figure 86. - Expected J_{cmax} at 77 K versus grain diameter and pore fraction for bars cut from samples 52A, 53A, 59A and 60A. Sample cross-section dimensions were approximately the same. Expected J_{cmax} is inversely proportional to grain size (and thus directly proportional to pore fraction for our samples). (Equation (28), approximating $H_{1/2}$ by H_{c1J} (equation (23)) with $\lambda = 0.25$ μm).

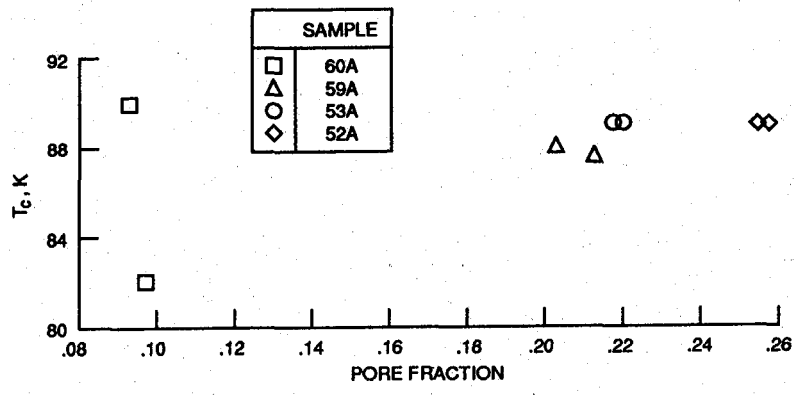

Figure 87. - Superconducting transition temperature (T_c) versus pore fraction for bars cut from samples 52A, 53A, 59A and 60A. T_c determined at the onset temperature in the magnetic transition (χ' susceptibility response).

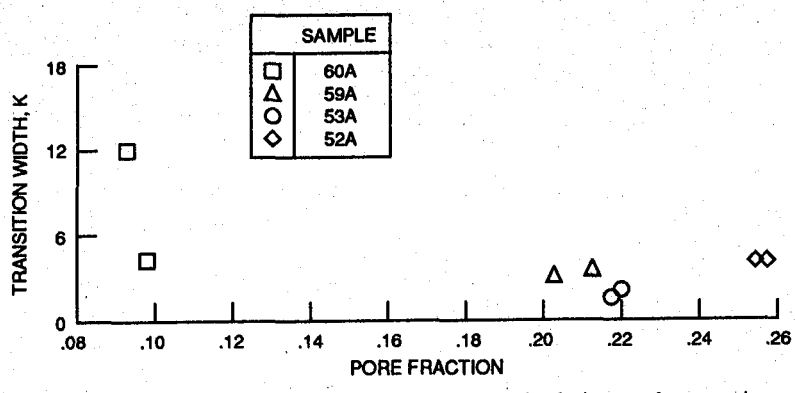

Figure 88. - Magnetic transition width versus pore fraction for bars cut from samples 52A, 53A, 59A and 60A. Transition width defined as the difference in temperature for which 10 and 90 percent of complete shielding was achieved in χ' susceptibility response.

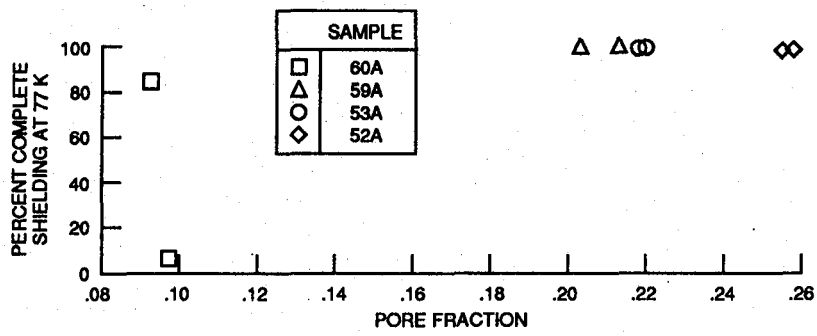

Figure 89. - Percent complete shielding versus pore fraction at 77 K for bars cut from samples 52A, 53A, 59A and 60A. Obtained from χ' susceptibility response.

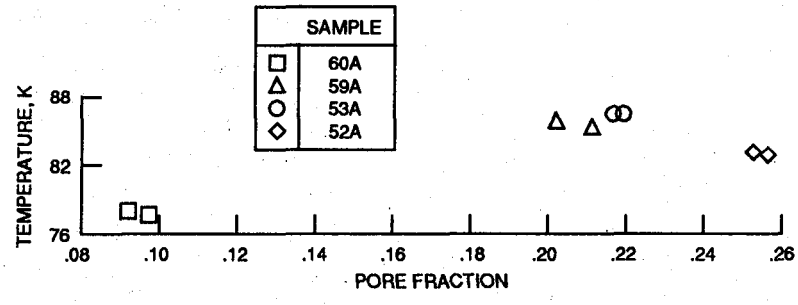

Figure 90. - Loss peak center temperature obtained from χ'' susceptibility response versus pore fraction for bars cut from samples 52A, 53A, 59A and 60A. This is the temperature where the intergranular critical current density (J_{cJ}) is calculated.

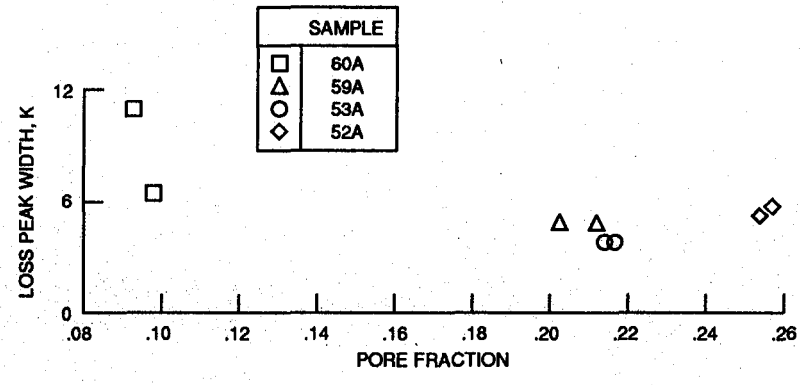

Figure 91. - Width of loss peak obtained from χ'' susceptibility response versus pore fraction for bars cut from samples 52A, 53A, 59A and 60A.

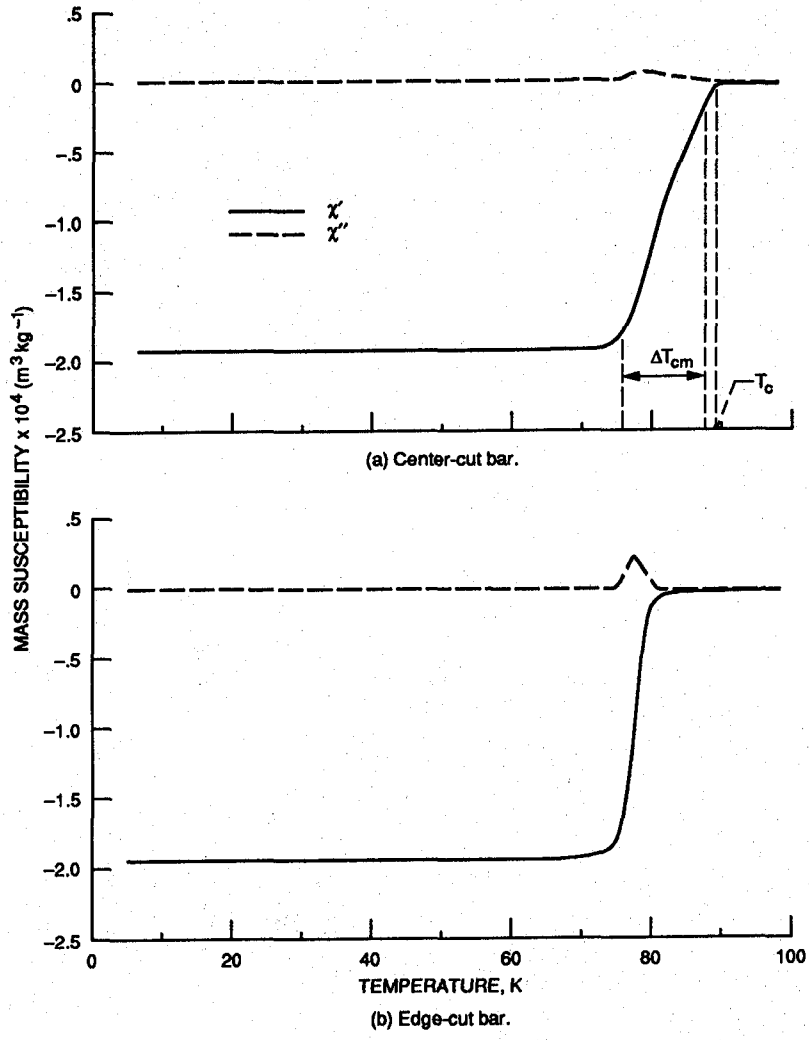

Figure 92. - A.c. susceptibility versus temperature for bars cut from sample 60A. H_{ac} = 0.02 Oe. Frequency = 100 Hz.

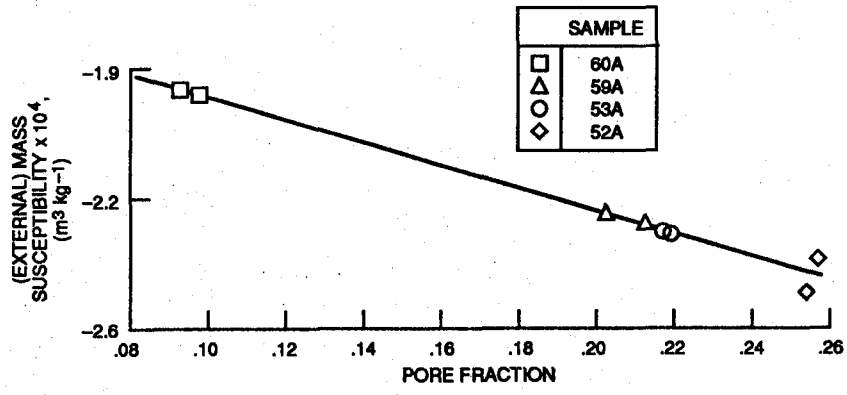

Figure 93. - External mass susceptibility (X') at 4.2 K versus pore fraction for bars cut from samples 52A, 53A, 59A and 60A.

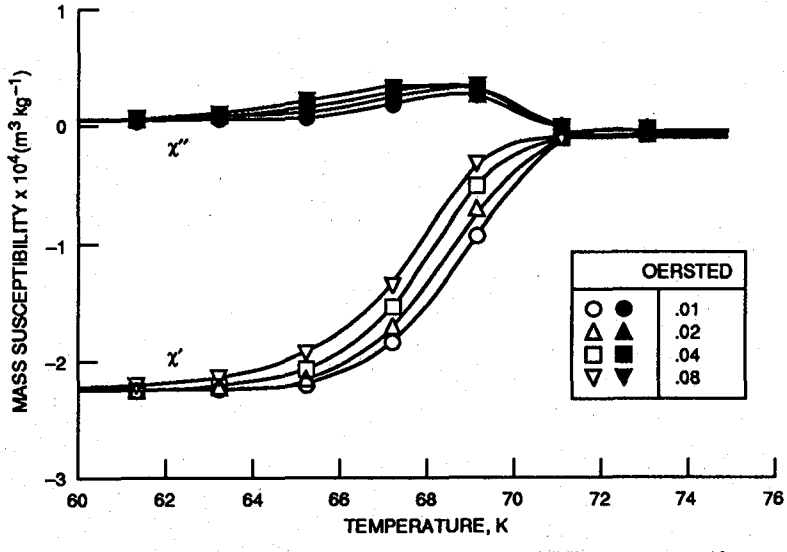

Figure 94. - Field (H_{ac}) dependence of the a.c. susceptibility measurement for a center-cut bar from sample 46B, frequency = 100 Hz.

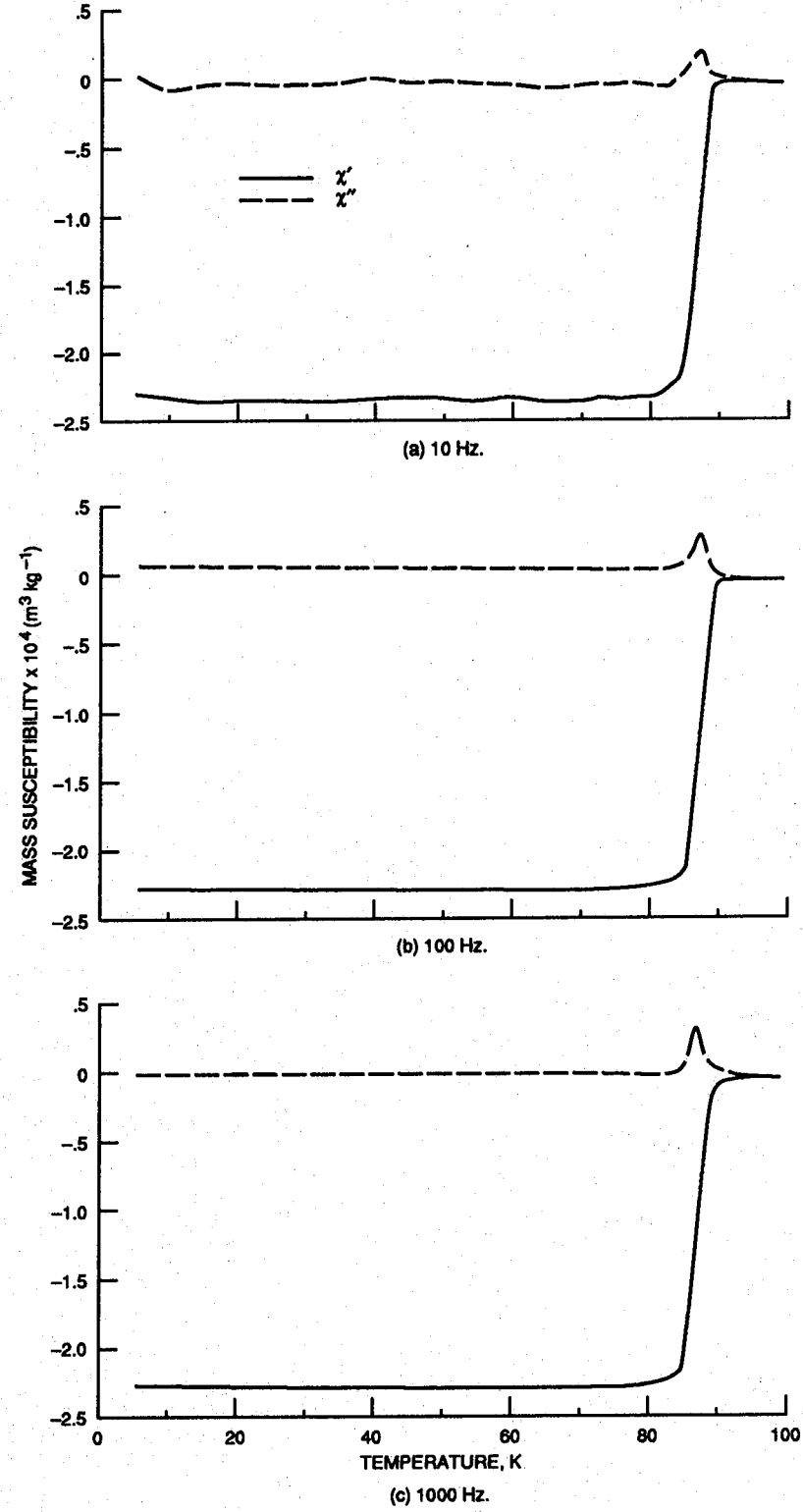

Figure 95. - Frequency dependence of the a.c. susceptibility for a bar cut from sample 52A. H_{ac} = 0.02 Oe.

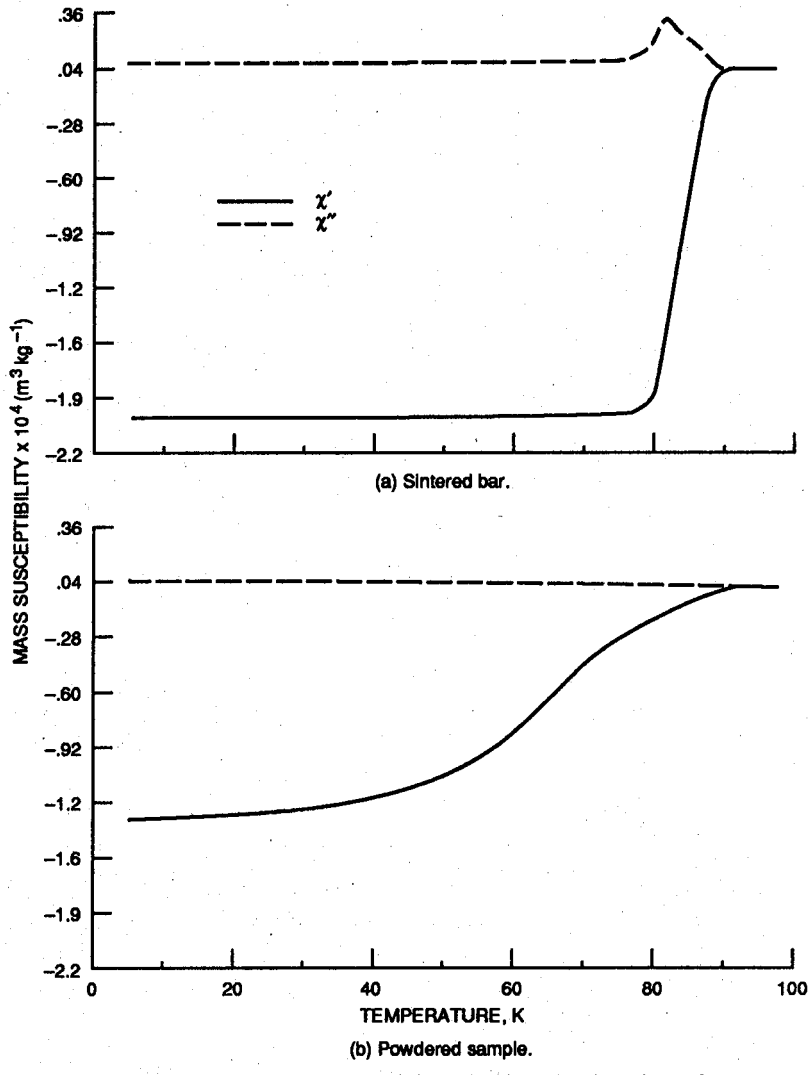

Figure 96. - A.c. susceptibility of sintered and powdered specimens from sample 51A. H_{ac} = 0.02 Oe. Frequency = 100 Hz. Note disappearance of loss peak in χ'' response for powdered sample.

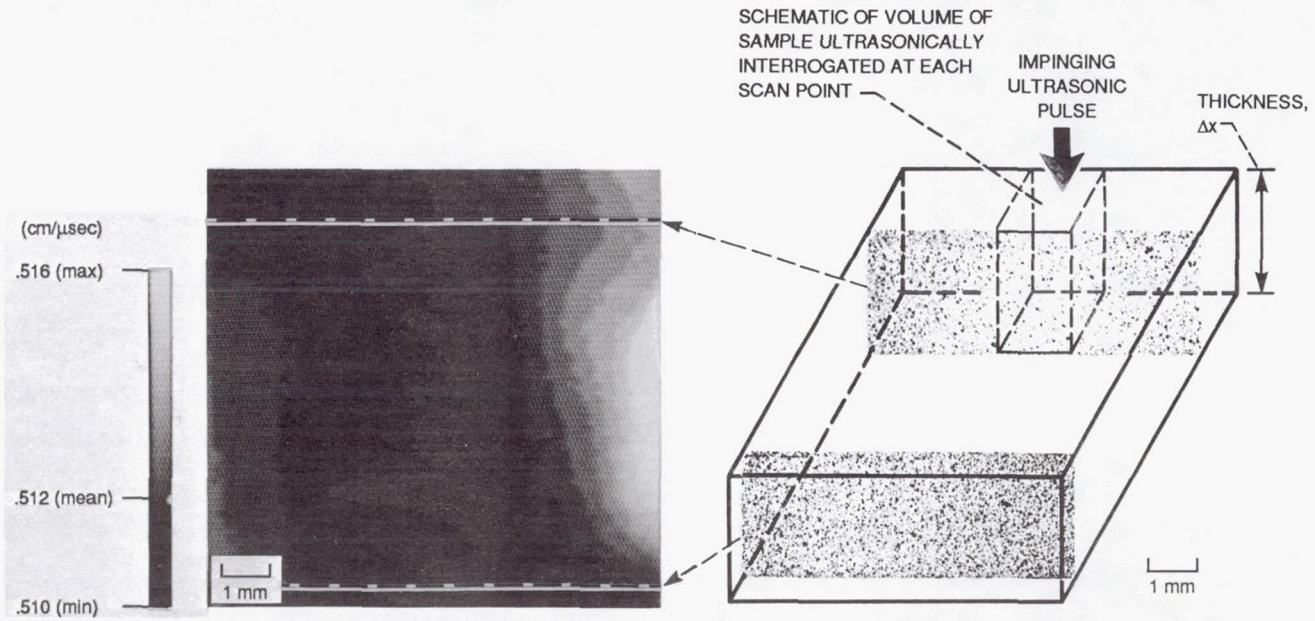

(a) Velocity image constructed from scan data obtained over 8 mm by 8 mm region of the sample. 20 MHz center frequency.

(b) Optical micrographs of thickness cross-sections from sample.

Figure 97. - Ultrasonic velocity image showing variations present in the scanned region of sample 99. Dashed arrows point from thickness cross-sections to corresponding horizontal location within velocity image.

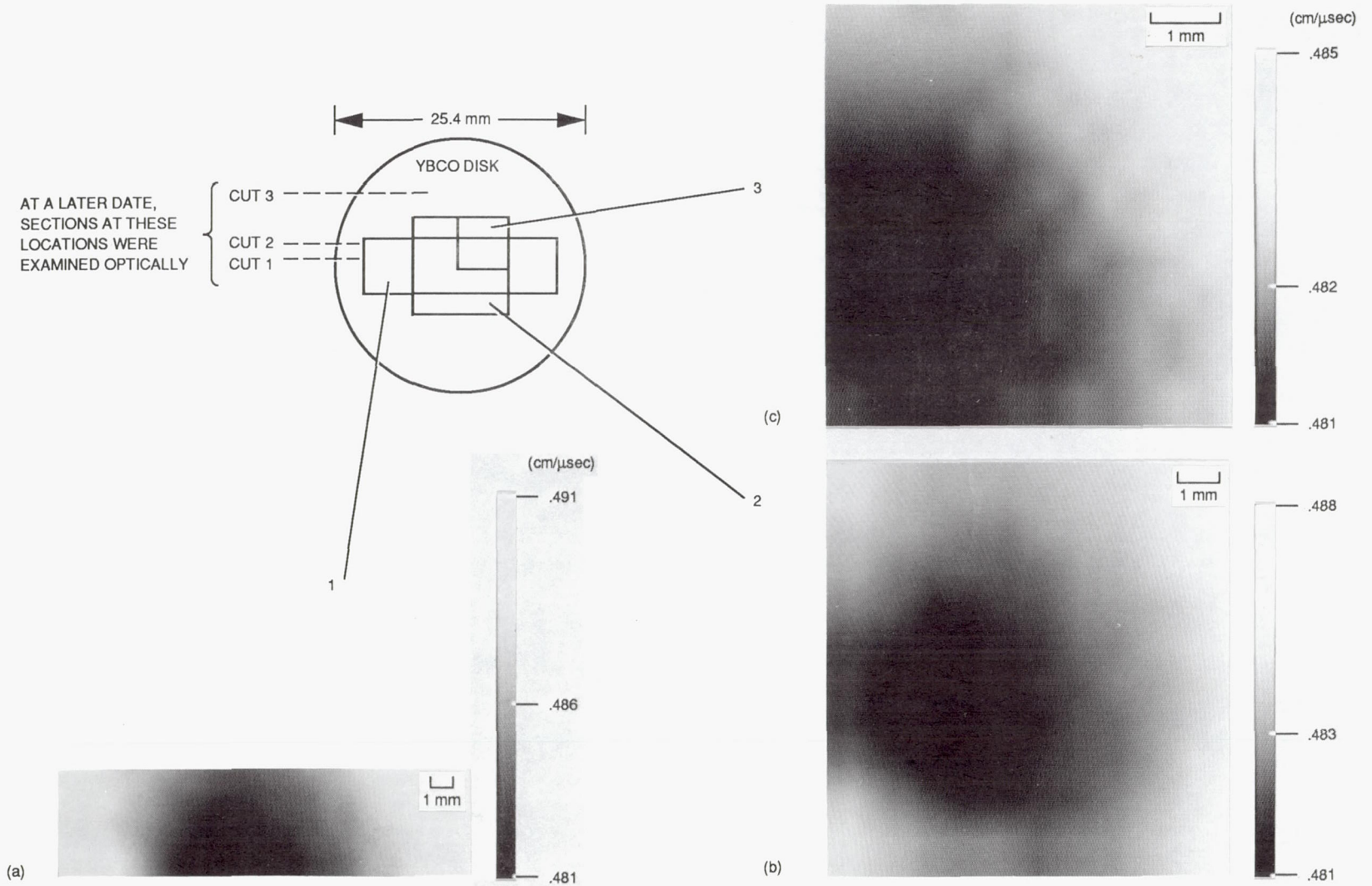

Figure 98. - Velocity images constructed from ultrasonic scans over the regions of sample 46B indicated. 20 MHz center frequency.

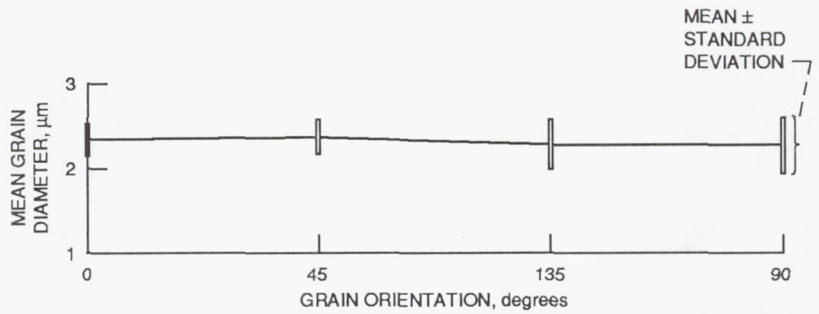

Figure 99. - Mean grain diameter versus micrograph orientation for sample 46B. Mean +/– standard deviation of average values for 4 orientations (at 5 positions) along the thickness cross-section (means are joined). Grain diameter values obtained using Heyn-intercept method.

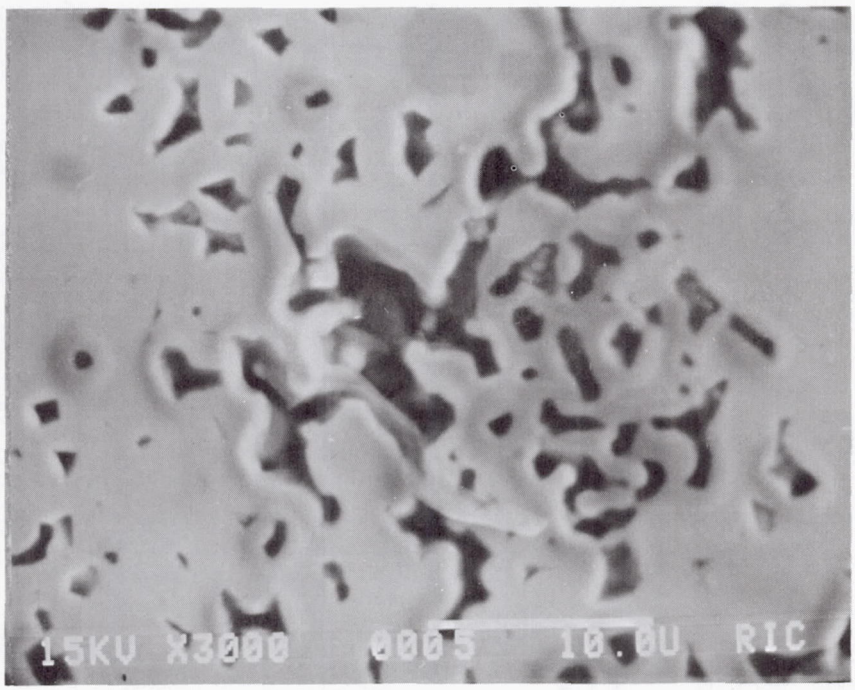

Figure 100. - SEM micrograph (secondary electron mode) showing morphology of pores.

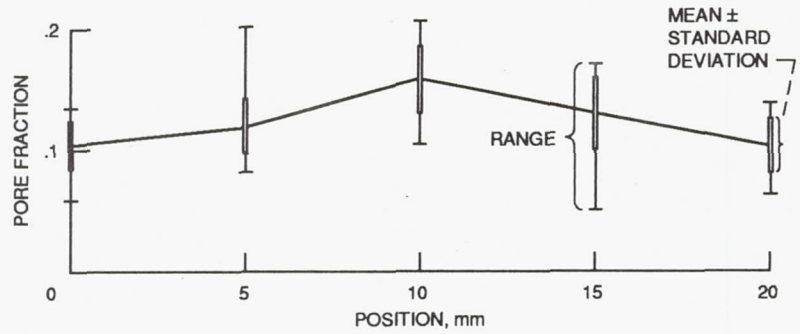

(a) First cut - 0.1 mm from midplane.

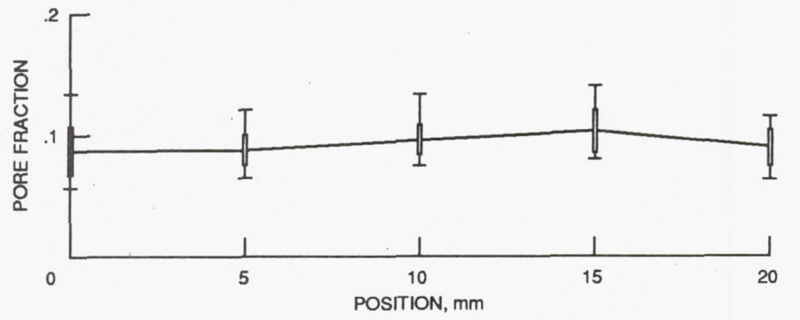

(b) Second cut - 1.2 mm from midplane.

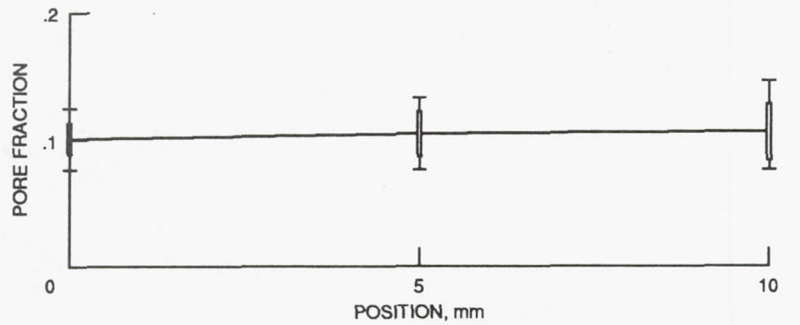

(c) Third cut - 7.2 mm from midplane.

Figure 101. - Pore fraction versus position for sample 46B. Mean +/– standard deviation and range values for 21fields at each position along the thickness cross-sections (means are joined).

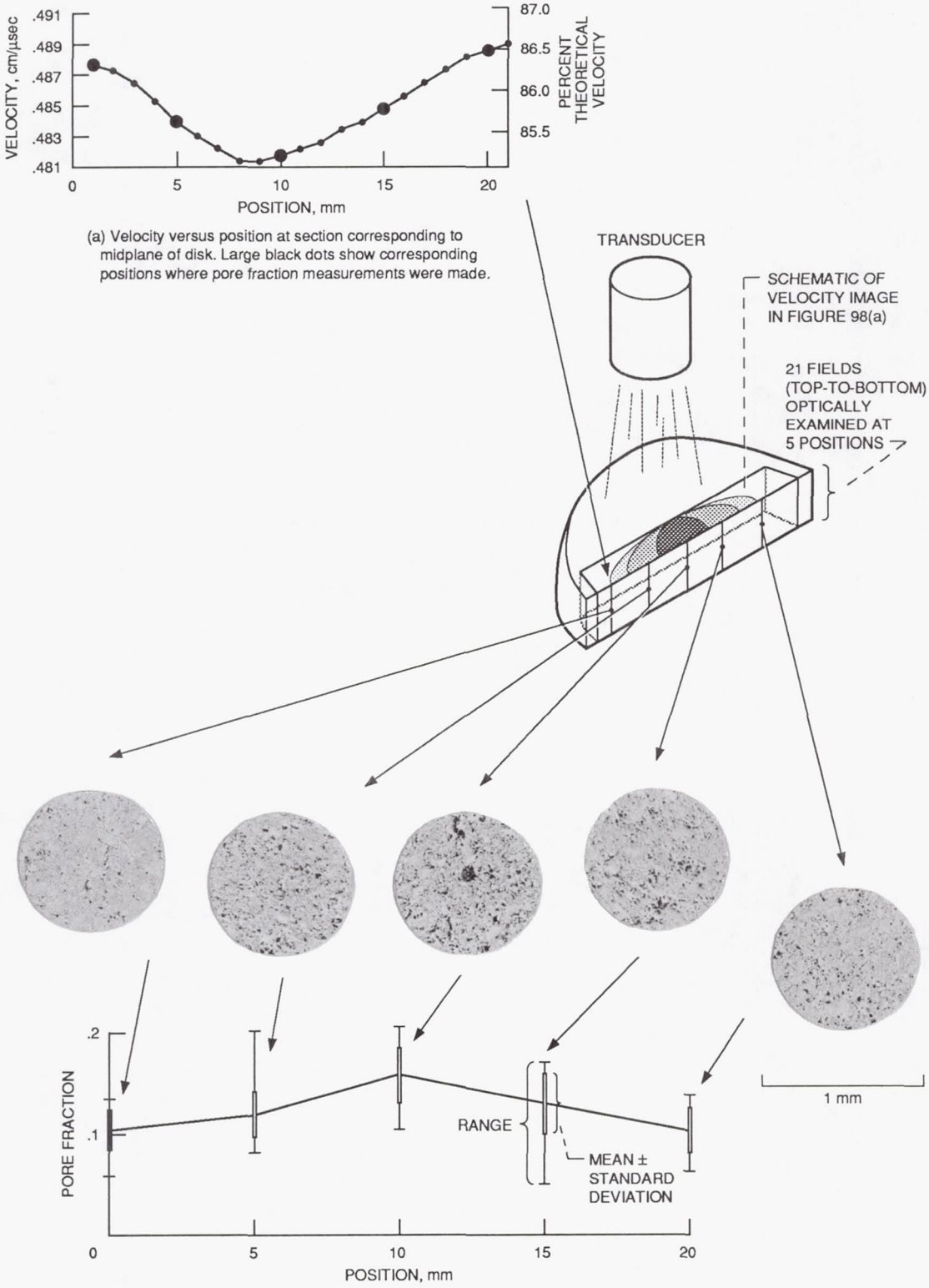

(a) Velocity versus position at section corresponding to midplane of disk. Large black dots show corresponding positions where pore fraction measurements were made.

(b) Pore fraction versus position. Black spots in photomicrographs indicate pores.

Figure 102. - Correlation of pore fraction and ultrasonic velocity results for sample 46B.

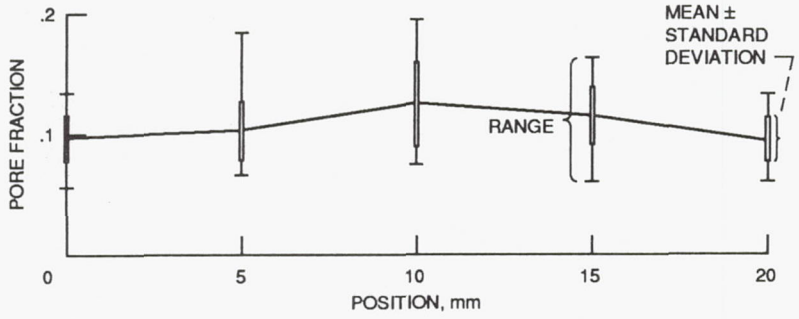

Figure 103. - Pore fraction versus position for sample 46B for combined data of cuts 1 and 2. Mean +/– standard deviation and range values for (21 x 2) fields at each position along the thickness cross-sections (means are joined).

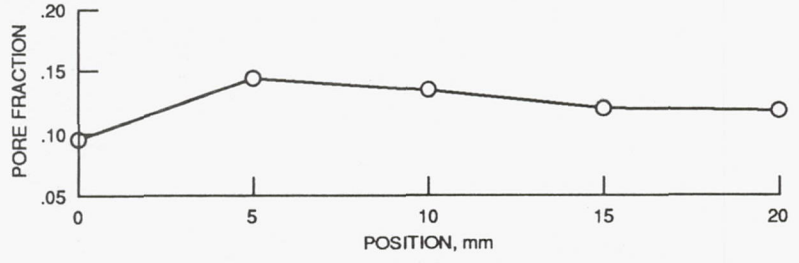

Figure 104. - Pore fraction versus position for sample 46b for 5 positions along the semi-circle top section edge. One field at each position. Means are joined.

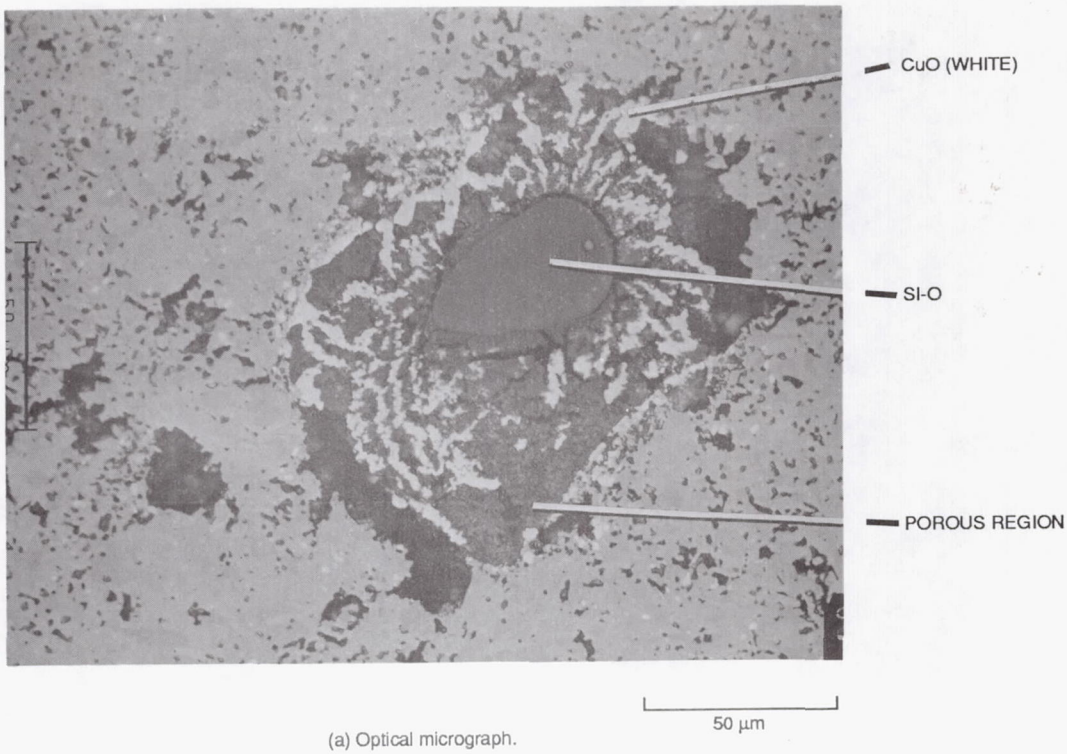

(a) Optical micrograph.

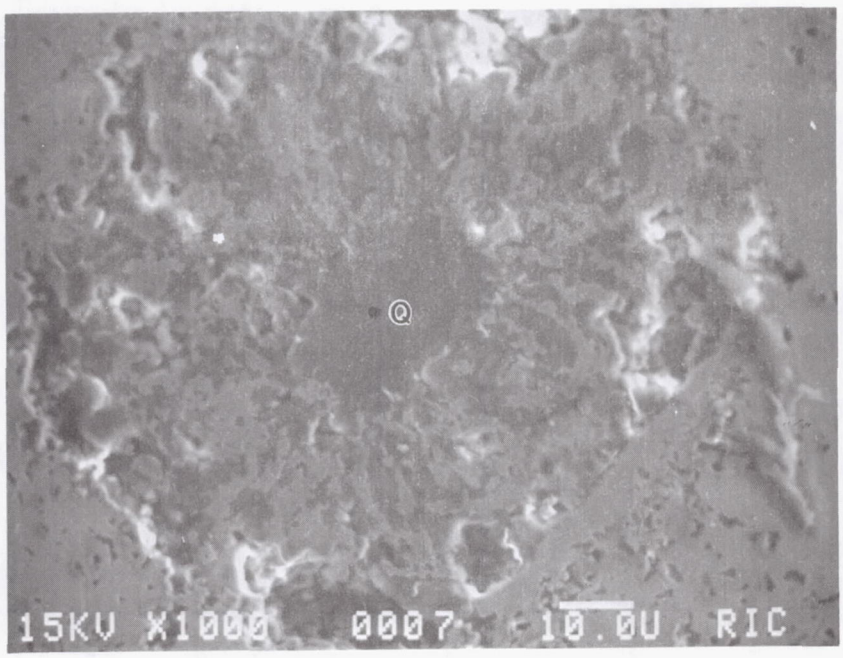

(b) SEM (secondary electron mode) micrograph.

Figure 105. - Si-O inclusions in sample 46B.

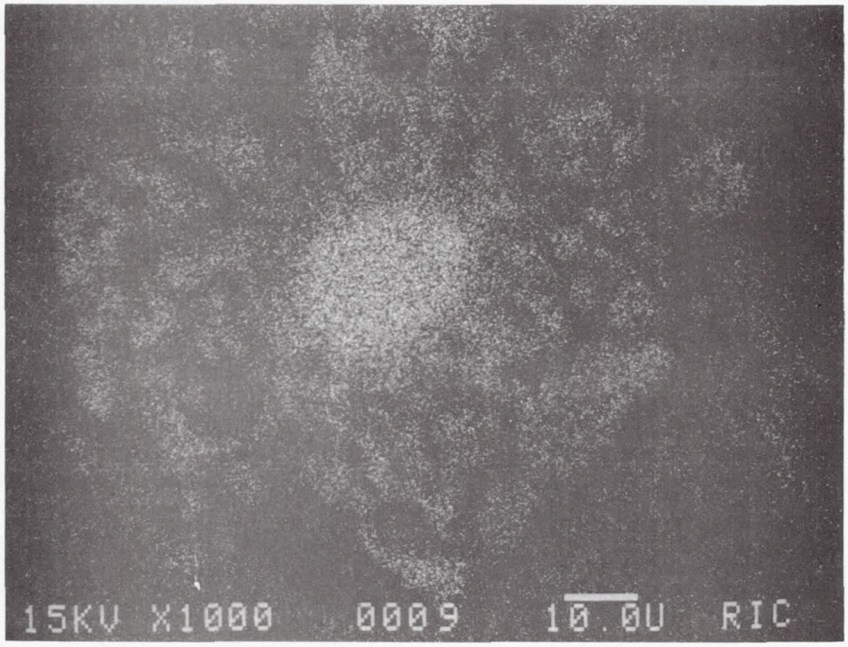

(c) Si x-ray dot map with Energy Dispersive Spectrometry.

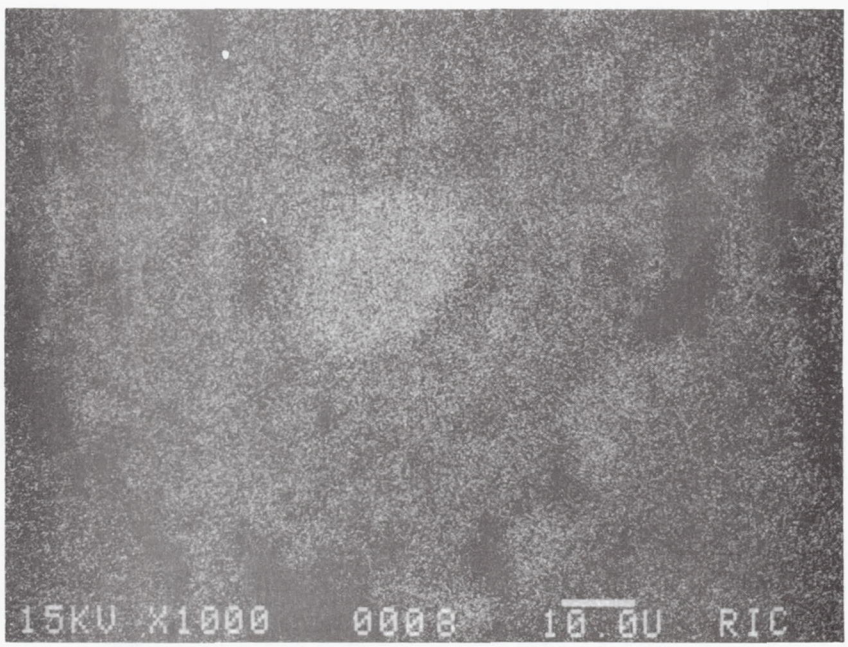

(d) Oxygen x-ray dot map with Wavelength Dispersive Spectrometry.

Figure 105. - Concluded.

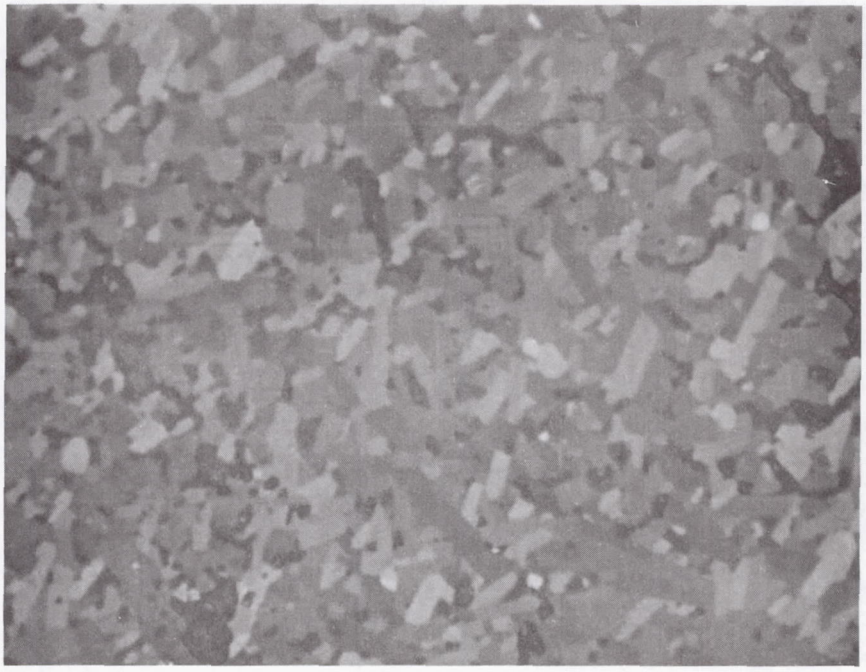

10 μm

(a) Center-cut bar.

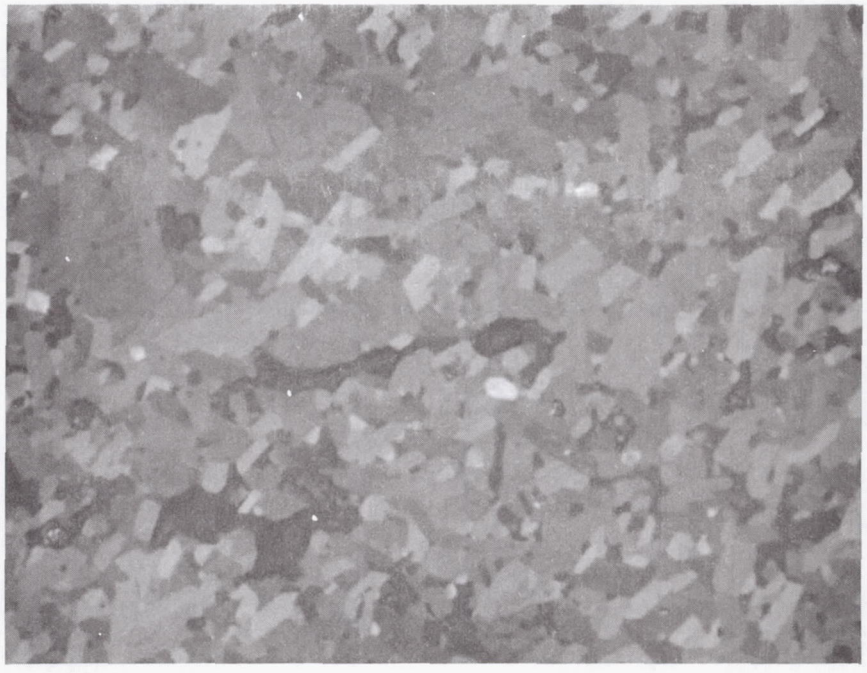

10 μm

(b) Edge-cut bar.

Figure 106. - Optical micrographs of grain distribution for bars cut from sample 46B. Polarized light.

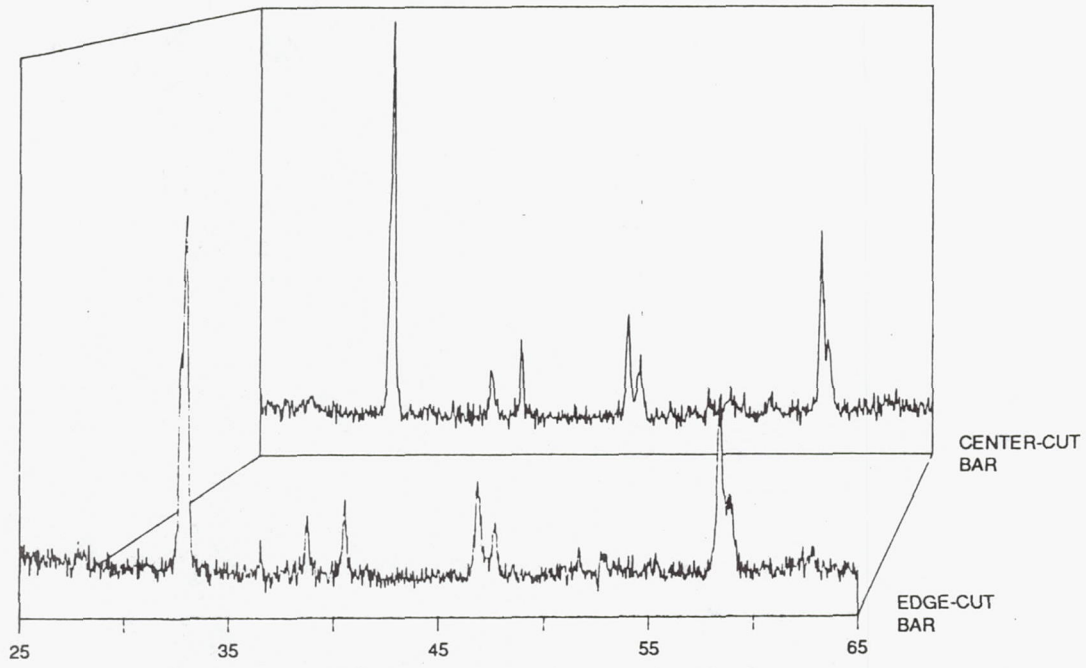

Figure 107. - X-ray diffraction patterns for bars cut from samples 46B.

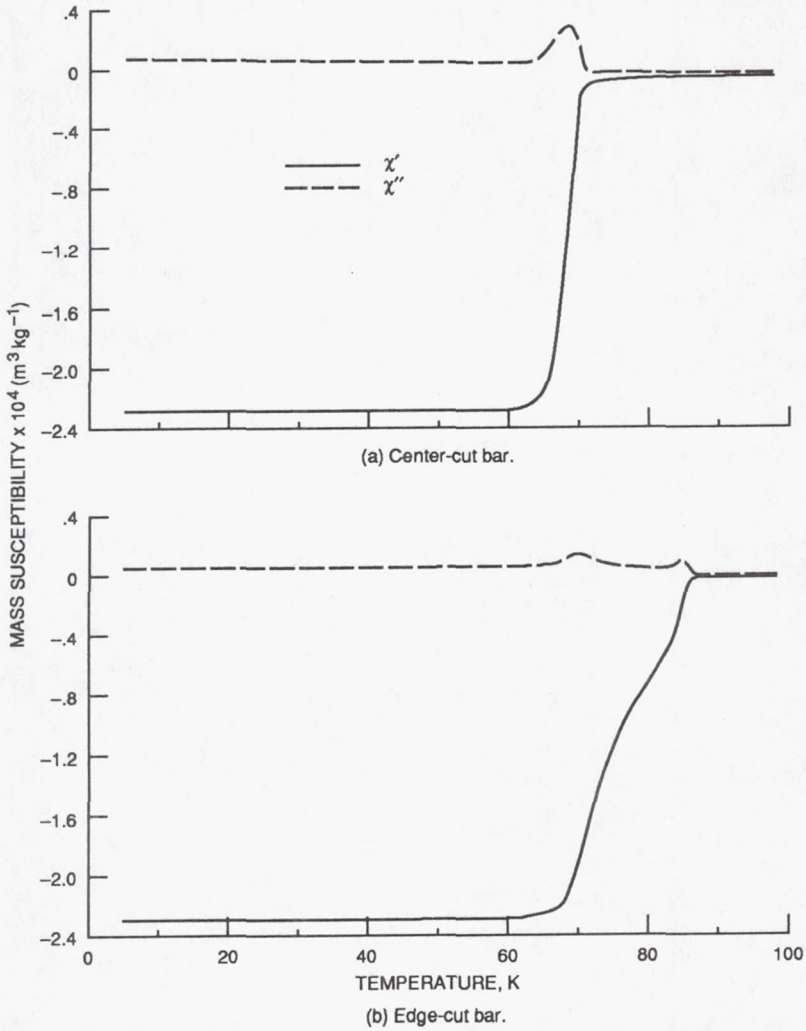

Figure 108. - A.c. susceptibility versus temperature for bars cut from sample 46B. H_{ac} = 0.02 Oe. Frequency = 100 Hz.

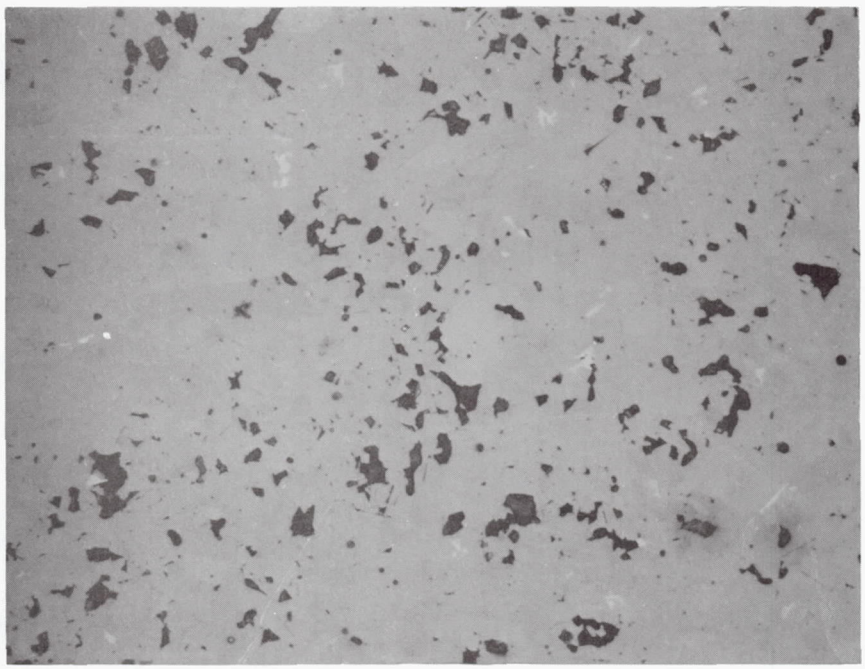

50 μm

(a) Unoxidized - schedule 2 (table 6b).

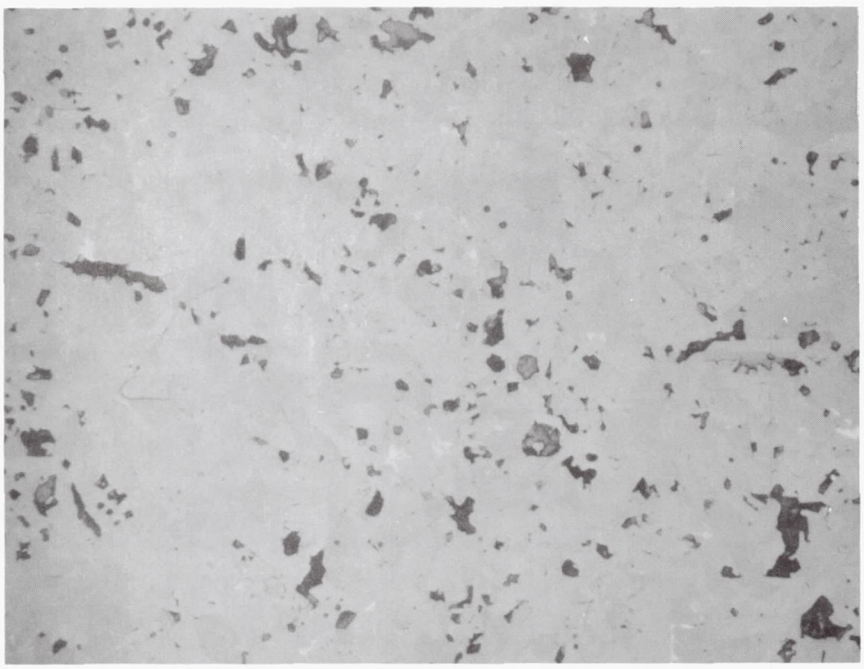

50 μm

(b) Oxidation - schedule 3 (table 7).

Figure 109. - Optical micrographs of porosity distribution for sample 51A after oxidation and reduction treatments. Pore distribution (size and fraction) appears unaffected by treatments.

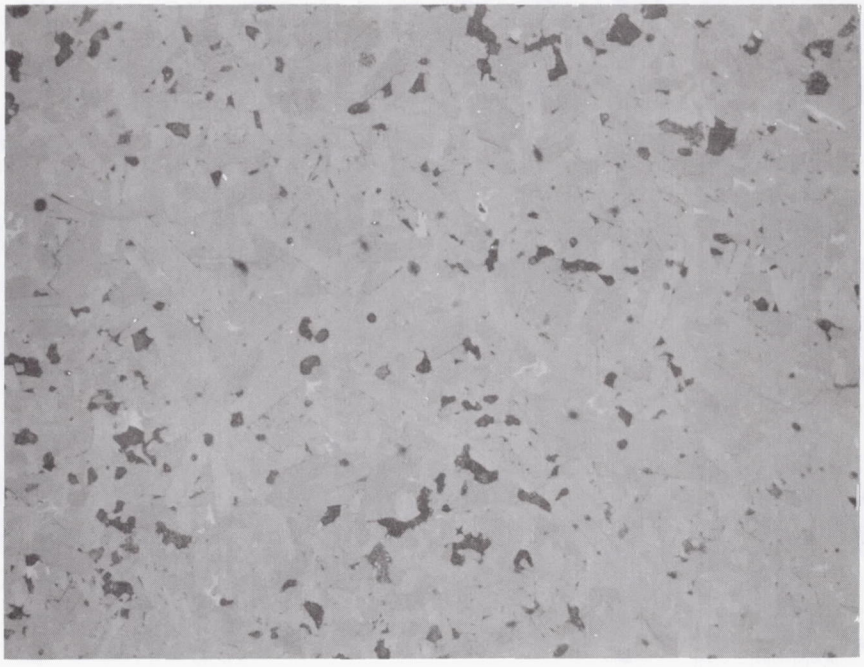

50 μm

(c) Reoxidation - schedule 4 (table 8).

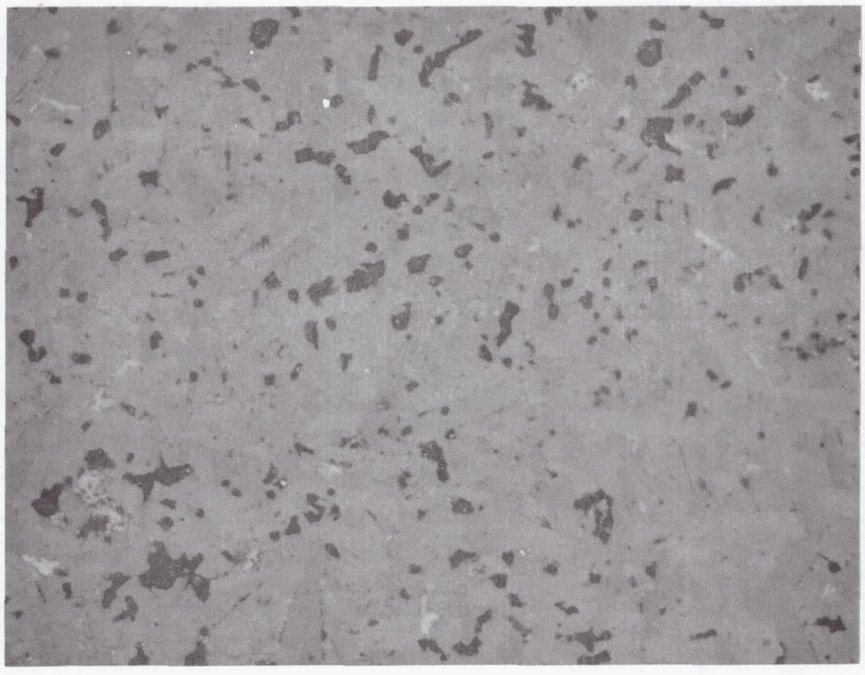

50 μm

(d) Reduction - schedule 5 (table 9).

Figure 109. - Concluded.

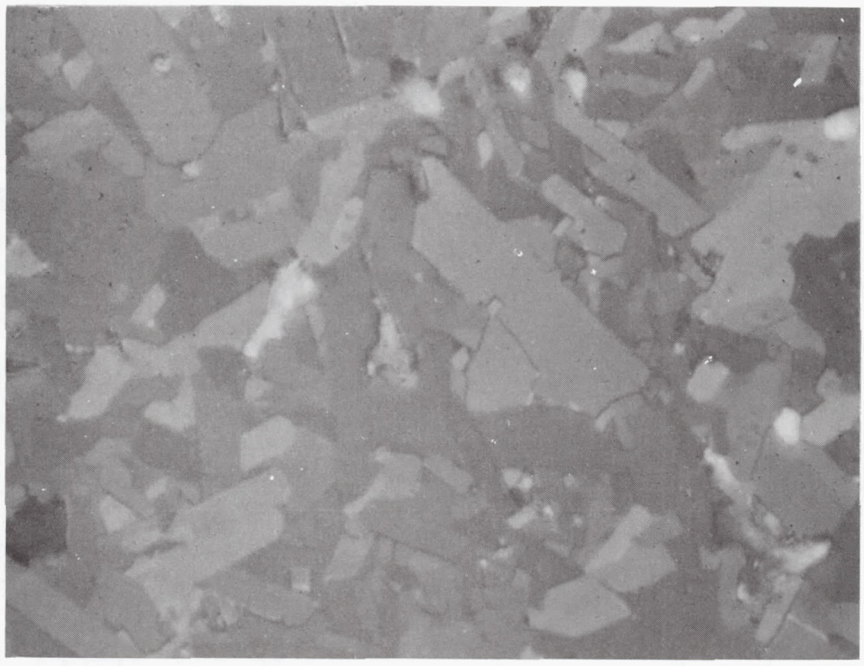

10 μm

(a) Unoxidized - schedule 2 (table 6b).

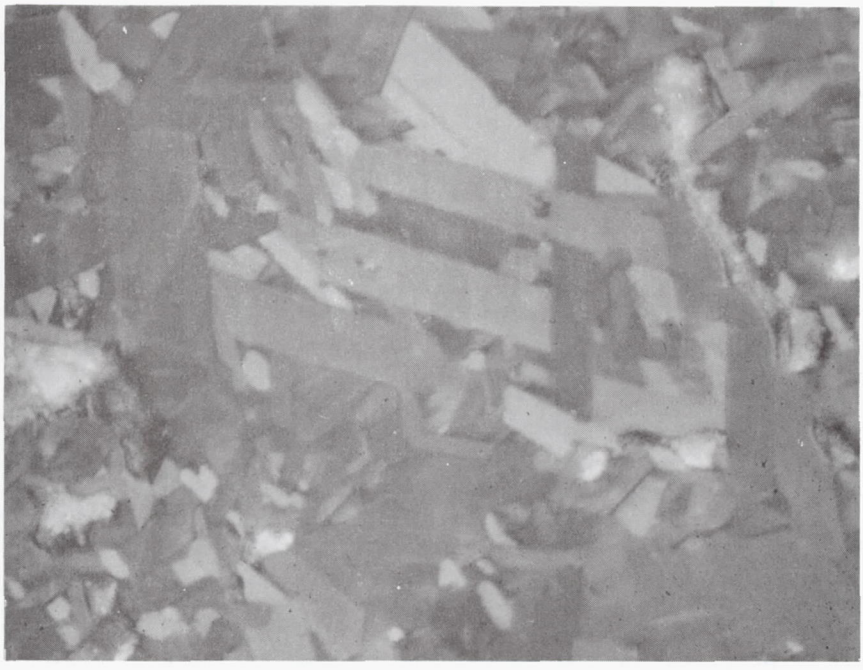

10 μm

(b) Oxidation - schedule 3 (table 7).

Figure 110. - Optical micrographs showing grain distribution for sample 51A after oxidation and reduction treatments. Polarized light. Note strong twinning in (c).

10 μm

(c) Reoxidation - schedule 4 (table 8).

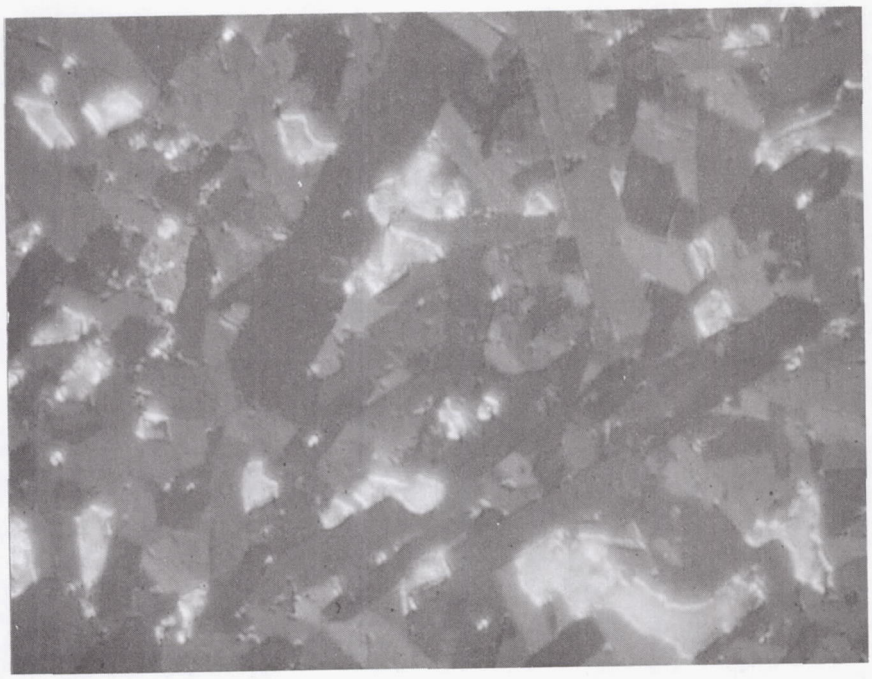

10 μm

(d) Reduction - schedule 5 (table 9).

Figure 110. - Concluded.

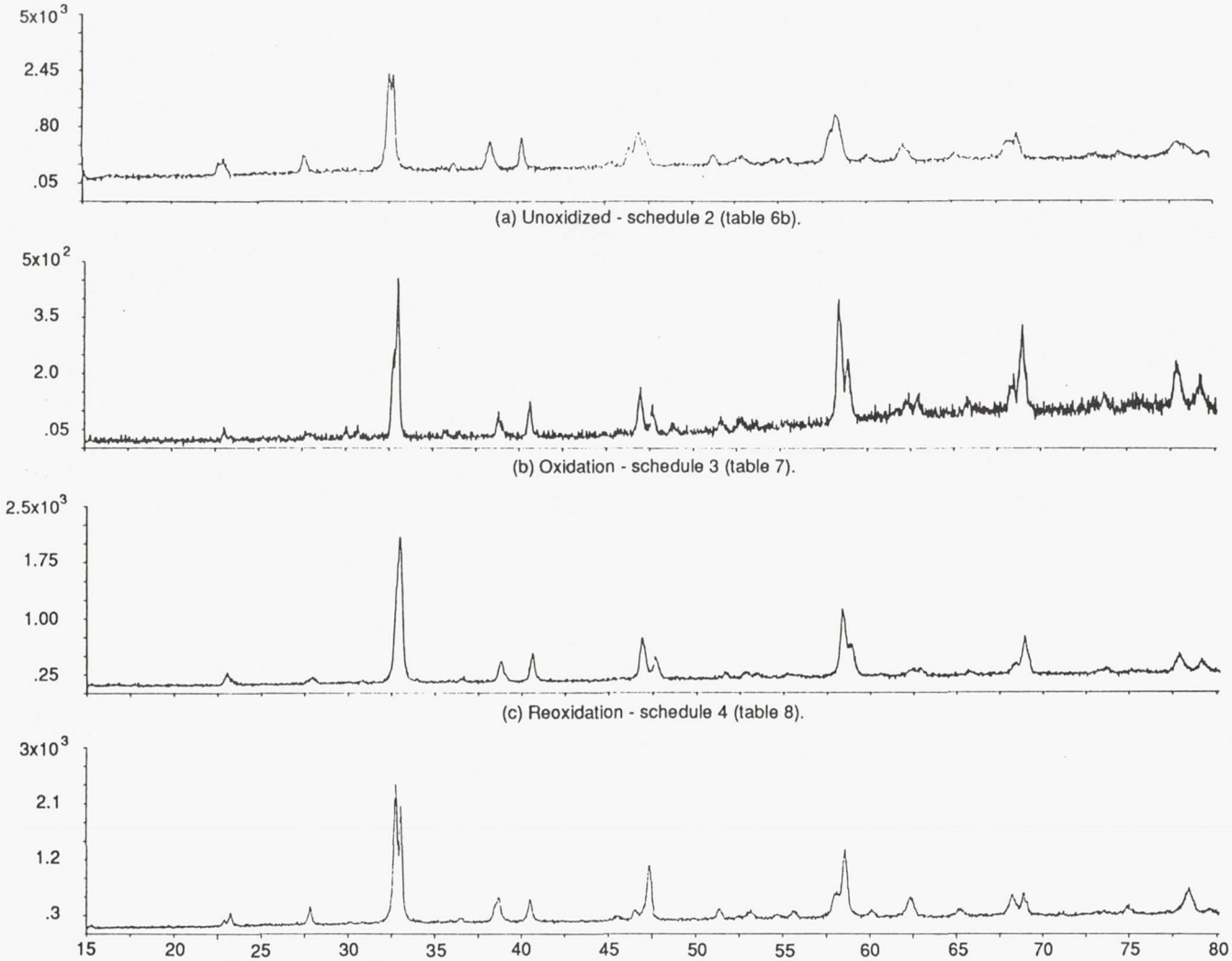

Figure 111. - X-ray diffraction patterns for sample 51A after oxidation and reduction treatments. Note relative intensities of two peaks at $2\theta = 32.5° - 33°$.

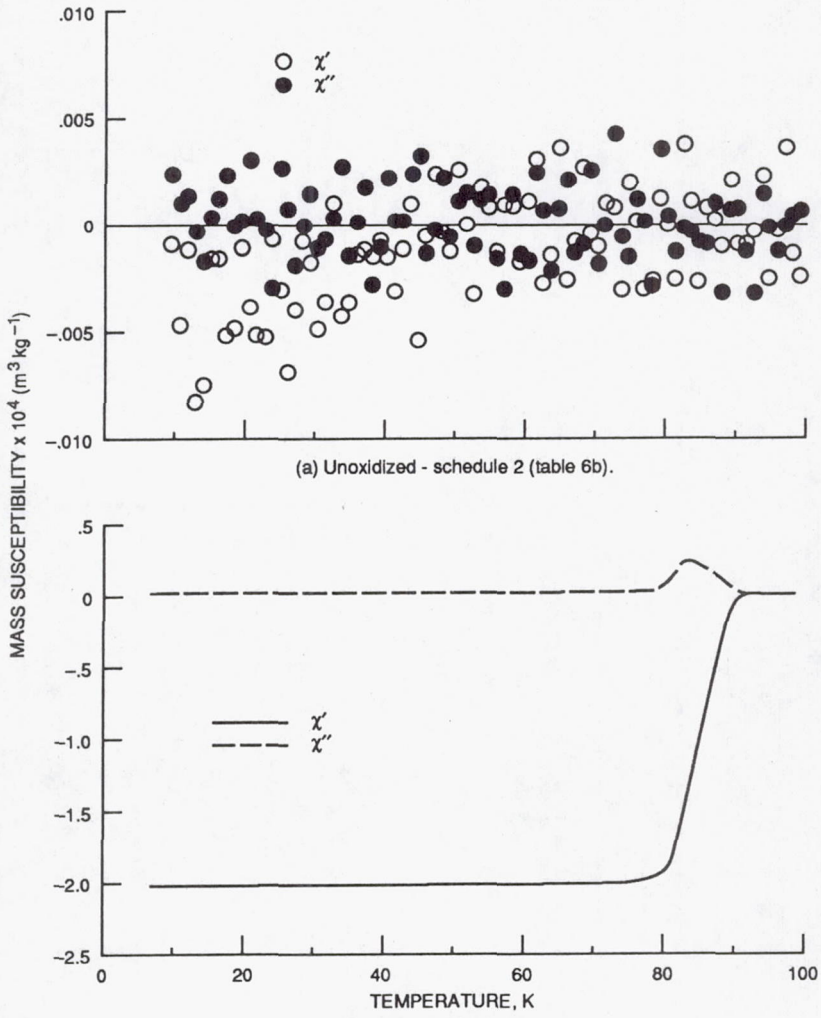

(a) Unoxidized - schedule 2 (table 6b).

(b) Oxidation - schedule 3 (table 7).

Figure 112. - A.c. susceptibility versus temperature for sample 51A after oxidation and reduction treatments. H_{ac} = 0.02 Oe. Frequency = 100 Hz.

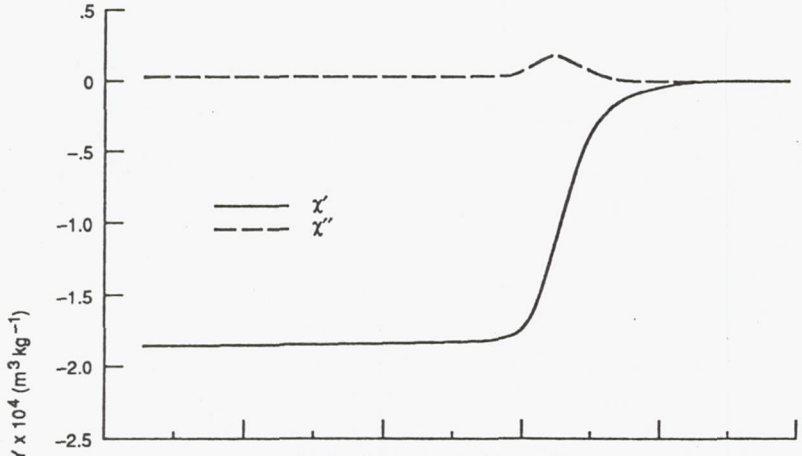

(c) Reoxidation - schedule 4 (table 8).

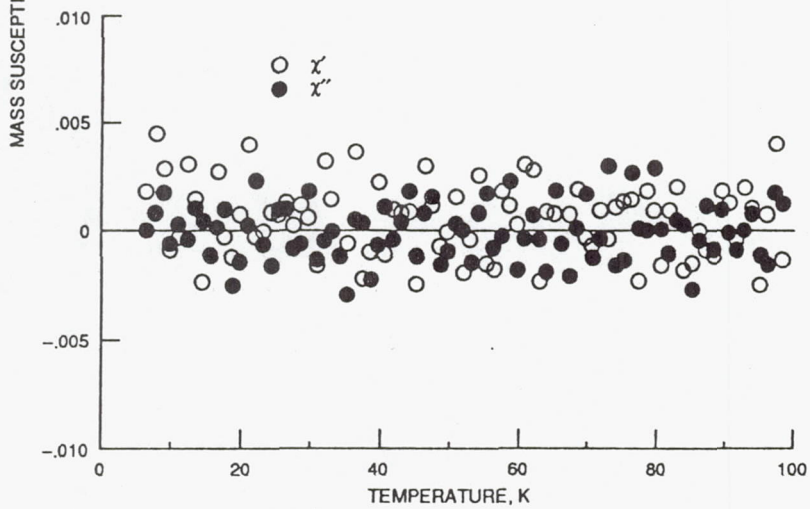

(d) Reduction - schedule 5 (table 9).

Figure 112. - Concluded.

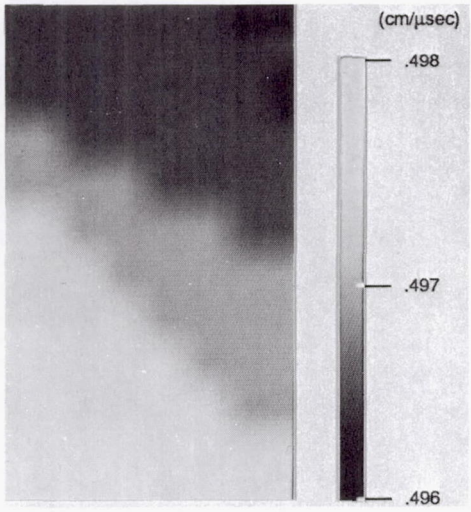

(a) Unoxidized - schedule 2 (table 6b).

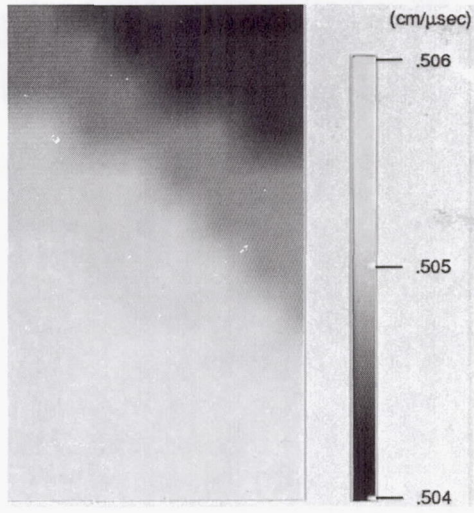

(b) Reoxidation - schedule 4 (table 8).

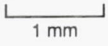

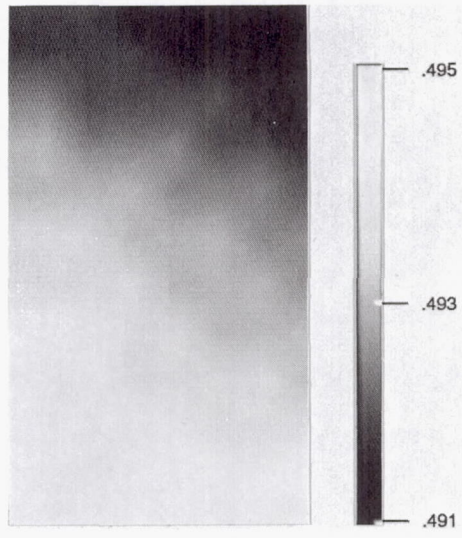

(c) Reduction - schedule 5 (table 9).

Figure 113. - Ultrasonic velocity images of sample 51A after oxidation and reduction treatments. Center frequency = 10 MHz. Scan was run over 3 mm by 5 mm region of sample with measurements made every 0.5 mm. Mean, minimum and maximum values change but global pattern stays approximately the same after treatments.

XIII. TABLES

LIST OF SYMBOLS AND ABBREVIATIONS FOR TABLE 1

V = Velocity (cm/μsec)
SV = Shear wave velocity (cm/μsec)
LV = Longitudinal wave velocity
%TV = Percent Theoretical Velocity
%P = Percent Porosity
Wt. = Weight
β_0 = Predicted value of intercept (Theoretical velocity)
β'_0 = Predicted value of intercept (Percent theoretical velocity)
β_1 = Predicted value of slope (Velocity / percent porosity)
β'_1 = Predicted value of slope (Percent theoretical velocity / percent porosity)
N/A = Not Applicable
RBSN = Reaction-bonded silicon nitride
Δ = change in

(A blank appearing in a table entry indicates that the author did not mention the subject or the information was otherwise unavailable)

Table 1. - ULTRASONIC VELOCITY VERSUS PERCENT POROSITY: REVIEW AND STATISTICAL ANALYSIS

Material	Reference	Processing Notes/ Chemical Additives	Microstructural Anisotropy	Velocity Measurement Technique	Velocity Measurement Uncertainty (%)	Density Measurement Technique	Density Measurement Uncertainty (%)	Theoretical Density, ρ_o, Used to Calculate % Porosity (g/cc)	Predicted Line Equation ($V = \beta_1 \cdot \%P + \beta_0$)	Predicted Line Equation ($\%TV = \beta'_1 \cdot \%P + \beta'_0$)	Correlation Coefficient / Level of Significance	95% Confidence Intervals for Predicted Intercept (β_0) and Slope (β_1)	95% Confidence Intervals for Predicted Intercept (β'_0) and Slope (β'_1)	$\frac{\Delta\% P}{\Delta\% TV}$	Largest Velocity Variation Across One Surface of Specimen (%)	Comments	Corresponding Figure Number
Al_2O_3	24	1.5 mol % Sintering aids	Insignificant	Longitudinal waves, 10 MHz	≤ 0.1	Dry-wt. dimensional	≤ 1	3.98	$LV = -0.018 \cdot \%P + 1.09$	$\%TV = -1.65 \cdot \%P + 100$	$\frac{-0.999}{0.0001}$	$1.07 \leq \beta_0 \leq 1.12$ $-0.019 \leq \beta_1 \leq -0.017$	$97.7 \leq \beta'_0 \leq 102$ $-1.77 \leq \beta'_1 \leq -1.52$	−0.61	15	5 data points lumped together in low % porosity region separated widely from 1 data point in high % porosity (Partially-fired specimen)	1
Al_2O_3	25	Sintering aid, Binder, Plasticizer, Water		Thru-transmission and pulse-echo overlap, Longitudinal waves, Dry and wet coupling, 5 MHz	≤ 0.8	Dry-wt. dimensional and liquid-immersion	≤ 2	3.98	$LV = -0.019 \cdot \%P + 1.13$	$\%TV = -1.64 \cdot \%P + 100$	$\frac{-0.992}{0.0001}$	$0.994 \leq \beta_0 \leq 1.27$ $-0.022 \leq \beta_1 \leq -0.015$	$87.8 \leq \beta'_0 \leq 112$ $-1.94 \leq \beta'_1 \leq -1.34$	−0.61	1	Velocity may be very slightly sensitive to the type of agglomerates found in ceramic samples, which may depend on whether sample is calcined or not; 2 data points in low % porosity region widely separated from other 4 data points in high % porosity region (Green samples)	2
Al_2O_3	16	Starting powders of various mean particle size, Binder		Pulse-echo transit time, Longitudinal waves, 10 MHz	≤ 1	Dry-wt. dimensional	< 0.5	3.98	$LV = -0.007 \cdot \%P + 1.00$	$\%TV = -0.736 \cdot \%P + 100$	$\frac{-0.928}{0.0001}$	$0.987 \leq \beta_0 \leq 1.02$ $-0.008 \leq \beta_1 \leq -0.007$	$98.3 \leq \beta'_0 \leq 102$ $-0.818 \leq \beta'_1 \leq -0.654$	−1.36		16 data points	3
Al_2O_3	26	Lubricants, Plasticizer, Water	Insignificant	Pulse-echo/cross-correlation, Longitudinal waves, 50 MHz	≤ 0.2	Liquid-immersion	≤ 2	3.98	$LV = -0.004 \cdot \%P + 1.01$	$\%TV = -0.377 \cdot \%P + 100$	$\frac{-0.698}{0.302}$	$0.923 \leq \beta_0 \leq 1.09$ $-0.016 \leq \beta_1 \leq 0.008$	$92.2 \leq \beta'_0 \leq 108$ $-1.54 \leq \beta'_1 \leq 0.782$	−2.65	1	Limited data region; 4 data points	4
Al_2O_3	16, 24-26			Longitudinal waves				3.98	$LV = -0.016 \cdot \%P + 1.10$	$\%TV = -1.43 \cdot \%P + 100$	$\frac{-0.949}{0.0001}$	$1.06 \leq \beta_0 \leq 1.15$ $-0.018 \leq \beta_1 \leq -0.013$	$95.7 \leq \beta'_0 \leq 104$ $-1.61 \leq \beta'_1 \leq -1.25$	−0.699		32 data points, all longitudinal wave data	5
Al_2O_3	27		Insignificant	Pulse-echo overlap, Shear waves, 5 MHz	≤ 1	Dry-wt. dimensional	≤ 1	3.98	$SV = -0.003 \cdot \%P + 0.669$	$\%TV = -0.477 \cdot \%P + 100$	$\frac{-0.94}{0.006}$	$0.646 \leq \beta_0 \leq 0.692$ $-0.005 \leq \beta_1 \leq -0.002$	$96.7 \leq \beta'_0 \leq 103$ $-0.669 \leq \beta'_1 \leq -0.284$	−2.10	2	6 data points	6
Al_2O_3	24	1.5 mol % Sintering aids	Insignificant	Shear waves, 5 MHz	≤ 0.2	Dry-wt. dimensional	≤ 1	3.98	$SV = -0.012 \cdot \%P + 0.655$	$\%TV = -1.87 \cdot \%P + 100$	$\frac{-1.0}{0.0001}$	$0.648 \leq \beta_0 \leq 0.663$ $-0.013 \leq \beta_1 \leq -0.012$	$98.9 \leq \beta'_0 \leq 101$ $-1.93 \leq \beta'_1 \leq -1.81$	−0.53	15	5 data points lumped together in low % porosity region separated widely from 1 data point in high % porosity region (Partially-fired specimen)	7
Al_2O_3	25	Sintering aid, Binder, Plasticizer, Water		Thru-transmission and pulse-echo overlap, Shear waves, Dry and wet coupling, 1-5 MHz	≤ 1.8	Dry-wt. dimensional and liquid-immersion	≤ 2	3.98	$SV = -0.010 \cdot \%P + 0.666$	$\%TV = -1.55 \cdot \%P + 100$	$\frac{-0.987}{0.0003}$	$0.571 \leq \beta_0 \leq 0.762$ $-0.008 \leq \beta_1 \leq -0.013$	$85.7 \leq \beta'_0 \leq 114$ $-1.90 \leq \beta'_1 \leq -1.20$	−0.65	1	Velocity may be very slightly sensitive to the type of agglomerates found in ceramic samples, which may depend on whether sample is calcined or not; 2 data points in low % porosity region widely separated from other 4 data points in high % porosity region (Green samples)	8
Al_2O_3	16	Starting powders of of various mean particle size, Binder		Pulse-echo transit time, Shear waves, 10 MHz	≤ 1	Dry-wt. dimensional	< 0.5	3.98	$SV = -0.004 \cdot \%P + 0.628$	$\%TV = -0.662 \cdot \%P + 100$	$\frac{-0.990}{0.0001}$	$0.622 \leq \beta_0 \leq 0.635$ $-0.005 \leq \beta_1 \leq -0.004$	$99.0 \leq \beta'_0 \leq 101$ $-0.705 \leq \beta'_1 \leq -0.610$	−1.51		17 data points	9
Al_2O_3	16, 24, 25, 27			Shear waves				3.98	$SV = -0.009 \cdot \%P + 0.693$	$\%TV = -1.35 \cdot \%P + 100$	$\frac{-0.910}{0.0001}$	$0.656 \leq \beta_0 \leq 0.729$ $-0.011 \leq \beta_1 \leq -0.008$	$94.8 \leq \beta'_0 \leq 105$ $-1.57 \leq \beta'_1 \leq -1.14$	−0.741		35 data points, all shear wave data	10
Al_2O_3	16, 24-27															Comparison	11
CuO	28	Starting powders different for each of 2 disks		Pulse-echo/cross-correlation, Longitudinal waves, Dry coupling, 5 MHz	≤ 0.4	Dry-wt. dimensional	≤ 1	6.40	$LV = -0.006 \cdot \%P + 0.474$	$\%TV = -1.34 \cdot \%P + 100$	$\frac{-0.990}{0.0100}$	$0.400 \leq \beta_0 \leq 0.549$ $-0.009 \leq \beta_1 \leq -0.004$	$84.3 \leq \beta'_0 \leq 116$ $-1.92 \leq \beta'_1 \leq -0.760$	−0.746		4 data points, 4 specimens cut from 2 disks, CuO phase confirmed from x-ray diffraction	12
"Green" MgO	29	20 wt.% Binder		Pulse-echo overlap, Longitudinal waves, 2.25 MHz	≤ 0.5	Dry-wt. dimensional	≤ 1	2.70	$LV = -0.014 \cdot \%P + 0.817$	N/A	$\frac{-1.0}{0.012}$	$0.673 \leq \beta_0 \leq 0.961$ $-0.017 \leq \beta_1 \leq -0.010$	N/A	−0.60	2	3 data points; material is unsintered, green compact	13

Table 1. -ULTRASONIC VELOCITY VERSUS PERCENT POROSITY: REVIEW AND STATISTICAL ANALYSIS—CONTINUED

Material	Reference	Processing Notes/ Chemical Additives	Microstructural Anisotropy	Velocity Measurement Technique	Velocity Measurement Uncertainty (%)	Density Measurement Technique	Density Measurement Uncertainty (%)	Theoretical Density, ρ_0, Used to Calculate % Porosity (g/cc)	Predicted Line Equation ($V = \beta_1 \bullet \%P + \beta_0$)	Predicted Line Equation ($\%TV = \beta'_1 \bullet \%P + \beta'_0$)	Correlation Coefficient / Level of Significance	95% Confidence Intervals for Predicted Intercept (β_0) and Slope (β_1)	95% Confidence Intervals for Predicted Intercept (β'_0) and Slope (β'_1)	$\frac{\Delta\% P}{\Delta\% TV}$	Largest Velocity Variation Across One Surface of Specimen (%)	Comments	Corresponding Figure Number
Porcelain	7		Preferred granular orientation	Pulse-echo overlap, Longitudinal waves, 2 MHz	≤ 0.1	Dry-wt. dimensional	≤ 1	2.6	$LV = -0.013 \bullet \%P + 0.728$	$\%TV = -1.78 \bullet \%P + 100$	$\frac{-0.993}{0.0001}$	$0.713 \le \beta_0 \le 0.743$ $-0.0014 \le \beta_1 \le -0.0012$	$97.9 \le \beta'_0 \le 102$ $-1.87 \le \beta'_1 \le -1.70$	−0.56		27 data points; multiphase ceramic; sample composition and thus theoretical density vary slightly with firing temperature; measurements made along extrusion axis	14
Porcelain	7		Preferred granular orientation	Pulse-echo overlap, Shear waves, 2 MHz	≤ 0.1	Dry-wt. dimensional	≤ 1	2.6	$SV = -0.009 \bullet \%P + 0.448$	$\%TV = -1.93 \bullet \%P + 100$	$\frac{-0.998}{0.0001}$	$0.442 \le \beta_0 \le 0.454$ $-0.009 \le \beta_1 \le -0.008$	$98.7 \le \beta'_0 \le 101$ $-1.98 \le \beta'_1 \le -1.88$	−0.52			15
Porcelain	7															Comparison	16
Porcelain	30			Longitudinal waves, 1.5-3 MHz				2.60	$LV = -0.006 \bullet \%P + 0.618$	$\%TV = -0.935 \bullet \%P + 100$	$\frac{-0.987}{0.0001}$	$0.606 \le \beta_0 \le 0.630$ $-0.007 \le \beta_1 \le -0.005$	$98.1 \le \beta'_0 \le 102$ $-1.11 \le \beta'_1 \le -0.760$	−1.07		7 data points, multiphase ceramic, sample composition and thus theoretical density vary slightly with firing temp.	17
Porcelain P1 (See ref.)	31	(See ref.)		Longitudinal waves, 15 MHz	≤ 1	Dry-wt. dimensional	≤ 1	2.51	$LV = -0.002 \bullet \%P + 0.611$	$\%TV = -0.312 \bullet \%P + 100$	$\frac{-0.586}{0.414}$	$0.553 \le \beta_0 \le 0.668$ $-0.010 \le \beta_1 \le 0.006$	$90.5 \le \beta'_0 \le 109$ $-1.34 \le \beta'_1 \le -1.28$	−3.21		4 data points; multiphase ceramic; sample composition and thus theoretical density vary slightly with firing temp.	18
Porcelain P2 (See ref.)	31	(See ref.)		Longitudinal waves, 15 MHz	≤ 1	Dry-wt. dimensional	≤ 1	2.56	$LV = -0.005 \bullet \%P + 0.615$	$\%TV = -0.740 \bullet \%P + 100$	$\frac{-0.983}{0.017}$	$0.598 \le \beta_0 \le 0.631$ $-0.007 \le \beta_1 \le -0.002$	$97.3 \le \beta'_0 \le 102$ $-1.04 \le \beta'_1 \le -0.436$	−1.35			19
Porcelain T1 (See ref.)	31	(See ref.)		Longitudinal waves, 15 MHz	≤ 1	Dry-wt. dimensional	≤ 1	2.58	$LV = -0.001 \bullet \%P + 0.623$	$\%TV = -0.167 \bullet P + 100$	$\frac{-0.894}{0.106}$	$0.612 \le \beta_0 \le 0.632$ $-0.003 \le \beta_1 \le 0.0005$	$98.6 \le \beta'_0 \le 101$ $-0.422 \le \beta'_1 \le 0.088$	−5.99			20
Porcelain T2 (See ref.)	31	(See ref.)		Longitudinal waves, 15 MHz	≤ 1	Dry-wt. dimensional	≤ 1	2.64	$LV = -0.0008 \bullet \%P + 0.626$	$\%TV = -0.121 \bullet \%P + 100$	$\frac{-0.947}{0.053}$	$0.621 \le \beta_0 \le 0.631$ $-0.002 \le \beta_1 \le 0.003$	$99.2 \le \beta'_0 \le 101$ $-0.246 \le \beta'_1 \le 0.004$	−8.26			21
Unpoled PZT4	8		Insignificant	Pulse-echo overlap, Longitudinal waves, 50 MHz	≤ 0.1	Liquid-immersion	≤ 2	8.0	$LV = -0.007 \bullet \%P + 0.443$	$\%TV = -1.68 \bullet \%P + 100$	N/A / N/A	N/A	N/A	−0.60		2 data points for each set; PZT4, PZT5, and PZT7 are each different solid solution combinations of $PbZrO_3$ and $PbTiO_3$ but theoretical density is ~8.0 g/cc for each; poling orients electric domains; velocity measured along polarized direction for poled specimens; no correlation coefficient is given since only 2 data points for each set; all poled sets have higher theoretical velocity than corresponding unpoled set	22
Poled PZT4	8		Preferred electrical domain orientation	Pulse-echo overlap, Longitudinal waves, 50 MHz	≤ 0.1	Liquid-immersion	≤ 2	8.0	$LV = -0.009 \bullet \%P + 0.483$	$\%TV = -1.93 \bullet \%P + 100$	N/A / N/A	N/A	N/A	−0.52			23
PZT4	8															Comparison	24
Unpoled PZT5	8		Insignificant	Pulse-echo overlap, Longitudinal waves, 50 MHz	≤ 0.1	Liquid-immersion	≤ 2	8.0	$LV = -0.008 \bullet \%P + 0.443$	$\%TV = -1.85 \bullet \%P + 100$	N/A / N/A	N/A	N/A	−0.54		2 data points for each set; PZT4, PZT5, and PZT7 are each different solid solution combinations of $PbZrO_3$ and $PbTiO_3$ but theoretical density is ~8.0 g/cc for each; poling orients electric domains; velocity measured along polarized direction for poled specimens; no correlation coefficient is given since only 2 data points for each set; all poled sets have higher theoretical velocity than corresponding unpoled set	25
Poled PZT5	8		Preferred electrical domain orientation	Pulse-echo overlap, Longitudinal waves, 50 MHz	≤ 0.1	Liquid-immersion	≤ 2	8.0	$LV = -0.010 \bullet \%P + 0.486$	$\%TV = -2.12 \bullet \%P + 100$	N/A / N/A	N/A	N/A	−0.47			26
PZT5	8															Comparison	27

Table 1. -ULTRASONIC VELOCITY VERSUS PERCENT POROSITY: REVIEW AND STATISTICAL ANALYSIS—CONTINUED

Material	Reference	Processing Notes/ Chemical Additives	Microstructural Anisotropy	Velocity Measurement Technique	Velocity Measurement Uncertainty (%)	Density Measurement Technique	Density Measurement Uncertainty (%)	Theoretical Density, ρ_o, Used to Calculate % Porosity (g/cc)	Predicted Line Equation ($V = \beta_1 \cdot \%P + \beta_0$)	Predicted Line Equation ($\%TV = \beta'_1 \cdot \%P + \beta'_0$)	Correlation Coefficient / Level of Significance	95% Confidence Intervals for Predicted Intercept (β_0) and Slope (β_1)	95% Confidence Intervals for Predicted Intercept (β'_0) and Slope (β'_1)	$\frac{\Delta\% P}{\Delta\% TV}$	Largest Velocity Variation Across One Surface of Specimen (%)	Comments	Corresponding Figure Number
Unpoled PZT7	8		Insignificant	Pulse-echo overlap, Longitudinal waves, 50 MHz	≤ 0.1	Liquid-immersion	≤ 2	8.0	$LV = -0.004 \cdot \%P + 0.464$	$\%TV = -0.760 \cdot \%P + 100$	N/A / N/A	N/A	N/A	−1.32		2 data points for each set; PZT4, PZT5, and PZT7 are each different solid solution combinations of $PbZrO_3$ and $Pb\,TiO_3$ but theoretical density is ~8.0 g/cc for each; poling orients electric domains; velocity measured along polarized direction for poled specimens; no correlation coefficient is given since only 2 data points for each set; all poled sets have higher theoretical velocity than corresponding unpoled set	28
Poled PZT7	8		Preferred electrical domain orientation	Pulse-echo overlap, Longitudinal waves, 50 MHz	≤ 0.1	Liquid-immersion	≤ 2	8.0	$LV = -0.005 \cdot \%P + 0.494$	$\%TV = -0.952 \cdot \%P + 100$	N/A / N/A	N/A	N/A	−1.05			29
PZT7	8															Comparison	30
Unpoled PZT	8															Comparison	31
Poled PZT	8															Comparison	32
"Green" α-SiC	32	Binder		Thru-transmission transit time, Longitudinal waves, 500 KHz	≤ 1	Liquid-immersion	≤ 2	3.22	$LV = -0.007 \cdot \%P + 0.464$	N/A	−0.974 / 0.0001	$0.397 \le \beta_0 \le 0.535$ $-0.009 \le \beta_1 \le -0.006$	N/A	−0.633	30	8 data points; material is unsintered green compact; large velocity variation even though small density variation within specimen; quality of contact between individual powder particles may affect velocity	33
α-SiC	33	Boron and carbonaceous resin binders	Some specimens have preferred pore orientation	Pulse-echo/cross-correlation, Longitudinal waves, 100 MHz	≤ 0.1	Dry-wt. dimensional	≤ 1	3.22	$LV = -0.014 \cdot \%P + 1.23$	$\%TV = -1.16 \cdot \%P + 100$	−0.993 / 0.0001	$1.22 \le \beta_0 \le 1.24$ $-0.016 \le \beta_1 \le -0.013$	$99.4 \le \beta'_0 \le 101$ $-1.29 \le \beta'_1 \le -1.03$	−0.862	≤ 0.1	8 data points; each data point is for a particular batch and is the average of ~ 24 measurements on ~ 8 specimens. Velocity not greatly sensitive to mean pore size, mean pore orientation, and mean grain size	34
α-SiC	34			Pulse-echo overlap, Longitudinal waves, 25 MHz	≤ 1	Liquid-immersion	≤ 2	3.22	$LV = -0.011 \cdot \%P + 1.21$	$\%TV = -0.916 \cdot \%P + 100$	−0.999 / 0.0001	$1.21 \le \beta_0 \le 1.22$ $-0.012 \le \beta_1 \le -0.011$	$99.8 \le \beta'_0 \le 100$ $-0.962 \le \beta'_1 \le -0.870$	−1.09	< 5	6 data points	35
α-SiC	35		Insignificant	Pulse-echo overlap, Longitudinal waves, 20 MHz	≤ 1	Dry-wt. dimensional	≤ 1	3.22	$LV = -0.011 \cdot \%P + 1.22$	$\%TV = -0.883 \cdot \%P + 100$	−0.957 / 0.0001	$1.22 \le \beta_0 \le 1.22$ $-0.011 \le \beta_1 \le -0.010$	$99.9 \le \beta'_0 \le 100$ $-0.939 \le \beta'_1 \le 0.832$	−1.13	< 1	194 data points	36
α-SiC	33-35			Longitudinal waves				3.22	$LV = -0.011 \cdot \%P + 1.22$	$\%TV = -0.912 \cdot \%P + 100$	−0.964 / 0.0001	$1.216 \le \beta_0 \le 1.220$ $-0.012 \le \beta_1 \le -0.011$	$99.9 \le \beta'_0 \le 100$ $-0.939 \le \beta'_1 \le -0.832$	−1.10		208 data points, all longitudinal wave data	37
α-SiC	26	Boron and carbonaceous resin binders	Some specimens have preferred pore orientation	Pulse-echo/cross-correlation, Shear waves, 20 MHz	≤ 0.1	Liquid-immersion	≤ 2	3.22	$SV = -0.009 \cdot \%P + 0.786$	$\%TV = -1.16 \cdot \%P + 100$	−0.991 / 0.0001	$0.711 \le \beta_0 \le 0.859$ $-0.010 \le \beta_1 \le -0.008$	$99.0 \le \beta'_0 \le 101$ $-1.32 \le \beta'_1 \le -1.01$	−0.86	≤ 0.1	8 data points; most specimens from same batches used by Baaklini	38
α-SiC	26, 33-35															Comparison	39
Si_3N_4	36	Hot-pressed silicon nitride has 1% MgO sintering aid and 0.5–1% impurities; RBSN has < 1% impurities and various amounts of unreacted silicon	Insignificant	Pulse-echo overlap, Longitudinal waves, 25–45 MHz	≤ 1	Dry-wt. dimensional	≤ 1	3.30	$LV = -0.015 \cdot \%P + 1.11$	$\%TV = -1.34 \cdot \%P + 100$	N/A / N/A	N/A	N/A	−0.75		No correlation coefficient is given since only 2 data points; but each point is average of measurement on 25 specimens. data point in low % porosity region is for hot-pressed Si_3N_4 while data point in high % porosity is for reaction bonded Si_3N_4	40

Table 1. - ULTRASONIC VELOCITY VERSUS PERCENT POROSITY: REVIEW AND STATISTICAL ANALYSIS—CONTINUED

Material	Reference	Processing Notes/ Chemical Additives	Microstructural Anisotropy	Velocity Measurement Technique	Velocity Measurement Uncertainty (%)	Density Measurement Technique	Density Measurement Uncertainty (%)	Theoretical Density, ρ_0, Used to Calculate % Porosity (g/cc)	Predicted Line Equation ($V = \beta_1 \bullet \%P + \beta_0$)	Predicted Line Equation ($\%TV = \beta'_1 \bullet \%P + \beta'_0$)	Correlation Coefficient / Level of Significance	95% Confidence Intervals for Predicted Intercept (β_0) and Slope (β_1)	95% Confidence Intervals for Predicted Intercept (β'_0) and Slope (β'_1)	$\frac{\Delta\% P}{\Delta\% TV}$	Largest Velocity Variation Across One Surface of Specimen (%)	Comments	Corresponding Figure Number
Si_3N_4	37	Injection-molded, slip-cast, and hot-pressed specimens		Thru-transmission transit time, Longitudinal waves, 5 MHz				3.30	$LV = -0.016 \bullet \%P + 1.14$	$\%TV = -1.41 \bullet \%P + 100$	$\frac{-0.997}{0.0001}$	$1.12 \le \beta_0 \le 1.16$ $-0.017 \le \beta_1 \le -0.015$	$98.6 \le \beta'_0 \le 101$ $-1.48 \le \beta'_1 \le -1.34$	−0.71		13 data points	41
Si_3N_4	38	RBSN has < 1% impurities and various amounts of unreacted silicon	Insignificant	Pulse-echo overlap, Longitudinal waves, 15 MHz	≤ 0.1	Dry-wt. dimensional	≤ 0.1	3.30	$LV = -0.013 \bullet \%P + 1.12$	$\%TV = -1.15 \bullet \%P + 100$	$\frac{-0.991}{0.001}$	$0.928 \le \beta_0 \le 1.25$ $-0.016 \le \beta_1 \le -0.010$	$88.0 \le \beta'_0 \le 111$ $-1.44 \le \beta'_1 \le -0.864$	−0.87		5 data points	42
Si_3N_4	36-38			Longitudinal waves				3.30	$LV = -0.014 \bullet \%P + 1.12$	$\%TV = -1.27 \bullet \%P + 100$	$\frac{-0.981}{0.0001}$	$1.08 \le \beta_0 \le 1.15$ $-0.016 \le \beta_1 \le -0.013$	$97.1 \le \beta'_0 \le 103$ $-1.40 \le \beta'_1 \le -1.15$	−0.787		20 data points, all longitudinal wave data	43
Si_3N_4	37	Injection-molded, slip-cast, and hot-pressed specimens		Thru-transmission transit time, Shear waves, 5 MHz				3.30	$SV = -0.008 \bullet \%P + 0.652$	$\%TV = -1.18 \bullet \%P + 100$	$\frac{-0.991}{0.0001}$	$0.636 \le \beta_0 \le 0.667$ $-0.008 \le \beta_1 \le 0.007$	$97.6 \le \beta'_0 \le 102$ $-1.30 \le \beta'_1 \le -1.06$	−0.85		11 data points	44
Si_3N_4	38	RBSN has < 1% impurities and various amounts of unreacted silicon	Insignificant	Pulse-echo overlap, Shear waves, 15 MHz	≤ 0.1	Dry-wt. dimensional	≤ 0.1	3.30	$SV = -0.007 \bullet \%P + 0.675$	$\%TV = -1.10 \bullet \%P + 100$	$\frac{-0.984}{0.002}$	$0.574 \le \beta_0 \le 0.776$ $-0.011 \le \beta_1 \le -0.004$	$85.0 \le \beta'_0 \le 115$ $-1.62 \le \beta'_1 \le -0.580$	−0.91		5 data points	45
Si_3N_4	37, 38			Shear waves				3.30	$SV = -0.007 \bullet \%P + 0.645$	$\%TV = -1.07 \bullet \%P + 100$	$\frac{-0.973}{0.0001}$	$0.624 \le \beta_0 \le 0.666$ $-0.008 \le \beta_1 \le -0.006$	$96.6 \le \beta'_0 \le 103$ $-1.22 \le \beta'_1 \le -0.928$	−0.935		16 data points, all shear wave data	46
Si_3N_4	36-38															Comparison	47
Steel A-direction (See ref.)	39		Possibly particle contact anistropy (≤ 5%) based on pressing direction	Thru-transmission pulse-echo overlap, Dry coupling, Longitudinal waves, 1.5-2.25 MHz	≤ 0.01	ASTM B-328-60	Undetermined, probably ≤ 2%	7.85	$LV = -0.007 \bullet \%P + 0.563$	$\%TV = -1.19 \bullet \%P + 100$	$\frac{-0.972}{0.0001}$	$0.551 \le \beta_0 \le 0.574$ $-0.007 \le \beta_1 \le -0.006$	$98.0 \le \beta'_0 \le 102$ $-1.32 \le \beta'_1 \le -1.06$	−0.84		Measurements made in 3 directions (A, B, C) with respect to pressing direction for sintered steel rectangles; some residual particle contact anistropy may be responsible for small directional dependence of velocity; velocity also may be path-length dependent 22 data points for A-direction 16 data points for B-direction 18 data points for C-direction	48
Steel B-direction (See ref.)	39			Thru-transmission pulse-echo overlap, Dry coupling, Longitudinal waves, 1.5-2.25 MHz	≤ 0.01	ASTM B-328-60	Undetermined, probably ≤ 2%	7.85	$LV = -0.009 \bullet \%P + 0.588$	$\%TV = -1.53 \bullet \%P + 100$	$\frac{-0.985}{0.0001}$	$0.573 \le \beta_0 \le 0.602$ $-0.010 \le \beta_1 \le -0.008$	$97.6 \le \beta'_0 \le 102$ $1.68 \le \beta'_1 \le -1.37$	−0.65			49
Steel C-direction (See ref.)	39			Thru-transmission pulse-echo overlap, Dry coupling, Longitudinal waves, 1.5-2.25 MHz	≤ 0.01	ASTM B-328-60	Undetermined, probably ≤ 2%	7.85	$LV = -0.009 \bullet \%P + 0.590$	$\%TV = -1.48 \bullet \%P + 100$	$\frac{-0.996}{0.0001}$	$0.583 \le \beta_0 \le 0.597$ $-0.009 \le \beta_1 \le -0.008$	$98.8 \le \beta'_0 \le 101$ $-1.54 \le \beta'_1 \le -1.41$	−0.68			50
Steel	39															Comparison	51

Table 1. -ULTRASONIC VELOCITY VERSUS PERCENT POROSITY: REVIEW AND STATISTICAL ANALYSIS—CONTINUED

Material	Reference	Processing Notes/ Chemical Additives	Microstructural Anisotropy	Velocity Measurement Technique	Velocity Measurement Uncertainty (%)	Density Measurement Technique	Density Measurement Uncertainty (%)	Theoretical Density, ρ_o, Used to Calculate % Porosity (g/cc)	Predicted Line Equation ($V = \beta_1 \bullet \%P + \beta_0$)	Predicted Line Equation ($\%TV = \beta'_1 \bullet \%P + \beta'_0$)	Correlation Coefficient / Level of Significance	95% Confidence Intervals for Predicted Intercept (β_0) and Slope (β_1)	95% Confidence Intervals for Predicted Intercept (β'_0) and Slope (β'_1)	$\frac{\Delta\% P}{\Delta\% TV}$	Largest Velocity Variation Across One Surface of Specimen (%)	Comments	Corresponding Figure Number
Tungsten	2	Kenna nominal 4 micron starting powder size		Thru-transmission pulse-echo overlap, Longitudinal waves, 1 MHz	≤ 0.5	ASTM C20-46 Liquid-immersion	≤ 2	19.3	$LV = -0.005 \bullet \%P + 0.520$	$\%TV = -0.939 \bullet \%P + 100$	$\frac{-0.960}{0.010}$	$0.465 \le \beta_0 \le 0.575$ $-0.007 \le \beta_1 \le -0.003$	$89.4 \le \beta'_0 \le 111$ $-1.38 \le \beta'_1 \le -0.501$	-1.06		Velocity shown to be sensitive to pore size distribution/mean pore size and grain size distribution/mean grain size which is a function of starting powder size distribution. These results show different theoretical velocity for tungsten depending on the starting powder size. 5 data points for Kenna 4 μm powder; 5 data points for GE 4 μm powder; 4 data points for GE 18 μm powder. Each data point is average of 17 measurements across sample	52
Tungsten	2	G.E. nominal 4 micron starting powder size		Thru-transmission pulse-echo overlap, Longitudinal waves, 1 MHz	≤ 0.5	ASTM C20-46 Liquid-immersion	≤ 2	19.3	$LV = -0.006 \bullet \%P + 0.558$	$\%TV = -1.13 \bullet \%P + 100$	$\frac{-0.918}{0.028}$	$0.387 \le \beta_0 \le 0.729$ $-0.007 \le \beta_1 \le -0.006$	$69.3 \le \beta'_0 \le 131$ $-1.92 \le \beta'_1 \le -0.351$	-0.88			53
Tungsten	2	G.E. nominal 18 micron starting powder size		Thru-transmission pulse-echo overlap, Longitudinal waves, 1 MHz	≤ 0.5	ASTM C20-46 Liquid-immersion	≤ 2	19.3	$LV = -0.008 \bullet \%P + 0.554$	$\%TV = -1.38 \bullet \%P + 100$	$\frac{-0.992}{0.008}$	$0.471 \le \beta_0 \le 0.637$ $-0.011 \le \beta_1 \le -0.005$	$85.1 \le \beta'_0 \le 115$ $-1.92 \le \beta'_1 \le -0.832$	-0.72			54
Tungsten	2			Longitudinal waves				19.3	$LV = -0.006 \bullet \%P + 0.533$	$\%TV = -1.11 \bullet \%P + 100$	$\frac{-0.916}{0.0001}$	$0.482 \le \beta_0 \le 0.583$ $-0.008 \le \beta_1 \le -0.004$	$90.5 \le \beta'_0 \le 109$ $-1.41 \le \beta'_1 \le -0.802$	-0.901		14 data points, all longitudinal wave data	55
Tungsten	2															Comparison	56
UO_2	40			Thickness-cum-velocity meter, Longitudinal waves, 10 MHz	≤ 1	ASTM C-753-88	≤ 2	10.96	$LV = -0.008 \bullet \%P + 0.550$	$\%TV = -1.49 \bullet \%P + 100$	$\frac{-0.997}{0.0001}$	$0.547 \le \beta_0 \le 0.552$ $-0.009 \le \beta_1 \le 0.008$	$99.5 \le \beta'_0 \le 100$ $-2.09 \le \beta'_1 \le -0.883$	-0.67		17 data points	57
$(U_{0.30}Pu_{0.70})C$	41			Thickness-cum-velocity meter, Longitudinal waves, 15 MHz	≤ 1	ASTM C-753-88	≤ 2	12.19	$LV = -0.004 \bullet \%P + 0.460$	$\%TV = -0.958 \bullet \%P + 100$	$\frac{-0.949}{0.051}$	$0.422 \le \beta_0 \le 0.496$ $-0.009 \le \beta_1 \le 0.00003$	$92.0 \le \beta'_0 \le 108$ $-1.92 \le \beta'_1 \le 0.005$	-1.04		4 data points	58
$YBa_2Cu_3O_{7-x}$	43	Different starting powders		Pulse-echo/cross-correlation, Longitudinal waves, Dry and wet coupling, 5-20 MHz	≤ 0.4	Dry-wt. dimensional	≤ 1	6.38	$LV = -0.007 \bullet \%P + 0.565$	$\%TV = -1.28 \bullet \%P + 100$	$\frac{-0.991}{0.0001}$	$0.554 < \beta_0 < 0.576$ $-0.008 < \beta_1 < -0.007$	$98.0 < \beta'_0 < 102$ $-1.39 < \beta'_1 < -1.16$	-0.781		13 data points	59

Table 1.-ULTRASONIC VELOCITY VERSUS PERCENT POROSITY: REVIEW AND STATISTICAL ANALYSIS—CONCLUDED

Material	Reference	Processing Notes/ Chemical Additives	Microstructural Anisotropy	Velocity Measurement Technique	Velocity Measurement Uncertainty (%)	Density Measurement Technique	Density Measurement Uncertainty (%)	Theoretical Density, ρ_0, Used to Calculate % Porosity (g/cc)	Predicted Line Equation ($V = \beta_1 \bullet \%P + \beta_0$)	Predicted Line Equation ($\%TV = \beta'_1 \bullet \%P + \beta'_0$)	Correlation Coefficient / Level of Significance	95% Confidence Intervals for Predicted Intercept (β_0) and Slope (β_1)	95% Confidence Intervals for Predicted Intercept (β'_0) and Slope (β'_1)	$\frac{\Delta\% P}{\Delta\% TV}$	Largest Velocity Variation Across One Surface of Specimen (%)	Comments	Corresponding Figure Number
$YBa_2Cu_3O_{7-x}$ Superconductor	43		Insignificant	Pulse-echo/cross-correlation, Shear waves, 10 MHz	≤ 0.4	Dry-wt. dimensional	≤ 1	6.38	SV = −0.002 • %P + 0.313	%TV = −0.768 • %P + 100	−0.814 / 0.0486	$0.252 \le \beta_0 \le 0.373$ $-0.005 \le \beta_1 \le -0.00002$	$81.6 \le \beta'_0 \le 119$ $-1.53 \le \beta'_1 \le -0.007$	−1.30		1 data point; sample was single-phase, untextured, and free of nonuniform stress	60
	42			Phase comparison method, Shear waves, 50 MHz	≤ 2											1 data point	
	11			Pulse-echo overlap, Shear waves, 3-10 MHz	≤ 1 dimensional	Dry-wt.	≤ 1									2 data points, samples are not compositionally homogeneous	
	44			Pulse-echo matchup, Shear waves, 3-4 MHz	≤ 1	Dry-wt. dimensional	≤ 1									1 data point	
	45			Thru-transmission pulse-echo overlap, Shear waves, 5 MHz	≤ 3	Liquid-immersion	≤ 2									1 data point	
$YBa_2Cu_3O_{7-x}$	11, 42–45															Comparison	61

Table 2. --COMPARISON OF V_o PREDICTED FROM REGRESSION ANALYSIS WITH THAT CALCULATED FROM EQUATIONS 7 (LONGITUDINAL VELOCITY) AND 7a (SHEAR WAVE VELOCITY)

		Longitudinal Wave Velocity			Shear Wave Velocity			Values substituted into eqs. (7) [For Longitudinal Wave Velocity] and (7a) [For Shear Wave Velocity] to obtain V_{oC}		
Material	Single crystal (S) or poly-crystalline (P)	Average V_o from regression (V_{oR}) [cm/μsec]	Calculated V_o from eq. (7) (V_{oC}) [cm/μsec]	% Variation between V_{oC} and V_{oR} $=\{100((V_{oC}-V_{oR})/V_{oC})\}$	Average V_o from regression (V_{oR}) [cm/μsec]	Calculated V_o from eq. (7a) (V_{oC}) [cm/μsec]	% Variation between V_{oC} and V_{oR} $=\{100((V_{oC}-V_{oR})/V_{oC})\}$	Fully-dense elastic modulus, E_0 (x 10-6) psi /(ref.)	Poisson's ratio, ν/(ref.)	Theoretical density, ρ_0 (g/cm^3)
Al_2O_3	S		1.10	3.6		0.643	2.2	58.4/(Ref. 3)	0.25/(Ref. 48)	3.98
	P	1.06	1.12	5.4	0.657	0.659	0.30	61.2/(Ref. 3)	0.25/(Ref. 48)	3.98
SiC	S		1.16	5.5		0.730	7.7	58.2/(Ref. 3)	0.17/(Ref. 49)	3.22
	P	1.22	1.22	0.0	0.786	0.769	2.2	64.6/(Ref. 3)	0.17/(Ref. 49)	3.22
Si_3N_4	P	1.12	0.977	15.4	0.657	0.585	12.3	40.0/(Ref. 3)	0.22/(Ref. 3)	3.30
UO_2	S		0.558	1.4				33.4/(Ref. 3)	0.33/(Ref. 3)	10.69
	P	0.550	0.551	0.2				32.6/(Ref. 3)	0.33/(Ref. 3)	10.69
$YBa_2Cu_3O_{7-x}$	P	0.565	0.594	4.8	0.313	0.374	16.3	32.8/(Ref. 46)	0.27/(Ref. 11)	6.38
Steel	P	0.580	0.614	5.5				29.0/(Ref. 47)	0.33/(Ref. 47)	7.85
Tungsten	P	0.541	0.509	6.1				58.0/(Ref. 47)	0.27/(Ref. 47)	19.3

Table 3. Examples of Property Variation in the YBCO Superconductor

Property	Range of Variation	Reference	Comments
Transition Temperature (T_c)	80 - 90 K	Beyers, et al., 1989 Park, et al., 1988	Depends Strongly on Oxygen Content
Resistive and Magnetic Transition Width	1 - 30 K	Beyers, et al., 1987 Cima, et al., 1987 Clarke, et al., 1989 Gaiduk, et al., 1988 Kupfer, et al., 1988 Park, et al., 1988	Traditionally, an indicator of phase and compositional purity
Transport Critical Current Density (J_c) at 77 K	10 - 1000 A/cm^2	Alford, et al., 1988 Camps, et al., 1987 Davis, et al., 1989 Flukiger, et al., 1988 Shelton, et al., 1988 Stephens, 1989	Higher in textured bulk samples and epitaxial thin films
Sharpness of The Resistive Transition (n) at 77 K	10 - 60	Evetts, et al., 1989 Tenbrink, et al., 1990	$V = kI^n$ where V and I are voltage and current, respectively, and k and n are constants

Table 4. Summary of Intergranular Coupling for the High-T_c Polycrystalline Superconductors

Situation	Condition	Result
Very weak intergranular coupling	$j_{cJ} < [(2.07 \times 10^{-7}\ \text{Gauss/cm}^2)/(L\lambda)] \cdot [(a+b)/ab]$	$J_c = j_{cJ}$
Very strong intergranular coupling	$j_{cJ} > j_{cG}(\lambda/L)^2$	$J_c = j_{cJ}$
Intermediate coupling	Weak-Link, self-field- and cross-section-limited J_c	$J_c = (5/\pi)[(a+b)/ab]H_{1/2}$

Table 5. Summary of Specimens Used in Experiments 1, 2, and 3

Experiment	Specimens[a]	Oxygenation Condition
1: Pore Fraction Effects	52A - E,C	oxidized
	53A - E,C	oxidized
	59A - E,C	oxidized
	60A - E,C	oxidized
	51A	oxidized
	46B	oxidized
2: Spatial Variations	46B, 99 & others	oxidized
3: Oxygen Content Effects	52A	unoxidized, oxidized
	53A	oxidized, reduced
	59A	oxidized, reduced
	60A	oxidized, reduced
	51A	unoxidized, oxidized, reduced

[a]C and E denote center- and edge-cut bars, respectively

Table 6. Heating/Sintering/Cooling Schedules for YBCO Samples

a. Schedule 1 - Sinter and Cool in Oxygen

Segment	Heat to: (temp, °C)	Cool to: (temp, °C)	For: (time, hrs.)	Atmosphere
1	100		0.167	oxygen
2	peak		4.5	oxygen
3	peak hold		1.5	oxygen
4		600	2	oxygen
5		300	13	oxygen
6		200	1	oxygen
7		39	1	oxygen
8		25	-----	air

b. Schedule 2 - Sinter in Oxygen and Then Cool in Argon

Segment	Heat to (temp, °C)	Cool to: (temp, °C)	For: (time, hrs.)	Atmosphere
1	100		0.167	oxygen
2	peak		4.5	oxygen
3	peak hold		1.5	oxygen
4		825	0.75	oxygen
5		hold at 825	2	O → Ar
6		600	1.25	Argon
7		300	13	Argon
8		200	1	Argon
9		39	1	Argon
10		25	-	air

Table 7. Schedule 3 - Oxidation For YBCO samples

Segment	Heat to: (temp, °C)	Cool to: (temp, °C)	For: (time, hrs.)	Atmosphere[a]
1	100		0.167	argon
2	825		4.5	argon
3	hold at 825		2	Ar → O
4		600	1.25	oxygen
5		300	13	oxygen
6		200	1	oxygen
7		39	1	oxygen
8		25	-	air

[a]Argon was flushed through the furnace for 2 hours prior to the run

Table 8. Schedule 4 - Oxidation For YBCO samples

Segment	Heat to: (temp, °C)	Cool to: (temp, °C)	For: (time, hrs.)	Atmosphere
1	100		0.167	oxygen
2	825		4.5	oxygen
3		600	1.25	oxygen
4		hold at 600	53[a]	oxygen
5		300	13	oxygen
6		200	1	oxygen
7		39	1	oxygen
8		25	-	air

[a]Power outage occured 45 hours into 48 hour hold; the schedule was started over and another 8 hour hold took place

Table 9. Schedule 5 - Reduction For YBCO samples

Segment	Heat to: (temp, °C)	Cool to: (temp, °C)	For: (time, hrs.)	Atmosphere
1	100		0.167	oxygen
2	800		4	oxygen
3	hold at 800		7	O → Ar
4		600	1.25	argon
5		300	13	argon
6		200	1	argon
7		39	1	argon
8		25	-	air

Table 10a. Dimensional Characteristics For Bars Cut From Samples 52A, 53A, 59A, and 60A

Sample	Length (cm)[c]	Width (cm)[c]	Height (cm)[c]	Cross-Sectional[d] Area (cm^2)
52A-C[a]	0.9995	0.2993	0.1802	0.05393
52A-E[b]	0.9993	0.2996	0.1800	0.05393
53A-C	0.9996	0.2999	0.2499	0.07495
53A-E	0.9996	0.2990	0.2501	0.07478
59A-C	0.9999	0.3002	0.2501	0.07508
59A-E	0.9992	0.2997	0.2499	0.07490
60A-C	1.0003	0.2995	0.2495	0.07475
60A-E	0.9990	0.2999	0.2509	0.07524

[a] C denotes bar cut from center of disk

[b] E denotes bar cut from edge of disk

[c] % uncertainty in dimensional measurements = ±0.0005 cm

[d] % uncertainty in cross-sectional area = 0.26 %

Table 10b. Microstructural Characteristics For Bars Cut From Samples 52A, 53A, 59A, and 60A

Sample	Peak Sintering Temp. (°C)	As-received Surface Macrocracked ?	Bulk[a] Density (g/cc)	Pore Fraction[b]	Ultrasonic[c] Velocity (cm/μsec)	Mean[d] Grain Diameter (μm)	Grain Diameter Range (μm)
52A-C	937	no	4.758	0.254	0.382	1.99	0.5 - 8
52A-E			4.743	0.257	0.383	2.09	0.5 - 8
53A-C	947	no	4.986	0.219	0.404	2.43	1 - 8
53A-E			4.994	0.217	0.406	2.43	1 - 10
59A-C	954	no	5.027	0.212	0.422	2.56	1 - 20
59A-E			5.089	0.202	0.427	2.47	1 - 15
60A-C	966	yes	5.793	0.092	0.494	4.65	2 - 45
60A-E			5.760	0.097	0.494	4.87	2 - 40

[a]Bulk density obtained from dimensions and dry weight (% uncertainty < 0.5 %)

[b]Theoretical density = 6.38 g/cc

[c]Ultrasonic (longitudinal wave) velocity obtained from dry-coupled, pulse-echo measurements at 10 MHz (center frequency); the cross-correlation method calculated the time delays to be identical for 25 repeated measurements

[d]Grain Diameter estimates obtained from Heyn-intercept method (ASTM E112-85) in four directions of photomicrograph with at least 100 grains sampled (estimated % uncertainty = ±20 %)

Table 10c. Unit Cell Parameters From X-ray Diffraction For Bars Cut From Samples 52A, 53A, 59A, and 60A

Sample	A-axis Length (Å)	B-axis Length (Å)	C-axis Length (Å)
52A-C	3.828±0.003	3.890±0.002	11.679±0.006
52A-E	3.828±0.002	3.888±0.002	11.676±0.005
53A-C	3.832±0.003	3.892±0.002	11.684±0.007
53A-E	3.828±0.002	3.883±0.002	11.664±0.005
59A-C	3.831±0.002	3.885±0.002	11.664±0.005
59A-E	3.837±0.005	3.890±0.003	11.686±0.010
60A-C	3.836±0.002	3.887±0.001	11.673±0.004
60A-E	3.833±0.001	3.886±0.001	11.672±0.003

[a]x-ray diffraction run at 2°/minute with Cu-Kα radiation; mean ± standard deviation from least-squares refinement of x-ray diffraction data using the same 16 peaks in all cases

Table 10d. Elemental Analysis of Samples 52A, 53A, 59A, and 60A

Sample	Yttrium (wt%)[a]	Barium (wt%)[a]	Copper (wt%)[a]	Y:Ba:Cu atomic ratio	CuO[b] phase (vol%)	Silicon[c] contamination (wt%)
52A	13.3±0.4	40.6±0.1	30.4±0.6	1:2:3	2 - 5	0.169
53A	13.4±0.4	40.6±0.2	30.4±0.6	1:2:3	< 1	0.084
59A	13.4±0.5	40.7±0.4	30.4±1.0	1:2:3	< 1	0.038
60A	13.4±0.4	40.6±0.1	30.3±0.6	1:2:3	< 1	0.096

[a]elemental analysis determined from Inductively Coupled Plasma-Atomic Emission Spectroscopy (ICP-AES), mean ± standard deviation for 3 trials; (estimated % uncertainty = 5 % of reading)

[b]estimated from white regions in porosity distribution photomicrographs

[c]elemental analysis obtained from colorimetric technique, mean ± standard deviation for 2 trials; (estimated % uncertainty = 10 % of reading)

Table 10e. Oxygen Content For Bars Cut From Samples 52A, 53A, 59A, and 60A

Sample	Oxygen (wt%)[a]	# of O atoms[b]	# of O atoms[c]	# of O atoms[d]
52A-C	18.1±0.11	7.65	6.91±0.04	6.81±0.03
52A-E	18.2±0.18	7.7	6.93±0.03	6.83±0.03
53A-C	17.9±0	7.55	6.88±0.04	6.79±0.04
53A-E	18.1±0.36	7.65	7.00±0.03	6.90±0.03
59A-C	18.0±0.18	7.6	7.00±0.03	6.90±0.03
59A-E	18.2±0.36	7.7	6.87±0.06	6.78±0.05
60A-C	18.2±0.18	7.7	6.95±0.02	6.85±0.02
60A-E	18.0±0.18	7.6	6.95±0.02	6.85±0.02

[a] inert gas fusion, mean ± standard deviation for 2 trials (estimated % uncertainty = 1 % of reading)

[b] Calculated from ratio of oxygen atomic weight to YBCO molecular weight, (assuming all oxygen is tied up in YBCO, i.e., ignoring CuO and other impurities)

[c] Calculated (mean ± standard deviation) from Wolf et al. (1988) relation {atoms O = 76.40 - 5.95*caxis}; (estimated uncertainty = ±0.05 atoms O) caxis = c-axis length obtained from least squares refinement of x-ray diffraction data

[d] Calculated (mean ± standard deviation) from Ono (1987) relation {atoms O = 70.512 - 5.454*caxis}; (estimated uncertainty = ±0.05 atoms O)

Table 11. Microstructural and Compositional Characteristics For Center-(C) and Edge-(E) Cut Bars from Sample 46B

Property	C	E
Dimensions (L x W x H) (cm)	L = 0.51±0.03 W = 0.310±0.001 H = 0.228±0.0005	L = 0.50±0.03 W = 0.304±0.001 H = 0.231±0.0005
Mean Grain Diameter[a] (μm)	2.41	2.58
A-axis length[b] (Å)	3.850±0.007	3.847±0.010
B-axis length[b] (Å)	3.889±0.006	3.889±0.007
C-axis length[b] (Å)	11.682±0.018	11.684±0.023
Oxygen (wt%)[c]	16.4±0.66	16.8±1.60
# of O atoms[d]	6.8	7.0
# of O atoms[e]	6.89±0.11	6.88±0.14
# of O atoms[f]	6.80±0.10	6.79± 0.13

[a]Grain diameter estimates obtained from Heyn-intercept method (ASTM E112-85) in four directions of photomicrograph with at least 100 grains sampled (estimated % uncertainty = ±20 %)

[b]X-ray diffraction; mean ± standard deviation from least-squares refinement technique

[c]Inert gas fusion, mean ± standard deviation for 2 trials (estimated % uncertainty = 1 % of reading)

[d]Calculated from ratio of oxygen atomic weight to YBCO molecular weight, (assuming all oxygen is tied up in YBCO, i.e., ignoring CuO and other impurities

[e]Calculated (mean ± standard deviation) from Wolf, et al. (1988) relation {atoms O = 76.40 - 5.95*caxis}; (estimated uncertainty = ±0.05 atoms O)

[f]Calculated (mean ± standard deviation) from Ono (1987) relation {atoms O = 70.512 - 5.454*caxis}; (estimated uncertainty = ±0.05 atoms O)

Table 12. Superconductor Behavior For Center- (C) and Edge- (E) Cut Bars of Sample 46B

Property	C	E
T_c(K)[a]	75	86
%CS (T=77.5)[a]	1	40
ΔT_{cm}[b]	4	16.5
Temperature of Loss[c] Peak(s) Initial Rise (K)	63.5	83, 67
Temperature of Loss[c] Peak(s) Center (K)	67.5	84, 70
Breadth of Loss[c] Peak(s) (K)	7	4.5, 9
Resistivity at 77 K[d] (Ω-cm)	0.00215	0.000706

[a] T_c determined from the temperature where 1% of complete shielding occurred; i.e., the onset of the magnetic transition (χ');
% complete shielding (%CS) determined from χ' susceptibility response;
Experimental uncertainty in the temperature measurement = ±0.5 K;
Percent uncertainty in χ' is estimated at ±6 % due to sample dimension uncertainty

[b] ΔT_{cm} determined from the difference in the temperature where 10% and 90 % of complete shielding occurred

[c] Loss peak data obtained from χ'' susceptibility response

[d] Resistivity determined from current (5 - 17 mA) and bulk dimensions; (ρ = R*A/l)

Table 13. Unit Cell Parameters From X-ray Diffraction For YBCO Samples

Sample	Processing	a-axis Length[f] (Å)	b-axis Length[f] (Å)	c-axis Length[f] (Å)
53A	oxidation[a]	3.832±0.003	3.888±0.002	11.684±0.006
	reduction[e]	3.855±0.012	3.855±0.012	11.717±0.012
59A	oxidation[a]	3.834±0.004	3.888±0.003	11.675±0.008
	reduction[e]	3.847±0.012	3.847±0.012	11.705±0.025
60A	oxidation[a]	3.835±0.002	3.887±0.001	11.673±0.004
	reduction[e]	3.850±0.004	3.850±0.004	11.711±0.020
51A	unoxidized[b]	3.871±0.004	3.871±0.007	11.761±0.009
	oxidation[c]	3.848±0.009	3.892±0.007	11.693±0.022
	reoxidation[d]	3.848±0.008	3.887±0.006	11.681±0.019
	reduction[e]	3.866±0.005	3.866±0.005	11.797±0.011
52A	unoxidized[b]	3.843±0.013	3.843±0.013	11.745±0.029
	oxidation[c]	3.828±0.003	3.890±0.002	11.679±0.006

[a]Schedule 1 - see table 6a
[b]Schedule 2 - see table 6b
[c]Schedule 3 - see table 7
[d]Schedule 4 - see table 8
[e]Schedule 5 - see table 9

[f]X-ray scans run at 2°/minute with Cu-Kα radiation mean ± standard deviation from least squares refinement procedure

Table 14. Oxygen Content and Superconducting Behavior of YBCO Samples

Sample	Processing	Oxygen (wt%)[f]	# of O atoms[g]	# of O atoms[h]	T_c (K)[i]
53A	oxidation[a]	18.0±0.18	6.94±0.04	6.84±0.03	89
	reduction[e]	17.4±0.17	6.68±0.15	6.61±0.14	0
59A	oxidation[a]	18.1±0.27	6.93±0.04	6.84±0.04	88
	reduction[e]	16.9±13.4	6.76±0.15	6.67±0.14	40
60A	oxidation[a]	18.1±0.27	6.95±0.04	6.85±0.02	86
	reduction[e]	16.4±0.0	6.71±0.12	6.64±0.11	0
51A	unoxidized[b]	15.0±0.45	6.42±0.05	6.37±0.05	0
	oxidation[c]	17.2±1.20	6.83±0.13	6.74±0.12	89
	reoxidation[d]	17.7±0.11	6.90±0.11	6.80±0.10	78
	reduction[e]	16.8±0.10	6.21±0.07	6.17±0.06	0
52A	unoxidized[b]	15.1±0.45	6.52±0.17	6.45±0.16	0
	oxidation[c]	17.7±0.53	6.92±0.03	6.82±0.03	89

[a]Schedule 1 - see table 6a
[b]Schedule 2 - see table 6b
[c]Schedule 3 - see table 7
[d]Schedule 4 - see table 8
[e]Schedule 5 - see table 9

[f]Inert gas fusion, mean ± standard deviation for 2 trials (estimated uncertainty = 1% or reading)

[g]Calculated (mean ± standard deviation) from Wolf et al. (1988) relation {atoms O = 76.40 - 5.95*caxis}; (estimated uncertainty = ±0.05 atoms O); (caxis = caxis length obtained from x-ray diffraction)

[h]Calculated (mean ± standard deviation) from Ono (1987) relation {atoms O = 70.512 - 5.454*caxis}; (estimated uncertainty = ±0.05 atoms O);

[i]Determined from χ' susceptibility response at H_{ac} = 20 mOe and f = 100 Hz; 0 indicates no superconducting transition was observed

Table 15. Microstructural Characteristics and Elastic Behavior of YBCO Samples

Sample	Processing	Bulk[f] Density (g/cc)	Ultrasonic[g] Velocity (cm/μsec)	Effective[h] Elastic Modulus x 10^{-6} (psi)	Mean grain[i] Diameter (μm)	Twinning ?
53A	oxidation[a]	4.99	0.374	8.10	2.43	yes
	reduction[e]	4.85	0.360	7.30	2.49	no
59A	oxidation[a]	5.06	0.420	10.4	2.53	yes
	reduction[e]	4.86	0.394	8.76	2.78	no
60A	oxidation[a]	5.78	0.497	16.6	4.76	yes
	reduction[e]	5.62	0.485	15.3	4.63	no
51A	unoxidized[b]	5.74	0.498	16.5	4.87	no
	oxidation[c]	5.87	0.498	16.9	4.56	yes
	reoxidation[d]	5.85	0.506	17.4	4.91	yes (more apparent than for previous case)
	reduction[e]	5.72	0.495	16.3	4.71	no
52A	unoxidized[b]	4.37	0.312	4.94	2.12	no
	oxidation[c]	4.76	0.377	7.85	2.05	not sure

[a]Schedule 1 - see table 6a
[b]Schedule 2 - see table 6b
[c]Schedule 3 - see table 7
[d]Schedule 4 - see table 8
[e]Schedule 5 - see table 9

[f]Bulk density calculated from dry weight and dimensions; experimental uncertainty < 0.5 %

[g]Ultrasonic (longitudinal wave) velocity obtained from dry-coupled, pulse-echo measurements at 5 MHz center frequency

[h]Effective Elastic Modulus calculated from equation 1 (assumed Poisson's ratio is constant = 0.27 (Blendell et al., 1987))

[i]Grain diameter estimates obtained from Heyn-intercept method (ASTM E112-85) in four directions of photomicrographs with at least 100 grains sampled (estimated uncertainty = ±20 %)

Table 16. Change in Oxygen Content, Properties, and Structure of YBCO Samples After Oxidation and/or Reduction Treatments

Sample	Upon (treatment)	% Δ in[a] oxygen atoms	Superconductor[b] Transformation	Structure[c] Transformation	% Δ in[d] density (ρ)	% Δ in[e] velocity (V)	% Δ in[f] Elastic Modulus (E)
53A	reduction	-3.7	S → NS	Or → T	-2.2	-2.5	-2.4
59A	reduction	-2.4	S → MPS	Or → OII	-3.1	-4.6	-5.0
60A	reduction	-3.4	S → NS	Or → T	-2.5	-2.1	-4.0
51A	oxidation	5.9	NS → S	T → Or	2.0	0	1.2
	reoxidation	1.0	S → PS	Some Or → T'	-0.3	1.4	1.5
	reduction	-9.9	PS → NS	Or → T	-2.0	-2.0	-3.4
52A	oxidation	5.7	NS → S	T → Or	6.1	11.6	8.9

[a] % Δ in O atoms = 100 * $[O_{new} - O_{old}]/7$; O values determined from Wolf relation described previously; 7 is the ideal number of O atoms for orthorhombic YBCO

[b] S = Superconductor
NS = Not Superconducting
PS = Poorer Superconductor
MPS = Much Poorer Superconductor

[c] Deduced from 1) a.c. susceptibility (χ') versus temperature response
2) relative intensities of x-ray diffraction peaks at 2θ = 32.5 - 33°
3) oxygen content
4) unit cell parameters
5) presence of twinning

Or = Orthorhombic (6.8 < O < 7.0)
OII = Orthorhombic II (6.5 < O < 6.8)
T = Tetragonal (6.5 < O < 6.0)
T' = Tetragonal (O > 7.0)

[d] % Δ in ρ = 100 * $[\rho_{new} - \rho_{old}]$/6.38 g/cc; 6.38 g/cc is the theoretical density of YBCO with 7 O atoms

[e] % Δ in V = 100 * $[V_{new} - V_{old}]$/0.560 cm/usec; 0.560 cm/usec is the velocity of fully-dense YBCO with 7 O atoms

[f] % Δ in E = 100 * $[E_{new} - E_{old}]/32.8 \times 10^6$ psi; 32.8×10^6 psi is the Elastic modulus of fully-dense YBCO with 7 O atoms (Alford et al., 1988b)

XIV. APPENDICES

A. APPENDIX A: Introduction to Magnetic and Superconductor Phenomena

1. Magnetism

The permeability of a material is given by

$$\mu = B/H \tag{A1}$$

where H is the applied field strength and B is the total magnetic induction given by (Cullity, 1972)

$$B = (\mu_o)H + M \tag{A2}$$

where μ_o is the permeability of free space and M is the intensity of magnetization. (Several systems of definitions are currently in use in the field of magnetism. It is noted here that

1 line of magnetic force /cm^2 = 1 maxwell/cm^2

= 1 Oersted = 1 gauss = 10^{-4} Tesla = 0.8 A/cm)

Alternating magnetic flux induces circular currents called eddy currents in a good (normal-state) conductor. The eddy currents in turn generate an a.c. magnetic field that opposes the applied field thus shielding the interior of the body from the applied field (Cullity, 1972). This shielding effect causes the strength of the applied field to decrease according to (Cullity, 1972)

$$H_{x'} = H_o\{[\cosh(2x'/\delta) + \cos(2x'/\delta)]/[\cosh(d/\delta) + \cos(d/\delta)]\}^{1/2} \tag{A3}$$

where H_o is the field strength at the surface of the material, x' is the distance from the center of the material, d is the material thickness, and δ is the normal-state skin depth. The skin depth is

the depth of penetration for which $H_{x'} = H_o/e$ (= $0.37H_o$) and is given by (Cullity, 1972)

$$\delta=5030\{[\rho/(\mu*f)]\}^{1/2} \quad \text{(cm)} \qquad \text{(A4)}$$

where ρ is the resistivity of the material and f is the applied a.c. frequency. Flux penetration increases with decreasing μ and f and increasing ρ.

2. Superconductivity

Alternating magnetic flux induces circular currents in superconductor material analagous to the eddy currents induced in normal conductors. The supercurrents generated shield the interior of the body from the field and the strength of the field decreases rapidly as the field penetrates into the sample according to (Tinkham, 1985)

$$H_x = H_o\exp(-x/\lambda(T)) \qquad \text{(A5)}$$

where x is the distance from the surface of the material, and $\lambda(T)$ is the the Bardeen-Cooper-Schrieffer (BCS) (Bardeen et al., 1957) London penetration depth at temperature T. The London penetration depth is the depth of penetration for which $H_x = H_o/e$ (= $0.37H_o$) and is dependent upon temperature according to the empirical relation (Ekin, 1983)

$$\lambda(T) = \lambda(0)[1-(T/T_c)^4]^{-1/2} \qquad \text{(A6)}$$

where $\lambda(0)$ is the penetration depth at temperature T = 0 K. For temperatures near T_c (Ekin, 1983)

$$\lambda(T)|_{T->Tc} = 0.707(\lambda(0))[1-(T/T_c)]^{-1/2} \qquad \text{(A7)}$$

$\lambda(0)$ for YBCO has been estimated to be approximately 300 A° - 500 A°

(Hor et al., 1987 and Perez-Ramirez et al., 1988) from magnetization methods. $\lambda(77)$ has been estimated to be approximately 0.25 μm (Gurvitch et al., 1987; Umezawa et al., 1988 and Worthington et al., 1987) which is comparable to that calculated from equation (A7).

The finite width (the BCS coherence length) defining the diffuse boundary between superconducting and normal regions in a pure superconductor is given by (Ekin, 1983)

$$\xi(T)|_{T->Tc} = 0.74(\xi(0))[1-(T/T_c)]^{-1/2} \qquad (A8)$$

where $\xi(0)$ is the BCS coherence length at T = 0K. The coherence length is, on average, the distance between electrons in a Cooper pair. It is a measure of the scale at which lattice interruptions can disrupt the supercurrent. $\xi(0)$ has been estimated to be approximately 15 A° - 20 A° for YBCO from magnetization methods (Hor et al., 1987 and Perez-Ramirez et al., 1988).

The Ginzburg-Landau parameter provides a precise distinction between type I and type II superconductors and is given by (Ekin, 1983)

$$k = \lambda(T) / \xi(T) \qquad (A9)$$

A superconductor with $k < 0.707$ exhibits type I superconductivity while a superconductor with $k > 0.707$ exhibits type II superconductivity. For YBCO, it is seen from the estimated values of $\xi(0)$ and $\lambda(0)$ that YBCO is a type II superconductor.

In type II superconductors, two critical magnetic fields are significant. $H_{c1}(T)$ is the field below which flux is completely excluded from the interior of the grain. Above H_{c1}, but below

another critical field designated $H_{c2}(T)$, flux penetrates the material in the form of small flux tubes parallel to the applied field. The core of each tube is normal (nonsuperconducting) but the material surrounding each flux tube remains superconducting. As the applied field is increased, the number of flux tubes penetrating the material increases until they completely overlap at $H_{c2}(T)$ and the material is no longer superconducting (Kittel, 1986). In general, the critical fields decrease with increasing temperature according to (Ekin, 1983)

$$H_{ci}(T) = H_{ci}(0)[1-(T/T_c)^2] \qquad (A10)$$

where $H_{ci}(0)$ is the critical field at 0K and i = 1 or 2 (or 3 although $H_{c3}(77)$ is not discussed here (Doss, 1989)). $H_{c1}(0)$ has been estimated to be approximately 500 - 2000 Gauss for YBCO (Hor et al., 1987 and Perez-Ramirez et al., 1988). $H_{c1}(77)$ has been estimated at approximately 100 Gauss for YBCO (Dersch et al., 1988 and Solin et al., 1988). $H_{c2}(0)$ has been estimated to be approximately 10^6 to 2×10^6 Gauss (Hor et al., 1987 and Perez-Ramirez et al., 1988) for YBCO. $H_{c2}(77)$ is estimated to be approximately 5×10^4 to 5×10^5 Gauss (Flukiger et al., 1988 and Kupfer et al., 1988a).

The above formulas for $\lambda(T)$ and $\xi(T)$ are altered by the addition of impurities and defects to a pure superconductor. Such material defects shorten the electronic mean free path (l), shorten $\xi(T)$, and lengthen $\lambda(T)$ (Kittel, 1986). Also, significant anisotropy with respect to the orientation of the Cu-O basal plane is apparent for

$\lambda(T)$, $\xi(T)$, and the critical fields. Smaller $\lambda(T)$, larger $\xi(T)$, and larger critical fields by about an order of magnitude are observed parallel to the Cu-O planes compared to those parallel to the c-axis (Doss, 1989; Flukiger et al., 1988 and Kupfer et al., 1987).

B. APPENDIX B: Summary of Superconductor Properties For Samples 52A, 53A, 59A and 60A.

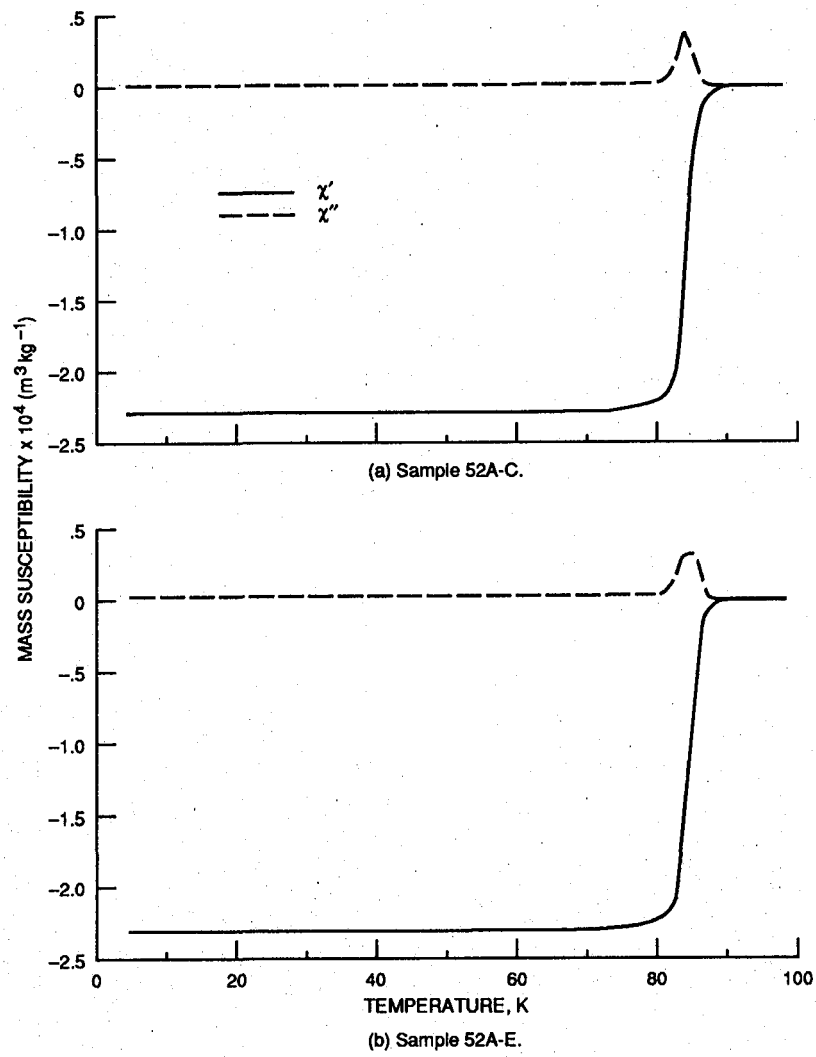

(a) Sample 52A-C.

(b) Sample 52A-E.

Figure B1. - A.c. susceptibility versus temperature for bars cut from samples 52A, 53A, 59A and 60A. H_{ac} = 0.02 Oe. Frequency = 100 Hz. C = center-cut bar, E = edge-cut bar.

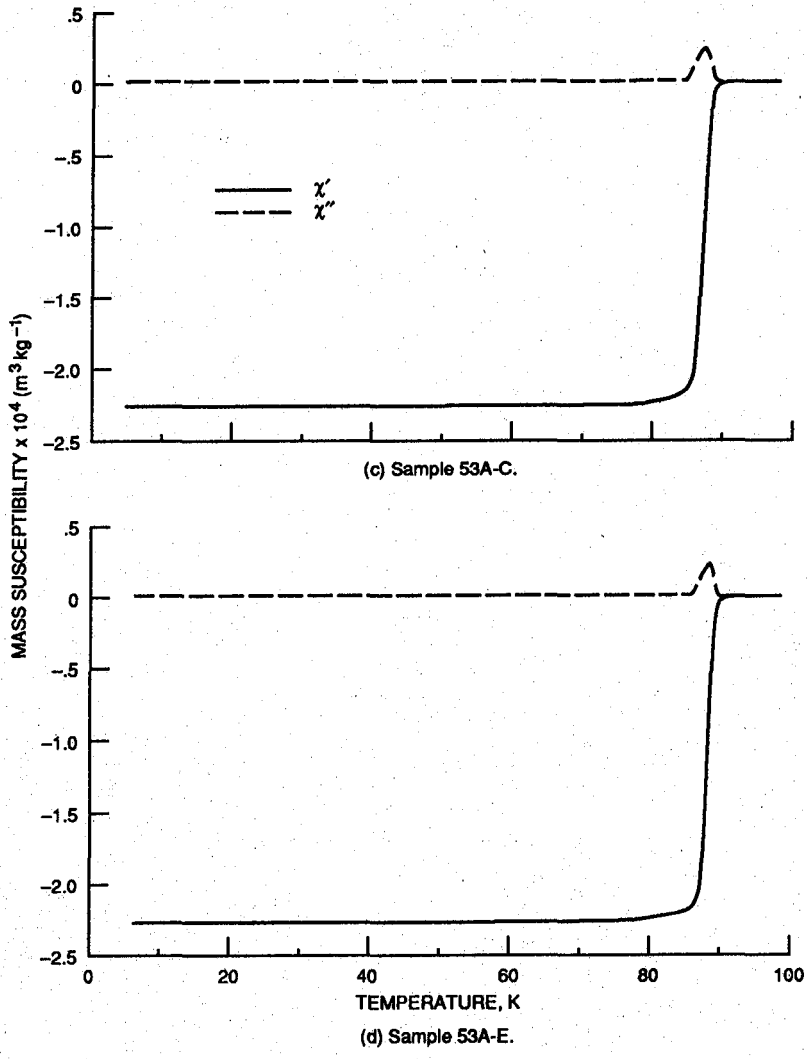

(c) Sample 53A-C.

(d) Sample 53A-E.

Figure B1. - Continued.

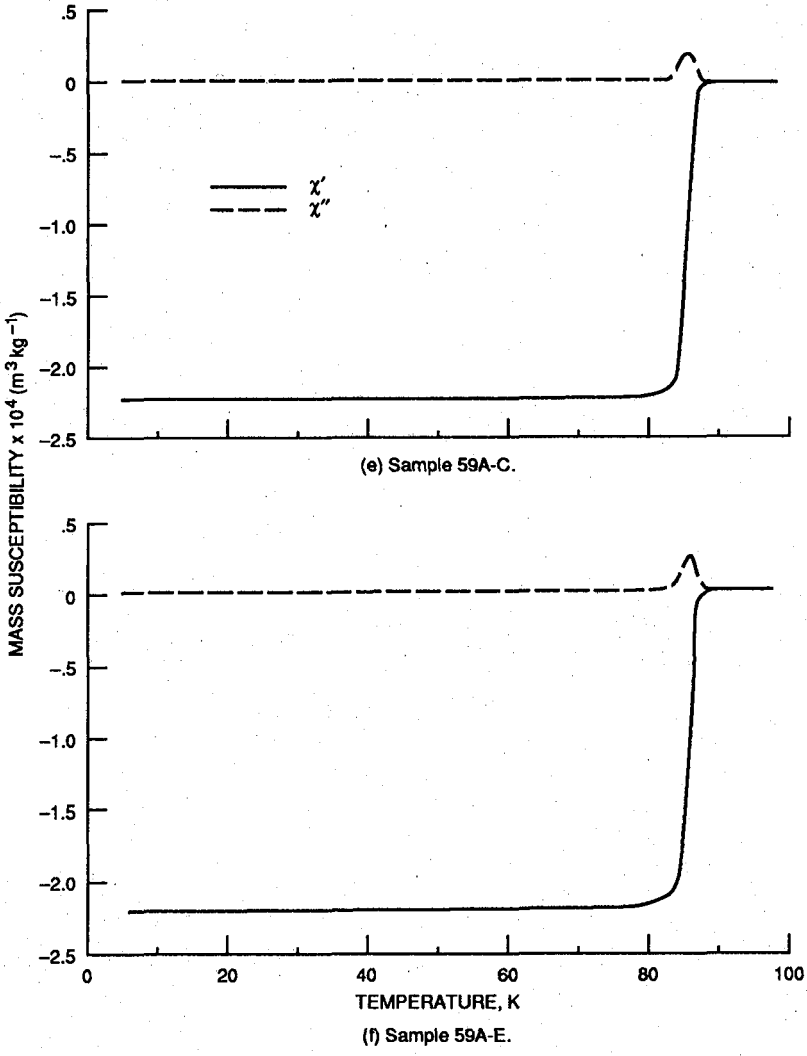

(e) Sample 59A-C.

(f) Sample 59A-E.

Figure B1. - Continued.

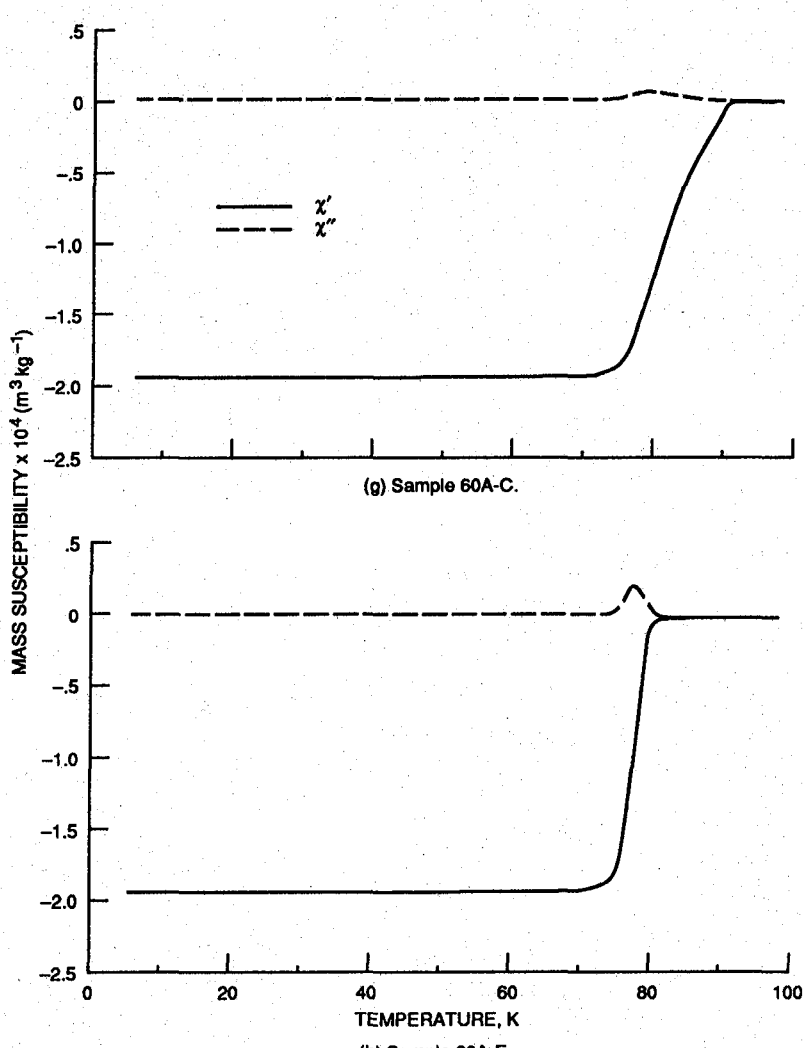

(g) Sample 60A-C.

(h) Sample 60A-E.

Figure B1. - Concluded.

Table B1. Predicted and Measured Electrical Properties at 77 K For Bars Cut From Samples 52A, 53A, 59A, and 60A

Sample	J_c[a] (A/cm^2)	Hs[b] (gauss)	n-value[c]	Correlation Coefficient of n-value fit	Predicted[d] J_{cmax} (A/cm^2)	H_{c1J}[e] (gauss)
52A-C	14.7	1.0	18.3	0.992	235	20.8
52A-E	17.3	1.2	12.3	0.988	224	19.8
53A-C	5.6	0.47	10.3	0.991	158	17.0
53A-E	----	----	----	-----	159	17.0
59A-C	20.75	1.8	25.4	0.998	151	16.2
59A-E	20.7	1.8	33.2	0.996	157	16.8
60A-C	----	----	----	-----	83	8.9
60A-E	1.6	0.1	3.9	0.988	79	8.5

[a] J_c determined at Ec = 10 uV/cm; average contact resitance (at I = 100 uAmps) = 1 Ω; ohmic contacts; estimated uncertainty in J_c = 10 %; Several trials within the same test run determined the reproducibility of the voltage-current characteristic

[b] H_s calculated from equation 29

[c] n-value determined from logarithmic fit of $E = kJ^n$; data at E > 0.1 uV/cm used for fit

[d] Predicted J_{cmax} calculated from equation 28 (approximating $H_{1/2}$ by H_{c1J} (equation (23)) with $\lambda = 0.25\ \mu m$)

[e] Predicted H_{c1J} calculated from equation 23; $\lambda = 0.25\ \mu m$; H_{c1J} is an estimate of $H_{1/2}$ (equation 27)

Table B2. Percent Complete Shielding at Various Temperatures For Bars Cut From Samples 52A, 53A, 59A, and 60A[a]

Sample	%CS(T = 90 °C)	%CS(T = 87.5 °C)	%CS(T = 85 °C)	%CS(T = 82.5 °C)	%CS(T = 80 °C)	%CS(T = 77.5 °C)	%CS(T = 75 °C)
52A-C	1	4	27	85	95	98	98
52A-E	1	3	40	88	96	98	99
53A-C	1	33	95	97	98	98	99
53A-E	1	46	96	98	99	99	99
59A-C	0	2	72	96	98	99	99
59A-E	0	4	84	97	99	99	99
60A-C	2	13	25	38	58	84	97
60A-E	0	0	0	1	6	50	93

[a]Percent complete shielding capability (%CS) data determined from χ'susceptibility response; percent uncertainty in χ' is estimated at ±0.5%; Experimental uncertainty in temperature measurement = ±0.5 K

Table B3. Transition Temperature T_c and Magnetic Transition Width (ΔT_{cm}) For The Bars Cut From Samples 52A, 53A, 59A, and 60A

Sample	T_c (K)[a]	ΔT_{cm} (K)[b]
52A-C	89	4
52A-E	89	4
53A-C	89	2
53A-E	89	1.5
59A-C	87.5	3.5
59A-E	88	3
60A-C	90	12
60A-E	82	4

[a] T_c determined from the temperature where 1 % of complete shielding occurred; i.e., the onset of the magnetic transition (χ');
% complete shielding determined from χ' susceptibility response;
Experimental uncertainty in the temperature measurement = ±0.5 K

[b] ΔT_{cm} determined from the difference in the temperatures where 10 % and 90 % of complete shielding occurred

Table B4. Loss Peak Characteristics for Bars Cut From Samples 52A, 53A, 59A, and 60A[a]

Sample	Temperature of Loss Peak initial rise (K)	Temperature of Loss Peak Center (K)	Width of loss peak (K)
52A-C	80	83.5	5.5
52A-E	80	84	6
53A-C	85	87.5	4
53A-E	85.5	87.5	4
59A-C	82.5	86	5
59A-E	83	86.5	5
60A-C	75	78	11
60A-E	74.5	77	6.5

[a]Loss peak data obtained from χ'' susceptibility response; Experimental uncertainty in temperature measurement = ± 0.5 K

NASA
National Aeronautics and Space Administration

Report Documentation Page

1. Report No.	2. Government Accession No.	3. Recipient's Catalog No.
NASA TM-103732		

4. Title and Subtitle

Property and Microstructural Nonuniformity in the Yttrium-Barium-Copper-Oxide Superconductor Determined from Electrical, Magnetic, and Ultrasonic Measurements

5. Report Date

January 1991

6. Performing Organization Code

7. Author(s)

Don J. Roth

8. Performing Organization Report No.

E-5842

10. Work Unit No.

506-43-11

9. Performing Organization Name and Address

National Aeronautics and Space Administration
Lewis Research Center
Cleveland, Ohio 44135-3191

11. Contract or Grant No.

13. Type of Report and Period Covered

Technical Memorandum

12. Sponsoring Agency Name and Address

National Aeronautics and Space Administration
Washington, D.C. 20546-0001

14. Sponsoring Agency Code

15. Supplementary Notes

This report was submitted as a dissertation in partial fulfillment of the requirements for the degree of Doctor of Philosophy to Case Western Reserve University, Cleveland, Ohio. Responsible person, Don J. Roth (216) 433-6017.

16. Abstract

The purpose of this dissertation was to 1) characterize the effect of pore fraction on a comprehensive set of electrical and magnetic properties for the yttrium-barium-copper-oxide (YBCO) high temperature ceramic superconductor and 2) determine the viability of using a room-temperature, nondestructive characterization method to aid in the prediction of superconducting (cryogenic) properties. The latter involved correlating ultrasonic velocity measurements at room temperature with property-affecting pore fraction and oxygen content variations. The dissertation is presented in two major chapters. In the first chapter, the use of ultrasonic velocity for estimating pore fraction in YBCO and other polycrystalline materials was reviewed, modeled and statistically analyzed. This chapter provided the basis for using ultrasonic velocity to interrogate microstructure. In the second chapter, 1) the effect of pore fraction (0.10 – 0.25) on superconductor properties of YBCO samples was characterized, 2) spatial (within-sample) variations in microstructure and superconductor properties were investigated and 3) the effect of oxygen content on elastic behavior was examined. Experimental methods used included a.c. susceptibility, electrical, and ultrasonic velocity measurements. Superconductor properties measured included transition temperature, magnetic transition width, transport and magnetic critical current density, magnetic shielding, a.c. loss, and sharpness of the voltage–current characteristic. Superconductor properties including within-sample uniformity were generally poorest for samples containing the lowest (0.10) pore fraction. Ultrasonic velocity was linearly related to pore fraction thereby allowing sample classification. An ultrasonic velocity image constructed from measurements at 1 mm increments across a YBCO sample revealed microstructural variations that correlated with variations in magnetic shielding and a.c. loss behavior. Destructive examination using quantitative image analysis revealed pore fraction to be the varying microstructural feature. Changes in superconducting behavior were observed consistent with changes in oxygen content. Velocity increases generally accompanied oxygen content increases, and this behavior was reversible. Similarly, elastic modulus increased with increasing oxygen content. Global patterns in velocity images were the same after oxidation and reduction treatments which correlated with destructive measurements showing insignificant changes in the pore distribution.

17. Key Words (Suggested by Author(s))	18. Distribution Statement
Superconductors; Ceramics; Microstructure; Porosity; Ultrasonics; Nondestructive testing; A.C. Susceptibility; Yttrium-Barium-Copper-Oxide; Shielding; A.C. loss	Unclassified–Unlimited Subject Category 38

19. Security Classif. (of this report)	20. Security Classif. (of this page)	21. No. of pages	22. Price*
Unclassified	Unclassified	252	A12

NASA FORM 1626 OCT 86

*For sale by the National Technical Information Service, Springfield, Virginia 22161